Vibronic Coupling in Light Diatomic Molecules:
The Hydrogen Halides

by

Gordon G. McFadyen

A thesis prepared for the degree of
Doctor of Philosophy
at the University of Edinburgh, 1991.

Acknowledgements

I would like to thank my supervisors Dr. P.R.R. Langridge-Smith and Dr. K.P. Lawley for initially stimulating my interest in the hydrogen halides and for their guidance and support throughout the course of this work. I would also like to thank Dr. M.A. Brown for helping me through my first year and Professor R.J. Donovan for many interesting discussions and for the use of experimental facilities. Dr. T. Ridley and Dr. S. Singleton were of invaluable assistance in the experimental sections and Dr. D.I. Austin introduced me to many of the computer programs which were central to this work.

I am grateful to the Science and Engineering Research Council for a post-graduate Research Studentship, to the Laser Support Facility for the use of the Nd:YAG pumped dye laser system and to Dr. A. Hopkirk of the Rutherford Appelton Laboratories for the use of a VUV photomultiplier tube. The staff of the mechanical, electronic and, in particular, glass-blowing workshops deserve great thanks for building and maintaining much of my experimental apparatus. The database used to prepare this thesis was provided by R.J. Hare of the EUCS.

Finally, I would like to thank the other research students in the laser group for their friendliness and encouragement in even the most adverse situations and for providing such a stimulating working environment. In particular I must thank Andrew Butler, Kevin Costello, Murray Brown, Andrew James, Jim Macdonald, and Scott Singleton.

Abstract

The electronic spectroscopy of the hydrogen halides has been investigated using laser multiphoton excitation techniques; the $(2+1)$REMPI spectra of HBr, DBr, and HI in the two-photon energy range 76000 - 83000 cm^{-1} and 67000 - 73000 cm^{-1}, the fluorescence excitation spectra of DCl and HI, and the fluorescence emission from ion-pair and Rydberg states in HCl, DCl, and HI have been recorded. New transitions were observed in the $(2+1)$REMPI spectra of HBr, DBr, and HI and a previously reported transition in HBr was reassigned. The fluoresence spectra recorded from a number of 0^+ Rydberg states in HCl, DCl, and HI showed structure characteristic of the ion-pair state which indicates that these states vibronically couple with the ion-pair state. In HCl and DCl the $g^3\Sigma^-$ (0^+) and $E^1\Sigma^+$ (0^+) Rydberg states are coupled to the ion-pair state while in HI the $E^1\Sigma^+$ (0^+) and $j^3\Sigma^-$ (0^+) Rydberg states are coupled to the ion-pair state.

Numerical modelling techniques were used in the analysis of both the previously reported spectra and the experimental results presented herein. The excited states and the coupling between them were modelled in both the diabatic and adiabatic representations. The vibrational energy levels and rotational constants have been calculated and the absorption and fluorescence spectra of HCl and DCl have been simulated. The comparison of observed and calculated data has been used to refine the model of the potential curves and the coupling between the states. The greatest amount of information was available for HCl and so the work reported here has concentrated on this molecule and DCl.

Table of Contents

Chapter 1
Introduction

The hydrogen halides are apparently simple, relatively light diatomic molecules with closed shell electronic ground states. They have been the subject of numerous experimental [1-36,59,60,63-65] and theoretical [37-47,56-58] studies but the electronic spectra have not yet been fully analysed and there is still very poor understanding of the electronic structure of the excited states. The electronic spectra of HF, HCl, HBr, HI and their respective deuterides are well known and in general follow the simple pattern expected [1]. There is a single bound valence state, the ion-pair state, and numerous Rydberg states. Purely valence repulsive states have also been observed. However, despite the great wealth of data available, the electronic absorption and emission spectra have resisted a full analysis because of the presence of gross perturbation of the excited states [11] [37].

The greatest perturbations are those which result from the homogeneous interaction of the ion-pair state and Rydberg states of the same Ω value, where Ω is the total electronic angular momentum of the electronic state. The vibrational progression of the ion-pair state is irregular and in HBr [11] and HI [13] [14] the value of T_e is still unknown. The perturbing Rydberg states also exhibit anomalous molecular constants. Since the interacting states possess the same symmetry the coupling is homogeneous [48] [54]. The absorption spectra involving these states are further complicated by extensive predissociation. This results in weak, diffuse lines in absorption and is responsible for the apparent absence of some states in REMPI spectroscopy.

The complexity of the spectra of the hydrogen halides may be contrasted with that of the diatomic halogen molecules. Both show evidence of predissociation and homogeneous perturbations. However, the analysis of the spectra of the ion-pair states of the halogens is much better developed than that ~~of~~ any of the hydrogen halides with the exception of HF. In common with HF the Rydberg states of the halogens have much higher T_e than those of the ion-pair states. Moreover, the halogen ion-pair states are displaced to greater internuclear separation, R, than in the hydrogen halides because of the greater size of the halogen ionic core, X^+, compared to a proton. The ion-pair states of the halogens are thus free of perturbations over a much wider energy range.

The presence of 10 valence electrons in the halogens results in a much richer variety of available electronic configurations than is possible for the hydrogen halides. The π valence orbitals of the hydrogen halides are essentially np halogen atomic orbitals because of the large energy gap between the halogen orbitals and the hydrogen orbitals of appropriate symmetry [37]. For the halogens the π orbitals feature more importantly because of the good overlap between the isoenergetic atomic orbitals. Consequently the halogen valence molecular orbitals are much more strongly bonding and antibonding than those of the hydrogen halides.

In view of this it is most surprising that the hydrogen halides have electronic spectra which are easily as complex as those of the halogens and which have proven impossible to analyse to the same degree. The complexity in the spectra of the hydrogen halide arises from *vibronic coupling*. This is a product of the break down of the Born-Oppenheimer approximation which allows the separation of nuclear and electronic motion. For the halogens, which have high reduced masses, the Born-Oppenheimer approximation remains valid. However, it breaks down for the much lighter hydrogen halides because the motion of the nuclei is much faster than in the halogens. As vibronic coupling is a homogeneous coupling, this is in agreement with the observation that the perturbations are predominantly homogeneous.

In Chapter 2 of this thesis the electronic structure of the hydrogen halides and the perturbations observed in the electronic spectra of these molecules are discussed in more detail. The theoretical background to the coupling of electronic states is presented including the two limiting cases of zeroth order corrections: the diabatic and adiabatic representations. A number of experimental observations reported in the literature are discussed with reference to the coupling between the ion-pair state and the 0^+ Rydberg states.

Chapter 3 contains details of the experimental apparatus which was used to record the ionisation and fluorescence spectra of the hydrogen halides reported in Chapter 4. There, resonance enhanced multi-photon ionisation (REMPI), laser induced fluorescence (LIF) and dispersed fluorescence spectra which were recorded for the molecules HCl, DCl, HBr, DBr, and HI are presented. The dispersed fluorescence spectra were of primary importance because of the information which they provide on the wavefunctions and potential energy curves of the initial and final states of the transitions studied. In most instances the excitation spectra were used to determine the identity of the fluorescing state. However, new excitation spectra of previously unreported vibrational levels were also recorded.

Numerical modelling techniques were used in the analysis of both previously reported spectra and the new spectra recorded during this work. The details of the potential curves, the coupling model and the numerical techniques employed are presented in Chapter 5 along with the results of the calculations. The excited states were modelled using both the diabatic and adiabatic bases. The vibrational and rotational energy levels have been calculated, and absorption and fluorescence spectra of the ion-pair state and Rydberg states of HCl and DCl have been simulated. The comparison of observed and calculated data has been used to refine the model potential curves and coupling parameters between the states.

Finally in Chapter 6 a number of conclusions are drawn as to the success of the modelling in explaining the perturbations in the electronic spectra of the hydrogen halides both in general and for HCl and DCl in particular. It is found that even for these least perturbed molecules the model is limited by the number of electronic states which can be allowed to interact.

Chapter 2
Background

2.1 The Electronic Structure of the Hydrogen Halides

2.1.1 The $X^1\Sigma^+$ Ground State

The hydrogen halides possess a closed shell electronic ground state. As both the electron spin and orbital angular momentum are zero these states are represented by the molecular term $^1\Sigma^+$ [48]. A simple LCAO MO-approach [61] to the bonding in these molecules may be used to qualitatively describe the electronic structure. Detailed *ab initio* calculations [37] [38] justify the use of this approach. A molecular energy diagram for the case of HCl is shown in figure 2.1.

The atomic orbitals available for bonding are the ns(σ), $np_{x,y}(\pi)$, and $np_z(\sigma)$ halogen orbitals (n=2,3,4, or 5 for F, Cl, Br or I) and the 1s(σ) hydrogen orbital. The symmetry of the orbital in the $C_{\infty v}$ point group is indicated in parenthesis. The π orbitals on the halogen are prevented from taking any major part in bonding with the σ orbitals by their symmetry. They are very slightly bonding because of the interaction with the hydrogen 2p orbitals, but essentially remain nonbonding π orbitals centred on the halogen atom [37].

The σ halogen orbitals can both combine with the hydrogen 1s orbital. However, while the best orbital overlap would result from the combination of the two s atomic orbitals, the energy match between hydrogen 1s and halogen ns is very poor. To a first approximation the halogen ns orbital can be regarded as

Figure 2.1 Molecular Energy Diagram for HCl

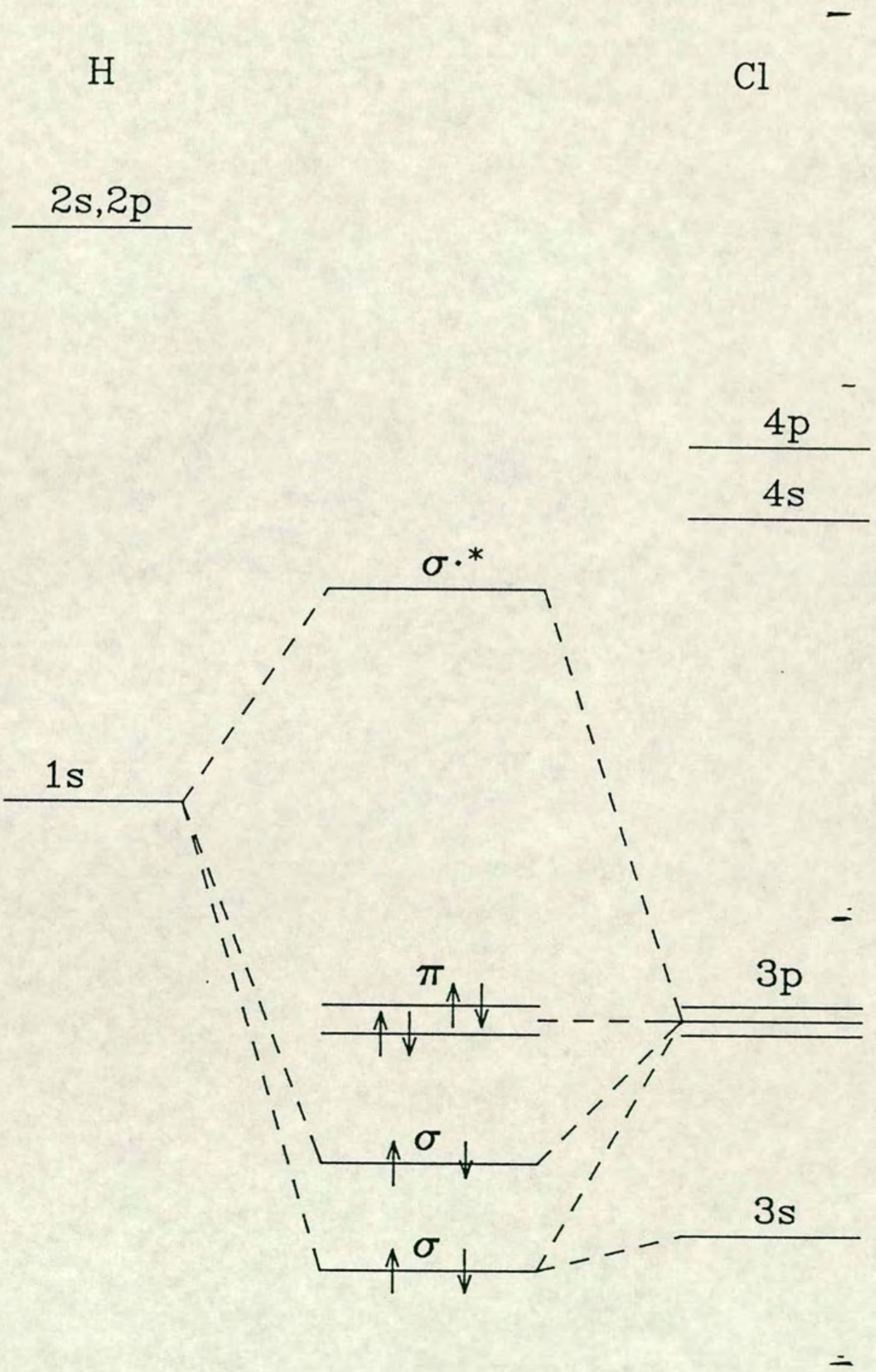

forming a nonbonding orbital. A better energy match is achieved for the halogen np_z atomic orbital which combines with the hydrogen 1s orbital to form σ bonding and σ^* antibonding molecular orbitals. The bonding and antibonding molecular orbitals are polarised towards the halogen and hydrogen nuclei respectively.

A better approximation is obtained by including the halogen ns orbitals which mix with the σ molecular orbitals. This interaction results in a slight stabilization of the halogen ns orbital which becomes slightly bonding and a slight destabilization of the σ and σ^* orbitals. The ground state configuration is thus $(\sigma^2\pi^4)$, which corresponds to a polarised molecule. The halogen nucleus will have a higher electron density than the hydrogen nucleus. The degree of polarisation decreases with increasing atomic number, z. As z increases the energy difference between the hydrogen 1s and halogen np atomic orbitals decreases and the molecular orbitals become less localised on one or the other nucleus. However, as the molecule dissociates to the neutral ground state products the configuration must change to $(\sigma^1\pi^4)\sigma^{*1}$ [37]. The ground state potential energy curve therefore results from a strongly avoided crossing between the potential for the ionic configuration, $(\sigma^2\pi^4)$, which behaves as 1/R at large R, and that for the steeply repulsive, neutral configuration, $(\sigma^1\pi^4)\sigma^{*1}$, [37] [48]. The other state formed from this configuration interaction is the $B^1\Sigma^+$ (0^+) ion-pair state.

Ab initio calculations on HF [38] [46], HCl [42-45] and HI [47] reveal that the ground state consists, as expected, predominantly of the $(\sigma^2\pi^4)$ configuration at small R and the $(\sigma^1\pi^4)\sigma^{*1}$ configuration at large R. A third configuration, corresponding to double excitation of the σ^* orbital, is important at intermediate R [37]. HBr is expected to behave similarly but there are no calculations available for this molecule.

This configurational switching is reflected in the R dependence of the dipole moment, D(R), of the ground state. For any dipolar molecule, which dissociates to neutral atoms, the dipole moment must initially increase from zero, pass through a maximum and decrease as R tends to infinity [62]. The dipole moment functions for the hydrogen halides have been observed to show the expected behaviour [63].

The potential energy curves for ground states of the hydrogen halide have been very well characterised experimentally. The lowest vibrational levels have been probed by IR and FTIR spectroscopy up to about 35% of dissociation [49]. The upper levels have been observed in emission from electronically excited molecules. The ion-pair state is the only state which can fluoresce to vibrational levels near the dissociation limit of the ground state. However, there is a gap in the observed vibrational progression of the ground state for most of these molecules between the highest state observed in absorption and the lowest observed in emission. This gap has in some cases been filled by the observation of flame emission. The available information is summarised in table 2.1.

All of the observed vibrational energy levels follow a smooth progressions to the dissociation limit. Although many of the observed levels have outer turning points which lie in the R range where the configuration will be varying most rapidly there is no indication of any perturbation in the ground state.

Table 2.1 Summary Vibrational Levels in the Ground State of the Hydrogen Halides Characterised Experimentally

	Levels	E_{max}(%D_e)	D_e	Reference	Technique
HF	0→19	95	49380	[4]	infra red, flame and emission
DF	0→5				infra red
	16→26	99			emission
HCl	0→17	96	37243	[19] [40] [41]	infra red, flame and emission
DCl	0→7			[20]	infra red
	11→23	94		[20]	emission
HBr	0→7	55	31625	[48] [67]	infra red
DBr	0→5	30		[48] [67]	infra red
HI	0→7	57	26090	[48] [68]	infra red
DI	0→5	32		[48] [68]	infra red

Excitation of an electron from the ground state to one of the higher lying orbitals will result in either a valence or a Rydberg state. In the valence states the excited electron occupies an orbital with the same principal quantum number, n, as the highest orbital in the ground state configuration. The only available valence orbital in the hydrogen halides is the σ^* antibonding orbital. Rydberg electrons have a higher value of principal quantum number and are characterised by the large separation of the excited electron from the core.

The observed single excitation configurations and resulting molecular states for the hydrogen halides are shown in table 2.2.

2.1.2 The Ion-pair Valence State

In the hydrogen halides there are four valence states; $a^3\Pi_{2,1,0}{}^{\pm}$, $A^1\Pi$, $t^3\Sigma^+$ and $B^1\Sigma^+$ (0^+). Of these only the $B^1\Sigma^+$ (0^+) ion-pair state is bound. The repulsive states dissociate to $H\,^2S_{1/2}$ plus either $X\,^2P^0_{3/2}$ or $X^*\,^2P^0_{1/2}$. The spin-orbit excited halogen atom is the dissociation product of the $^3\Sigma^+$ and $^3\Pi_0{}^+$ repulsive states [51]. The ion-pair state should dissociate to the H^+X^- limit although it may undergo interactions at large R with states correlating to other dissociation limits. In the case of HI the H^-X^+ dissociation limit lies at lower energy [55] but would not result in a state of Σ^+ symmetry [48].

The ion-pair state is characterised by a very wide, deep potential well, displaced to larger R than the ground state. Apart from the configuration interaction with the ground state, the ion-pair state is heavily perturbed by vibronic coupling with Rydberg states of $^1\Sigma^+$ or 0^+ symmetry.

Table 2.2 Molecular Terms

Configuration	**Molecular Terms**
$(\sigma^2\pi^4)$	$X^1\Sigma^+$
$(\sigma^2\pi^3)a\sigma^*$	$a^3\Pi_i(2,1,0^\pm), A^1\Pi(1)$
$(\sigma\pi^4)a\sigma^*$	$t^3\Sigma^+(1,0^-), B^1\Sigma^+(0^+)$
$(\sigma^2\pi^3)b\sigma$	$b^3\Pi_i(2,1,0^\pm), C^1\Pi(1)$
$(\sigma^2\pi^3)c\sigma$	$d^3\Pi_i(2,1,0^\pm), D^1\Pi(1)$
$(\sigma^2\pi^3)c\pi$	$e^3\Sigma^+(1,0^-), E^1\Sigma^+(0^+), f^3\Delta_i(3,2,1), F^1\Delta(2), g^3\Sigma^-(1,0^+), G^1\Sigma^-(0^-)$
$(\sigma^2\pi^3)d\pi$	$h^3\Sigma^+(1,0^-), H^1\Sigma^+(0^+), i^3\Delta_i(3,2,1), I^1\Delta(2), j^3\Sigma^-(1,0^+), J^1\Sigma^-(0^-)$
$(\sigma^2\pi^3)d\sigma$	$n^3\Pi_i(2,1,0^\pm), N^1\Pi(1)$
$(\sigma^2\pi^3)a\delta$	$k^3\Pi_i(0^\pm,1,2)), K^1\Pi(1), l^3\Phi_i(4,3,2), L^1\Phi(3)$
$(\sigma^2\pi^3)e\sigma$	$m^3\Pi_i(2,1,0^\pm), M^1\Pi(1)$
$(\sigma^2\pi^3)f\sigma$	$r^3\Pi_i(2,1,0^\pm), R^1\Pi(1)$

There have been a number of detailed *ab initio* calculations of the electronic structure of HF and HCl which indicate that the ion-pair - Rydberg interaction results in a mixed double minimum state with an inner Rydberg well and an outer ion-pair well as shown in figure 2.2. A good match between experiment and theory is achieved for HF [38]. However, the results for HCl are rather poor [37].

The double minimum potential of Bettendorf et al [37] has an outer minimum which is too high relative to the ground state and the inner minimum. The calculated values of ω_e and B_v for the outer well are too low. In addition the inner minimum is capable of supporting too many vibrational levels. A later calculation on this very demanding problem yielded much improved results but they still do not compare well with experimental data [66]. There have been no similar detailed calculations of the electronic structure of the bound excited states of HBr and HI.

2.1.3 The Repulsive Valence States

The repulsive valence states have also been studied in great detail. In particular, the repulsive states of HBr and HI have been of great interest for the production of translationally hot atomic hydrogen. The photodissociation continuum absorption bands have been recorded for all of the hydrogen halides [64] [26]. Only the $A^1\Pi$ state is dipole allowed in Λ,S coupling but the $^3\Pi_1$ and $^3\Pi_0{}^+$ states become allowed in Ω,ω coupling [56] [25]. Tendencies towards Ω,ω coupling will increase with increasing excitation and with increasing atomic number. The degree of transition towards Ω,ω coupling can be observed in the

Figure 2.2
Potential Curves for some of the Electronic States of HCl

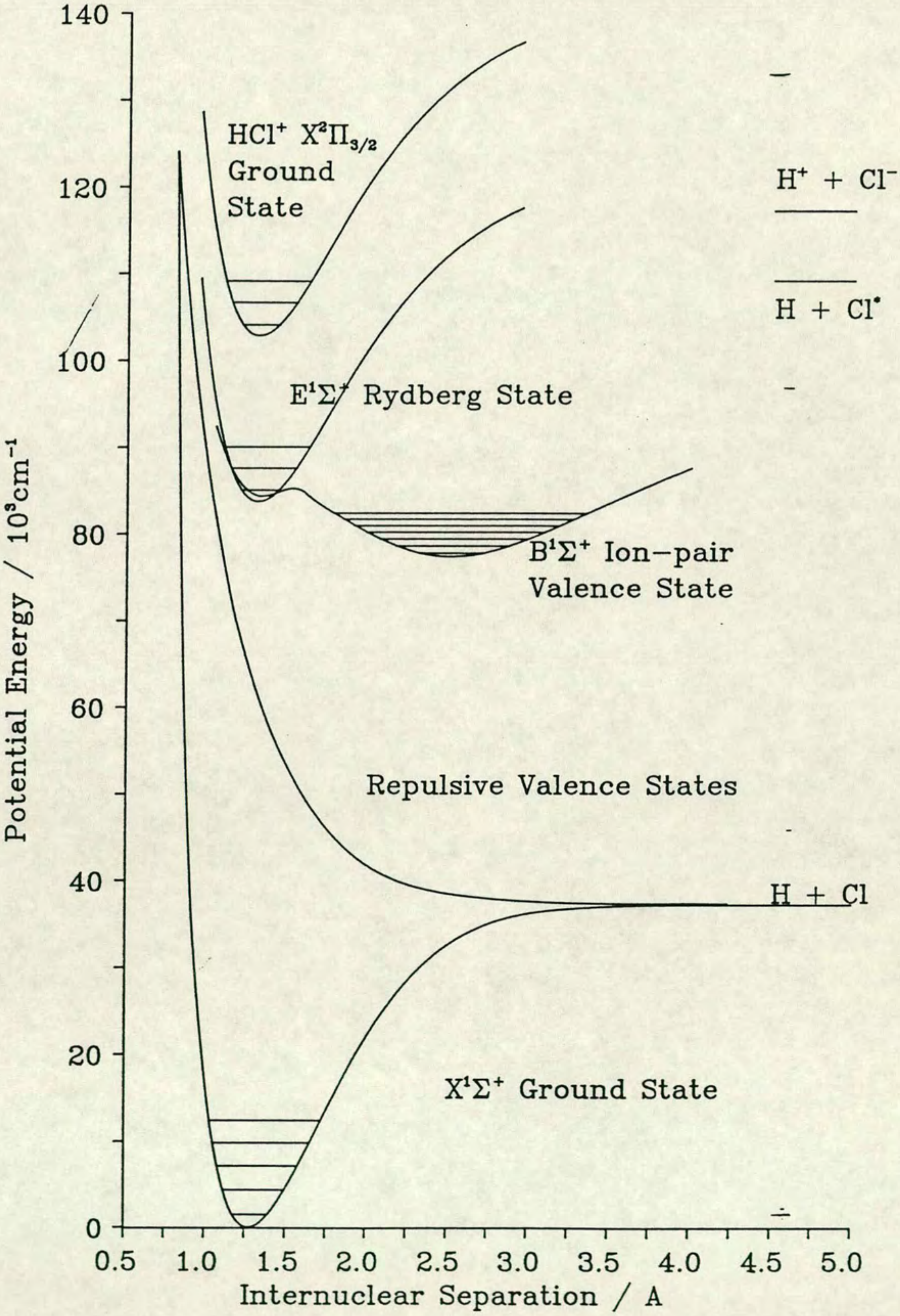

multiplet splitting and transition intensity ratios of the bound Rydberg states. In HCl [5] the lowest bound states are Λ,S coupled while in HBr [6] and HI [7] Ω,ω coupling is apparent in the lowest Rydberg states. The continuum absorption spectrum of HI is therefore a superposition of the three bands; $A^1\Pi \leftarrow X^1\Sigma^+$, $a^3\Pi_1$ (1) $\leftarrow X^1\Sigma^+$, and $a^3\Pi_0{}^+$ (0^+) $\leftarrow X^1\Sigma^+$.

The absorption spectrum can be used to determine the potential energy curve of the upper state by the reflection method. In an early analysis of the spectrum of HI this method was used to determine a single potential for the upper state [64]. Because there are three accessible repulsive states this single potential represented an average, effective potential. More recently the energy partitioning in the iodine photofragments has been used to determine the degree of dissociation via the a(0^+) state [25]. This has allowed the use of a three state model which more accurately describes the electronic structure.

The continuum absorption band of HBr, though well known experimentally [26], has not been studied in such great detail. It is expected that the photodissociation process in HBr should be very similar to that observed for HI.

In the case of HCl it has been shown that Λ,S coupling dominates and the observed spectrum is due to the absorption of the $A^1\Pi$ state alone [42]. *Ab initio* calculations of the potential energy curve of the A state and the transition dipole moment function for the $A^1\Pi \leftarrow X^1\Sigma^+$ transition give a good simulation of the observed spectrum, which is shown in figure 5.1. Calculations of the potential energy curve for the A state of HF show reasonable agreement with experimentally determined excitation energies [38].

The calculations on HF, HCl and HI indicate that the repulsive states have a single dominant configuration over almost the whole range of R. However, at small R, less than R_e of the ground state, the repulsive states interact with the manifold of Rydberg states. This interaction results in the observed electronic predissociation of the Rydberg states [66].

2.1.4 The Rydberg States

All of the observed Rydberg states of the hydrogen halides have the configuration $(\sigma^2\pi^3)n\lambda$ $(\lambda = \sigma, \pi, \delta)$ and converge to the ground state of the molecular ion, HX^+ $X^2\Pi_{3/2,1/2}$ [36]. There have been no direct observations of Rydberg states with a $(\sigma\pi^4)$ ion core although it has been suggested that they are important in the ionisation of the ion-pair state [65]. These states are expected to lie to much higher in energy and converge to the first excited state of the ion, HX^+ $^2\Sigma^+$. The analysis of the observed absorption spectra has been greatly assisted by a series of theoretical works by Mulliken [56-58]. There is insufficient information on the Rydberg states of HF to determine how well the predicted behaviour matches the observed data. However, for HCl, HBr and HI there is excellent agreement.

The lowest Rydberg states are those with the configuration $(\sigma^2\pi^3)m\sigma$. For this configuration, in Λ,S coupling, there is a $^3\Pi_{2,1,0}{}^{\pm}$ spin-orbit multiplet plus a $^1\Pi$ state. There is a fairly large singlet-triplet splitting with the $^1\Pi$ state at higher energy. The components of the multiplet will be equally spaced by about $\frac{1}{2}a$, where a is the spin-orbit splitting in the halogen atom. Apart from these strong diagonal spin-orbit splittings there will be a smaller iso-configurational interaction between the $^3\Pi_1$ component and the $^1\Pi$ state. These two states will be mixed and the equal spacing of the multiplet disrupted. The $b^3\Pi_i$ and $C^1\Pi$ Rydberg states in HCl are observed to show this behaviour while the next highest, $d^3\Pi_i$ and $D^1\Pi$, show Ω,ω coupling [5] [9]. The tendency towards Ω,ω coupling increases with increasing separation of the Rydberg electron and the core. All of the Rydberg states in HBr and HI show Ω,ω coupling [6-8,10,11,13,14].

In the limit of Ω,ω coupling there is no singlet-triplet distinction and the states have the labels 2, 1, $0^{\pm}$ and 1 [48]. The states split into two doublets separated by about a. Within the doublets the spacing is much less than a. The lower energy doublet is $^3\Pi_2(2)$ and $^3\Pi_1(1)$ and the upper is $^3\Pi_0{}^{\pm}(0^{\pm})$ and $^1\Pi(1)$. The Λ,S labels are retained to show the origin of the state. Again the two $\Omega=1$ states will be mixed by off-diagonal spin-orbit coupling.

The relative intensities of dipole transitions from the ground state can also be predicted and related to the observed splitting of the excited states [57]. For the case of Λ,S coupling only the transition to the $^1\Pi$ state is fully allowed [42], although transitions to the $^3\Pi_i$ states are also observed. The $\Delta S=0$ transition is much more intense than that to the $^3\Pi_1$ state, which is the most strongly absorbing triplet state. The transitions to the other states resulting from this configuration will be very weak. In Ω,ω coupling the $\Delta S=0$ selection rule does not hold and the transitions to $\Omega=1$ states have very similar intensities. These are somewhat stronger than the parallel transition to the 0^+ state.

The next lowest configuration is $(\sigma^2\pi^3)m\pi$. The states resulting from this configuration are: $^3\Sigma^+(1,0^-)$, $^1\Sigma^+(0^+)$, $^3\Delta_i(3,2,1)$, $^1\Delta(2)$, $^3\Sigma^-(1,0^+)$, and $^1\Sigma^-(0^-)$.

The ${}^{3,1}\Delta$ states show essentially the same behaviour as that exhibited by the ${}^{3,1}\Pi$ states of the $(\sigma^2\pi^3)\sigma$ configuration. All of the observed states of ${}^{3,1}\Delta$ symmetry show Ω,ω coupling [11].

The Σ states which have been observed also show the behaviour predicted by Mulliken [58]. But those of ${}^1\Sigma^+$ or 0^+ symmetry are heavily perturbed by vibronic coupling with the ion-pair state. This interaction results in irregular vibrational spacing and anomalously low B_v values in the ${}^1\Sigma^+$ and 0^+ Rydberg states. The bound Rydberg states are expected to have molecular constants similar to those observed for the ground states of the neutral molecule and the molecular ion. Many of the Rydberg states do show regular vibrational and rotational progressions. However, it is obvious that the molecular constants of the ${}^1\Sigma^+$ or 0^+ Rydberg states deviate quite sharply from the expected values. The greatest anomalies exist for the 0^+ states with Σ parentage although the ${}^3\Pi_0{}^+(0^+)$ states in HI are perturbed to a small extent.

A number of states resulting from the configuration $(\sigma^2\pi^3)m\delta$ have also been observed [11-14]. The predicted terms from this configuration are: ${}^3\Pi_i(0^{\pm},1,2))$, ${}^1\Pi(1)$, ${}^3\Phi_i(4,3,2)$, and ${}^1\Phi(3)$. Only the ${}^{3,1}\Pi$ states have been observed in absorption spectra and they exhibit the same behaviour as the ${}^{3,1}\Pi$ states from other configurations.

Ab initio calculations are available for the Rydberg states of HF [38] and HCl [37] only. In both of these molecules the calculated Rydberg potentials are parallel to the potential of the molecular ion state which forms the core of the Rydberg state. This is supported by the potentials calculated for the Rydberg states from experimental data as discussed in Chapter 5. Large discrepancies only occur for the ion-pair state and those Rydberg states which are mixed with it [37].

2.2 Perturbations in the Excited States of the Hydrogen Halides

A plot of the observed vibrational spacing and rotational constants, versus observed term value, in the ion-pair state of HCl [12], HCl [20], HBr, DBr [11] and HI [13] is shown in figure 2.3. It clearly illustrates the dependence of the perturbations in the ion-pair state on the position of the Rydberg levels. The corresponding data for HF [4] are not presented in this figure. For HF more than 60 levels have been observed and homogeneous perturbations such as those discussed above do not occur for vibrational levels with $v' \leqq 24$.

It is obvious from figure 2.3 that the perturbations present in the spectra become more severe as the atomic number of the halogen atom increases. Also, the perturbations in the deuterides are no less severe than in the hydrides. This is in apparent contradiction to the inverse mass dependence of vibronic coupling. However, there are a number of factors which contribute to the increased complexity of the spectra of the heavier molecules.

The coupling of the states becomes less restricted as the atomic number of the halogen, and hence the spin-orbit coupling increases [54]. In Hund's case (a) and (b) the orbital and spin angular momenta are each coupled strongly to the internuclear axis [48]. The projections of these angular momenta onto the internuclear axis, Λ and Σ, are good quantum numbers. This coupling scheme is

Figure 2.3a
Perturbations in the Ion-pair State of HCl and DCl

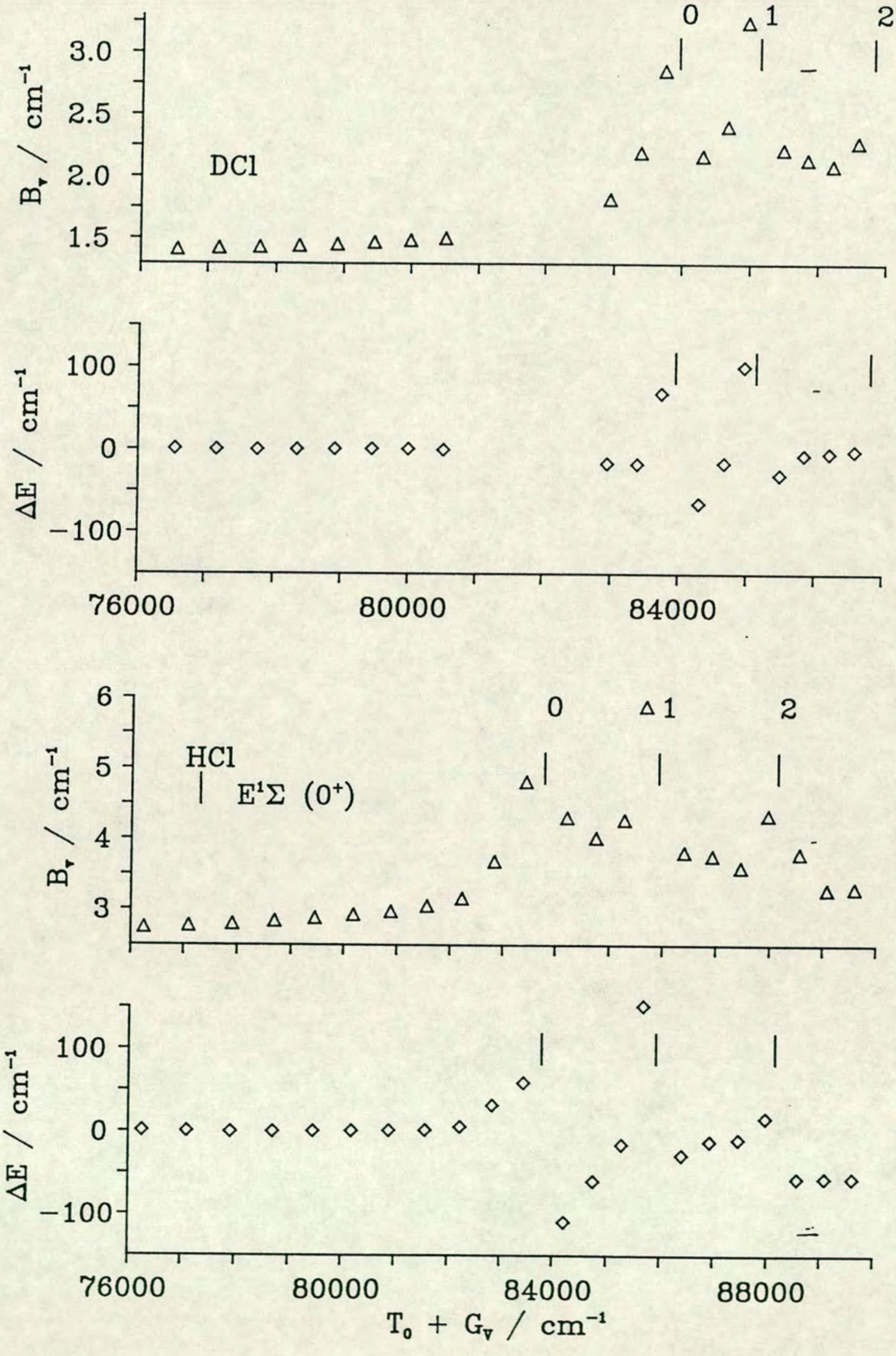

Figure 2.3b
Perturbations in the Ion-pair State of HBr and DBr

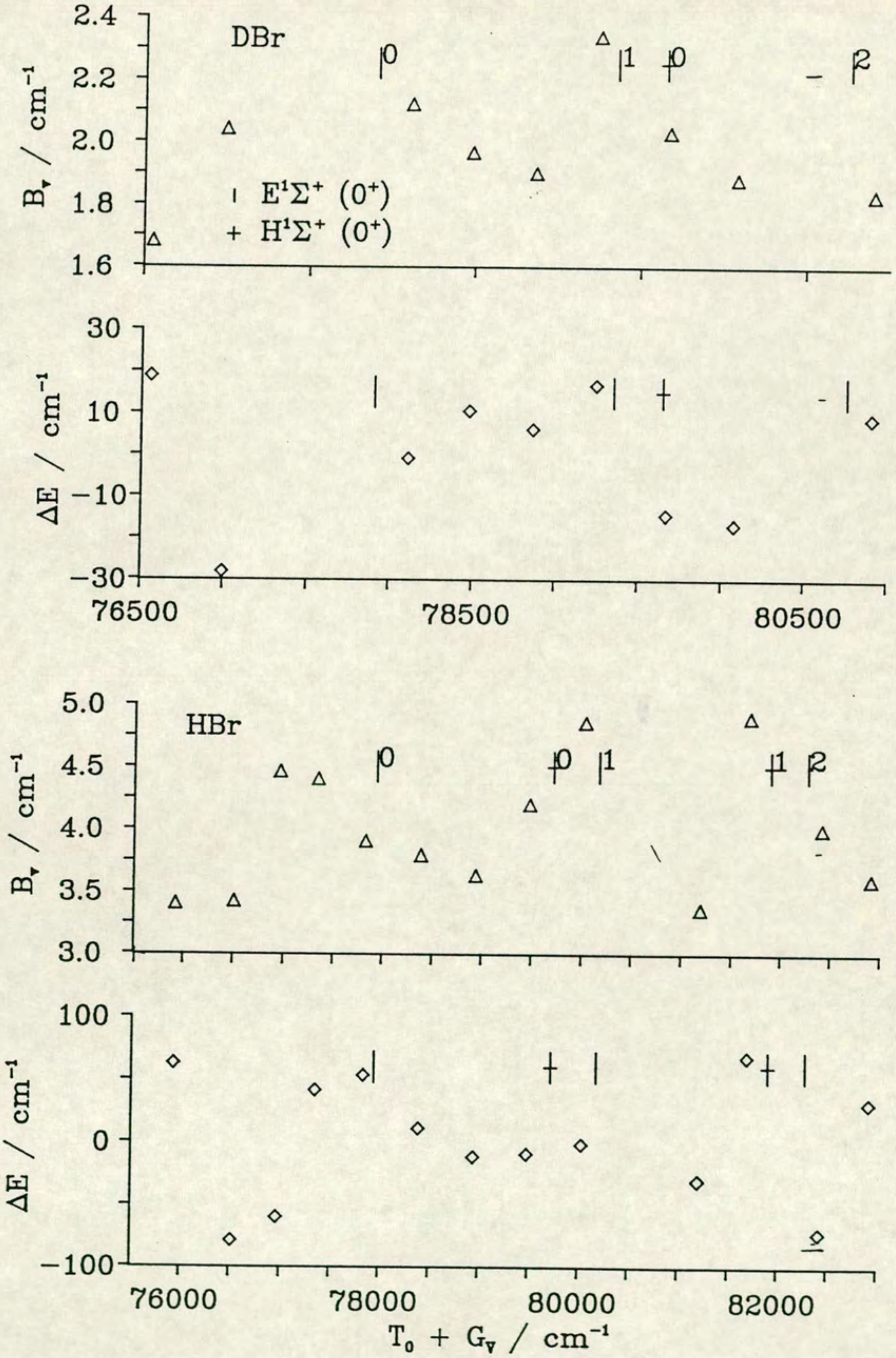

Figure 2.3c
Perturbations in the Ion-pair State of HI

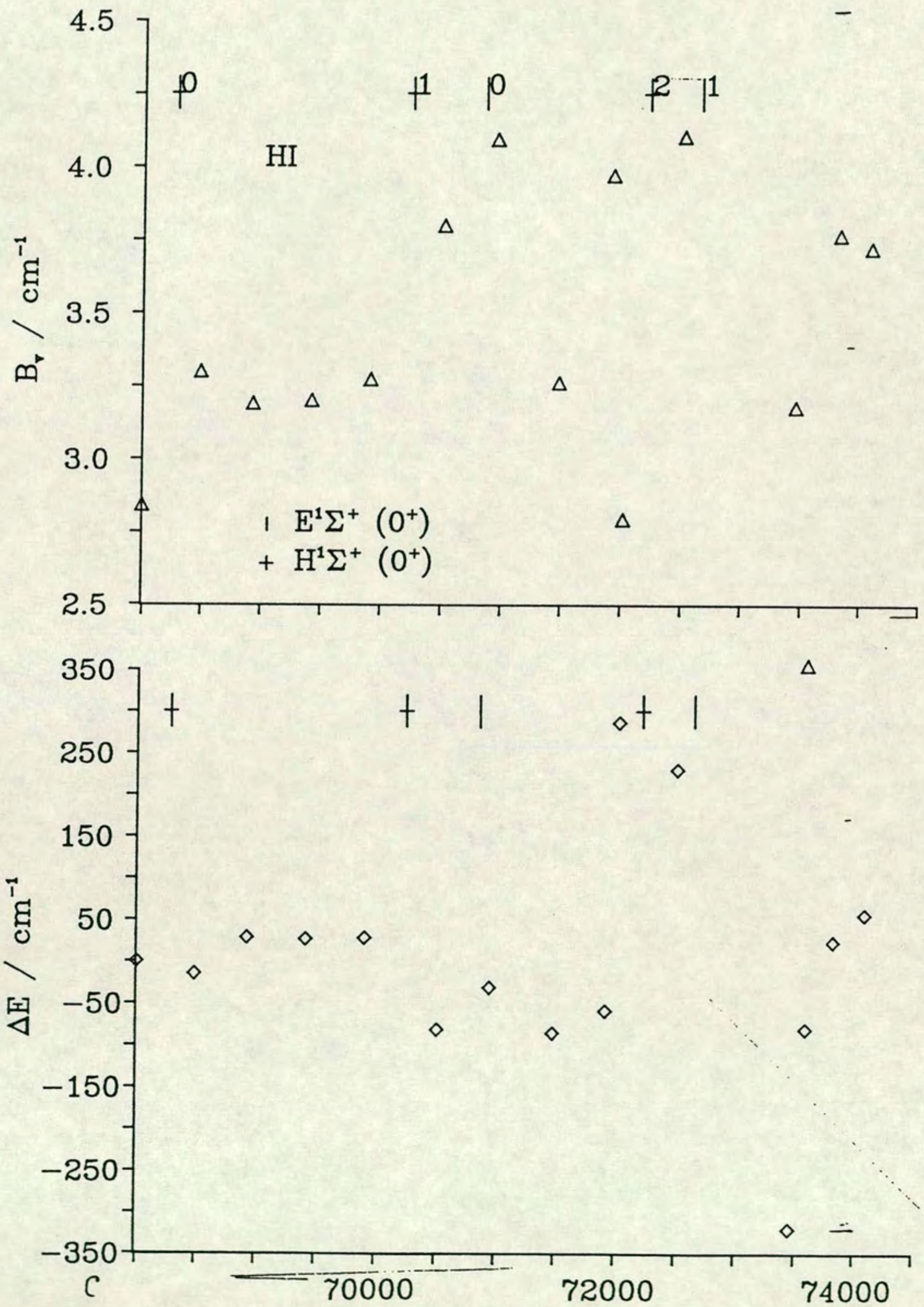

also called Λ,S coupling. A homogeneous coupling will only mix states with exactly the same symmetry. The ion-pair state has symmetry ${}^1\Sigma^+$ and so will only mix with other ${}^1\Sigma^+$ states. However, in Hund's case (c), Λ and Σ are no longer good quantum numbers and only Ω, the projection of the total electronic angular momentum is defined [48]. All $\Omega = 0^+$ states can therefore interact with the ion-pair state. The hydrogen halides are intermediate in coupling between Hund's case (a) and Hund's case (c). The heavier molecules, HBr and HI, exhibit strong core spin-orbit coupling and therefore are best described by Hund's case (c) coupling scheme. However, even in HCl Hund's case (c) effects can be important as shown by the interaction of the 0^+ component of the ${}^3\Sigma^-$ state with the ion-pair state [12].

In the Ω,ω coupling scheme the total angular momentum is the resultant of the angular momentum of the core, Ω, and that of the Rydberg electron, ω [58]. The tendency towards this form of coupling increases with the principal quantum number of the Rydberg electron and is quite marked even for the lowest members. Also as the atomic number increases the term values of the Rydberg states and the separation between the Rydberg levels in each series decreases [55]. The spacing of the vibrational levels within each electronic state also decreases with increasing reduced mass and so interacting levels are closer in energy.

These factors combine to bring an increasing amount of the ion-pair state within range of perturbing states as the atomic number increases. In HF [4] there are 25 unperturbed vibrational levels, in HCl [12] only 8, and for HBr [11] and HI [13] there are no vibrational levels which appear to be free from coupling with the Rydberg states. The perturbations present in HBr and HI have hampered the analysis of their spectra to such an extent that it has not been possible to determine either the electronic term value, T_e, or an absolute vibrational numbering for the ion-pair state. Only a relative numbering scheme is reported for HBr, DBr and HI, and for DI [14] the perturbations are so severe that even a relative vibrational numbering has not proven possible. Until recently, there was only a relative numbering scheme for DCl as well, but the lower vibrational levels have now been observed in emission [20]. The previous assignment of the lowest observed vibrational level as $v' = 12$ was confirmed. This numbering was based on detailed knowledge of the unperturbed energy levels for HCl [2].

Apart from the irregular spacing of energy levels the ion-pair levels also show a wide variation in linewidths and absorption intensity. Diffuse rotational lines, with J-dependent linewidths have been observed for many of the vibrational levels, particularly in the heavier molecules [11] [12] [13]. This dependence on rotational quantum number indicates that there is a rotational predissociation coupling the ion-pair state to the repulsive valence states. Many of the vibrational bands are very weak and some are absent, resulting in gaps in the progression where no levels are observed. Some of the observed gaps occur in the region of strong Rydberg transitions and the ion-pair absorption lines may thus be obscured. However, other gaps cannot be explained by this mechanism, and it is likely that the coupling of the states is adversely affecting the transition probability for ion-pair absorption. Table 2.3 summarises the information available on the vibronic progressions of the ion-pair states of the hydrogen

Table 2.3 Summary of Vibrational Levels in the Ion-pair State of the Hydrogen Halides Characterised Experimentally

	Levels	Technique	Reference	Comments
HF	0→10	emission	[4]	unperturbed
	14→65	absorption	[4]	v'>26 perturbed
	69→73	absorption	[4]	
	unassigned			higher 0^+ levels
DF	0→5	emission	[21]	
	n+27→n+40	REMPI	[31]	−3≦n≦3 perturbation of v'>
HCl	0→5	emission	[2]	unperturbed
	6→26	absorption	[2]	perturbed for v'>8 v'=22,23,25 not present
DCl	0→7	emission	[20]	unperturbed
	n→n+9	absorption	[2]	v`>n+ perturbed, n=12
	n−1	REMPI	[24]	probably misassigned
HBr	m→m+13	absorption	[11]	all perturbed or diffuse except m+13 m+9, m+10 missing
DBr	m'→m'+11	absorption	[11]	all perturbed except m' m'+2, m'+3, m'+10 missing
	?	absorption		one higher level which can not be numbered
HI	m→m+14	absorption	[13]	most perturbed and diffuse m+7 missing
DI	10 levels	absorption	[14]	most levels perturbed diffuse and weak, one strong line $\nu_0=73391.9\text{cm}^{-1}$ no relative numbering

halides.

The vibronically coupled Rydberg states also exhibit anomalous molecular constants such as irregular spacing of the vibrational levels and perturbed rotational constants. By comparison with the coupled states, the molecular constants observed for the uncoupled states are essentially identical to those of the molecular ion. They can be used therefore to accurately predict the vibrational terms in different isotopomers. This is of great assistance in the assignment of the vibrational levels of the Rydberg states. However, the predicted term values of the coupled states do not agree very well with the observed term values because the perturbation of each level depends on the relative energies of the vibrational levels in the coupled states. If the deperturbed constants of the mixed Rydberg states are used to determine potential energy curves, by the RKR method, then the curves are displaced to large internuclear separation. They differ markedly from the potential energy curves observed for the molecular ion, or the ground state of the neutral molecule, which they would be expected to resemble. Determination of the Franck-Condon factors for transitions to levels of these Rydberg states, based on calculations of the vibrational wavefunctions from these potential energy curves, reveal that the vibrational progression would be peaked at $v'>0$ rather than at $v'=0$ as is observed. The molecular constants R_e and ω_e alone do not, therefore, adequately describe such states. They must instead be described in terms of coupling between the parent Rydberg and ion-pair states which results in two mixed states with predominantly Rydberg or ion-pair character.

Although the strongest perturbations are observed for the ion-pair state and its vibronically coupled partners, many other interactions have been observed between the excited electronic states of the hydrogen halides. These interactions include predissociation of bound states by repulsive valence states, iso-configurational spin-orbit coupling [56] (see Appendix A), and heterogeneous coupling with the ion-pair state [31]. Predissociation has been observed to be important in all of the Rydberg states, resulting in very weak or diffuse rotational branches. The linewidths within some of these branches are dependent on J while others appear independent of J so there must be a number of coupling mechanisms in operation, among them rotational coupling. The most marked example of predissociation occurs in the lowest Rydberg states, the $C^1\Pi$ and $b^3\Pi_{2,1,0^\pm}$ states [5] [6] [7], which show very strong but diffuse absorption. The rotational branches of many of the vibrational levels are too diffuse to be analysed to determine rotational constants and in HCl, for example, it is not possible to resolve the chlorine isotopic splitting even for $v'=4$ of the $C^1\Pi$ state. In DCl however, the isotopic splitting is resolved for $v'\geqq 1$ although many of the rotational lines are blended [5]. The greater reduced mass of the deuteride reduces the vibrational overlap and results in a weaker predissociation. However, for the rest of the hydrogen halides the rotational lines are too diffuse to resolve isotopic splitting and in HI and DI they are too diffuse to allow rotational analysis in any of the observed vibrational levels.

The $C^1\Pi$ state is also observed to be heterogeneously coupled to the ion-pair state in HF and DF [31]. Analysis of the rotational branches of the $C^1\Pi\ (1) \leftarrow X^1\Sigma^+$ (0-0) transition reveals the presence of several strong interactions between the rotational levels of the $v'=0$ level of the $\underline{C}$ state and several vibrational levels in the ion-pair state. This affects only the e-parity Λ components of the C state which form the terminus of the P- and R-branches of the transition [48]. The Q-branch, resulting from the f-parity Λ component was used to determine a set of unperturbed rotational constants which could be used to quantify the perturbation of the coupled component. The perturbations of the lines in HF is observed to be greater than that in DF, this mass dependence is consistent with an off-diagonal spin-rotation coupling mechanism which would result in a dependency on the rotational constant, B, and the total angular momentum, J [54].

Both the homogeneous and the heterogeneous interactions which are observed in the hydrogen halides result from the breakdown of the Born-Oppenheimer approximation. A discussion of this concept is thus appropriate to this work and is presented in the following section.

2.3 The Breakdown of the Born-Oppenheimer Approximation

The Hamiltonian describing the nuclear and electronic interaction in diatomic molecules has been derived in detail by Bunker [50-53] who extended the analysis beyond the limitations of the Born-Oppenheimer approximation. The uncoupling of nuclear and electronic motion implied in this approximation leads to isotopically invariant potential energy curves [54]. Early experimental results for the diatomic hydrides had shown that this was not the case [50]. Inclusion of the effect of nuclear motion on the electronic wave functions of the hydrides was found to account for the discrepancy between experiment and theory.

This analysis was recently extended by Lefebvre-Brion and Field [54] to cover a wider range of interactions, including a more detailed discussion of relativistic effects, and experimentally observable phenomena. A brief description of the effects which are thought to be important for the hydrogen halides is presented in this section. It follows closely the arguments of Bunker [50-53] and Lefebvre-Brion and Field [54].

2.3.1 The Born-Oppenheimer Approximation

The exact, non-relativistic Hamiltonian for a diatomic molecule may be approximated by the sum of three operators;

$$\mathbf{H} = \mathbf{T}^N(R,\theta,\phi) + \mathbf{T}^e(r) + V(r,R) \tag{2.1}$$

where T^N is the nuclear kinetic energy operator, T^e is the electron kinetic energy operator, V is the electrostatic potential, r is the electron coordinate, R the internuclear separation, θ the polar angle and ϕ the azimuthal angle. Relativistic effects due to the electron spin are most conveniently introduced as perturbations to the solutions of this Hamiltonian.

The two kinetic energy terms may be expanded as :

$$\mathbf{T}^N(R,\theta,\phi) = \frac{-\hbar^2}{2\mu R^2}\left[\frac{\partial}{\partial R}\left(R^2\frac{\partial}{\partial R}\right) + \frac{1}{\sin\theta}\frac{\partial}{\partial\theta}\left(\sin\theta\frac{\partial}{\partial\theta}\right) + \frac{1}{\sin^2\theta}\frac{\partial^2}{\partial\phi^2}\right] \tag{2.2}$$

$$T^e(r) = \frac{-\hbar^2}{2m} \sum_i \nabla_i^2 \tag{2.3}$$

where μ is the reduced mass of the molecule, m the mass of an electron and the summation is over all the electrons, *i*. It can be seen that T^N will be smaller than T^e by a factor of μ/m, approximately 2000. The solution of the Schrödinger wave equation with the above Hamiltonian (equation (2.1)) is often expressed as a sum of energy contributions from the different modes of motion:

$$E_{Total} = E^{el} + G(v) + F(J) \tag{2.4}$$

where E_{Total} is an approximation to the exact energy, E^{el} is the electronic energy, and G_v and F are the vibrational and the rotational energy of the nuclei. The separation of the total energy into terms dependent on only electronic or nuclear motion is called the Born-Oppenheimer Approximation. The very much slower velocity of the nuclei compared to the electrons is often used as justification for this separation of the energy terms.

The wavefunction required for the solution of the Hamiltonian, equation (2.1), is the Born-Oppenheimer product function:

$$\psi^{BO}_{i,v} = \Phi_{i,\Lambda,S,\Sigma}(r,R)\chi_v(R,\theta,\phi) \tag{2.5}$$

where Φ is an electronic wavefunction, χ is a nuclear wavefunction, i, Λ, S, and Σ are electronic quantum numbers, v is a vibrational quantum number and r, R, θ and ϕ are the electronic and nuclear coordinates. Neglecting the effect of the nuclear and electronic operators on the electronic and nuclear wavefunctions results in equation (2.4).

Substituting the product function for Ψ, equation (2.5), into the Schrödinger wave equation, with the Hamiltonian, equation (2.1), multiplying by Φ^* and integrating over the electronic coordinate gives:

$$\langle \Phi_i | T^N(R,\theta,\phi) + T^e(r) + V(r,R) | \Phi_i \rangle \chi_v = E\chi_v \tag{2.6}$$

Because $\mathbf{T}^e$ is greater than $\mathbf{T}^N$, by a factor of m/μ, the $\mathbf{T}^N$ operator can be ignored initially. Thus we have the 'clamped nuclei' electronic Schrödinger equation:

$$\langle \Phi_i | \ T^e + V(r,R) \ | \Phi_i \rangle = E_i^{el}(R) \tag{2.7}$$

where $E_i^{el}(R)$ defines the potential energy curve in which the nuclei move. Although this is a very useful concept it must be remembered that it is a construct of the Born-Oppenheimer approximation rather that a physically observable feature of the system. The real energy levels of the molecule do not correspond to the energy eigenvalues of the potential curve defined by $E_i^{el}(R)$ and product functions, Ψ^{BO}, are not exact solutions of the total Hamiltonian.

However, within this approximation we can define a nuclear Schrödinger wave equation:

$$[\, T^N + E_i^{el}(R)\,]\chi_v(R,\theta,\phi) = E^T(R)\chi_v(R,\theta,\phi) \tag{2.8}$$

The potential energy curve E_i^{el} is isotopically invariant since the nuclear mass is assumed to be infinite. However, it has been shown for a number of molecules that the potential energy curve varies upon isotopic substitution. It is therefore necessary to include the effect of $\mathbf{T}^N$ on Φ and to add the neglected term:

$$\langle \Phi_i | \mathbf{T}^N | \Phi_i \rangle \tag{2.9}$$

where the integration is over the electronic coordinates, r, and θ and ϕ. An *adiabatic* potential curve can then be defined:

$$E_i^{ad}(R) = E_i^{el}(R) + \langle \Phi_i | \mathbf{T}^N | \Phi_i \rangle \tag{2.10}$$

The second, kinetic energy, term makes a very much smaller contribution to the total energy than the first term. This adiabatic correction is inversely proportional to the reduced mass and so is most important for very light molecules such as the hydrides. The shift in the value of T_e for DF from that for HF is found to be 23 cm^{-1} while for DCl and HCl it is 11 cm^{-1}.

Exact solutions of the total Hamiltonian must satisfy the condition:

$$\langle \Psi_i^T | \mathbf{H} | \Psi_j^T \rangle = E_i^T \delta_{ij} \tag{2.11}$$

While the Born-Oppenheimer product functions are not exact solutions, it is possible to construct exact solutions of the Hamiltonian by an infinite series of such product functions:

$$\Psi_i = \sum_{j,vj}^{\infty} c_{i,vj} \Phi_j^{BO} \chi_{vj} \tag{2.12}$$

where the coefficients, c_i, are determined by diagonalising the Hamiltonian in the basis set $\{\Psi\}$. The Born-Oppenheimer approximation is valid if the off-diagonal elements in the Hamiltonian matrix are small compared with the separation of the diagonal terms. In this case the observed spectra will conform to the behaviour predicted by equation (2.4). There will be few perturbations due to the interaction of electronic states.

When the Born-Oppenheimer approximation breaks down it is necessary to include further terms in the expansion of Ψ in the Born-Oppenheimer functions. The diagonal terms in the Hamiltonian will be altered and there will be additional off-diagonal terms between the components of Ψ.

There are two zeroth order representations which may be developed from the Born-Oppenheimer approximation by the inclusion of these neglected terms: the *diabatic* representation and the *adiabatic* representation.

2.3.2 Extension of the Born-Oppenheimer Approximation

The diabatic and adiabatic representations are limiting cases which describe the effect of off-diagonal matrix elements of the Hamiltonian. That is the interaction between two or more Born-Oppenheimer states. The non-zero matrix elements between the states Φ_1 and Φ_2 are those of the operators $\mathbf{T}^N$ and $\mathbf{H}^{el}$:

$$\begin{aligned} &\langle \Phi_1 | \mathbf{T}^N | \Phi_2 \rangle \\ &\langle \Phi_1 | \mathbf{H}^{el} | \Phi_2 \rangle \end{aligned} \tag{2.13}$$

Only states of identical symmetry can be coupled by these operators. In the Λ,S coupling scheme the two states must have identical values of Λ, S and Σ, while in Ω,ω coupling both must have the same value of Ω. This form of coupling is known as an *electrostatic perturbation* because it results from the neglect of the electrostatic part of the Hamiltonian rather than from neglect of the spin or rotation terms.

It is not possible to determine a basis set which simultaneously diagonalizes both off-diagonal terms of the Hamiltonian. Rather the diabatic and adiabatic representations are defined in which one of the two off-diagonal terms in equation (2.13) are set equal to zero.

The Diabatic Basis

The diabatic functions are assumed to be independent of R, thus they diagonalise the nuclear motion operator, $\mathbf{T}^N$. They are defined by:

$$\begin{aligned} \langle \Phi_1^d | \mathbf{H}^{el} | \Phi_2^d \rangle &= H_{12}{}^{el} \neq 0 \\ \langle \Phi_1^d | \mathbf{T}^N | \Phi_2^d \rangle &= 0 \end{aligned} \tag{2.14}$$

where H_{12}^{el} is the electronic matrix element between the two states, and the Φ^d are diabatic electronic functions. H_{12}^{el} is a function of the internuclear separation, (through V(r,R)), but is usually assumed to be a slowly varying function. It is often assigned a constant value, $H^e = H_{12}^{el}(R_c)$, where R_c is the internuclear separation at which the diabatic states cross. The Φ^d can be approximated with single configuration functions and because $\mathbf{H}^{el}$ is a two electron operator the interacting configurations may differ by two spin orbitals [54].

The diabatic basis is appropriate when there is little mixing of the configurations around R_c and so the diabatic coupling term, H^e, is small. Deperturbed potential energy curves for such coupled states will cross.

The gross perturbations observed in the ion-pair and Rydberg states of the hydrogen halides obviously result from very strong interactions. A diabatic representation of the coupling in these molecules would not be expected to yield particularly good results. However, a diabatic basis is still a valid starting point for the analysis even though it may not be the best starting point. It is also useful because the single configuration approach retains the electronic parentage of the interacting states. The Rydberg states may then be conveniently modelled by the ground state of the molecular ion which forms the ion core of all the observed Rydberg states.

The Adiabatic Basis

The adiabatic basis functions are those which diagonalise the electronic operator $\mathbf{H}^{el}$. Because the electronic matrix elements between different adiabatic states are zero the potential energy curves of these states cannot cross. The adiabatic functions are defined by:

$$\begin{aligned} \langle \Phi_1^{ad} | \mathbf{T}^N | \Phi_2^{ad} \rangle &= H_{1,v1,2,v2} \neq 0 \\ \langle \Phi_1^{ad} | \mathbf{H}^{el} | \Phi_2^{ad} \rangle &= 0 \end{aligned} \tag{2.15}$$

The off-diagonal nuclear motion matrix element, $\mathbf{H}_{1,v1,2,v2}$, is known as the *non-adiabatic* coupling term. The nuclear motion operator is a one electron operator which restricts the configurations of states which may be mixed by this interaction. Only configurations which differ in only one spin orbital can be mixed by the $\mathbf{T}^N$ operator.

If the states can mix then the *non-adiabatic* coupling term is a strongly varying function of R in the region near R_c. At R_c the configurations of the adiabatic functions are rapidly changing and so $\mathbf{H}_{1,v1,2,v2}$ can be expected to vary rapidly near R_c.

Generating adiabatic curves requires the use of either deperturbed potential energy curves, determined from experimental data, or *ab initio* potential curves.

If the spin-orbit operator is omitted then the *ab initio* curves will not be exact adiabatic potential curves. However, such effects are small for lighter molecules and are often neglected. In the hydrogen halides neither of these two approaches are useful starting points for analysis of the coupling. In the former-approach much information is lost on the electronic structure of the interacting states. The latter approach, while retaining information on the electronic structure, suffers from the lack of available potential energy surfaces. However, it is possible to construct the adiabatic potential curves in the diabatic basis. These curves may then be used to develop the coupling in the more appropriate adiabatic basis.

Close to an avoided crossing the adiabatic states are often closely approximated by two diabatic states, ϕ_1^d and ϕ_2^d. If the deperturbed diabatic curves are V_1^d and V_2^d, then the adiabatic curves are determined by diagonalising, at each value of R, the secular determinant:

$$\begin{vmatrix} V_1^d - E & H_{12}^e(R) \\ H_{12}^e(R) & V_2^d - E \end{vmatrix} = 0 \qquad (2.16)$$

where H_{12}^e is the electronic matrix element in the diabatic basis. The separation of the two adiabatic states at $R=R_c$ is $2H^e$ as shown in figure 2.4.

The adiabatic electronic functions may also be constructed as a linear combination of diabatic functions:

$$\begin{aligned} \Phi_1^{ad} &= \cos\theta(R)\Phi_1^d - \sin\theta(R)\Phi_2^d \\ \Phi_2^{ad} &= \sin\theta(R)\Phi_1^d + \cos\theta(R)\Phi_2^d \end{aligned} \qquad (2.17)$$

where θ is a function or R and has a value of $\pi/4$ at $R=R_c$.

Figure 2.4 Adiabatic and Diabatic Curves

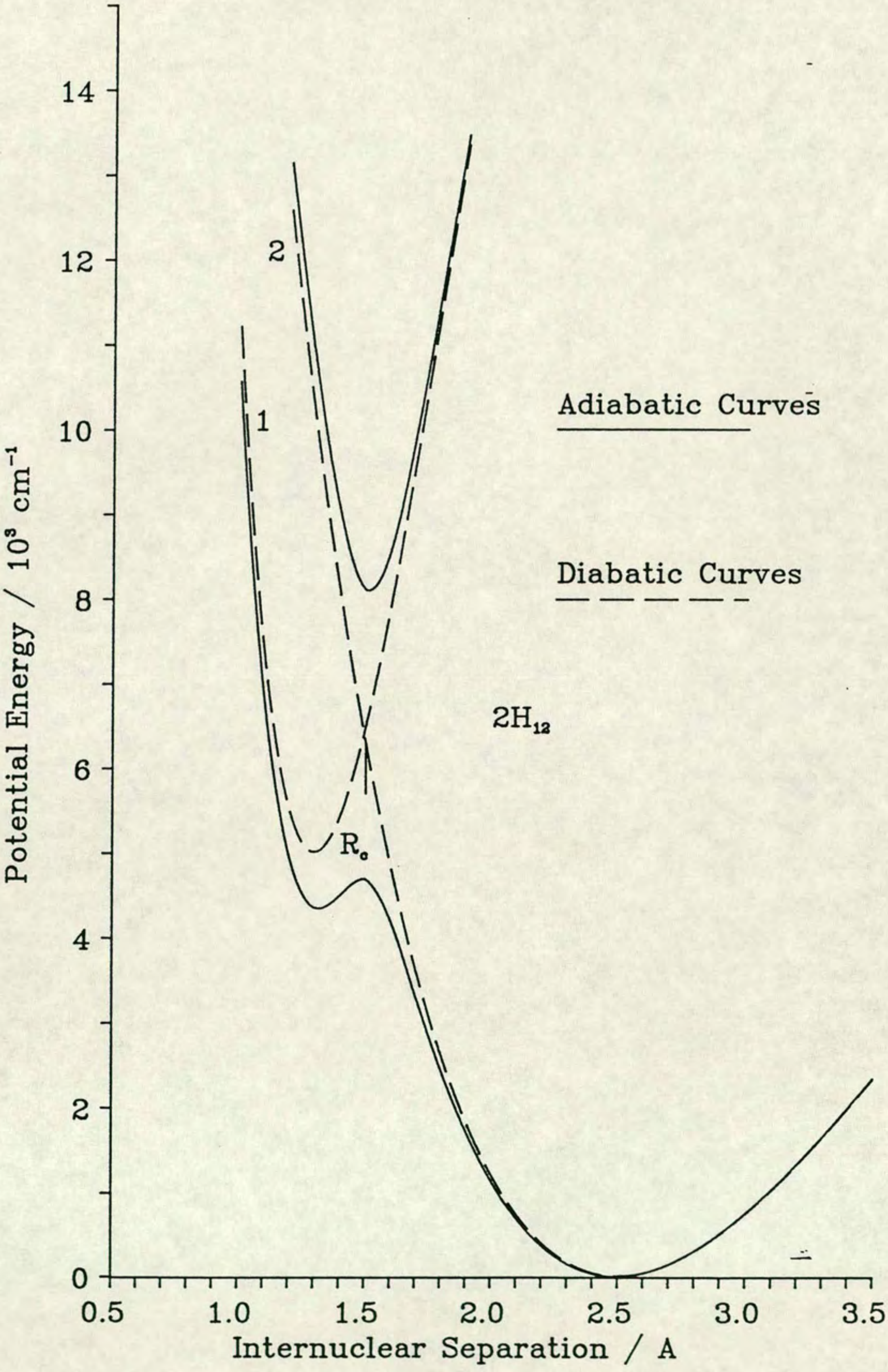

In the adiabatic basis if the off-diagonal matrix element of $\mathbf{T}^N$ is considered then the two adiabatic states will be mixed by the non-adiabatic coupling term. If only the radial part of $\mathbf{T}^N$ is considered then there are non-zero matrix elements of the first and second derivatives with respect to R:

$$\langle \Phi_1 | \frac{\partial}{\partial R} | \Phi_2 \rangle$$

$$\langle \Phi_1 | \frac{\partial^2}{\partial R^2} | \Phi_2 \rangle \tag{2.18}$$

Substituting equation (2.17) into the first term in gives:

$$\langle \Phi_1 | \frac{\partial}{\partial R} | \Phi_2 \rangle = [\sin^2 + \cos^2] \frac{\partial \theta}{\partial R} = \frac{\partial \theta}{\partial R} \tag{2.19}$$

To determine the form of $\theta(R)$ use is made of the definition:

$$\langle \Phi_1^{ad} | \mathbf{H}^{el} | \Phi_2^{ad} \rangle = 0 \tag{2.20}$$

followed by substitution of the expressions in equation (2.17) for Φ_1^{ad} and Φ_2^{ad} to yield:

$$\begin{aligned} E_1{}^d \sin\theta\cos\theta - H^e \sin^2\theta + H^e \cos^2\theta - E_2{}^d \sin\theta\cos\theta& \\ = 0& \end{aligned}$$

$$\Rightarrow \qquad \theta = \tfrac{1}{2} \tan^{-1} \left[\frac{-2H^e}{E_2^d - E^d{}_1} \right] \tag{2.21}$$

Near R_c the vertical energy separation of the diabatic curves will be a linear function of R:

$$E_2^d - E_1^d = a(R-R_c) \tag{2.22}$$

θ is thus given by:

$$\theta = \tfrac{1}{2}\tan^{-1}\left[\frac{-2H^e}{a(R - R_c)}\right] \tag{2.23}$$

and so:

$$\begin{aligned}\langle \Phi_1 | \frac{\partial}{\partial R} | \Phi_2 \rangle &= \frac{aH^e}{4(H^e)^2 + a^2(R - R_c)^2} \\ &= W^e(R)\end{aligned} \tag{2.24}$$

This is a lorentzian function, centred on R_c and inversely dependent on H^e_{12}.

It can be shown [54] that the matrix element of the second derivative is given by:

$$\langle \Phi_1 | \frac{\partial^2}{\partial R^2} | \Phi_2 \rangle = \frac{\partial}{\partial R} W^e(R) \tag{2.25}$$

The coupling is thus a rapidly varying function of R indicating the rapid change in configurations at R_c. If the adiabatic representation is good then the matrix element $W^e(R)$ will be low and wide. Consequently the diabatic coupling term will be large and the diabatic representation will be inappropriate.

It is possible to extend both the diabatic and the adiabatic representations further by considering more of the neglected terms in the Hamiltonian, equation (2.1) or by including contributions from more configurations. However, such a treatment is beyond the scope of this work.

2.3.3 Observable Features of the Breakdown of the Born-Oppenheimer Approximation

The effects of the breakdown of the Born-Oppenheimer approximation in the hydrogen halides can be observed in the disruption of the expected smooth progression of vibrational and rotational energy levels in the interacting states. Indications of strong vibronic coupling can also be observed in a number of other spectroscopic features.

The observed linewidths of strongly perturbed energy levels are much greater than those of comparable unperturbed levels. Many vibrational bands in the ion-pair state of all the hydrogen halides are observed to be both abnormally weak and diffuse [11-14]. In HBr and HI a number of levels appear to be missing. Although there are no $^1\Sigma^+$ repulsive states, the perturbing Rydberg states of $^3\Sigma^-$ and $^3\Pi_0{}^+$ symmetry may act as gateway states to predissociation. Apart from the coupling between the ion-pair states and Rydberg states of the same symmetry, perturbations are also observed between other states. The lowest Rydberg states of Π symmetry are very strongly predissociated by the repulsive states correlated to the ground state dissociation products.

The de-perturbed ion-pair state and Rydberg states have very different potential energy curves and, in the absence of coupling, would be expected to exhibit very different spectroscopic constants. However, because of the strong vibronic coupling between these states the perturbed Rydberg states display similar features to the ion-pair state. The coupling of a Rydberg state to the ion-pair state results in a contribution to the total wavefunction of the Rydberg state level from the ion-pair state. Consequently the Rydberg state supports an oscillation in the ion-pair well in addition to that in the Rydberg well. The Rydberg state may then evolve in the same manner as the ion-pair state.

Such coupled Rydberg levels when excited show characteristics similar to that of the ion-pair state. Chandler et al [33] observed that the strongly coupled $E^1\Sigma^+$ (0^+) Rydberg state of HCl showed the same propensity for production of Cl^+ and H^+ ions in mass resolved REMPI as the levels of the ion-pair state. REMPI of the $F^1\Delta_2$ (2) Rydberg state, which is not coupled to the ion-pair state, did not result in Cl^+ formation. Absorption of a third photon by molecules in this excited state results in direct ionisation of HCl, transition 1 of figure 2.5. The HCl^+ ions are produced in the ground state and the transition probability is greatly enhanced for $\Delta v=0$. For ionisation of the ion-pair state the $\Delta v=0$ rule is not followed and the dominant products are the atomic ions. Chandler et al proposed a four photon mechanism for the ionisation of HCl via the ion-pair state to explain the observed ratios of atomic to molecular ion formation.

Absorption of a single photon to a repulsive Rydberg state produces $H^*(n=2)$ and Cl($^2S^0$ and $^2D^0$), transition 3. The excited atoms can then be ionised by the absorption of one further photon, transition 4. The transition to the repulsive state can only occur at large R and so the production of atomic ions from the $E^1\Sigma^+$ (0^+) Rydberg state indicates that this state is mixed with the ion-pair state. A recent study of the REMPI-PES spectrum of HCl has confirmed that these excited atoms are formed thus supporting the above arguments [65] but the authors propose another mechanism to explain their observations. Because the ion-pair state has the configuration $(\sigma\pi^4)\sigma^*$ at small R there is a low probability for direct ionisation to the ground state of the

Figure 2.5
Photoioisation and Photodissociation Schemes

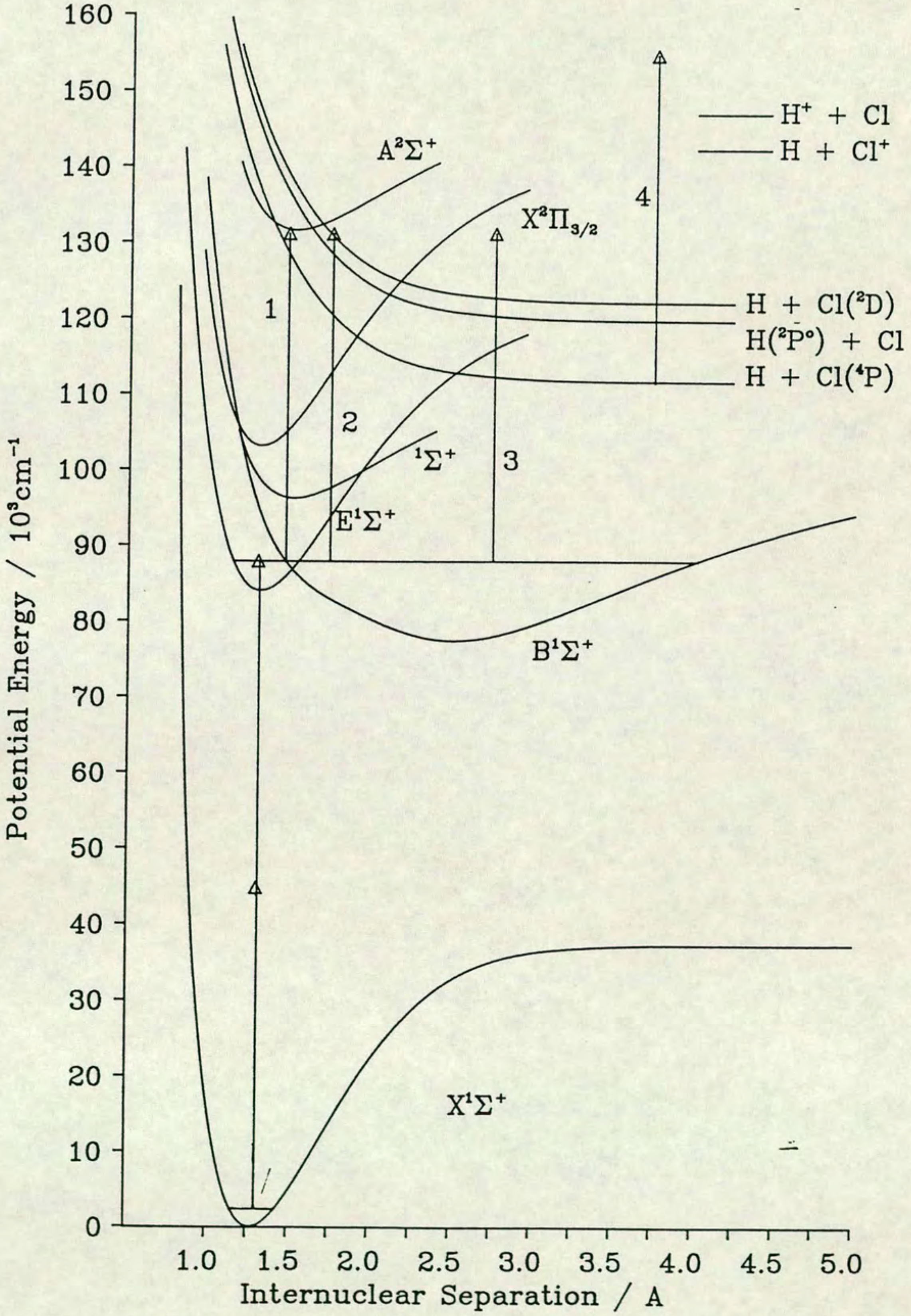

molecular ion. But it can readily absorb a further photon and be promoted to the super-excited $^1\Sigma^+$ state, transition 2, which may either auto-ionise or, as it is populated above it's dissociation energy, dissociate to $H^*(n=2)$ and Cl. At large R this state is known to cross a repulsive $^3\Pi_0$ Rydberg state which dissociates to hydrogen and $Cl^*(^2P)$. The two states are quite strongly spin-orbit coupled and so the super-excited state dissociates to $Cl^*(^2P)$ which is also observed.

Excitation of levels of the ion-pair state in the hydrogen halides, HCl and HI, results in characteristic bound-free fluorescence accompanying the transitions to the ground state at large R [32] [60] which is illustrated in figure 2.6. Similar fluorescence is observed from some of the strongly coupled Rydberg levels. This fluorescence is an important indication of the vibronic coupling between the Rydberg states and the ion-pair state.

In the case of HCl the ground state has been well characterised [40] [41]. Analysis of the fluorescence can therefore be used to directly probe the nature of the upper state wavefunction localised in the ion-pair well. It is important that, apart from producing the correct energy levels, any model of the electronic structure accurately reproduces the observed fluorescence spectra.

Figure 2.6
Ion−pair State Fluorescence

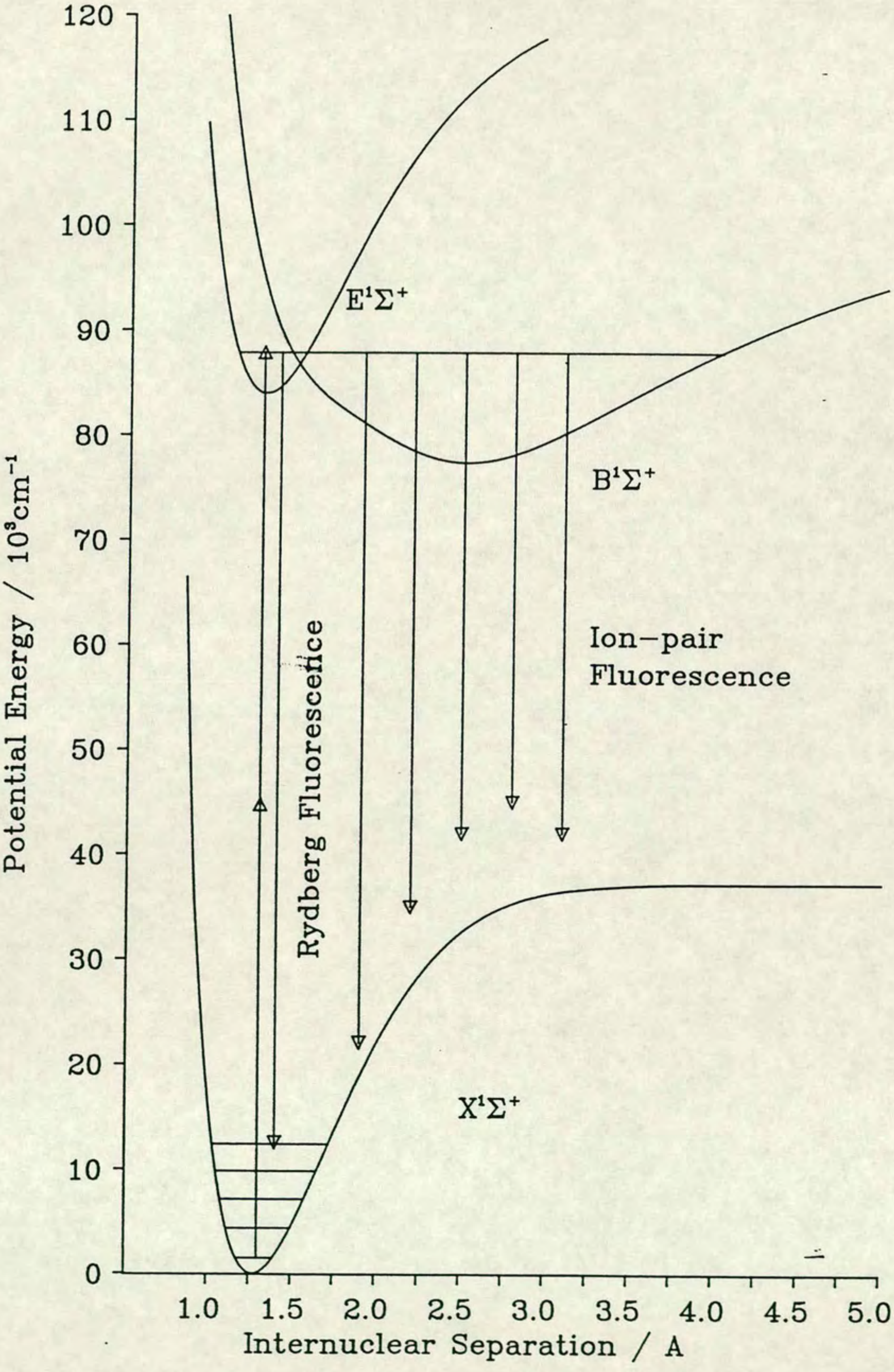

Chapter 3
Experimental Apparatus

3.1 Introduction

In the hydrogen halides even the lowest lying bound excited states have very high excitation energies. For HI the bound states all lie at energies greater than 60000 cm^{-1}. This is equivalent to a photon with a wavelength of 167nm in single photon absorption. It is therefore necessary to employ vacuum ultraviolet (VUV) radiation and the associated vacuum techniques to study the hydrogen halides.

High resolution absorption and emission spectra for the hydrogen halides have been recorded with conventional excitation sources such as continuum lamps and electric or microwave discharges. However, in the present study emission from a single ro-vibronic energy level was required. Therefore it was necessary to employ an excitation technique with both high resolution and high spectral brightness. These requirements can be met by synchrotron radiation or by the use of high peak power pulsed lasers. Emission spectra of single ro-vibronic levels, excited by VUV synchrotron radiation, have been recorded for the ion-pair and Rydberg states of HCl [32] [69].

High peak power pulsed lasers with wavelengths continuously tunable from the far infra-red through the visible spectrum and extending into the near UV with very high resolution are now readily available [70]. Although the fundamental radiation of most tunable lasers is restricted to wavelengths longer than 300nm the very high peak powers of pulsed lasers allow the use of nonlinear optical techniques to extend the available wavelength range. The techniques of second or higher harmonic generation in nonlinear crystals, parametric mixing, and Raman shifting are routinely used to generate laser radiation at short wavelengths. As with conventional sources it is necessary to exclude strongly absorbing gases such as molecular oxygen from the beam path. Very short wavelengths have been produced by generation of the third harmonic of near ultraviolet radiation in high pressure, static cells or free jet expansions of the rare gases Xe and Kr [31].

Alternatively it is possible to use tightly focussed, pulsed lasers to produce a laser field of sufficiently high intensity to induce simultaneous absorption of two or more photons [71]. The absorption rate for a resonant n photon transition (n = 1,2,3,.....) is given by

$$W = \sigma_n I^n \tag{3.1}$$

where I is the laser intensity (photons $cm^{-2}\ s^{-1}$). Typically , $\sigma_1 \simeq 10^{-18}\ cm^{2}$, $\sigma_2 \simeq 10^{-50}\ cm^{4}s$, $\sigma_3 \simeq 10^{-82}\ cm^{6}s^{2}$, which requires that the intensity, I, must be of the order 10^{28} photons $cm^{-2}\ s^{-1}$ to give a two or three photon absorption process as high a rate as a single photon absorption process [72]. Such high intensities are only readily available with tightly focussed, high peak power, pulsed laser sources.

Two-photon events have the advantage that they require photon energies only half that required for single photon absorption. Photons of the required longer wavelength are more easily generated and remove the need to operate *in vacuo*, greatly simplifying the experimental technique. Additionally, the excitation mechanism is governed by different selection rules to those of single photon absorption or, if the selection rules are not operating in cases of low symmetry they follow different propensity rules.

3.1.1 Multiphoton Spectroscopy

Analogously to conventional single photon spectroscopy the absorption probability for any molecule or atom is greatly enhanced when the energy of an integral number of photons (nhν) is equal to the energy difference between two states in the absorbing species. The transition between the two states must satisfy the selection rules for such an n-photon transition, which differ from those for one photon absorption and vary with the number of photons in the resonant step. By scanning the energy of the incident photons it is possible to determine the energy levels of the species or to specifically excite one particular level.

Non-resonant coherent MPI has also been observed for a number of systems. The species simultaneously absorbs sufficient photons from an intense laser field to reach the ionisation continuum. The cross-sections for such processes are much less than for resonance enhanced MPI.

However, although in single photon spectroscopy it is possible to detect an absorption by observing the decrease in transmittance of the sample, in multiphoton spectroscopy the input intensity is so high and the absorption so small that it is not possible to directly obtain absorption cross sections. Instead some property of the excited species must be monitored.

The excited state produced by the resonant multiphoton absorption can relax via a number of decay channels. If there is a very rapid non-radiative decay channel then the absorption may not be observed. However, if the lifetime of the state is longer then it may fluoresce and the absorption can be detected by monitoring the fluorescence from the sample in a process analogous to single photon Laser Induced Fluorescence (LIF). Or, it may absorb a further photon or photons from the laser field which often is sufficient to ionise the excited species, resulting in Resonance Enhanced Multiphoton Ionisation (REMPI). In the present work on the hydrogen halides two photons were required to reach the resonant intermediate state. A third photon of the same energy was sufficient to ionise all of the molecules studied and therefore this was a $(2+1)$ ionisation scheme.

In two-photon excitation spectra of the hydrogen halides three types of transitions were observed, $\Delta\Omega=0$, 1, and 2, and each transition having different rotational structure [24] [73]. For a $\Delta\Omega=0$ transition O-, Q- and S-branches are expected, and they appear in the intensity ratios Q >> S > O. In many cases only the Q-branch was observed. Only the Q-branch was observed for $\Delta\Omega=0$ and 1 transitions to the $^3\Pi_{0,1,2}$ states. Five rotational branches were observed for $\Delta\Omega=2$ transitions to $^1\Delta_2$ (2) states, O-, P-, Q-, R-, and S-branches. The Q-, R-, and S-branches were very strong and all of similar intensity, the P-branch was less intense and the O-branch was often rather weak.

The two forms of spectroscopy employed in this work, LIF and REMPI can yield further information on the nature of both the resonant and the final state if the products of the transition are observed : the wavelength dependence of the fluorescence in the case of LIF, and the energy, angular distribution of the photoelectrons or the identity of the photoions in the case of REMPI. Although in the LIF experiments the wavelength dependence of the fluorescence from many excited states was examined only the total photocurrent was measured in REMPI experiments. A brief description of the equipment and methods used is presented in this chapter.

3.2 Laser Sources

Three different laser systems were employed at various times throughout this work. Two types of excimer pumped dye laser were used for the studies on HCl, DCl, HBr, and DBr, whilst a Nd:YAG pumped dye laser was used for the work on HI.

3.2.1 Excimer Pumped Dye Lasers

A Lambda Physik EMG 201 MSC excimer dye laser operating on the 308 nm XeCl exciplex emission was used to pump either a Lambda Physik FL3002E or FL3002EC tunable dye laser. The FL3002E, like the FL3002EC, is of the oscillator/amplifier type and consists of an oscillator stage, one or more preamplifiers and a final main amplifier stage each optically pumped by the excimer. The oscillator had a Hansch Littrow configuration which includes a prismatic beam extender and a wavelength selection grating. The beam expander also served as the output coupler of the cavity via a surface reflection off one of the prisms. The grating was supported at one end on a stepper motor driven sine drive rod and was free to rotate in the plane perpendicular to its surface. Rotation of the drive rod adjusted the angle of the grating and hence the output wavelength of the laser. The stepper motor was under the control of a dedicated microprocessor.

The oscillator/amplifier arrangement for a tuneable dye laser produces high output intensity coupled with a very narrow spectral width of the output radiation. At the 5Hz pulse repetition frequency typically used the excimer produced 30 ns duration pulses at 308 nm with an energy per pulse between 300 and 400 mJ. The conversion efficiency achieved by the dye laser varied from 10 to 15%, resulting in pulse energies between 30 and 60 mJ with a pulse duration of 25 ns. All pulse energy measurements were made with a Gentech ED200 Joulemeter. The wavelength ranges and nominal efficiencies of the dyes used are detailed in table 3.1. Although the FL3002E laser, like the FL3002EC, can be operated in a high resolution mode using an intracavity line-narrowing etalon this was not necessary and typically the linewidth of the output radiation was found to be < 0.5 cm^{-1} for photon energies in the region of 40000 cm^{-1}.

UV laser radiation in the wavelength region 220 - 270 nm was generated from the visible output of the dye laser by frequency doubling in either a β-barium borate (BBO) or potassium pentaborate (KPB) crystal. The crystals were mounted in sealed housings to prevent damage of the crystal by moisture. The housing of the BBO crystal was also heated to 30°C. A Lambda Physik FL535B crystal tracking module, under the control of a microprocessor controlling the FL3002E/FL3002EC dye lasers, was used to maintain the optimum phase matching conditions for second harmonic generation (SHG). A quartz compensating crystal was also mounted on the crystal tracking module to compensate for the deviation of the laser beam by the SHG crystal. The SHG

Table 3.1 Laser Dyes Used in the FL3002E/FL3002EC Dye Lasers

Dye	Range/nm	Peak/nm	Efficiency/%
Coumarin 153	522-600	540	15.1
Coumarin 307	479-553	500	16.3
Coumarin 102	460-510	480	18.2
Coumarin 47	440-484	456	17.8

Table 3.2 Second Harmonic Generation Crystals Used with the FL3002E/Fl3002EC Dye Lasers

Crystal	Material	Range
FL32	KPB	456-550
FL33	KPB	440-470
FL34	KPB	443-434
FL37-1	BBO	430-630

crystals used are shown in table 3.2. The UV radiation was separated from the collinear visible radiation by either a prismatic separator or a Schott UG5 UV transmitting filter. It was steered by 90° uncoated quartz prisms and focussed into the sample cell with a 25 mm diameter quartz lens with a focal length of either 100 or 150 mm. A focal spot size of 180μm was previously determined for this arrangement [74]. For a 300 μJ pulse this results in a flux of 100 MWcm^{-2} for each laser pulse. At wavelengths in the range 200 - 300 nm this is equivalent to 10^{28} photons cm^{-2}s^{-1}.

3.2.2 Nd:YAG Pumped Dye Laser

The laser employed for the studies of HI was a Nd:YAG pumped dye laser. The visible output from this laser was then frequency doubled in a separate wavelength extender module. The pump laser was a Spectron 801 Nd:YAG operating on the 1064nm line of Nd^{3+}. This infra-red radiation was frequency doubled with a DCDA crystal to generate the 532 nm radiation used to pump the dye laser. At the operating pulse repetition rate of 10Hz this laser typically produced pulses of 130mJ with a duration of 6 - 10 ns. These were used to pump a Quanta Ray PDL2 dye laser which is also of the oscillator/amplifier design. The dye laser had an output pulse energy of around 30mJ with a bandwidth of 0.3cm^{-1}. This visible radiation was frequency doubled using a set of potassium dihydrogen phosphate (KDP) crystals in a Quanta Ray WEX 1A wavelength extender. The KDP crystals in the WEX were maintained at the optimum phase matching angle by a servotracking mechanism with a bi-photodiode sensor. Pulse energies of 0.3 to 1.2mJ with a band-width of 0.5cm^{-1} could be achieved. The ultraviolet radiation was steered and focussed into the sample cell in the same manner as employed with the other laser systems used.

3.2.3 Wavelength Calibration

The wavelength at which each of the dye lasers was operating was displayed on an LED display on the FL3002E/FL3002EC and on a mechanical counter on the PDL2. However, this was a measure of the current position of the wavelength selection grating rather than an absolute measurement of the laser wavelength. Errors in the wavelength displayed could results either from the counter being incorrectly set or from mechanical slippage in the connections between the grating drive and the counter. The visible laser wavelength could be calibrated against Ne transitions using a hollow cathode opto-galvanic lamp. In the case of the FL3002E/FL3002EC lasers it was possible to update the memory of the microprocessor with the correct wavelength.

The opto-galvanic lamp provided a series of quite closely spaced absolute wavelength measurements which could be used to calibrate excitation spectra. When recording a (2+1)REMPI spectrum a portion of the fundamental laser beam was split off the main beam and directed into the hollow cathode lamp. The lamp output was recorded concurrently with the (2+1)REMPI signal on a two channel chart recorder or on a microcomputer. An additional relative wavelength marker could be added by monitoring the fundamental laser beam intensity after transmission through a quartz etalon (FSR 3.5 cm^{-1}). Apart from providing a convenient method of accurately measuring the position of rotational lines the etalon fringes provided a check on the linearity of the wavelength tracking of the dye lasers.

For the spectra of HI, which were recorded exclusively with the Nd:YAG pumped PDL2 dye laser, an internal calibration was provided by the (2+1)REMPI spectrum of atomic iodine. In most of the excitation spectra recorded there were at least two two-photon resonant atomic iodine transitions which provided absolute energy calibration points. All of the HI (2+1)REMPI spectra were also recorded together with etalon fringes but it did not prove necessary to use these in the analysis of the spectra.

Wavelength calibration and nonlinear wavelength scanning were found to be important for the spectra recorded using the FL3002E/FL3002EC dye lasers. A sine drive is employed for the movement of the grating to provide a linear relationship between the position of the stepper motor and the wavelength of the laser. As the stepper motor moves the grating the *air wavelength* of the laser will vary linearly with stepper motor position. If this linear relationship does not hold, either because of slippage of the mechanical connections or as a result of any error in the sine drive, then an error will be introduced into the apparent laser wavelength in addition to any wavelength shift due to an incorrect counter reading.

Such nonlinear dye laser wavelength scanning was observed for the (2+1)REMPI spectra of HBr which were not recorded in conjunction with calibration lines from an opto-galvanic lamp and etalon fringes as discussed above. The absolute wavelength of the HBr excitation spectra was corrected by comparison of the observed rotational line positions with those reported in the literature. A constant error would have been expected if the wavelength tracking of the laser had been linear. In fact a varying error, dependent on the laser wavelength, was observed which prevented the accurate determination of rotational line positions from the (2+1)REMPI spectra of HBr. An average wavelength correction was calculated for each spectrum rather than attempting to fit the correction.

For DBr the (2+1)REMPI spectra were also recorded without independent wavelength calibration. However, in this case the variation in the wavelength correction was not as severe as for HBr and a simple wavelength shift was sufficient.

3.3 Signal Detection

Multiphoton absorption by the molecules under study was detected either by an increase in total photoion current (REMPI), or by observation of fluorescence from the sample (LIF). Also it was possible to set the laser at a fixed wavelength, therefore exciting one particular ro-vibronic level of the molecule, and observe the variation of the intensity of fluorescence with wavelength.

3.3.1 Resonance Enhanced Multiphoton Ionisation Spectroscopy

The photoions and photoelectrons produced by (2+1)REMPI of the sample were collected by two biased nickel plates positioned in the sample cell. The bias voltage was provided by two batteries at ±90V. A home built balanced bias differential current amplifier was used to amplify the resulting ion current [75]. The gain of the amplifier could be set to 10^3, 10^5 or 10^7 volts per amp by varying the resistance of the output load.

In most cases the amplifier was set on the 10^5 or 10^7 settings with an output voltage ranging from a few tens of millivolts to several volts. This is consistent with the known intensity of the laser in the focal region and typical values for one- and two-photon absorption cross-sections [72]. Because, the photodiode used to monitor the intensity of the laser radiation provided only a relative measurement it was not possible to normalise the MPI spectra to the absolute laser intensity. Therefore a quantitative comparison could not be made of the REMPI cross-sections for different states and molecules.

The REMPI signal for any resonant transition was found to be dependent on the sample pressure. The signal level increased rapidly with pressure from 0.25 to 0.5 torr reaching a maximum at 1.0 torr and then slowly decreased. At sample gas pressures greater than 10 torr no REMPI signal could be detected. The initial increase in signal can be explained by the increase in number density of molecules in the focal region. Since the absorption does not significantly affect the intensity of the laser beam then the number of ions produced will only depend on the number density of the gas, if all other factors remain constant. However, the increased pressure also increases the collision rate for the photoproducts, retarding their flight to the electrode plates and hence decreasing the size of the photocurrent. For those experiments in which only the ion current was monitored, the sample gas pressure was maintained in the range 0.5 to 1.0, torr but generally a higher pressure was required to observe dispersed fluorescence.

3.3.2 Fluorescence Excitation and Dispersed Fluorescence Spectroscopy

Fluorescence from the sample was detected at right angles to the direction of the laser beam. A lens system was used to image the focal region of the laser beam onto the entrance slit of a monochromator. At the exit slit of the monochromator the emission was detected by a photomultiplier tube (PMT). To record LIF spectra the grating could be set to zeroth order, reflecting all wavelengths at the same angle, or the monochromator could be used as a variable bandpass filter. In the latter case the wavelength of the monochromator could be set to a wavelength characteristic of a particular type of fluorescence and an LIF spectrum recorded. Alternatively, if the laser wavelength was fixed at a resonant absorption, then the monochromator wavelength could be scanned to generate dispersed fluorescence spectra. Both fluorescence excitation and dispersed fluorescence spectra were recorded for the molecules HCl, DCl, DBr and HI in conjunction with the measurement of (2+1)REMPI spectra.

The imaging system for collecting the fluorescence consisted of two lenses : a short focal length, collimating lens which subtended a large solid angle to collect as much emission as possible and, a longer focal length, field lens chosen to match the aperture ratio of the monochromator. The optics of monochromators are designed to focus the image of the entrance slit onto the exit slit and have the grating completely filled by the image of the slit. Therefore the collection optics must be designed to have the same aperture ratio to achieve the optimum throughput of radiation.

Three monochromators were used : a McKee-Pederson 1018B 0.45m monochromator, which was used with Hamamatsu R928 and R955 PMT's to observed the fluorescence spectra of HI, a Jobin-Yvon HRS2 0.6m monochromator with the same Hamamatsu PMT's, which was used to record fluorescence spectra of HCl and DCl, (and also one spectrum from DBr) and an Acton Research Corporation VM-502-V 0.2m evacuable monochromator with an EMI G-type 26G314LF PMT which was used to record the dispersed fluorescence spectrum of DCl. The Hamamatsu PMTs were both side-on cage structure tubes with multi-alkali photocathodes, but differed in envelope material: the R928 had an ultraviolet glass envelope, while the R955 had a synthetic silica envelope resulting in an extended blue response. The EMI tube was of the head-on, fast linear focussed type with a MgF_2 window and RbTe photocathode. It was mounted in an EMI ambient temperature housing which could be sealed on to the monochromator. Generally all of the PMT's were used with an output impedance of 1 MΩ to give a high gain (10^7) but slow time response. An output impedance of 50 Ω provided a much smaller gain but it was then possible to study the temporal decay of the fluorescence. Observations of this nature were made for HI fluorescence with the Hamamatsu R955 PMT, which has a rise time of 2.2ns.

The transmittance of the monochromators varied with wavelength because of the varying reflectance of the gratings and the varying quantum efficiency of the PMT photocathode. A correction function to correct the observed spectra for this effect was determined for both the Jobin-Yvon and the Acton monochromators with the PMT's used. However, as yet no such function has been determined for the McKee-Pederson monochromator.

The bandwidth resolution of each monochromator was determined by observation of the ultraviolet and visible lines of a mercury atomic resonance lamp. The highest resolution was achieved with the Jobin-Yvon and the lowest with the Acton monochromator.

3.4 Signal Handling and Data Storage

Because of the pulsed nature of these experiments and the relatively low repetition rate of the pump lasers, there was a large dead time between each laser pulse during which there was no signal from the sample. If the signal was monitored continuously then this would have the effect of decreasing the signal strength and increasing the level of random noise. To avoid this the signals from the detectors were input into a Stanford Research Systems SR250 Gated Integrator and Boxcar Averager. This device generates a variable width gate which can be continuously delayed from a trigger pulse supplied by the laser. During the gate period the input signal is integrated and then normalised by the gate duration. This time-averaged continuous signal is then amplified. Finally an average over 3, 10 or 30 samples is taken which has the effect of increasing the signal-to-noise ratio. By using more than one boxcar averager it was possible to simultaneously record fluorescence excitation, ionisation and calibration spectra or some combination of these three.

The output from the boxcars was recorded on either a Kipp and Zonen BD8 single channel or a Kipp and Zonen BD9 two channel multi-range chart recorder and could also be digitised using an eight channel Stanford Research Systems SR245 Computer Interface Module and then stored on an IBM PC-XT 286 microcomputer. The interface module had an input range of ±10.24 volts DC with 13-bit resolution. It had an input impedance of 1 MΩ, equal to the output impedance of the boxcar. A major advantage of recording experimental data on the computer was the ease with which it could be subsequently processed. For example, corrections for wavelength error and instrument response could be made directly, simulated spectra and observed spectra could be compared more easily and, if the laser power was recorded over the spectrum then the signal could be power normalised.

The "raw" fluorescence or ionisation signals could also be directly observed on a Tektronix 2445 150 MHz oscilloscope. This could be used either to check the position and width of the gate relative to the signal, or, if fluorescence was being observed, to observe the emission in real time. If the PMT was set to the 50Ω, low gain fast response setting and the input impedance of the oscilloscope was matched to this , then it was possible to observe the fluorescence with a time base as short as 20ns/division. This time resolution was great enough to separate direct fluorescent emission from that due to recombination or reaction of excited species in the laser focus. Unfortunately because of the long delay needed on the SR250 it was not possible to record such time discriminated spectra.

3.5 Vacuum Cells

All of the optical cells used to hold the low pressure gas samples were derived from a common, basic design: a long glass tube with short side arms, a male ball and socket joint and "Young's" tap for connection to a vacuum line and a set of REMPI electrode plates. A schematic of this basic design is shown in figure 3.1. The main axis and side arms were sealed by 2 mm thick 50 mm

Figure 3.1

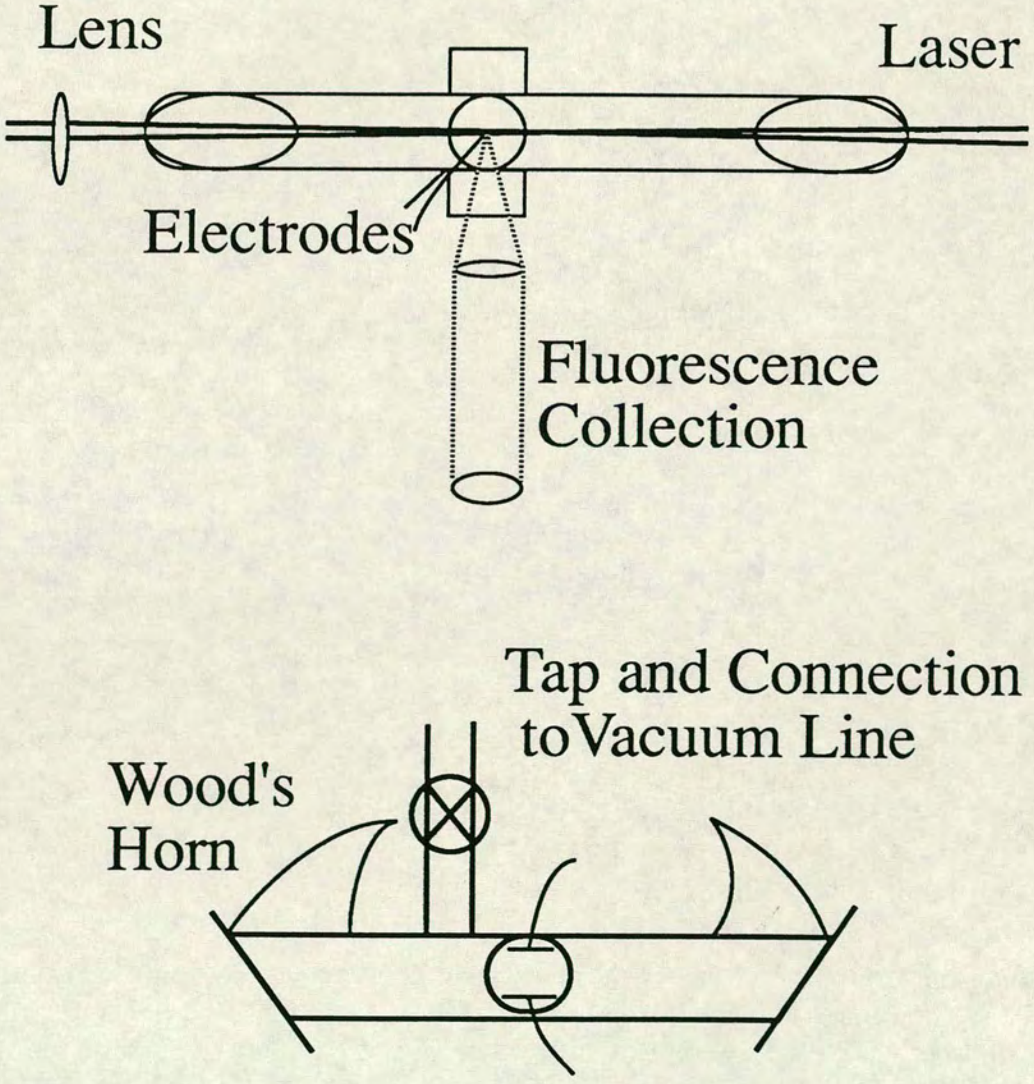

Sample Cell

diameter quartz windows attached onto the ground glass ends of the tubes with halocarbon wax. The laser beam was directed along the main axis of the cell and brought to a focus at the centre of the cross formed by the main axis and the side arms. The ends of the main axis were cut at the Brewster's angle for the wavelengths used, and fitted with light collecting Wood's horns to decrease the level of scattered laser light within the cell. The nickel electrode plates were positioned above and below the centre of the cross with a separation of 15 - 20 mm. Thin nickel wire leads were spot welded to the plates and passed through pinholes in the glass wall of the cell. Varian "Torr Seal" epoxy resin was used to form the vacuum seal between the wires and the glass. Fluorescence emission from the focal region was viewed through the side windows at right angles to the laser beam.

Some alterations were made to the cell design to allow it to be attached to the vacuum monochromator. The side arm through which the fluorescence was viewed was glued onto an aluminium flange with Varian "Torr Seal". This flange had an O-ring seal for the 25mm diameter, 2mm thick, lithium fluoride window which sealed the side arm. An aluminium optics flange, containing two lenses connected this flange to the monochromator. All of the flanges had viton O-ring seals. To reduce the scattered light entering the monochromator the other side arm was replaced by a Wood's horn. A cold trap was added to the cell to allow the temperature, and hence the pressure of the sample gas, to be controlled and to remove the traces of halogen gas produced by disproportionation and the recombination of photodissociated molecules.

The temperatures of the cold baths required to reduce the pressure of the sample gas to the correct level were below 140 K. Cold baths at such a low temperatures are difficult to maintain and can generally only be used for between 1 and 2 hours before they must be replaced. It would have been more convenient and more accurate to use a flow cell with an attached vacuum line instead of a static cell. Also it would have been possible to reduce the effect of leaks of air into the cell which would result in absorption of the fluorescence by molecular oxygen. However, it was not possible to use such a system at the time these experiments were carried out.

3.6 Sample Preparation and Gas Handling

All gas handling, preparation and purification of sample gases was performed on a glass vacuum line, pumped by a mercury diffusion pump which was backed by a mechanical rotary pump. An ultimate pressure of 10^{-4} torr could be achieved with this pumping system. Pressure measurements in the range 0.1 to 100 torr were made with an MKS model 222BA 100 torr Baratron whilst for pressures greater than 100 torr an MKS model 221AHS 1000 torr Baratron was used.

The hydrogen chloride and deuterium chloride samples used were BDH electronic grade, 99.99% minimum purity and MSD 99.5 atom % D. They were purified before use by several freeze/pump/thaw cycles to remove volatile impurities. No further purification was necessary. The vacuum line and cell were passivated with 10 to 15 torr of deuterium oxide (Aldrich 99.8 atom %) overnight to prevent the formation of hydrogen chloride by exchange with hydrogen containing impurities in the system. This procedure was followed whenever deuterated species were used unless the vacuum cell was fitted with LiF windows. Because of the hygroscopic nature of this material the cell and line had to be passivated with the sample gas rather than D_2O.

The hydrogen bromide and hydrogen iodide samples were prepared using standard vacuum preparation methods by Dr S.G.D. Henderson and Mr S. Morton of the Inorganic Chemistry Section of the Chemistry Department. The deuterium bromide was BOC 99 atom % D stabilised with tetrachloromethane. Because of the rapid dissociation rate of HI it was stored in a cold trap in liquid nitrogen. All other gases were stored in 2 litre glass bulbs fitted with cold traps. Dark cloth was wrapped around the bulbs containing HBr, DBr and DI to decrease the rate of photodissociation of these molecules, which all have continuum absorption systems in the ultraviolet.

Some photodissociation of these four molecules did occur resulting in a build up of H_2 (or D_2) and X_2 contaminants in the cell. The H_2 was volatile enough to be removed by the freeze/pump/thaw method but the X_2 contaminant had to be removed by vacuum trap distillation. The cold trap on the contaminated bulb was held at a temperature at which the halogen had a negligible vapour pressure but the hydride had a much higher vapour pressure. The hydrogen halide was then frozen down into a second bulb with a liquid nitrogen cold finger. This was repeated whenever the halogen contamination became significant and several cycles of distillation were used each time.

Chapter 4
Experimental Results

4.1 Introduction

The experimental spectra reported in this chapter include (2+1)REMPI, two-photon fluorescence excitation and dispersed fluorescence spectra of the hydrogen halides and their deuterated analogues. Single photon absorption spectra of these molecules have been extensively studied [1-17]. However, there have been few studies employing two-photon excitation [18-20] [76] [77], or which have examined the fluorescence emission [69] [74] of the excited states. The two-photon excitation mechanism discriminates against the very strong diffuse absorption to the $^1\Pi$ states, which have previously been observed and which obscure weaker $\Delta\Omega \neq 1$ transitions [24]. It was therefore thought that it would be possible to observe previously unreported absorption bands, and in particular the "missing" vibrational levels of the ion-pair state for HBr and HI. (2+1)REMPI spectra of all of the hydrogen halides were recorded with this aim, and also to identify the appropriate excitation wavelengths for recording dispersed fluorescence spectra.

Fluorescence excitation spectra were recorded both in addition to REMPI spectra, to determine rovibronic energy levels, and also simultaneously with REMPI spectra to investigate the coupling of Rydberg states with the ion-pair state. Fluorescence excitation spectra were recorded in two modes of operation, either zeroth order or wavelength gated. In the former case the diffraction grating of the monochromator used to analyse the emission was set to the zeroth order position so that all of the fluorescence imaged on the entrance slit of the monochromator was detected. This type of excitation spectroscopy was particularly important for recording very weak fluorescence, when samples at high pressure had to be used, because the ionisation detection system employed for recording (2+1)REMPI spectra was not suitable for use with sample pressures greater than 10 torr.

In the wavelength gated mode of operation the monochromator was set to pass a small band of wavelengths. Only those states which fluoresced within the selected bandpass of the monochromator were detected. In both HCl and HI the ion-pair state has a characteristic continuum fluorescence band in the wavelength range 190-270 nm. If fluorescence in this wavelength range was observed from a state, other than the ion-pair state, then it could be inferred that this excited state was coupled to the ion-pair state. Gated fluorescence excitation spectra, recorded in parallel with (2+1)REMPI spectra, provided therefore a powerful diagnostic technique for identifying such states.

Dispersed fluorescence spectra were recorded for HCl, DCl and HI from many rovibronic levels of the ion-pair state and for a number of Rydberg states. For HCl and DCl, transitions to both the ground state and the repulsive valence states were observed. However, the latter transitions were obscured in HI by very strong molecular iodine emission bands, primarily $D' \rightarrow A'$ and $D \rightarrow X$. A similar, though much weaker, band was the only emission feature observed for DBr.

The dispersed fluorescence spectra recorded were principally structured continua since the bound-bound transitions were in the VUV. The analysis and simulation of such spectra provides detailed information on the vibronic wavefunction of the emitting level [78]. It is therefore appropriate to discuss the general features of the dispersed fluorescence spectra observed for the hydrogen halides, and how this is influenced by the potential energy surfaces of the initial and final states involved in the transition. A good qualitative, and in many cases quantitative, understanding of dispersed fluorescence spectra can be achieved, semiclassically, with the stationary phase approximation and the concept of the Mulliken difference potential [79]. This is dealt with in greater detail in Appendix B. Briefly, the stationary phase approximation limits electronic transitions to those which preserve the nuclear momentum of the initial state in the final state [78]. The Mulliken difference potential is a potential energy surface which defines the locus of points which satisfies this condition. Thus transitions only occur to points on the difference potential.

For the hydrogen halides there are two possible initial states, namely the Rydberg states and the ion-pair state, and two final states, namely the ground state and the repulsive valence states. The four possible transitions are depicted schematically in figures 4.1 and 4.2 along with the appropriate Mulliken difference potentials and simulated spectra. It is , of course, possible for transitions to occur from the ion-pair or Rydberg states to other , lower energy excited states, but these transitions would lie in the infra-red. Because of the cubic dependence of the Einstein A coefficient on the frequency of the emitted light any emission accompanying such transitions must be several orders of magnitude weaker than the visible or UV fluorescence observed.

Figure 4.1 Rydberg Type Fluorescence Spectra

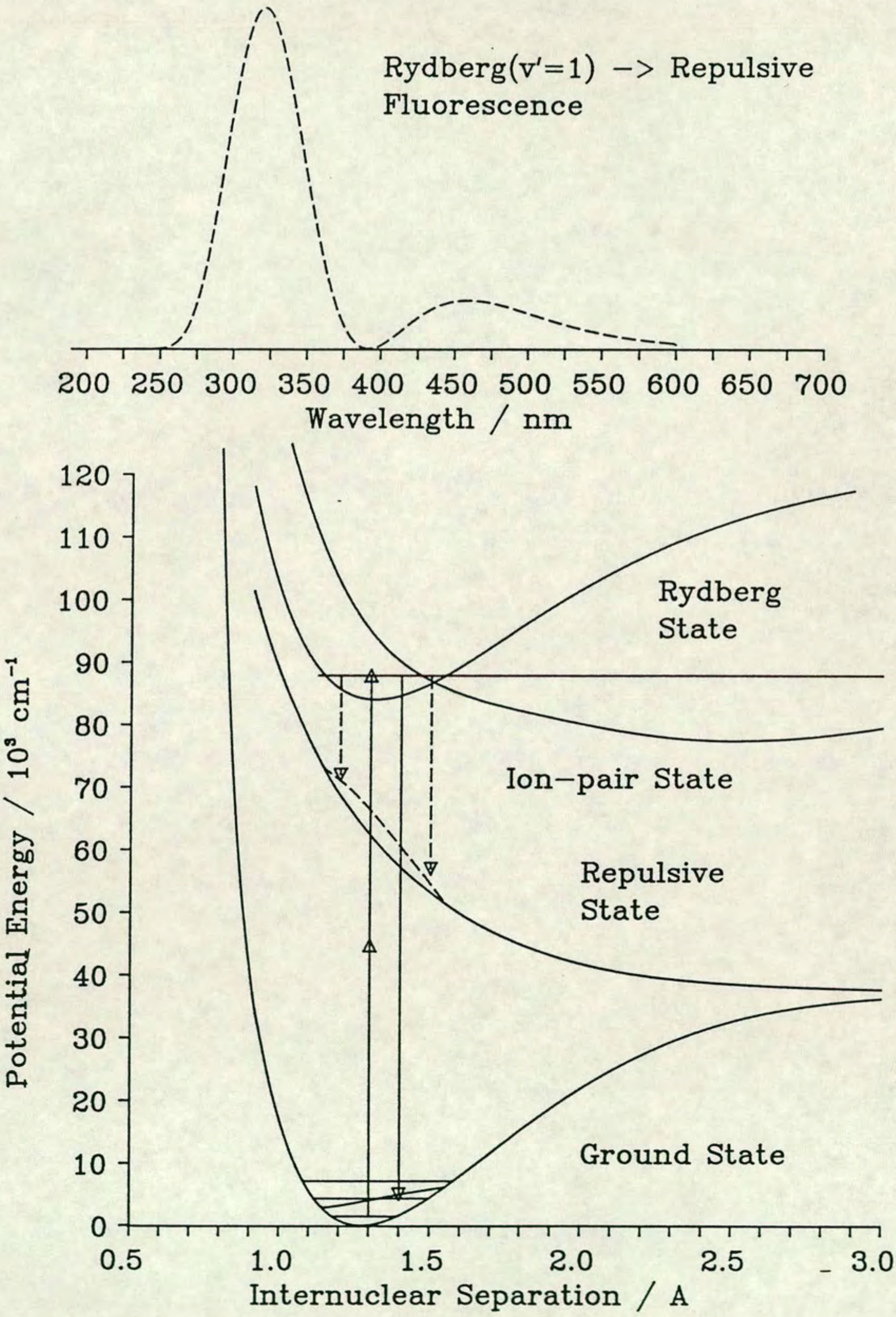

Due to Franck-Condon factors the emission from a Rydberg state to the ground state is dominated by the $\Delta v=0$ transition, which lies in the VUV and could not be observed in this work. The emission accompanying a transition from a Rydberg state to a repulsive state consists of a broad continuum band extending from the UV into the visible wavelength region. The intensity of the fluorescence is modulated by the Franck-Condon density for the transition at each wavelength and so reflects the vibrational wavefunction of the emitting state. For a vibrational level with n nodes there will $n+1$ peaks in the bound-free fluorescence spectrum. The fluorescence spectrum shown in figure 4.1 is from a $v'=1$ level, and therefore has two maxima corresponding to the two maxima in the vibrational wavefunction of the upper level. The long wavelength maximum corresponds to the inner maximum of the wavefunction. Similar reflection structure is observed in the emission spectrum from the ion-pair to a repulsive state but it is 'squeezed' at short wavelength because the repulsive state potential has a small gradient at large R.

For ion-pair state emission to the ground state the situation is more complex. Below a particular ground state energy , usually the dissociation energy , the difference potential is single valued and the spectra exhibit essentially the same behaviour as is observed for the emission from Rydberg states to the ground state. However, above this energy the difference potential is double valued and has a maximum . A semiclassical analysis of the fluorescence spectrum expected for such a difference potential predicts that the continuum spectrum will be the product of a low frequency term , with the form of a squared Airy function , modulated by a higher frequency cosine squared term [78] [80]. The latter

Figure 4.2 Ion-pair Type Fluorescence Spectra

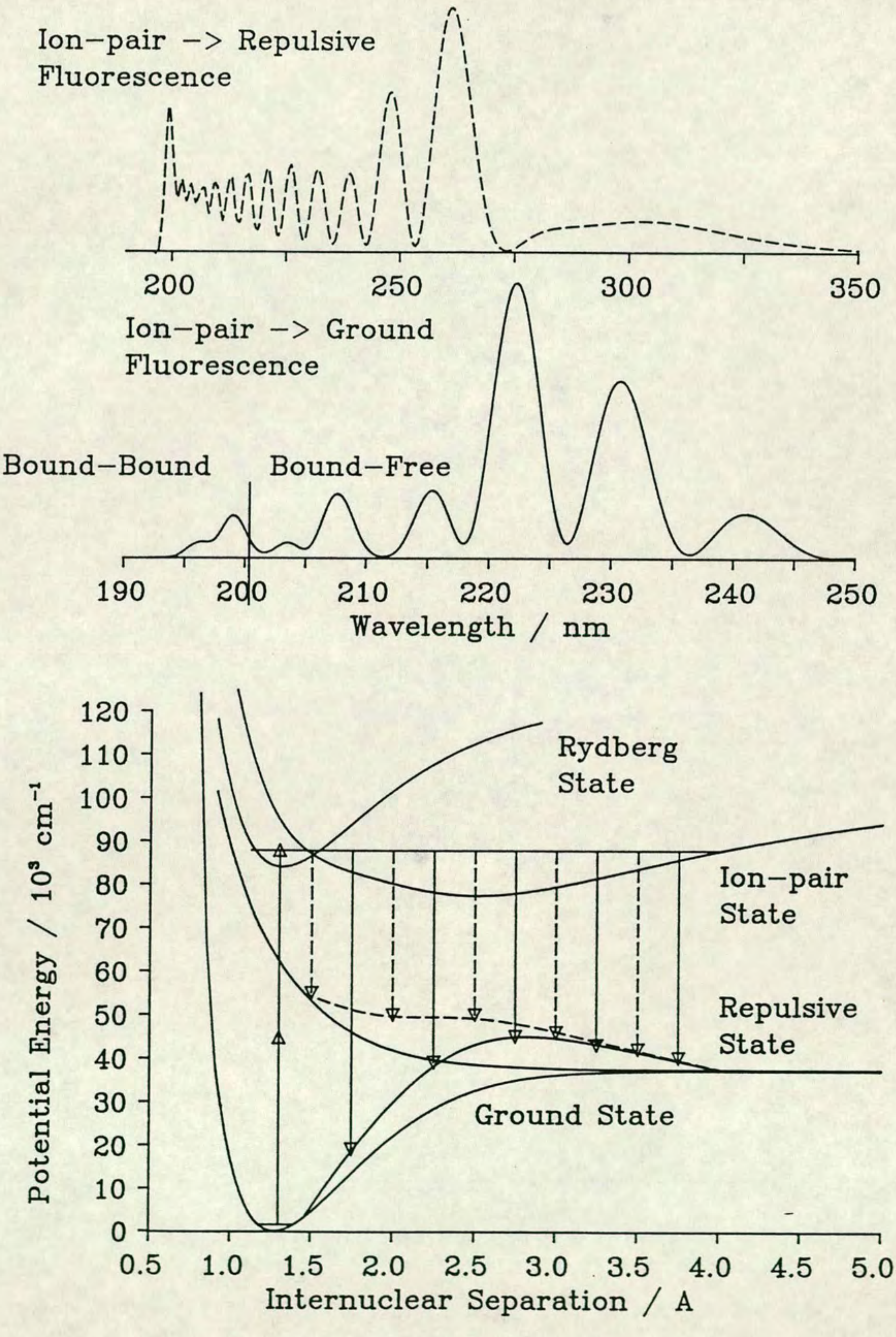

results from the interference of the two limbs of the difference potential. The origin of the Airy function corresponds to the wavelength of the transition to the maximum of the difference potential. This occurs at the internuclear separation for which the gradients of the upper and lower potential energy surfaces are equal. To a first approximation this is at the minimum of the ion-pair state. Because of conservation of momentum the wavelength of the origin depends only on the separation of the electronic term values of the two states but not on the vibrational energy in the excited state. Therefore, all of the spectra will have the same long wavelength limit corresponding to the term value of the initial state. The periods of the two frequency components in the spectra depend inversely on the reduced mass of the molecule. The heavier, deuterated isotopomers thus have a more fully developed squared Airy function envelope with higher frequency modulation.

A further complication in the analysis of fluorescence spectra is due to the effects of the transition dipole moment function, which is not a constant but varies with internuclear separation. Because fluorescence at a particular wavelength corresponds to emission from molecules with a particular internuclear separation this results in a wavelength dependent modulation of the fluorescence intensity. Generally, the transition dipole moment function decreases with increasing internuclear separation, which results in a decrease in the intensity of short wavelength fluorescence. If the whole fluorescence band can be observed, it is possible to determine the form of the transition dipole moment function from the deviation of the relative peak heights from that predicted purely on the basis of the vibrational wavefunctions. Unfortunately, this was not possible in the case of the hydrogen halides where only a small portion of the fluorescence spectrum was observed.

In the remaining sections of this chapter the experimental spectra obtained are presented and discussed in detail.

4.2 Hydrogen Chloride and Deuterium Chloride

4.2.1 Fluorescence Excitation Spectra of DCl

Fluorescence excitation spectra of DCl were recorded, with gated wavelength detection, to demonstrate the use of this technique for simplifying congested spectra and in analysing dispersed fluorescence spectra. Because of the low fluorescence yields observed, the spectra were recorded using a very high pressure of DCl in the sample cell, typically 30 - 300 torr. This precluded the recording of (2+1)REMPI spectra in conjunction with the fluorescence excitation spectra.

Fluorescence excitation spectra to the $v' = 16$ and 17 levels of the ion-pair state and to the $v' = 1$ level of the $F^1\Delta_2(2)$ Rydberg state of DCl, recorded at detection wavelengths of 227 nm and 300 nm, are presented in figure 4.3. In the upper trace the five rotational branches of the Rydberg state can be clearly seen. The detection wavelength of 300 nm is near the peak of the fluorescence emitted by this level. There is very little fluorescence emitted from either of the ion-pair state levels at 300 nm and hence few peaks corresponding to rotational structure in these spectra are observed. However, for the lower trace the detection wavelength is set to a peak in the high frequency structure of the bound-free

Figure 4.3 Fluorescence Excitation Spectra of DCl

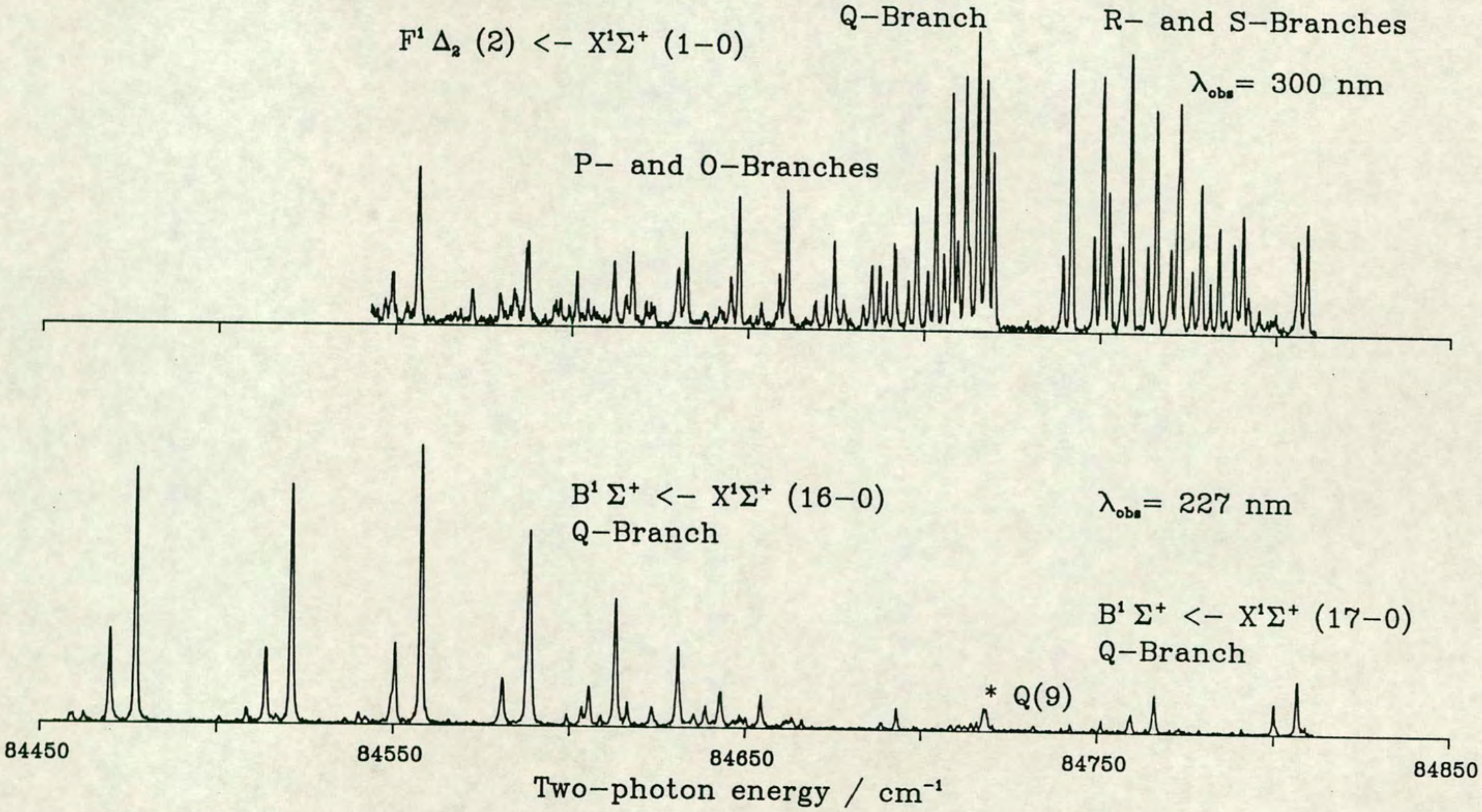

ion-pair type fluorescence. The Rydberg state does not fluoresce at this wavelength and so is not observed in this fluorescence excitation spectrum. From the two spectra it can be seen that the Q(9) line of the v' =17 level of the ion-pair state is at the same excitation energy as the Q(3) line of the Rydberg state. Dispersed fluorescence spectra if recorded at this excitation energy will therefore show ion-pair type fluorescence in addition to the Rydberg state fluorescence.

Similar behaviour is seen in the fluorescence excitation spectra to the v' =21 level of the ion pair state which is overlapped by the v' =2 level of the $F^1\Delta_2(2)$ Rydberg state, as shown in figure 4.4. The shorter detection wavelengths discriminate against the Rydberg state and only the ion-pair levels are observed at 222 nm. At longer wavelength, 257 nm, the stronger rotational branches of the Rydberg state can be observed but the ion-pair fluorescence dominates. For the longest detection wavelength, 300 nm, the Q, R, and S rotational branches of the Rydberg state are present, although the low fluorescence yield from the Rydberg state results in a poor signal to noise ratio at this detection wavelength. It is also possible to observe several of the stronger lines in the ion-pair state level because of the long wavelength fluorescence to the repulsive $A^1\Pi$ state, although this fluorescence is very weak in comparison to the ion-pair → ground state fluorescence.

4.2.2 Dispersed Fluorescence Spectra of HCl and DCl

The $B^1\Sigma^+$ (0^+) Ion-pair State

Strong fluorescence was observed from the ion-pair state in both HCl and

Figure 4.4 Fluorescence Excitation Spectra of DCl

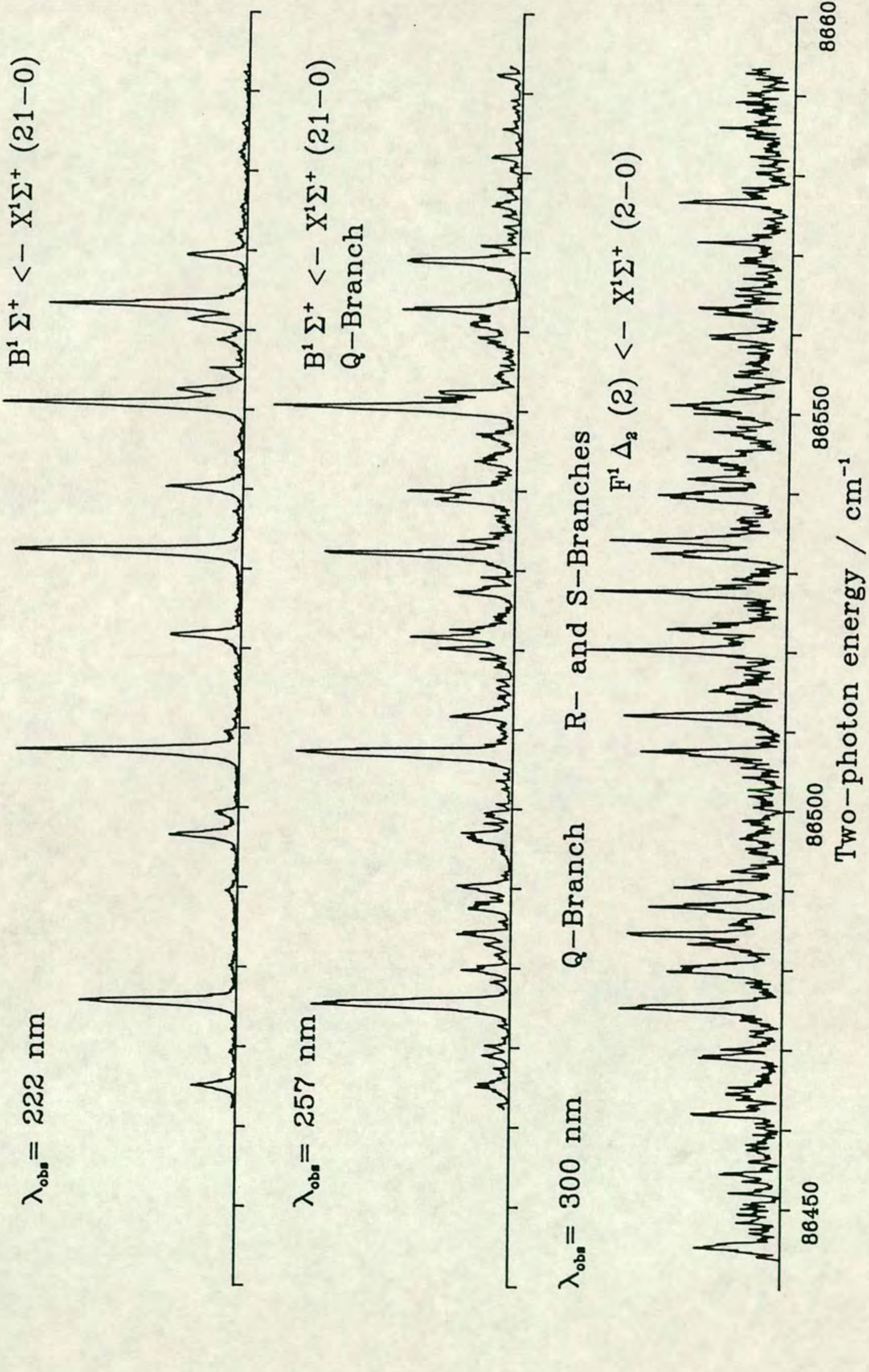

DCl. All of the vibrational levels which were detected via (2+1)REMPI spectroscopy were observed to fluoresce. Typical spectra are shown in figure 4.5 for the fluorescence from the v' =11, 12, 15, and 16 levels of HCl. Similar fluorescence spectra for DCl, from the levels v' =14 to 21, are shown in figure 4.6. Simulated dispersed fluorescence spectra from these levels of the ion-pair state in HCl and DCl are shown in figures 5.5 to 5.16. In most cases the Q(3) rotational line of a given band was excited when recording dispersed fluorescence spectra. This corresponds to the most highly populated rotational level in the ground state and was the strongest line observed in both (2+1)REMPI and fluorescence excitation spectra. Dispersed fluorescence spectra recorded using other rotational lines within the same vibronic band were identical, but weaker, to those for the Q(3) line. In a $\Sigma^+ \rightarrow \Sigma^+$ transition each rotational level with J = 3 can emit to either J = 2 or J = 4 in the final state. This results in two emission bands which have the same structure but are shifted in energy and have slightly different overall intensities because of the different Honl-London factors.

For bound-bound transitions this results in two rotational lines, a P- line and an R- line, whereas for bound-free transitions there is an energy and phase shift between the peaks in the two structured continua. In HCl and DCl both the P- and R-lines of bound-bound transitions can be observed in spectrographs of electric discharge excited emission spectra. In bound-free spectra the energy shifts are much smaller than the width of the peaks and so this effect is apparent only as a slight broadening of the peaks from the width expected for a single rotational transition. Also, because of the initial two-photon excitation the intensity of the fluorescence was very low and, since a high monochromator

Figure 4.5
Dispersed Fluorescence from the Ion−pair State in HCl

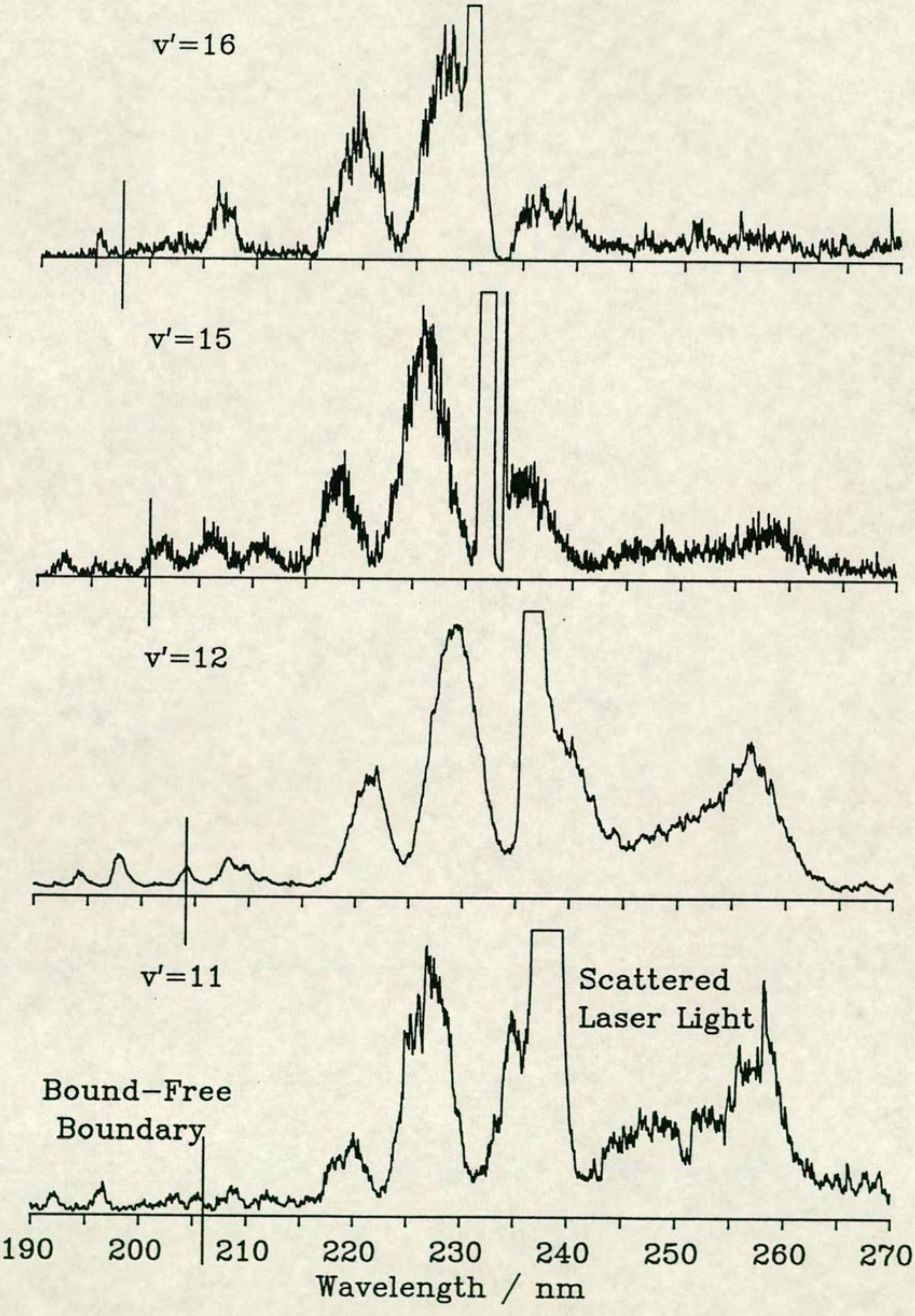

Figure 6b
Dispersed Fluorescence fron the Ion-pair State in DCl

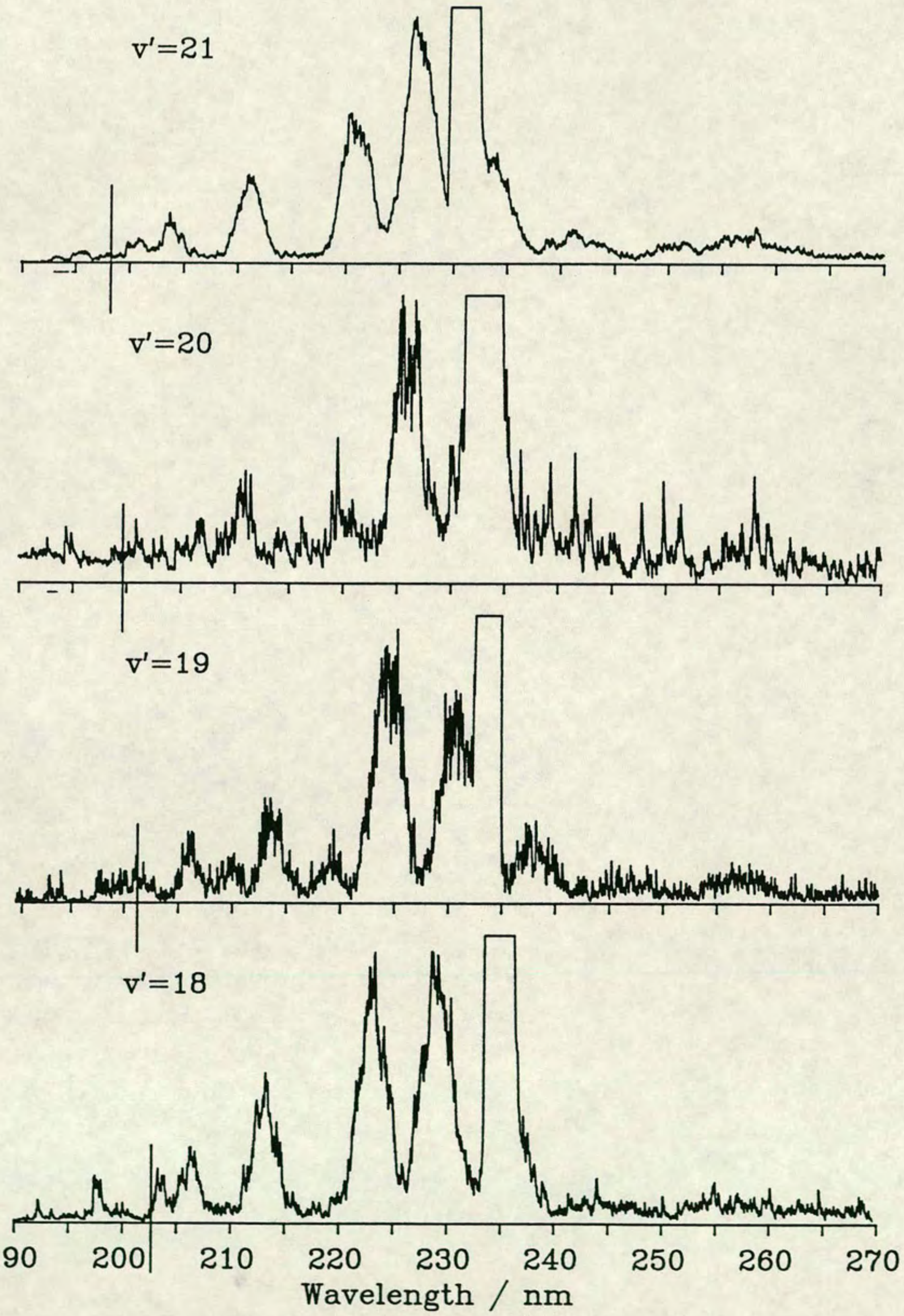

Figure 4.6a
Dispersed Fluorescence from the Ion-pair State in DCl

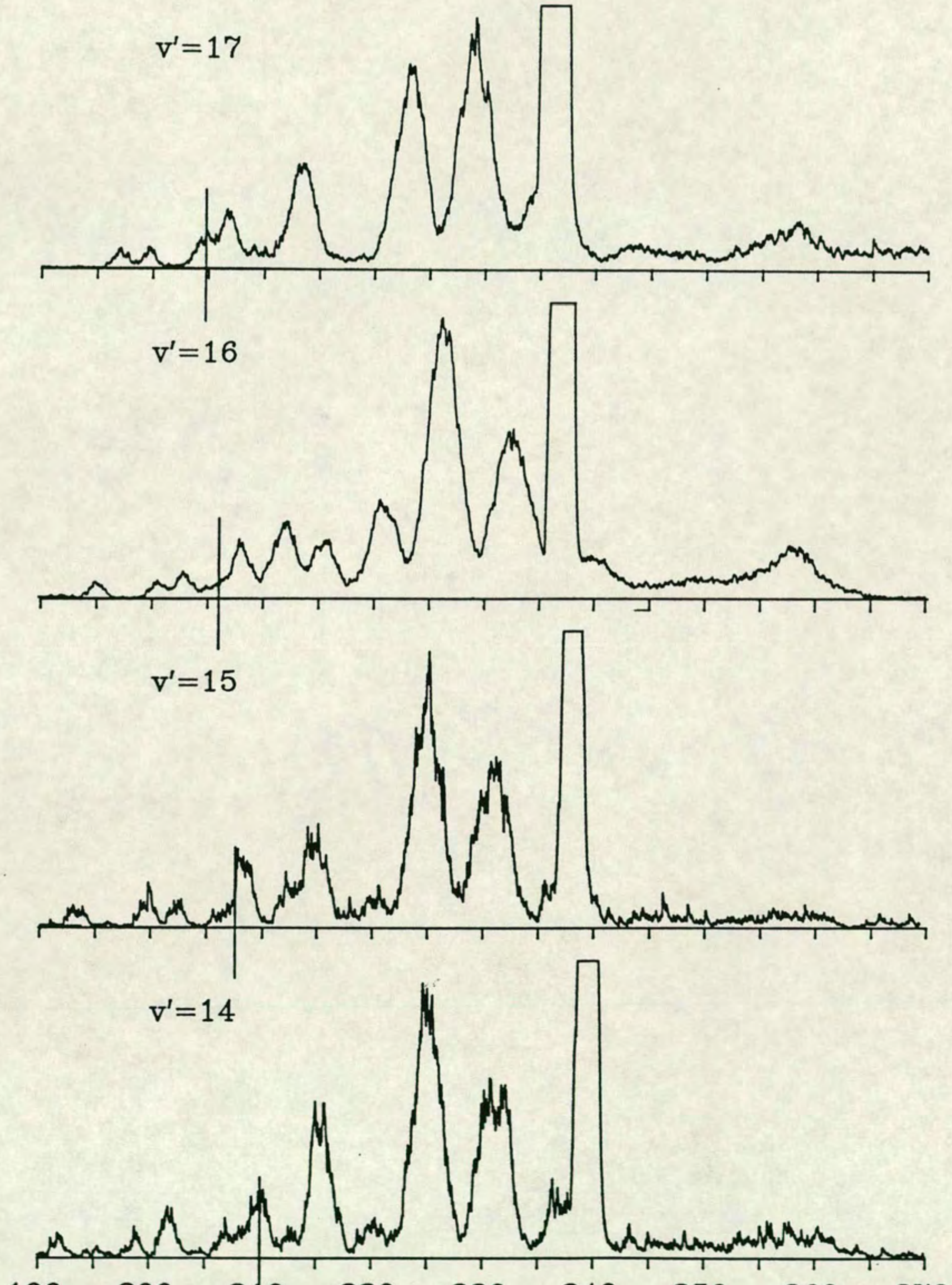

bandpass setting was required, it was not possible to record spectra at high resolution. Individual rotational lines therefore could not be resolved in the dispersed fluorescence spectra of bound-bound transitions and the interference peaks in the structured continua were broadened by the bandpass of the monochromator.

A characteristic bound-free emission band is evident in all of the spectra shown in figures 4.5 and 4.6, although in each one the red end of the spectrum is partially obscured by scattered laser radiation. The low frequency squared Airy function envelope, predicted by semiclassical analysis, can be clearly seen. More of this envelope is present in the DCl spectra because of the much greater reduced mass of this molecule. In addition to the bound-free structured continuum , bound-bound transitions to the highest vibrational levels of the ground state can be identified. As well as the factors discussed in section 4.1, the intensity of the fluorescence emission detected is affected by the absorption of the fluorescence by molecular oxygen present in the atmosphere (no special precautions were taken to excluded the ambient atmosphere from the apparatus). This is negligible at wavelengths longer than 200 nm but becomes increasingly strong at shorter wavelengths and from 190 nm all wavelengths are completely absorbed.

To the red of the laser line another emission band can be observed in a number of the DCl spectra. From the wavelength of this band it is possible to assign it to fluorescence from the ion-pair state to the $A^1\Pi$ repulsive valence state. The principal features of this band consist of a relatively narrow peak at 258 nm and a much broader , flat-topped peak which extends to 320 nm. In some spectra a further peak can be observed at 308 nm due to scattered laser light from the XeCl excimer laser used to pump the dye laser. This band would be expected to extend much further to the blue than is observed but is swamped by the stronger $B^1\Sigma^+$ $(0^+) \rightarrow X^1\Sigma^+$ fluorescence. The very low oscillator strength of this transition compared to that of the $B^1\Sigma^+$ $(0^+) \rightarrow X^1\Sigma^+$ emission implies that the transition dipole moment function is very small. This is in agreement with the ab initio calculations of reference [42].

Unlike the $B^1\Sigma^+$ $(0^+) \rightarrow X^1\Sigma^+$ fluorescence band this emission does not vary greatly in each of the observed levels. Any variation in the spectra from different levels is obscured by the overlap with the $B^1\Sigma^+$ $(0^+) \rightarrow X^1\Sigma^+$ emission. Although the HCl spectra recorded do not extend to wavelengths longer than 270 nm a similar $B^1\Sigma^+$ $(0^+) \rightarrow A^1\Pi$ fluorescence band is expected. The peak at 258 nm observed in some of the spectra is a strong indication of the presence of this band in HCl as well as in DCl.

The $E^1\Sigma^+$ (0^+) Rydberg State

The dispersed fluorescence spectra from the $v' = 1$ and $v' = 0$ vibrational levels of the $E^1\Sigma^+$ (0^+) Rydberg state in HCl and DCl are shown in figure 4.7. These spectra show very similar features to those observed for the ion-pair state. As discussed in Chapter 2 the $E^1\Sigma^+$ (0^+) Rydberg state is vibronically coupled to the ion-pair state which results in a mixing of the vibronic wavefunctions of the two states. Consequently, emission from a vibronic level of either state will contain features which can be assigned to transitions originating from both states.

Over the wavelength region studied, 190 - 550 nm, the only Rydberg

Figure 4.7 Dispersed Fluorescence from $E^1\Sigma^+$ Rydberg State in HCl and DCl

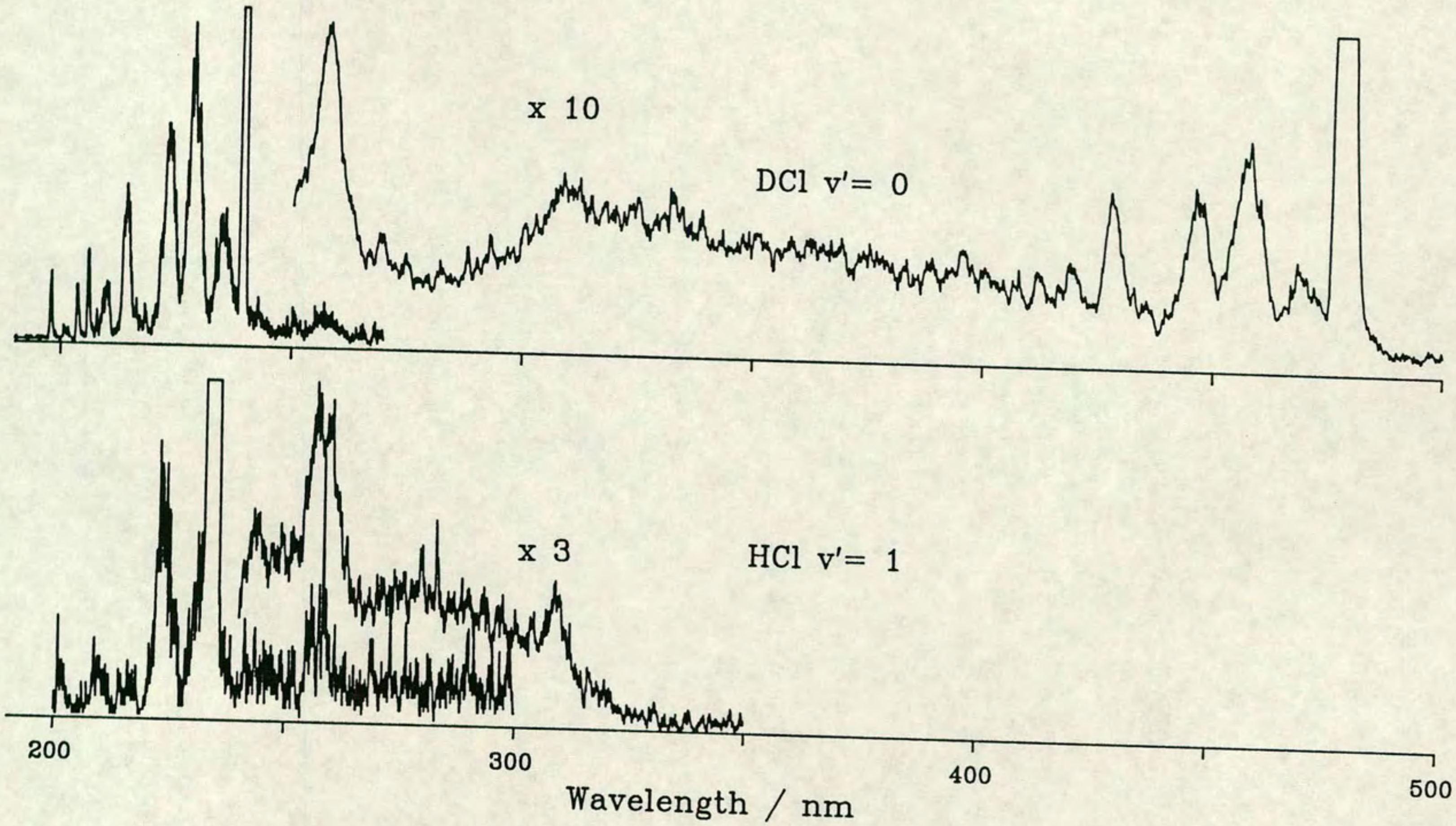

fluorescence spectrum expected is the bound free $E^1\Sigma^+ (0^+) \rightarrow A^1\Pi$ emission band. Such a fluorescence system is expected to be broad and diffuse and to reflect the vibrational wavefunction of the excited state. For the $v' = 0$ vibrational level in DCl this emission system is evident only as an extended long wavelength tail to the $B^1\Sigma^+ (0^+) \rightarrow A^1\Pi$ emission band. The emission from HCl does not appear to show this additional long wavelength feature. However, the emission from a $v' = 1$ level is bimodal and the shorter wavelength peak would be obscured by the $B^1\Sigma^+ (0^+) \rightarrow X^1\Sigma^+$ emission while the longer wavelength peak would be very broad and weak. If the oscillator strength in HCl is similar to that in DCl then it is most unlikely that this emission would be observed. Observation of the dispersed fluorescence from the $v' = 0$ level in HCl would resolve this point but it was not recorded in this work. The relatively low intensity of the $E^1\Sigma^+ (0^+) \rightarrow A^1\Pi$ fluorescence observed results from a small transition dipole moment function for this transition. The much larger transition dipole moment function of the $B^1\Sigma^+ (0^+) \rightarrow X^1\Sigma^+$ emission results in it swamping the $E^1\Sigma^+ (0^+) \rightarrow A^1\Pi$ band. A comparison of the total fluorescence intensity in Rydberg type and ion-pair type fluorescence from the mixed levels would be of great assistance in determining the relative strengths of the contribution of individual states to the total wavefunction.

The $g^3\Sigma^- (0^+)$ Rydberg State

The $g^3\Sigma^- (0^+)$ Rydberg state has also been shown to be vibronically coupled to the ion-pair state in the hydrogen halides. A dispersed fluorescence spectrum from the $v' = 0$ level of this state in DCl is presented in figure 4.8. The spectrum is dominated by a broad asymmetric peak centred near 350 nm which was

Figure 4.8 Dispersed Fluorescence Spectrum from v'=0 of $g^3\Sigma^-(0^+)$ State in DCl

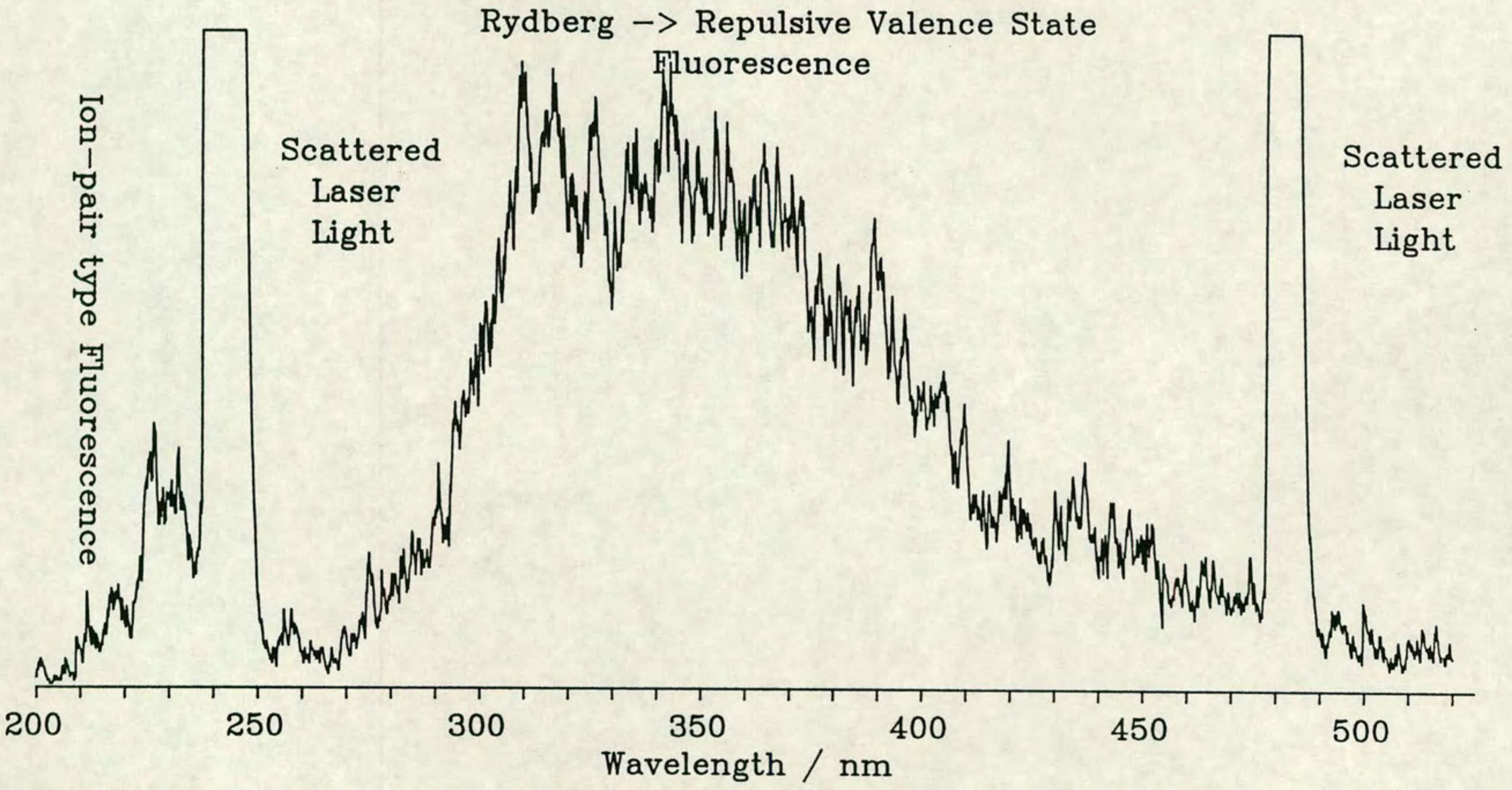

initially assigned to $g^3\Sigma^-$ $(0^+) \rightarrow A^1\Pi$ fluorescence. The single peak is indicative of emission from a v' =0 level which confirms the previous assignment of this level. However, the emission band is asymmetric and has a maximum at a much shorter wavelength than is expected for such a transition. The shift in the peak of the fluorescence from that expected for the $g^3\Sigma^-$ $(0^+) \rightarrow A^1\Pi$ fluorescence is 4000 cm^{-1}. This is in close agreement with the calculated separation of the $A^1\Pi$ state from the $a^3\Pi$ states. The fluorescence has therefore been assigned as a $g^3\Sigma^-$ $(0^+) \rightarrow a^3\Pi$ transition which is confirmed by the simulation of the fluorescence spectrum reported in Chapter 5 and shown in figure 5.22.

There is also a much weaker structured fluorescence to the blue of the laser line which can be assigned to ion-pair state fluorescence. All of the emission from the $g^3\Sigma^-$ (0^+) state was very weak and it was necessary to record the fluorescence spectra at the lowest resolution setting of the monochromator. Consequently the high frequency interference structure of the $B^1\Sigma^+$ $(0^+) \rightarrow X^1\Sigma^+$ fluorescence could not be fully resolved. In the light of the comparatively large oscillator strength observed for ion-pair type fluorescence from the $E^1\Sigma^+$ (0^+) coupled Rydberg state and the nearest ion-pair levels, this must be interpreted as resulting from the presence of only a weak coupling between this $g^3\Sigma^-$ (0^+) state vibrational level and the ion-pair state.

The $F^1\Delta_2$ (2) Rydberg State

Dispersed fluorescence spectra were also recorded from the $F^1\Delta_2$ (2) Rydberg state in HCl and DCl. As this is an $\Omega = 2$ state it cannot vibronically couple to the ion-pair state because the states must have the same value of Ω if they are to interact. In HCl the fluorescence spectrum from only one level, the v' =1 level, was recorded while for DCl it was possible to record spectra from v' =0, 1, and 2. The dispersed fluorescence spectra from these levels are presented in figure 4.9. All of the observed features, except those at wavelengths shorter than 260 nm in the spectrum of v' =1 in DCl, have been assigned to the $F^1\Delta_2$ (2) → $A^1\Pi$ bound-free transition. A single broad band, centred at 380 nm and with a full width at half maximum of 130 nm (9000 cm^{-1}) is observed for the v' =0 emission. It is a reflection of the vibrational wavefunction in the excited state.

A bimodal fluorescence band is expected for the v' =1 level. In HCl the dispersed fluorescence spectrum was only recorded between 200 and 400 nm so only the short wavelength peak was observed. It is centred at 300 nm and is 60 nm wide. The peak at 308 nm is due to scattered XeCl radiation from the excimer pump laser. For DCl the wavelength range was extended to 520 nm and it was possible to identify both peaks of the reflection structure. The long wavelength peak is very much the weaker of the two due to the fall-off in intensity with increasing wavelength, which has a very marked effect over such a wide spectral range. Also it is partially obscured by the second order line corresponding to the exciting laser radiation. Because of this it was not possible to determine the maximum of this peak.

The intensity of the fluorescence from the v' =2 level was very weak and had a low signal to noise ratio. The Franck-Condon factors for the (0-0), (1-0) and (2-0) transitions are in the ratio 1:0.1:<0.01 and so excitation of the v' =2 level is much less efficient than for the lower vibrational levels. In order to record the

Figure 4.9 Dispersed Fluorescence Spectra from the $F^1\Delta_2$ (2) Rydberg State in HCl and DCl

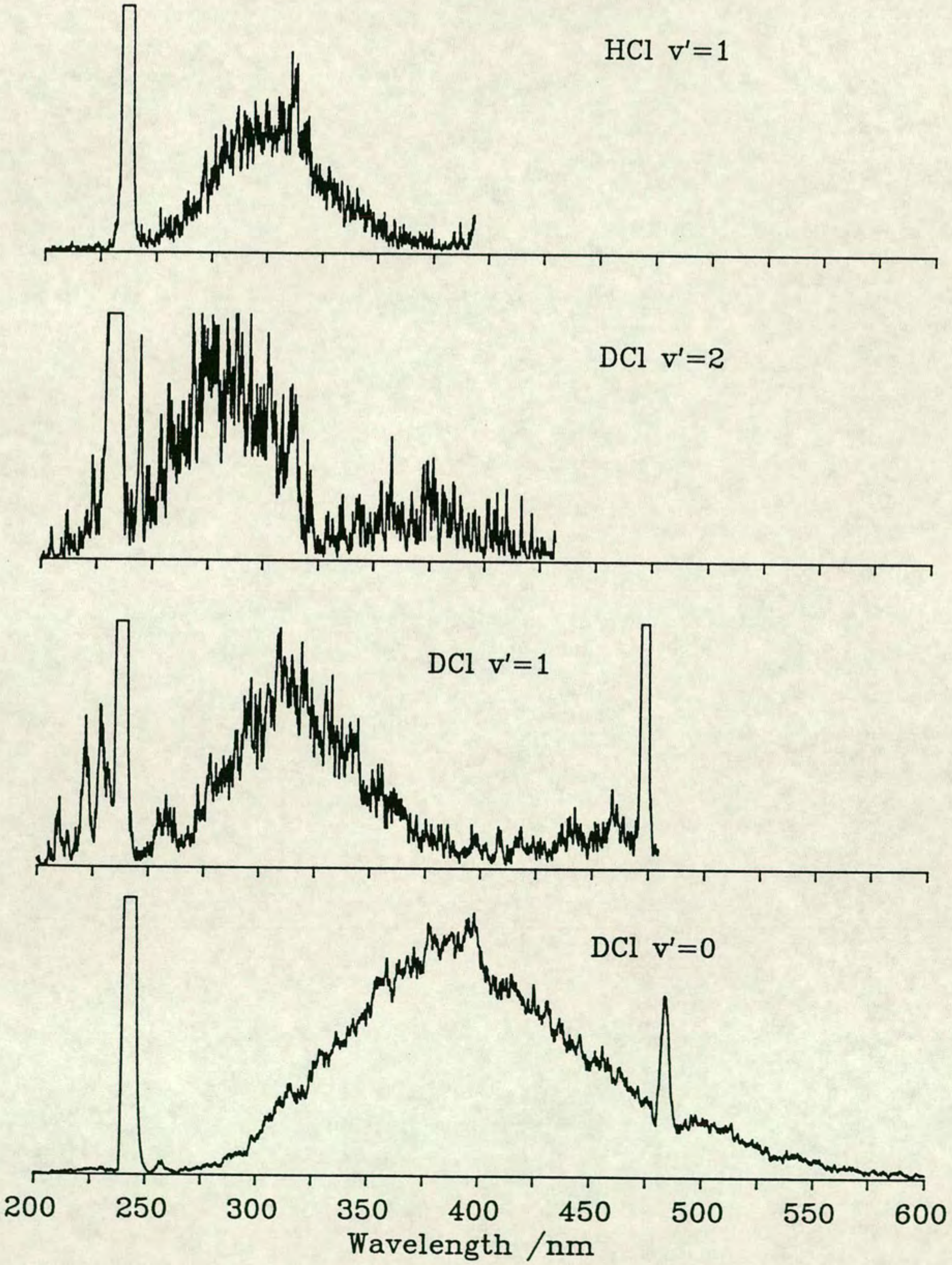

spectrum presented in figure 4.9 it was necessary to use a high pressure of DCl, 110 torr, and to use a low resolution setting on the monochromator. The high pressure used did not appear to collapse the vibrational population into the lower vibrational levels. This observation is in agreement with the fluorescence spectra of other states which have shown no change in fluorescence for pressures varying over two orders of magnitude.

The fluorescence spectrum from the $v'=2$ level is expected to show 3 peaks corresponding to the reflection of the vibrational wavefunction of the emitting state. Only two of these can be identified in figure 4.9 because the spectrum only extends to 460 nm and the signal to noise ratio is too low. The shortest wavelength peak is at 275 nm and has a width of 60 nm. Although the longer wavelength peak is much weaker a maximum can be identified at 375 nm. If this spectrum is compared with those of $v'=0$ and $v'=1$ the trends expected in the structured continuum of emission from a $v'=2$ level are obvious, as shown in figure 5.20.

In addition to the expected $F^1\Delta_2\,(2) \rightarrow A^1\Pi$ fluorescence observed there is evidence of ion-pair type fluorescence in the dispersed fluorescence spectrum from $v'=1$ in DCl. This is due to an accidental overlap with the Q(9) rotational line of the ion-pair state which was noted in the fluorescence excitation spectra discussed in section 4.2.1.

4.3 Hydrogen Bromide and Deuterium Bromide

For both HBr and DBr the intensity of fluorescence observed in emission from the excited electronic states was too low to permit the recording of either fluorescence excitation or dispersed fluorescence spectra. Therefore only (2+1)REMPI spectra were recorded for these two molecules.

The quality of the (2+1)REMPI spectra recorded for HBr and DBr is rather poor compared to the corresponding spectra recorded for HCl and DCl. All of the HBr spectra exhibit a large, non-resonant background ionisation signal and many of the HBr and DBr spectra have very high noise levels. The low signal to noise ratio is exacerbated by the diffuseness of the higher J rotational lines of several of the excited states.

All of the vibronic levels observed in the (2+1)REMPI spectra are summarised in table 4.1 and the measured rotational line positions are listed in Appendix C. The molecular constants determined from the experimental spectra are in poor agreement with those reported in the literature [11] [76].

The wavelength region studied for HBr and DBr was chosen to coincide with the most strongly absorbing vibronic levels of the ion-pair state reported in single photon absorption spectra. This restricted the energy range under study and so it was not possible to make a complete survey of all of the excited electronic states of HBr and DBr within the wavelength ranges of the dyes available. For HBr (2+1)REMPI spectra were recorded in the wavelength ranges 486 - 502 nm and 518 - 522 nm and for DBr in the ranges 481.5 - 483 nm, 485.75 - 487.25 nm, 493 - 498 nm, 499 - 500 nm, and 501.5 - 503.5 nm.

Table 4.1a Observed Term Values and Rotational Constants of HBr

State	v'	/ cm^{-1}		B_v / cm^{-1}		$D_v 10^4$ / cm^{-1}		Rotational
		Obs.[1]	Lit.[2]	Obs.[3]	Lit.[2]	Obs.[4]	Lit.[2]	lines
$f^3\Delta_1$ (1)	0	76648.2	76650.9	7.73	7.92	-2.2	3.8	Q(2-8), R(1-4), S(0)
$F^1\Delta_2$ (2)	0 +	77011.5	77009.3	8.26	8.202	0.21	4.0	R(1-6), P(3-7)
	0 -	77009.7		8.4	8.25	22.5	66	Q(2-6), S(0-6)
$H^1\Sigma^+$ (0^+)	0	79643.6	79645.5	6.86	7.193	-3.6	6	Q(0-7)
$B^1\Sigma^+$ (0^+)	m+8	80030.4	80029.7	4.550	4.737	84	100	Q(0-5)
$E^1\Sigma^+$ (0^+)	1	80168.8	80168.8	6.413	5.93	-92	-280	Q(0-6)
$k^3\Pi_1$ (1)	0	80392.1	80386.0	8.23	8.13		0.7	Q(1-5)
$B^1\Sigma^+$ (0^+)	m+10	81198.3 81197.0	81197.2 81196.2	3.654 3.653	3.36		-30	Q(0-4) Q(0-4)
$I^1\Delta_2$ (2)	0	81317.2	81311.5	7.93	7.958	-1.3	11	R(1-7), P(3-6)
		81315.7		8.0	7.792	0.3	-15	Q(2-9), S(0-4)
$B^1\Sigma^+$ (0^+)	m+11	81685.7	81683.4	4.97	4.9			Q(0-3)
$H^1\Sigma^+$ (0^+)	1	81898.8	81899.2	5.84	5.62		-88	Q(0-3)
Unassigned		82032.8		7.95		-41		Q(1-6)
$j^3\Sigma^-$ (0^+)	0	82184.3	82184.7	7.33	6.97	19	7.4	Q(0-6)
$E^1\Sigma^+$ (0^+)	2	82276.3	82275.9	6.74	6.595		3	Q(0-2), Q(4-6)

---

[1] Error in measurement of position of sharp lines 0·05cm^{-1}, uncertainty in calculated ν_0 0·25cm^{-1}

[2] References [11] and [76]

[3] Uncertainties in calculated B_v values ± 5 in last decimal place quoted

[4] Uncertainties in calculated D_v values ±25%

Table 4.1b Observed Term Values and Rotational Constants of DBr

State	v'	/ cm^{-1}		B_v / cm^{-1}		$D_v 10^4$ / cm^{-1}		Rotational
		Obs.	Lit.[1]	Obs.[1]	Lit.	Obs.	Lit.[1]	lines
Unassigned	>0	77519.8		3.822		5.5		Q(0-8)
$B^1\Sigma^+$ (0^+)	m+8	79666.4	79668.0	2.195	2.03	29.5	4.0	Q(0-7)
		79664.9	79666.6	2.219	2.07	33.9	8.6	Q(0-7)
$H^1\Sigma^+$ (0^+)	0	79716.1	79716.7	3.59	3.424	-20	-67	Q(0-9)
$E^1\Sigma^+$ (0^+)	2	80754.9	80756.3	3.718	3.684	37	32	Q(0-7), S(1-4)
		80755.9		3.720		37		Q(0-7), S(1-4)
$B^1\Sigma^+$ (0^+)	m+11	80904.7	80905.3	1.764	1.83	-41	20	Q(0-7)
		80902.7	80903.6	1.755	1.82	-44	-25	Q(0-7)
$E^1\Sigma^+$ (0^+)	3	82204.4	82204.7	3.784	3.624		-22	Q(0-5)
		82204.0		3.783				Q(0-5)
Unassigned	Ω=2	82745.6		4.0				Q(2-10)
$m^3\Pi_1$ (1)	1	82872.9	82873.0	3.97	3.964		0.1	Q(2-6)
		82872.6		3.965				Q(2-6)

See notes to Table 4.1a

[1] Reference [71]

4.3.1 (2+1)REMPI Spectroscopy of HBr

The $B^1\Sigma^+ (0^+) \leftarrow X^1\Sigma^+$ Transition

Three vibronic levels of the ion-pair state of HBr were observed in the (2+1)REMPI spectra, namely the v' = m+8, m+10, and m+11 levels. The v' = m+2, 3, 7, 8, 11, 12, and 13 levels have previously been observed in single photon absorption studies [11]. These states have also been reported in a recent (2+1)REMPI-TOFMS study of HBr in which the additional level, v' = m+10, was also observed [76].

The strongest vibronic band observed in the (2+1)REMPI spectra was the $B^1\Sigma^+ (0^+) \leftarrow X^1\Sigma^+$ (m+8-0) transition, a spectrum of which is shown in figure 4.10. It was not possible to resolve the isotopic splitting of the Q-branch features in this band. Spectra of the other $B^1\Sigma^+ (0^+) \leftarrow X^1\Sigma^+$ transitions observed, namely (m+10-0) and (m+11-0) are also shown in figure 4.10. These spectra are very noisy and the peaks are weak and diffuse. The Q-branches, the only rotational branch observed for both transitions, are overlapped by the much more intense, high J rotational lines of an $\Omega = 2$ Rydberg state. As well as the lines which can be assigned to either of the ion-pair state levels or the $\Omega = 2$ state there are many other sharp, strong lines in the spectra. In particular, in the spectrum of the v' = m+11 level there are numerous sharp lines, some of which show an appreciable isotopic splitting indicating that they correspond to vibronic levels with v' ≧ 1. However, it was not possible to assign any of these lines to known vibronic bands nor was it possible to identify rotational progressions.

The bound-free fluorescence emission from the ion-pair state to the ground

Figure 4.10 (2+1)REMPI Spectra of the Ion-pair State in HBr

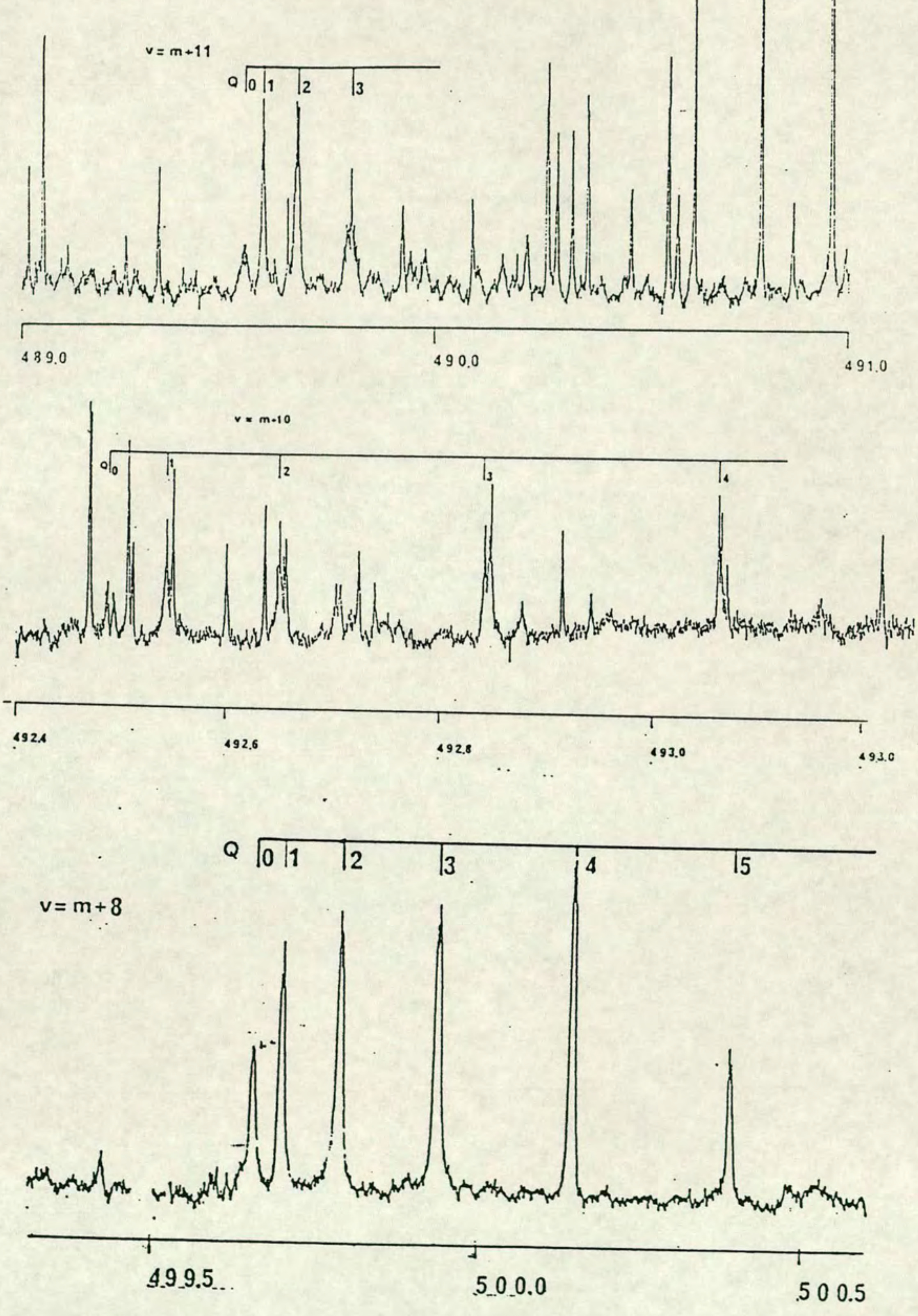

electronic state was expected to show similar features to the spectra observed for the other hydrogen halides and to occur at a similar wavelength. However, no fluorescence was detected from any of the ion-pair vibronic levels which were excited. While it was not possible to directly compare the ion yields in the HBr (2+1)REMPI spectra with those observed for HCl and DCl, the signal obtained for HBr was considerably weaker. Under similar conditions of sample pressure, laser power density, and ion detection plate bias voltage the HBr (2+1)REMPI signals were less than one tenth as strong as the HCl or DCl signals. The same differential amplifier was used, at the same amplification, in each case. If the observed decrease in ion yield was a reflection of a smaller cross-section for the two-photon resonant step, then the resulting decrease in the excited state population would be sufficient to explain why it was not possible to identify fluorescence from the ion-pair levels of HBr.

The $E^1\Sigma^+ (0^+) \leftarrow X^1\Sigma^+$ Transition

As well as the ion-pair state, a number of Rydberg states of HBr were observed in the (2+1)REMPI spectra. Several 0^+ states, which have the correct angular momentum to vibronically couple with the ion-pair state, were detected, the $E^1\Sigma^+ (0^+)$, $H^1\Sigma^+ (0^+)$, and $g^3\Sigma^- (0^+)$ Rydberg states. Of these the lowest energy state is the $E^1\Sigma^+ (0^+)$ state. Two vibronic levels of this Rydberg state lie in the energy range studied, v' = 1 and 2, and both were observed in the (2+1)REMPI spectra. Typical spectra are presented in figure 4.11. Although the rotational lines in both bands are broad only the v' = 1 level appears to suffer from a rotationally dependent predissociation. The rotational lines in this band become increasingly diffuse and weak with increasing J and can only be observed

Figure 4.11
(2+1)REMPI Spectra of the E $^1\Sigma^+$ (0^+) Rydberg State in HBr

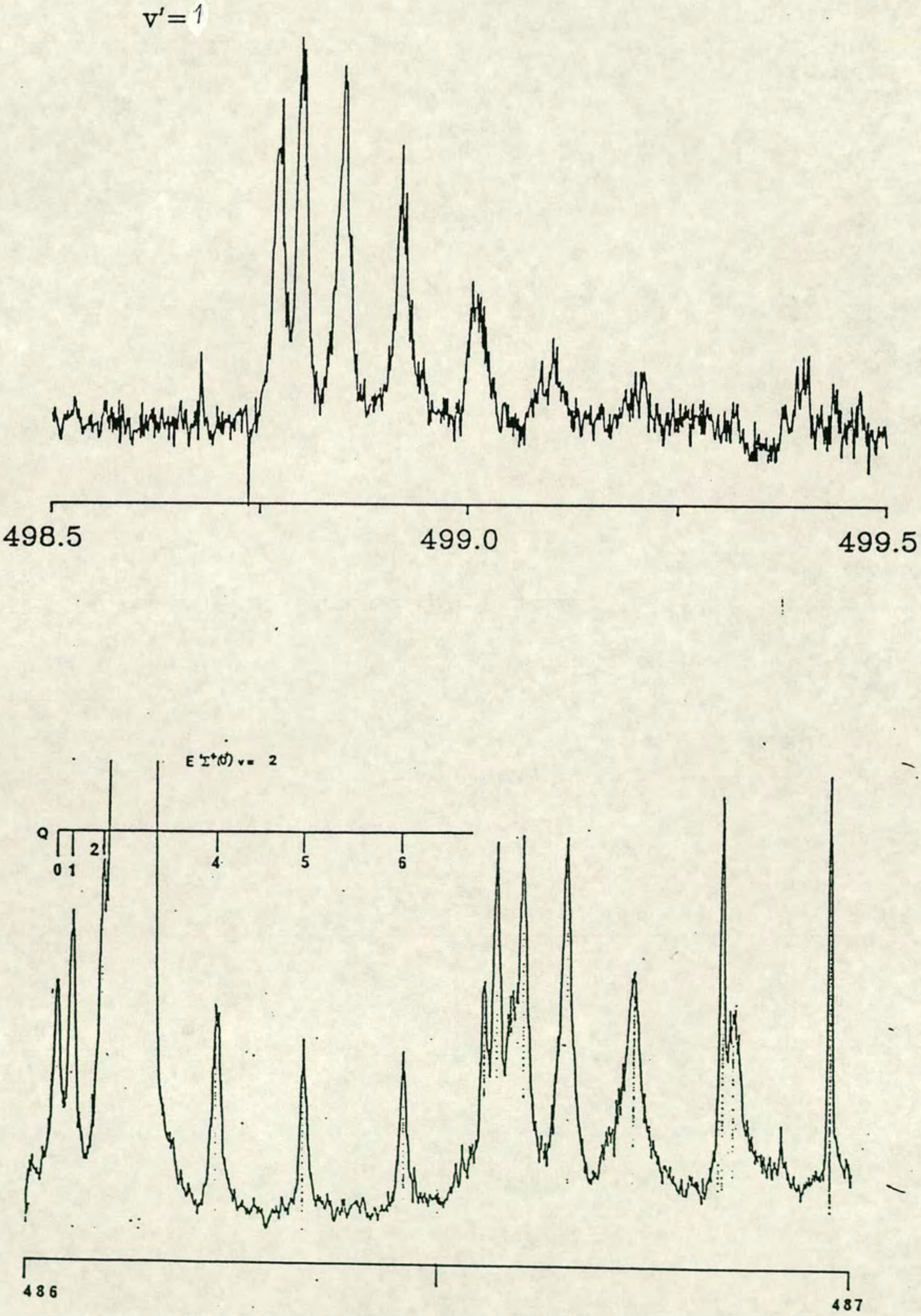

up to Q(6). In contrast the rotational lines in the (2-0) band, while broad, do not exhibit the same behaviour. The width of these lines may be due to the unresolved isotopic splitting expected for a higher v' level rather than to any perturbation of this level.

The Q(2) and Q(3) features of the $E^1\Sigma^+ (0^+) \leftarrow X^1\Sigma^+$ (2-0) transition are obscured by a very strong broad feature centred near 242 nm. The structure of this REMPI signal can be seen in more detail in figure 4.12. It results from the (2+1)REMPI signal of atomic hydrogen which is generated by photodissociation of HBr via the single photon absorption $A^1\Pi \leftarrow X^1\Sigma^+$. At the central wavelength of the feature, 242 nm, the dissociating molecule has an excess energy of 11000 cm^{-1}. Because of conservation of momentum, most of this is released as translational kinetic energy of the hydrogen atom. As the two photon absorption wavelength of the hydrogen atom is dependent on it s velocity relative to the propogation vector of the laser the absorption peak is Doppler broadened [81]. The $A^1\Pi \leftarrow X^1\Sigma^+$ transition is a perpendicular transition and since the laser radiation is horizontally polarized, the dissociating molecules lie mainly in the vertical plane containing the propagation vector of the dissociating laser radiation. The Doppler shift of the absorption wavelength for each molecule is dependent on the projection of the fragment recoil velocity on the laser propagation vector. The velocity distribution is peaked in the forward and backwards direction and results in the bimodal distribution observed.

The $H^1\Sigma^+ (0^+) \leftarrow X^1\Sigma^+$ Transition

The next highest energy 0^+ Rydberg state observed was the $H^1\Sigma^+ (0^+)$ state.

Figure 4.12 (2+1)REMPI Signal from Translationally Hot Hydrogen

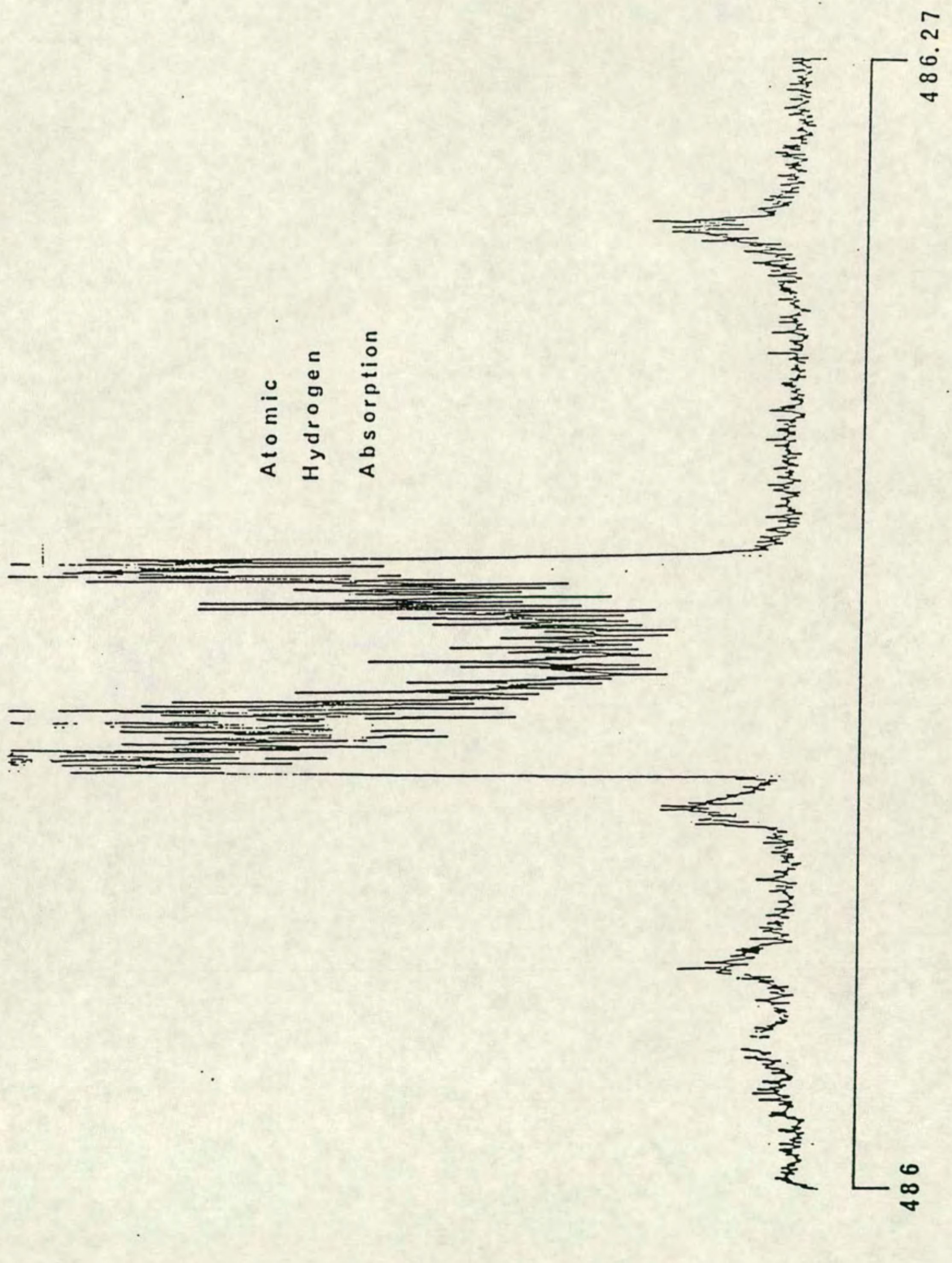

(2+1)REMPI spectra of the $H^1\Sigma^+ (0^+) \leftarrow X^1\Sigma^+$ (0-0) and (1-0) transitions are shown in figure 4.13. The rotational lines in the (0-0) band are sharp and strong, similar to the atomic lines observed in the same spectrum. There is no indication of any diffuseness in the rotational lines resulting from predissociation of this state. However, the rotational progression terminates abruptly at Q(8) in this spectrum. This line is considerably weaker than the Q(7) line which would be expected to be of similar intensity in the absence of any perturbation. In the spectrum shown the Q(5) to Q(7) lines have saturated the detection system and so the observed intensities do not reflect the relative two-photon absorption linestrengths correctly. Consequently it is not clear whether the higher J lines, which have been observed in previous studies, cannot be observed because they are predissociated or because the (2+1)REMPI signal is below the detection threshold. Although the single photon absorption studies of Ginter et al [11] suggest that this state is subject to rotational predissociation, the current work taken together with the results of the more recent study of the (2+1)REMPI-TOFMS spectra [77] point to lack of detection sensitivity.

A shorter progression of rotational lines is observed in the Q-branch of the $H^1\Sigma^+ (0^+) \leftarrow X^1\Sigma^+$ (1-0) transition. There are six strong lines in the spectrum of which four show appreciable isotopic splitting. If all of the lines are used to fit a polynomial in $J(J+1)$ then the B_v and D_v values determined are in very poor agreement with those reported in the literature. A much improved fit is achieved if both the highest and lowest energy lines are removed from the fit and the remaining lines are numbered as indicated in figure 4.13. The B_v value determined for both isotopomers are then in good agreement with the average

Figure 4.13 (2+1)REMPI Spectra of the H$^1\Sigma^+$ (0$^+$) Rydberg State in HBr

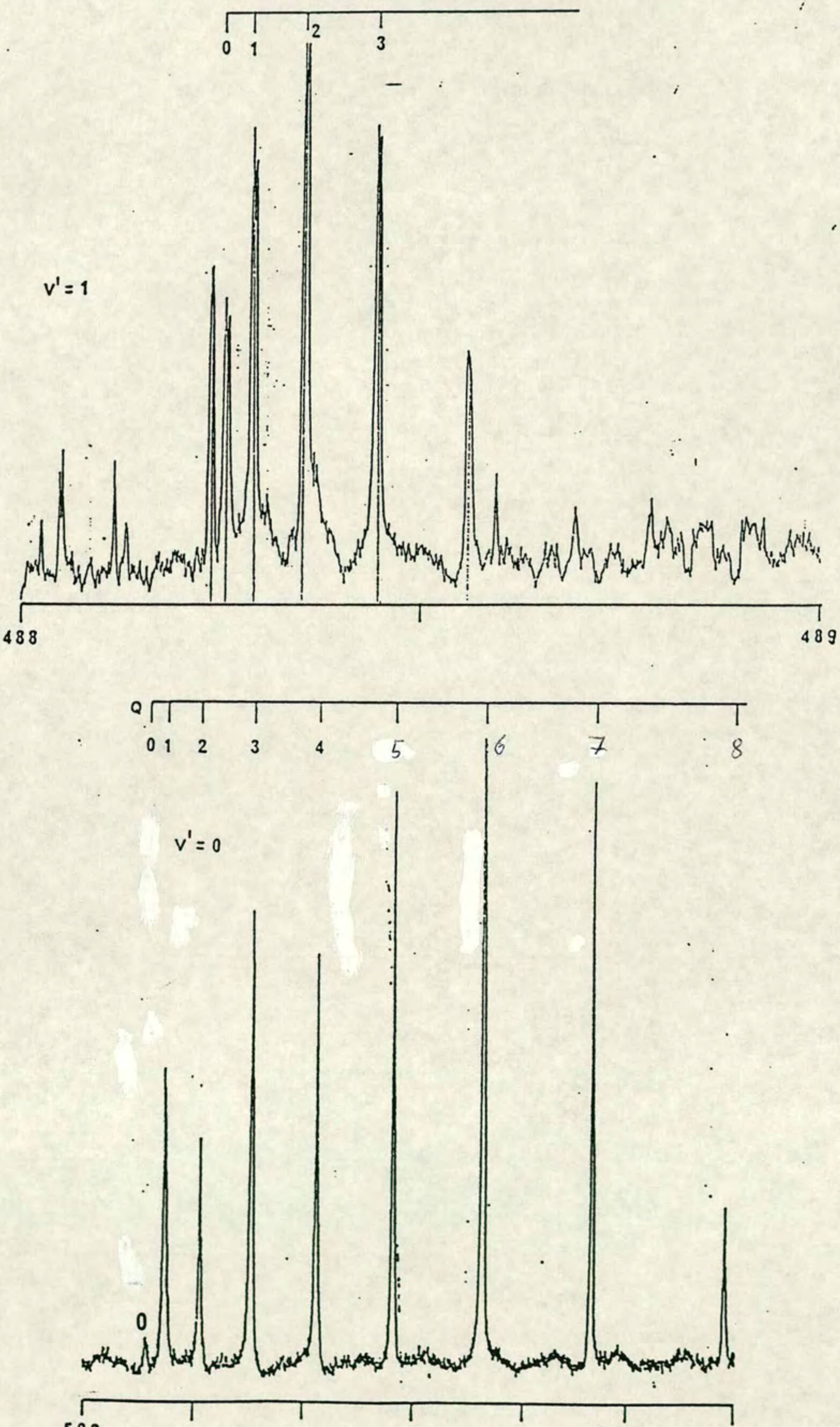

values reported in other studies where the isotopic splitting could not be resolved [11].

The $j^3\Sigma^-$ (0^+) ← $X^1\Sigma^+$ Transition

The highest energy 0^+ Rydberg state observed was the 0^+ component of the $j^3\Sigma^-$ (0^+) state which results from the same electronic configuration as the $H^1\Sigma^+$ (0^+) state, namely 5dπ. The (2+1)REMPI spectrum of the $j^3\Sigma^-$ (0^+) ← $X^1\Sigma^+$ (0-0) transition is shown in figure 4.14. This was the only vibronic level of this state within the range of excitation energies studied. The rotational lines are strong but are very broad and become increasingly diffuse with increasing J. Only lines up to, and including, Q(6) have been assigned. There is a broad feature with a sharp peak superimposed at the expected position of Q(7), extrapolated from the experimentally determined molecular constants, but this very much weaker, diffuse peak was not assigned to the rotational progression. The calculated molecular constants are in good agreement with the values reported in the literature. The small shift in the rotationless band origin, ν_0, of 2.8cm^{-1} is consistent over the whole rotational band. This corresponds to an absolute error in the fundamental laser wavelength of 0.017 nm.

The $f^3\Delta_1$ (1) ← $X^1\Sigma^+$ Transition

Two transitions to $\Omega = 1$ Rydberg states were identified in the (2+1)REMPI spectra of HBr: the $f^3\Delta_1$ (1) ← $X^1\Sigma^+$ (0-0) and $k^3\Pi_1$ (1) ← $X^1\Sigma^+$ (0-0). In addition to these a third transition was observed for which the upper level could not be assigned to any previously known level. REMPI spectra of these two transitions are presented in figure 4.15. The spectrum of the $f^3\Delta_1$ (1) ← $X^1\Sigma^+$

Figure 4.14 (2+1)REMPI Spectra of Rydberg States in HBr

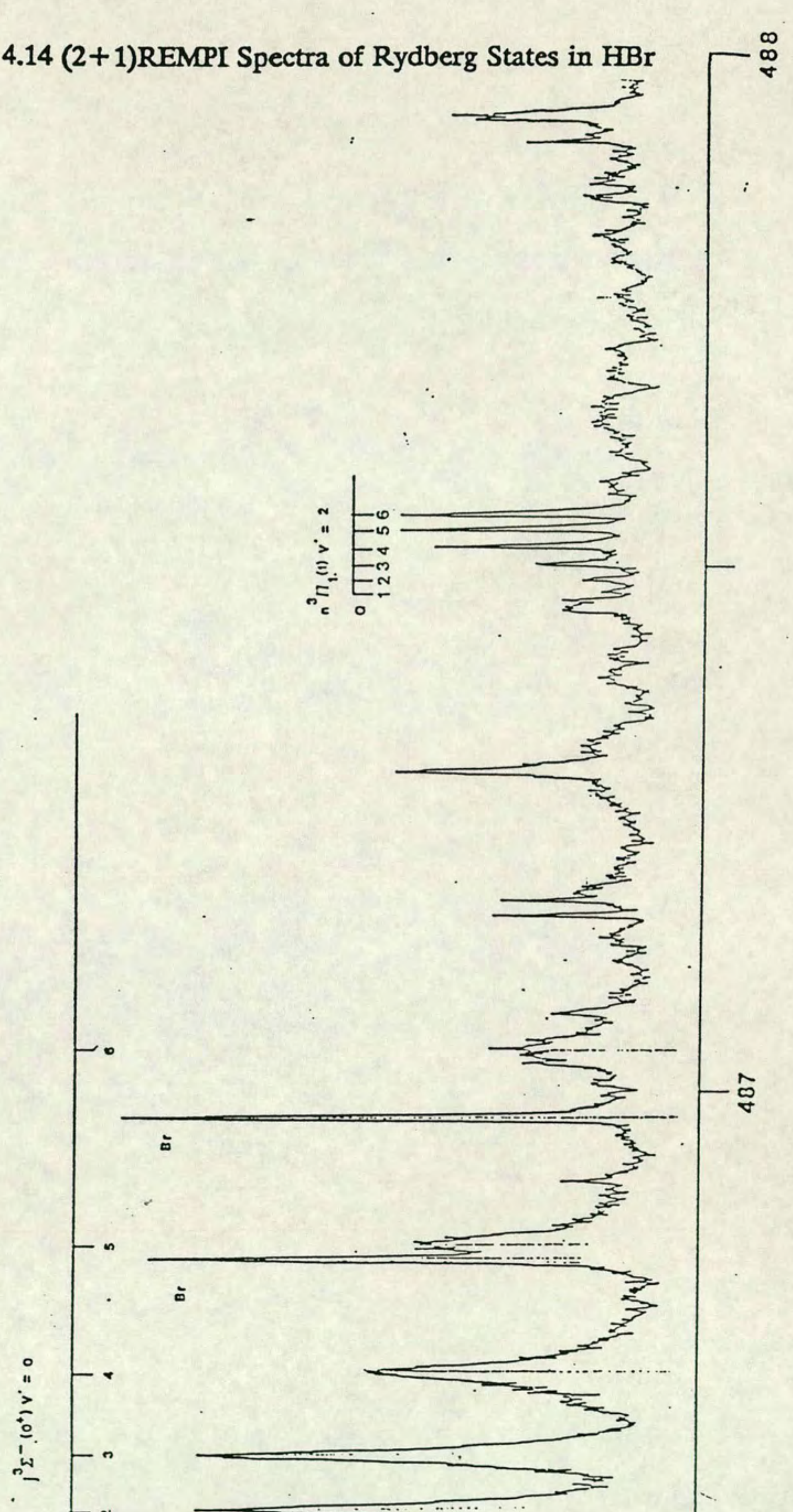

Figure 4.15 (2+1)REMPI Spectra of $\Omega=1$ Rydberg States in HBr

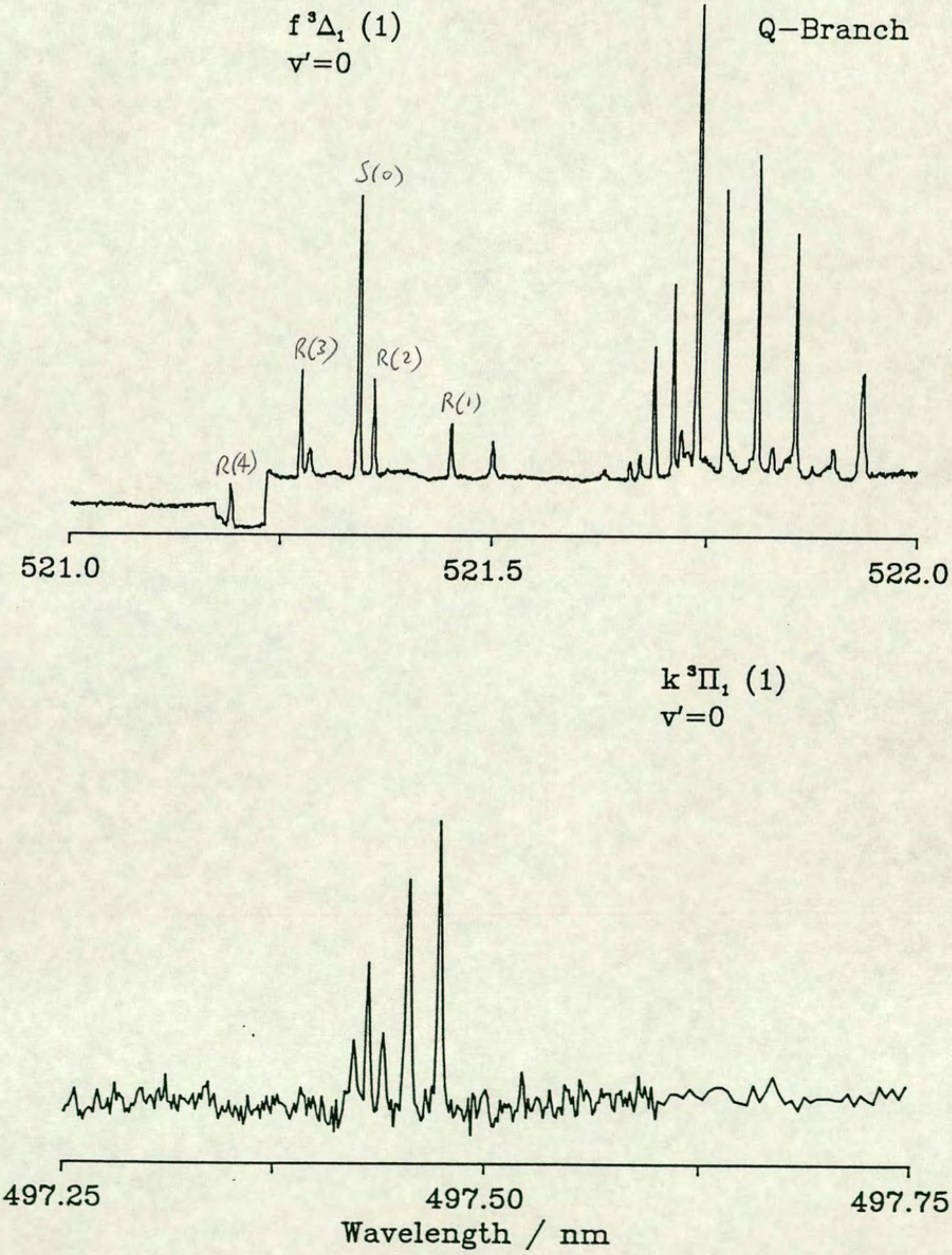

(0-0) transition has a strong Q-branch composed of seven rotational lines, a shorter, weaker R-branch and only one S-branch line, S(0). The Q-branch numbering is somewhat uncertain. If only the Q-branch is used in the fit then it is possible to number the lines from Q(1) to Q(7). However, if the other rotational lines are included in the fit then the Q-branch must be numbered as indicated in figure 4.15. If this numbering is accepted then there are no lines corresponding to $J' = 1$ in the spectrum. Previous studies of single photon absorption and (2+1)REMPI spectra have however, established that this is an $\Omega = 1$ level and therefore it should be possible to observe lines terminating on $J' = 1$. It is not clear why the Q(1) and R(0) features could not be observed in these spectra.

The $k^3\Pi_1$ (1) ← $X^1\Sigma^+$ Transition

For the $k^3\Pi_1$ (1) ← $X^1\Sigma^+$ (0-0) transition only the Q-branch is observed in the (2+1)REMPI spectra. The branch consists of five rotational lines and is truncated at Q(5). The Q(3) line has an anomalously weak intensity but there are no other indications that the state is perturbed. The single photon absorption studies indicated that there was a small perturbation of the state but a more extensive rotational progression was observed in absorption spectroscopy [11]. Because only low J' rotational lines were observed only ν_0 and B_v were determined from the observed line positions. The fitted constants for this short rotational progression agree well with those obtained from the absorption data.

The $n^3\Pi_1$ (1) ← $X^1\Sigma^+$ Transition

At higher energy a previously unreported rotational branch was observed. The branch appears to be a Q-branch with a very similar structure to that observed for the $k^3\Pi_1$ (1) ← $X^1\Sigma^+$ (0-0) transition and so the upper level of the transition has been assigned as an $^3\Pi_1(1)$ state. The best fit to a rotational progression was achieved with this assumption and using the rotational numbering indicated in figure 4.14. Because this branch was observed in the same spectral region as the $j^3\Sigma^-$ (0^+) v' = 0 and $E^1\Sigma^+$ (0^+) v' = 2 levels the error in the laser wavelength is known to be small. The calculated value of ν_0 is therefore quite accurate. If this value is compared with ν_0 for the $^3\Pi_1(1)$ levels observed at lower energy it is found that only one level is at an acceptable energy separation to be part of the same vibrational progression. The level at ν_0 = 82031cm^{-1} has therefore been assigned as the v' = 2 level of the $n^3\Pi_1$ (1) Rydberg state.

The $F^1\Delta_2$ (2) and $I^1\Delta_2$ (2) Rydberg States

Two transitions to $\Omega = 2$ Rydberg vibronic levels were observed in the (2+1)REMPI spectra: $F^1\Delta_2$ (2) ← $X^1\Sigma^+$ (0-0) and $I^1\Delta_2$ (2) ← $X^1\Sigma^+$ (0-0). Both states have previously been observed in single photon absorption studies but the latter was initially wrongly assigned as the $N^1\Pi$ v' = 1 level [11]. For each state it was possible to observe at least four rotational branches P, Q, R, and S. The REMPI spectra of these transitions are shown in figures 4.16 and 4.17. An O-branch was also observed for the $F^1\Delta_2$ (2) state but the O-branch of the $I^1\Delta_2$ (2) state was overlapped by the Q-branch of an ion-pair vibronic level and could

Figure 4.16 (2+1)REMPI Spectrum of the $F^1\Delta_2$ (2) ← $X^1\Sigma^+$ (0-0) Transition in HBr

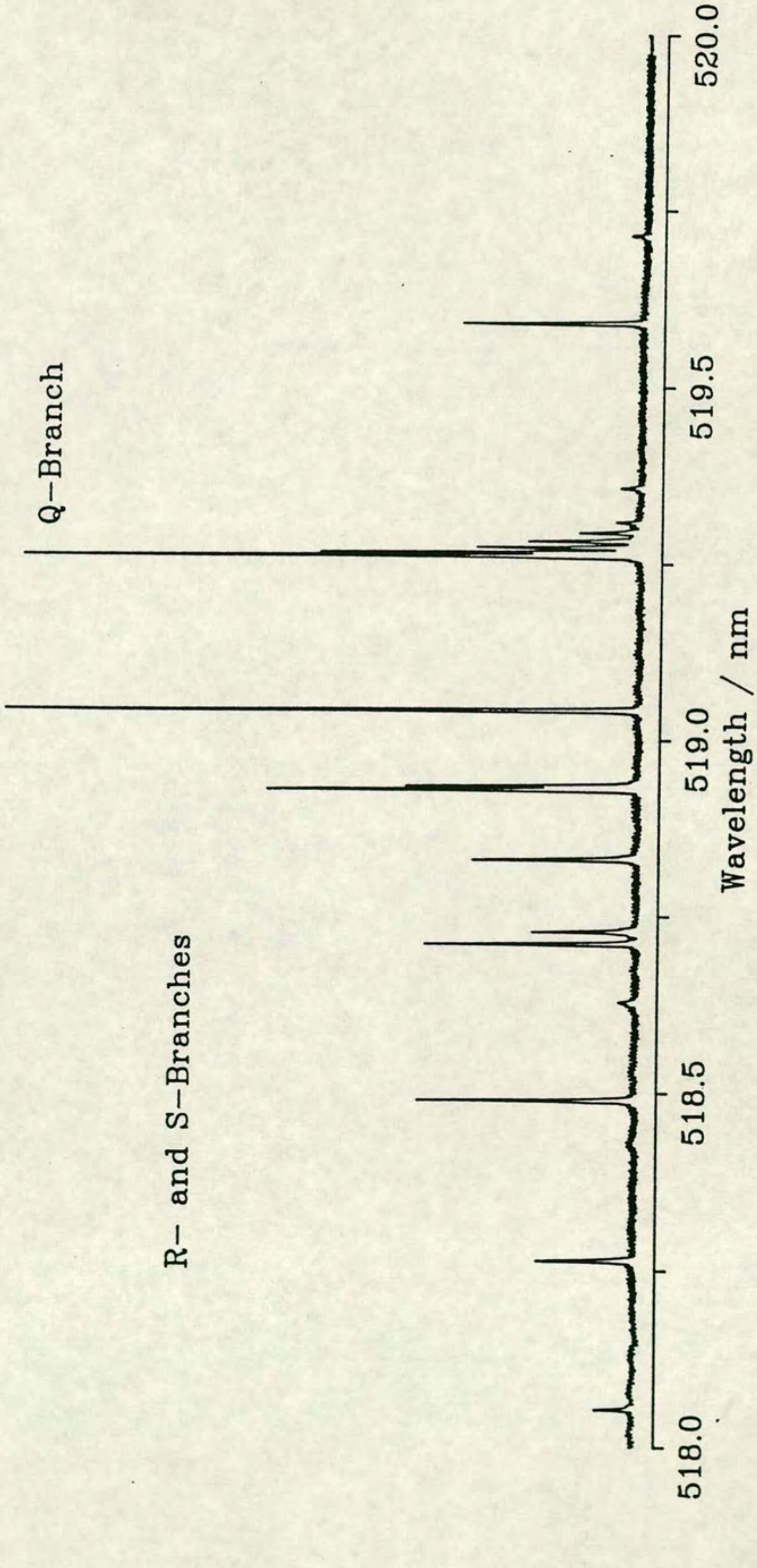

Figure 4.17 (2+1)REMPI Spectrum of the $I^1\Delta_2$ (2) ← $X^1\Sigma^+$ (0-0) Transition in HBr

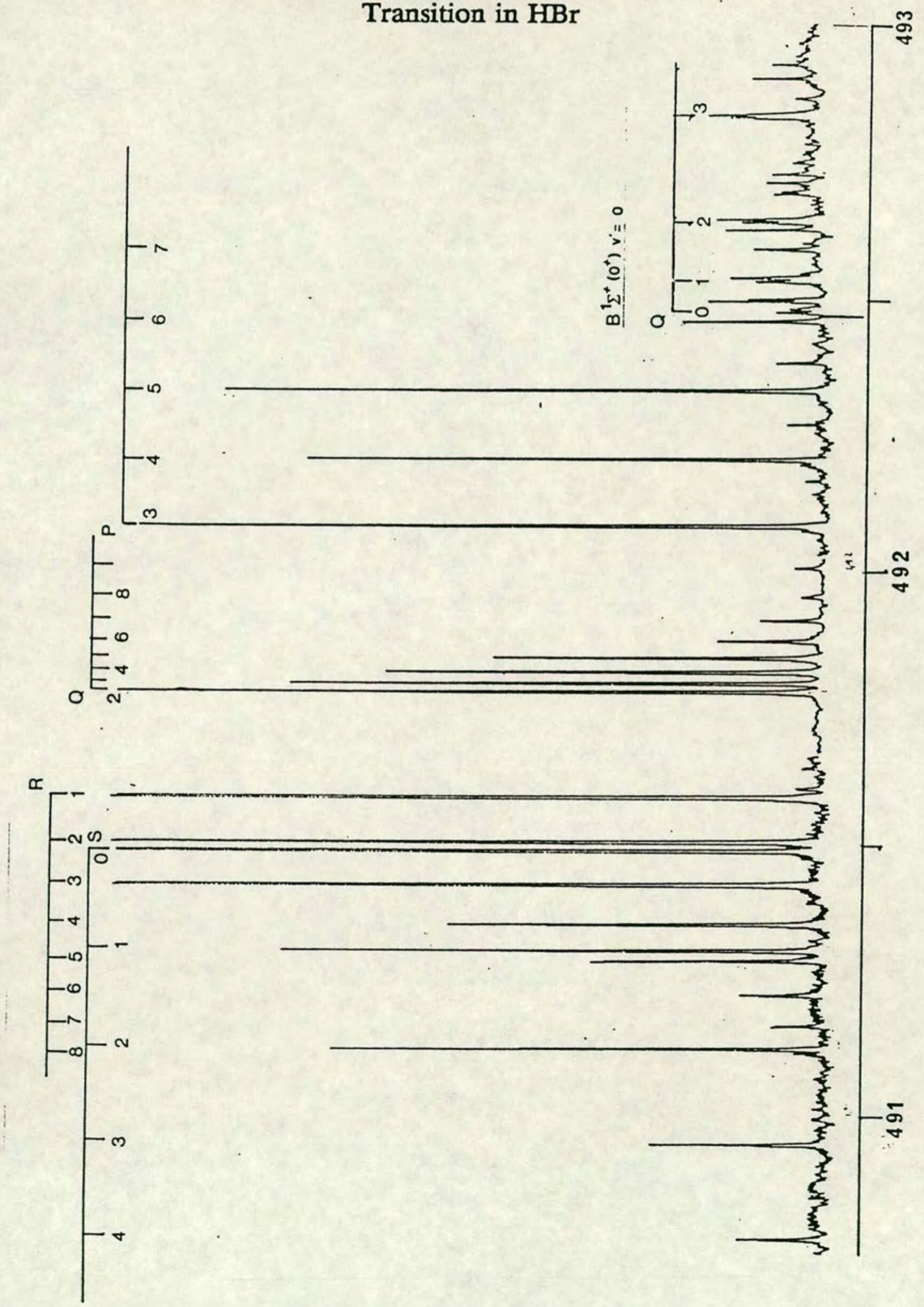

not be assigned unambiguously.

4.3.2 (2+1)REMPI Spectroscopy of DBr

Very few excited vibronic levels of DBr were identified in the (2+1)REMPI spectra recorded. This was partly due to the poor quality of some of the data which meant that several bands could not be rotationally analysed, and this was compounded by the fact that only a few narrow spectral regions were studied.

The $B^1\Sigma^+ (0^+) \leftarrow X^1\Sigma^+$ Transition

It was however possible to rotationally analyse two $B^1\Sigma^+ (0^+) \leftarrow X^1\Sigma^+$ transitions, (m+8-0) and (m+11-0). A transition to one additional level, v' = m+9, was observed but the rotational lines were weak and diffuse and could not be analysed. REMPI spectra of these three transitions are presented in figure 4.18. For the (m+8-0) band the Q(0) line of both isotopomers is obscured by a high J line belonging to the $H^1\Sigma^+ (0^+) \leftarrow X^1\Sigma^+$ (0-0) band. However, the position of both lines were determined and have been included in the rotational fitting procedure. The Q(8) line is also obscured and in this case it was not possible to determine the line positions. There is good agreement between the constants determined from the (2+1)REMPI spectra and those reported from single photon absorption spectra. The Q(0) line of the (m+11-0) band was also partially obscured by the presence of a number of weak lines which could not be identified. But again there is good agreement between the calculated constants and those reported in the literature.

Figure 4.18
(2+1)REMPI Spectra of Ion-pair State Levels in DBr

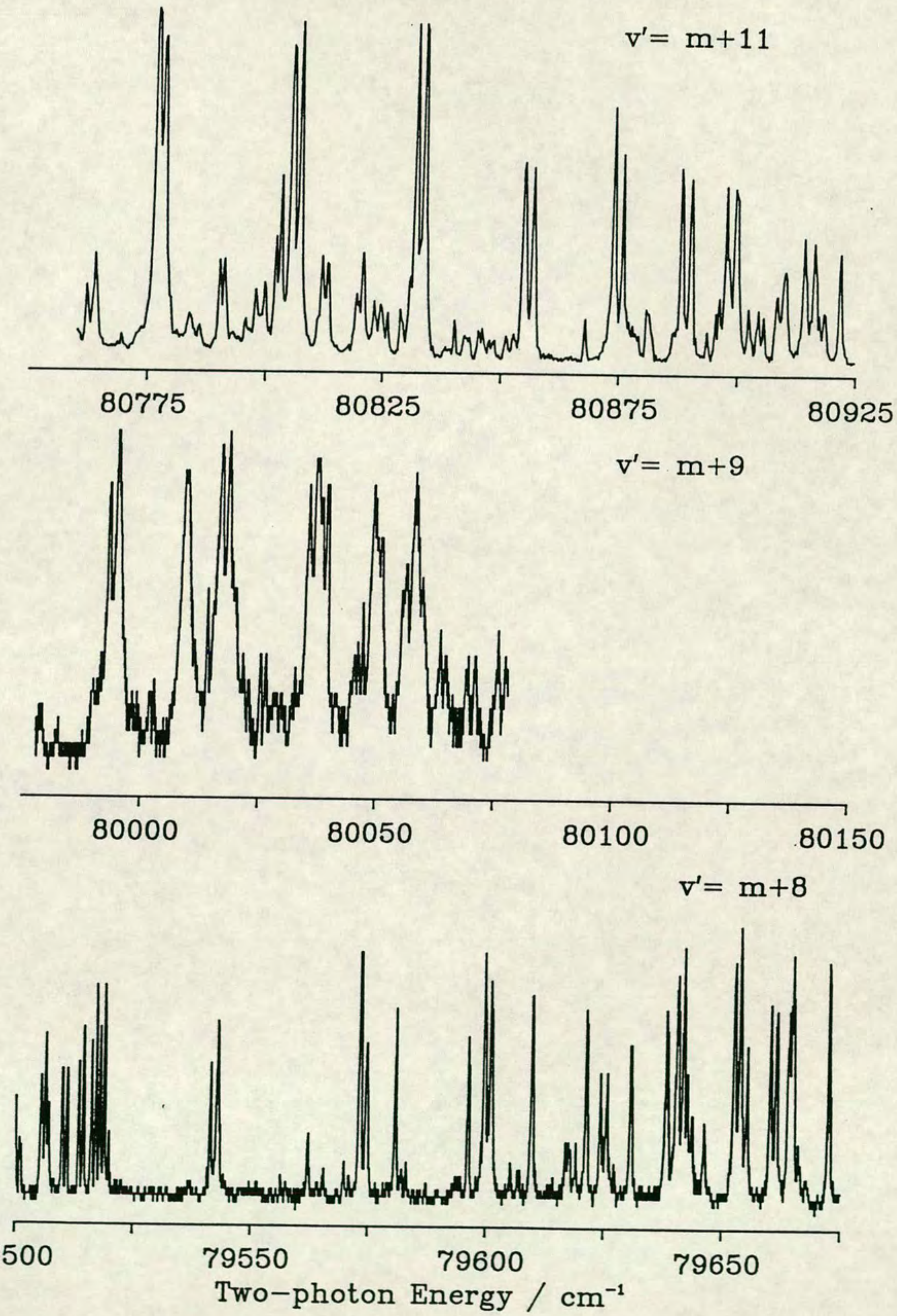

The $E^1\Sigma^+$ (0^+) ← $X^1\Sigma^+$ Transition

Two $E^1\Sigma^+$ (0^+) ← $X^1\Sigma^+$ bands were observed in the (2+1)REMPI spectra, namely (2-0) and (3-0) and spectra of both are shown in figure 4.19. Both have a strong Q-branch with a weaker S-branch. The spectra are too congested and noisy to identify an O-branch which is considerably weaker than the S-branch. Isotopic splitting of the rotational lines is evident in both bands as expected. However, the observed splitting in the (3-0) band is less than that in the (2-0) band. In the absence of any perturbation the upper level would exhibit the greater splitting.

For the (2-0) band both rotational branches were employed in the fit to determine rotational constants. Nine Q-branch lines, Q(0-8) and four S-branch lines, S(1-4), were observed but the Q(8) line was excluded from the fit because it appears to be perturbed. The rotational constants determined agree well with those reported from single photon absorption studies [11]. However, the resolution obtained in these (2+1)REMPI spectra is much greater and, because of the two photon selection rules, there is less congestion of rotational lines.

The spectrum of the (3-0) band is more congested and has a poorer signal to noise ratio. In this case it was not possible to resolve the S-branch which forms a head rather than the progression observed for the lower vibrational level. The best fit to the Q-branch progression for both isotopomers was achieved with the rotational numbering indicated, which excludes the Q(1) line of the $D^{79}Br$ isotopomer. The absence of this line from the spectrum is attributed to a fluctuation in the power of the laser, since it is unlikely that a single line of the

Figure 4.19
(2+1)REMPI Spectra of $E^1\Sigma^+$ (0^+) Rydberg State in DBr

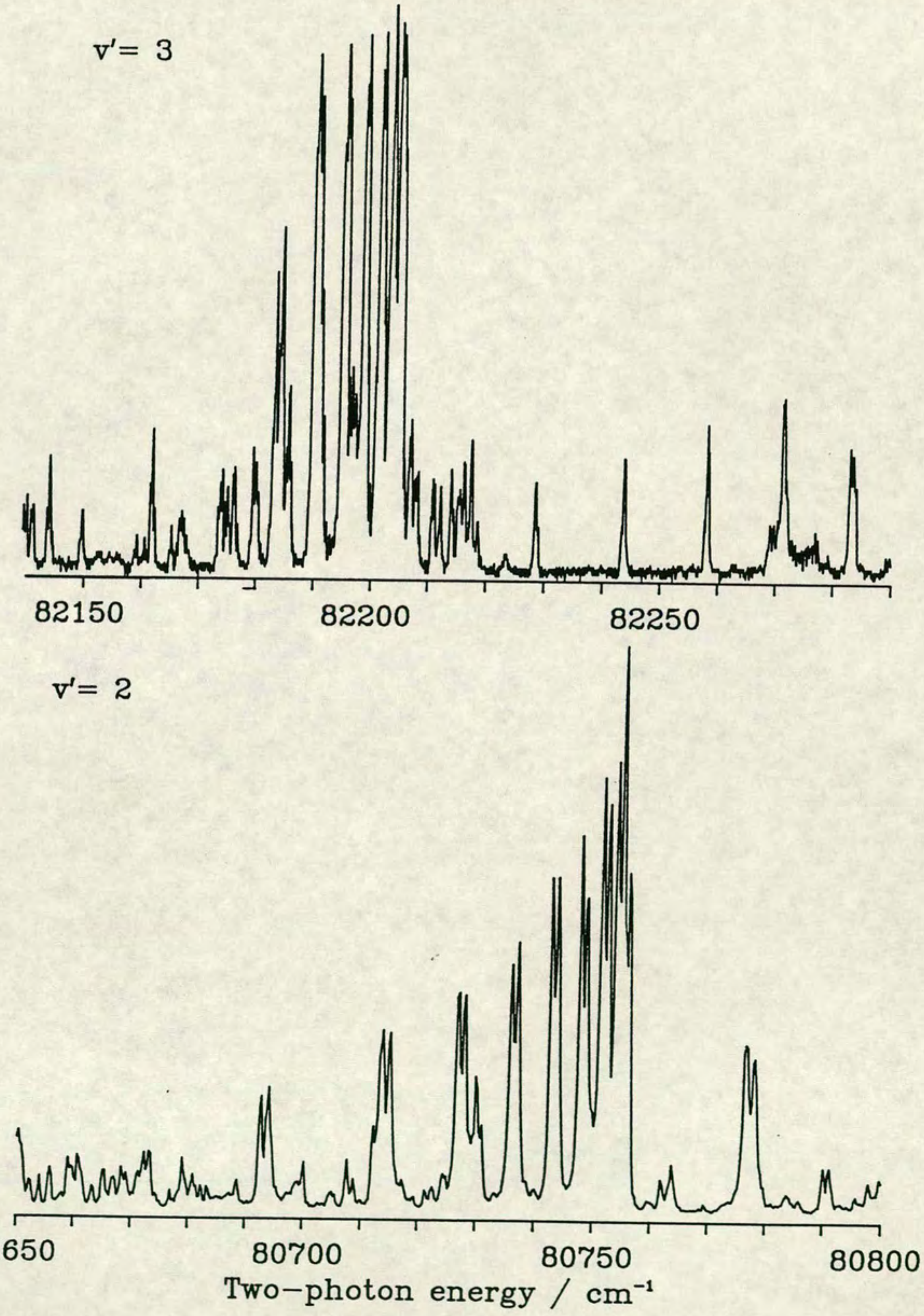

rotational progression would be missing and that there would be no corresponding affect on the heavier isotopomer. A small shoulder is observed on the high energy side of the $D^{81}Br$ peak but, while it is at the appropriate energy, it is of similar appearance to the noise observed on other peaks. It has therefore not been used in the rotational fitting procedure.

$H^1\Sigma^+ (0^+) \leftarrow X^1\Sigma^+$ Transition

One $H^1\Sigma^+ (0^+) \leftarrow X^1\Sigma^+$ transition was observed, the (0-0) band. The origin of the Q-branch is perturbed by a baseline shift due to a fault in the detection system. No S-branch lines were observed. Some of the higher J lines overlap the Q-branch involving the $v' = m+8$ level of the ion-pair state. The number of lines observed is considerably greater than for the other 0^+ states. There is an additional line between Q(5) and Q(6) in the progression which could not be assigned to either an HBr or a Br transition.

The $m^3\Pi_1$ (1) $\leftarrow X^1\Sigma^+$ Transition

Only one further, previously reported vibronic level was observed in the (2+1)REMPI spectra. A fragment of the Q-branch of the $m^3\Pi_1 (1) \leftarrow X^1\Sigma^+$ (1-0) transition was observed. This feature is presented in figure 4.20. It appears as a weak progression of lines overlapped by the S-branch of a very strong transition to an $\Omega = 2$ state. A large wavelength shift is required for this assignment, almost 1 nm, which is much greater than the 0.06 to 0.16 nm shifts found for other spectra. However, there are few vibronic levels in this energy region which could give rise to this progression and there is very strong agreement between the corrected energy of the rotational lines and that observed

Figure 4.20 (2+1)REMPI Spectrum of the $m^3\Pi_1$ (1) Rydberg State in DBr

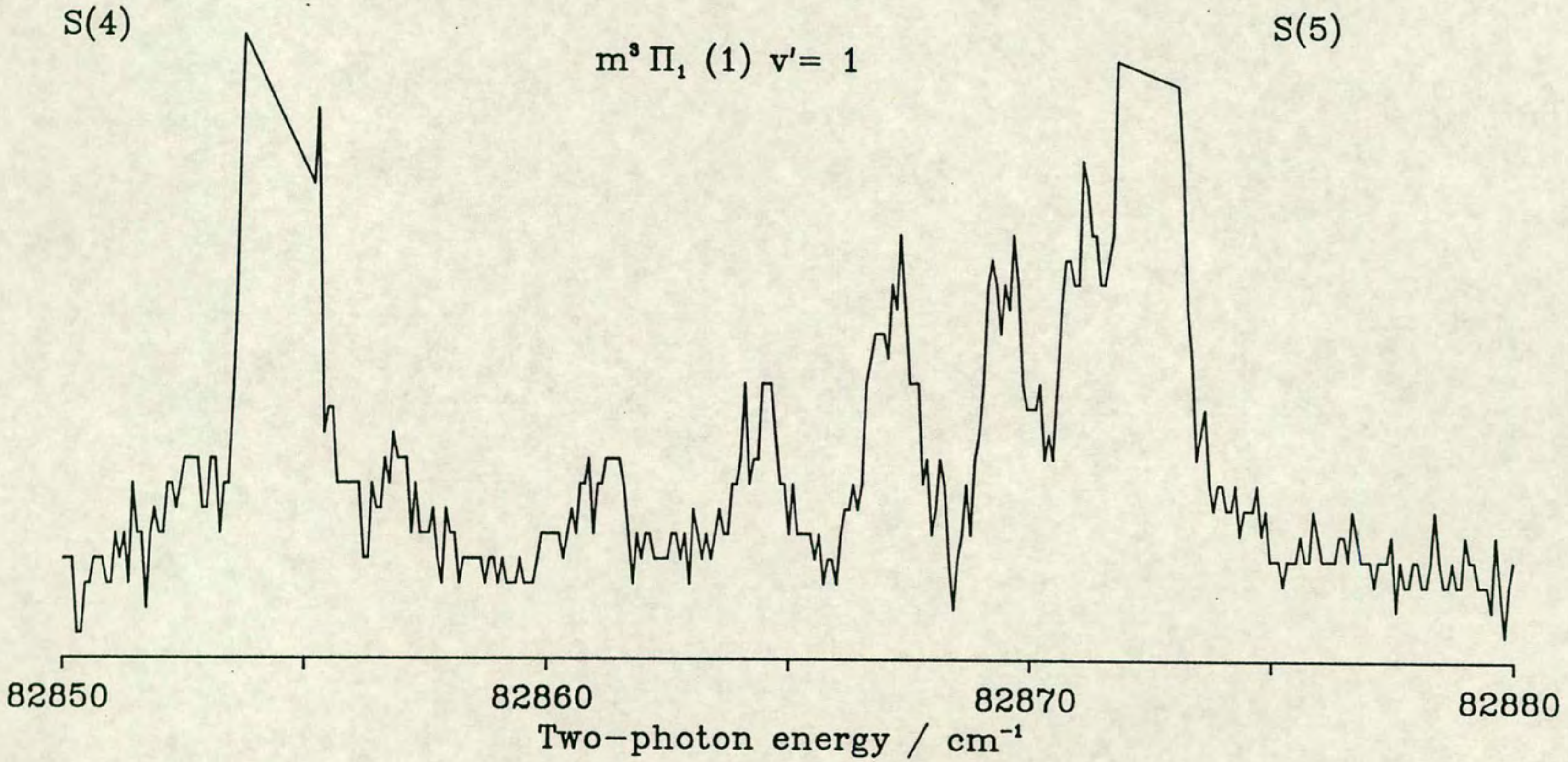

in absorption spectra.

Unassigned Transitions

In addition to the previously reported vibronic levels of DBr which were identified in the (2+1)REMPI spectra there were several other bands which could not be assigned. There are four progressions of rotational lines which appear to form Q-branches with origins at 79519.76, 79645, 80745, and 81040 cm^{-1} respectively. At higher energy there is a transition to an $\Omega=2$ state exhibiting P, Q, R, and S rotational branches.

The lowest energy band forms a progression of sharp, isotopically split rotational lines to the red of the $B^1\Sigma^+ (0^+) \leftarrow X^1\Sigma^+$ (m+8-0) transition and is of comparable intensity relative to this band. The isotopic splitting is quite large and the rotational lines can be fully resolved. The Q(5) doublet is overlapped and obscured by the Q(8) doublet of the ion-pair state level and neither of these lines were included in the rotational fitting procedure. The calculated molecular constants of this level do not match any of the reported DBr or HBr vibronic levels. The large value of the isotopic splitting indicates that this is a high v' level but it has not been possible to assign it to a vibrational progression.

Three separate rotational progressions can be observed to higher energy than the Q-branch of the $B^1\Sigma^+ (0^+) \leftarrow X^1\Sigma^+$ (m+8-0) transition. The highest energy progression has the appearance of a P-branch but the line positions are not consistent with any previously observed level of DBr. Both of the other features resemble Q-branches but it was not possible to determine either the origins of the branches or a unique rotational numbering for the lines. Because of this it

Figure 4.21 (2+1)REMPI Spectrum of the Ω = 2 Rydberg State in DBr

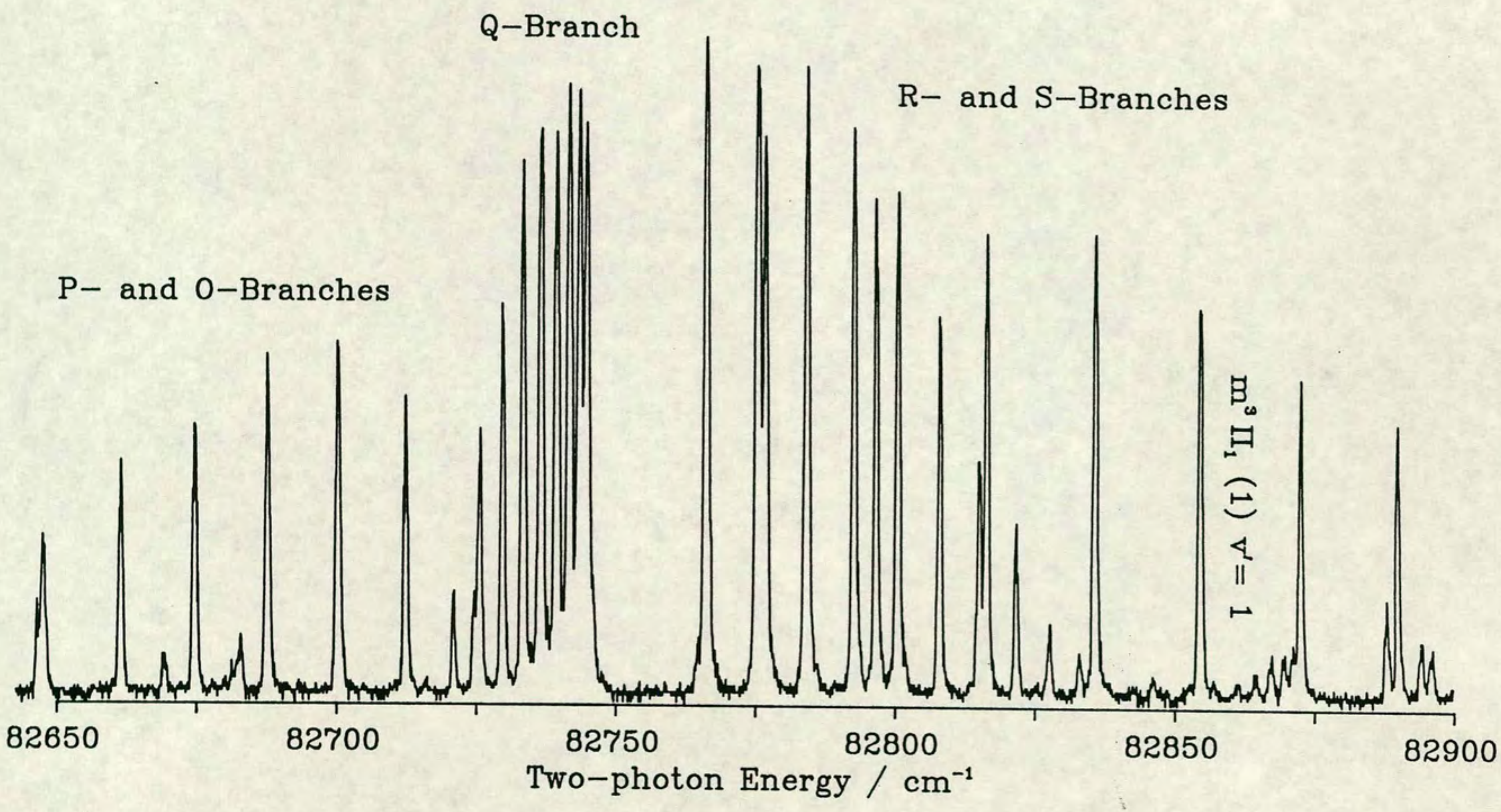

was not possible to rotationally analyse these novel features in the (2+1)REMPI spectra.

A very strong $\Omega=2$ state was observed in the (2+1)REMPI spectra at 82745 cm^{-1}. A spectrum of the transition to this state is presented in figure 4.21. The rotational lines are sharp and show no sign of isotopic splitting and so this was assumed to be a $v'=0$ level. Although transitions to two $\Omega=2$ states near the energy of this level were observed in single photon absorption spectroscopy [11] it could not be assigned as either of these. The wavelength correction factor for this spectrum was calculated from a fragment of the Q-branch of the $v'=1$ level belonging to the $m^3\Pi_1$ (1) Rydberg state, which can be observed as a progression of weak lines partially overlapped by the S(5) line of the $\Omega=2$ state.

The $H^1\Sigma^+$ (0^+) $\leftarrow$ $X^1\Sigma^+$ Transition in HBr

A band was observed at 79645 cm^{-1} embedded in the Q-branch of the $B^1\Sigma^+$ (0^+) $\leftarrow$ $X^1\Sigma^+$ (m+8-0) transition. The origin band is partially overlapped by the Q(3) line of the latter band and it was not possible to identify all of the rotational lines. The progression cannot be fit to any DBr level but is a good fit to the $H^1\Sigma^+$ (0^+) Rydberg state belonging to $v'=0$ level of HBr. This rotational branch has therefore been assigned as the $v'=0$ level of the $H^1\Sigma^+$ (0^+) state of HBr. The observation of this state was the only indication of contamination of the DBr sample with HBr.

Figure 4.22 (2+1)REMPI Spectra of Ion-pair State of HI

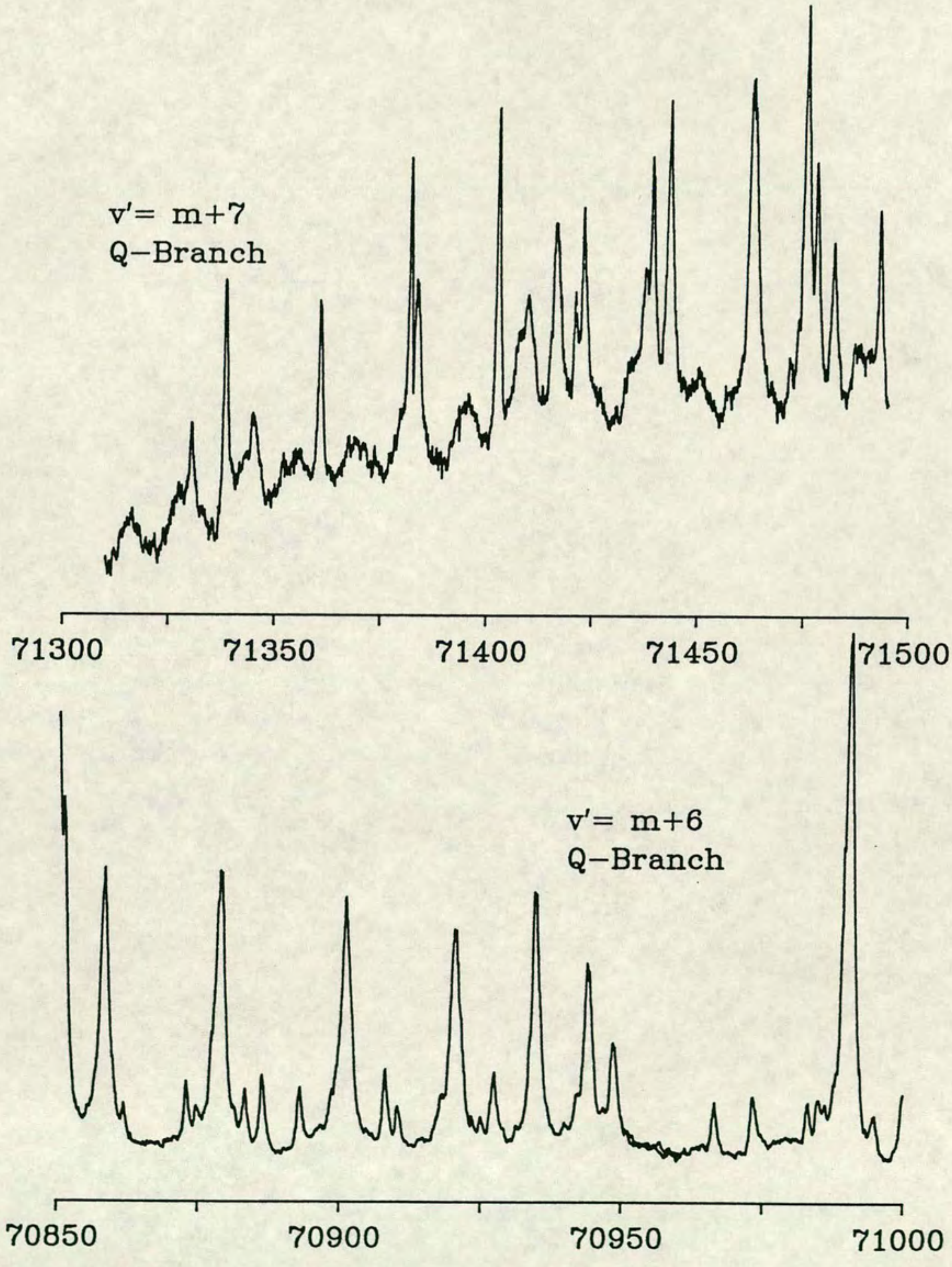

4.4 Hydrogen Halide

4.4.1 (2+1)REMPI Spectroscopy

The (2+1)REMPI spectrum of HI was recorded in the wavelength range 286 to 271 nm. This corresponds to a two-photon energy of 70000 to 73800 cm^{-1}. The spectra were recorded with low pressure gas samples in glass ionisation cells as described in Chapter 2. Ginter and co-workers have previously reported the high resolution single photon absorption spectrum of HI in the energy range studied in this work. All of the features identified in this work were assigned with reference to the work of Ginter et al [6] [10] [13]. Apart from these bands, three vibronic bands which had not previously been reported were observed. The molecular constants of all of the bands observed in the (2+1)REMPI spectra of HI are presented in table 4.2.

The $B^1\Sigma^+$ (0^+) Ion-pair State

In the energy range studied there are seven reported vibrational levels of the ion-pair state; v' = m+5, 6, 8, 9, 10, 11, and 12. The "missing" v' = m+7 level was predicted to lie in a region dominated by strong $^1\Pi$ absorption and so could not be observed in single photon spectra. In the present work it has been possible to observe the v' = m+7 level. However, it was not possible to identify the v' = m+8, 9, and 12 levels. A very strong $\Omega=2$ absorption band overlaps the region in which the v' = m+8 and 9 levels lie while the v' = 12 level lies at the extreme short wavelength limit of the tuning range of the due laser.

The (2+1)REMPI spectra of two of the three lowest lying ion-pair state vibrational levels observed in this work, v' = m+6, and 7, are presented in figure 4.22. There are no atomic iodine two-photon resonances in the wavelength

Table 4.2 Observed Term Values and Rotational Constants of HI

State	v'	/ cm^{-1}		B_V / cm^{-1}		$D_V 10^4$ / cm^{-1}		Rotational lines
		Obs.	Lit.	Obs.	Lit.	Obs.	Lit.	
$F^1\Delta_2$ (2)	0	70229.4	70228.3	6.33	6.30		1.26	Q(2-8), S(0-3), O(4-7)
		70229.2	70228.0	6.32	6.37		3.3	R(1-8), P(3-11)
$H^1\Sigma^+$ (0^+)	1	70243.6	70242.1	5.97	5.95		125	Q(0-2)
$k^3\Pi_0$ ($0^\pm$)	1	70321.2	70320.4	5.15	5.058		-21	Q0-1), Q(3-5)
$B^1\Sigma^+$ (0^+)	m+5	70512.0	70512.1	3.76	3.80	-77	-70.2	Q(0-6), Q(8)
$E^1\Sigma^+$ (0^+)	0	70850.6	70850.5	5.93	6.00	101	128	Q(0-6)
$B^1\Sigma^+$ (0^+)	m+6	70948.3	70948.6	4.11	4.095	31	44	Q(0-4)
$k^3\Pi_1$ (1)	1	71125.1	71125.1	6.17	6.184		2.66	Q(3-7)
Unassigned	0^+	71302.4		5.92				Q(1-6), S(0-4), O(2-4)
$B^1\Sigma^+$ (0^+)	m+7	71481.5		3.26		60		Q(0-4)
$I^1\Delta_2$ (2)	0	71988.8		6.2				R(1-7), P(3-8)
		71988.0		6.36		8.7		Q(6-8), Q(10-12), S(1-2), S(4-7), O(4-10)
$k^3\Pi_0$ ($0^\pm$)	2	72352.6	72353.1	5.66	5.650		-5.49	Q(0-4)
$B^1\Sigma^+$ (0^+)	m+10	72506.0	72506.0	4.12	4.106		14.7	Q(0-4)
$E^1\Sigma^+$ (0^+)	1	72651.6	72650.8	5.22	5.29	3.0	3.96	Q(0-1), Q(5-8)
$k^3\Pi_1$ (1)	2	73180.0	73180.7	6.065	6.034	12.6	8.72	Q(4-7)
$j^3\Sigma^-$ (0^+)	0	73254.5	73254.9	5.7	5.706	47	47.5	Q(1-6)
0^+		73383.9	73383.6	5.79	5.819		4.46	Q(1-7)
$B^1\Sigma^+$ (0^+)	m+11	73458.1	73457.8	3.18	3.177	-23	-23.7	Q(0-4)

See notes to Table 4.1a

[1] Reference [13]

region near the $v' = m+5$ vibrational level and so the wavelength correction for the (2+1)REMPI spectrum of this level was determined from the position of the Q(1) rotational line calculated with the molecular constants determined by Ginter et al [13]. Good agreement is obtained between the constants calculated in this work and those reported in the literature. In general D_v, the centrifugal distortion term, is small and only becomes important for J greater than 8. However, the rotational structure of the ion-pair state vibrational levels exhibit strong perturbations and large D_v values are often observed. It was therefore necessary to include the centrifugal distortion term in fitting the rotational lines to a polynomial in $J(J+1)$. If this term is included it is possible to fit the Q(8) rotational line. The Q(7) line is obscured by the S(5) line belonging to the $v' = 0$ level of the $F^1\Delta_2$ Rydberg state. No higher rotational lines were identified in this study.

For the $B^1\Sigma^+ (0^+) \leftarrow X^1\Sigma^+$ (m+6-0) transition the Q-branch is obscured above Q(6) by an overlap with the Q-branch of the $E^1\Sigma^+ (0^+) \leftarrow X^1\Sigma^+$ (0-0) transition. The two highest J rotational lines observed in the ion-pair state progression, Q(5) and Q(6), appear perturbed and have been excluded from the calculation of the molecular constants of this level.

A previously unreported feature at 71481.84 cm^{-1} was observed in the (2+1)REMPI spectrum of HI. This feature had the appearance of a Q-branch for a state with a low B_v value. The B_v value determined was similar to that determined for the ion-pair state levels. The vibrational term value of this state is also consistent with it being a member of the ion-pair state vibrational progression. It has therefore been assigned as the $B^1\Sigma^+ (0^+) \leftarrow X^1\Sigma^+$ (m+7-0)

Figure 4.23 (2+1)REMPI Spectra of Ion−pair State of HI

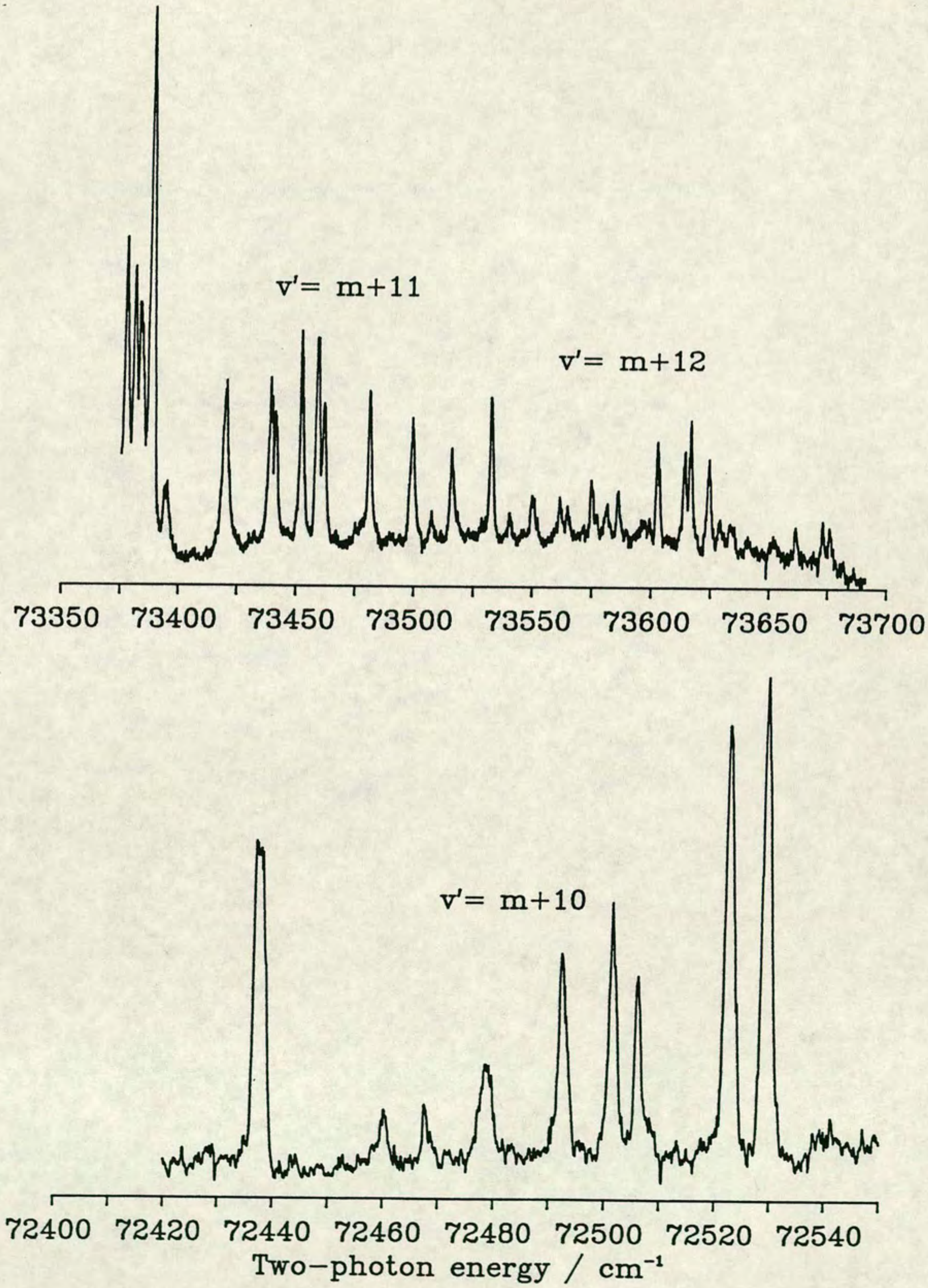

transition. The observed vibrational term value of the v' = m + 7 level is rather higher than that calculated by Ginter et al on the assumption of a smooth progression of vibrational energy levels [13]. However, this calculation did not fully take into account the effect of Rydberg state perturbations on the vibrational progression of the ion-pair state.

The (2 + 1)REMPI spectra of the $B^1\Sigma^+ (0^+) \leftarrow X^1\Sigma^+$ (m + 10-0) and (m + 11-0) transitions are presented in figure 4.23. Both transitions exhibit very short Q-branches which are diffuse and perturbed at high J. The decrease in rotational line intensity with increasing J is much greater for these levels than for the lower vibrational levels. The calculated molecular constants, determined from a least squares fit to the (2 + 1)REMPI line positions, are in good agreement with the results of Ginter et al [13].

Also shown in figure 4.23 is the (2 + 1)REMPI spectrum over the wavelength region in which the $B^1\Sigma^+ (0^+) \leftarrow X^1\Sigma^+$ (m + 12-0) transition should be present. A number of weak diffuse lines can be observed near ν_0 of the v' = m + 12 level but these could not be positively identified. The series of four sharp peaks between 73600 and 73625 cm^{-1} are due to the (2 + 1)REMPI signal of iodine atoms produced by single-photon photodissociation of HI.

The 0^+ Rydberg States

The $E^1\Sigma^+ (0^+) \leftarrow X^1\Sigma^+$ Transition

The Q-branch of the $E^1\Sigma^+ (0^+) \leftarrow X^1\Sigma^+$ (0-0) transition was observed at 70850.6 cm^{-1}. The (2 + 1)REMPI spectrum is complicated by the high J tail of

Figure 4.24 (2+1)REMPI Spectrum of the $v' = 0$ Level of the $E^1\Sigma^+$ (0^+) Rydberg State

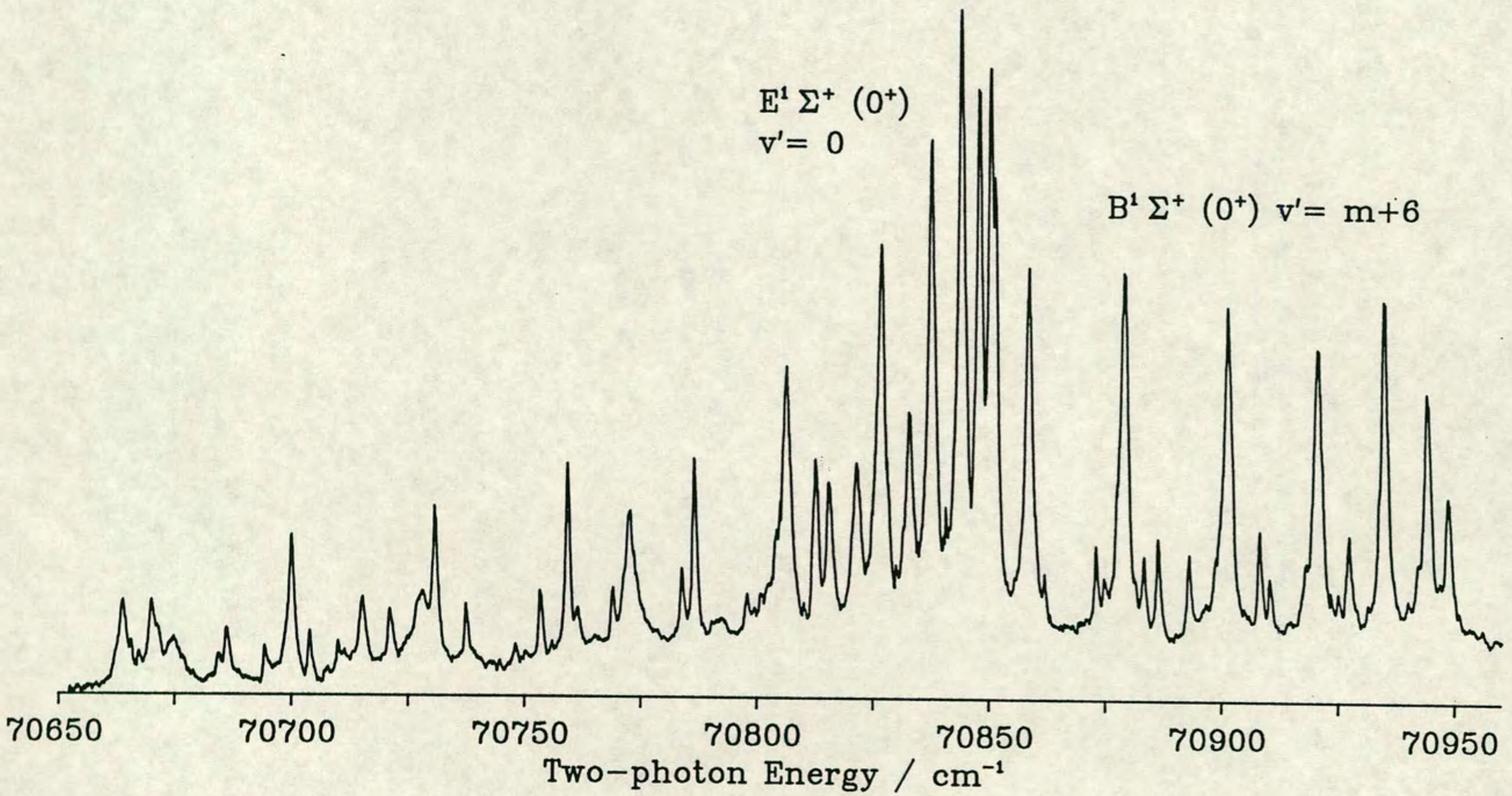

the Q-branch of the $B^1\Sigma^+ (0^+) \leftarrow X^1\Sigma^+$ (m+6-0) transition which is also observed in this spectral region. The spectrum of both of these transitions is presented in figure 4.24. The lower J rotational lines of the $E^1\Sigma^+ (0^+)$ state progression are sharp but become more diffuse with increasing J. This J dependence of the linewidth is indicative of a rotational predissociation of the Rydberg state.

Both the Rydberg state and the ion-pair state levels are expected to have O and S rotational branches in addition to the Q-branches which have been assigned. However, the O- and S-branches are expected to be weak and could not be unambiguously assigned. Many of the lines observed in this spectral region could not be assigned to known HI transitions.

The spectrum of the transition to the v' =2 vibrational level of the $E^1\Sigma^+ (0^+)$ Rydberg state is shown in figure 4.25. Only the Q-branch is observed for this vibrational level of the E state. The Q(2-4) lines are perturbed and have been excluded from the fit of rotational constants. Because high J lines were observed, D_v was calculated in addition to B_v. Apart from the perturbations at low J this vibronic level also suffers from a rotational predissociation which results in increasingly weak and diffuse rotational lines as J increases.

The $H^1\Sigma^+ (0^+)$ and $k^3\Pi_0 (0^\pm)$ Rydberg States

The two lowest lying Rydberg state vibrational levels observed were the v' =0 levels of the $H^1\Sigma^+ (0^+)$ and the $k^3\Pi_0 (0^\pm)$ states. REMPI spectra of the transitions to these two states are shown in figure 4.26. Both states are overlapped by the strong $F^1\Delta_2 (2) \leftarrow X^1\Sigma^+$ (0-0) transition and only short rotational progressions were observed: Q(0-2) for the $H^1\Sigma^+ (0^+) \leftarrow X^1\Sigma^+$ (0-0) transition

Figure 4.25 (2+1)REMPI Spectra of HI

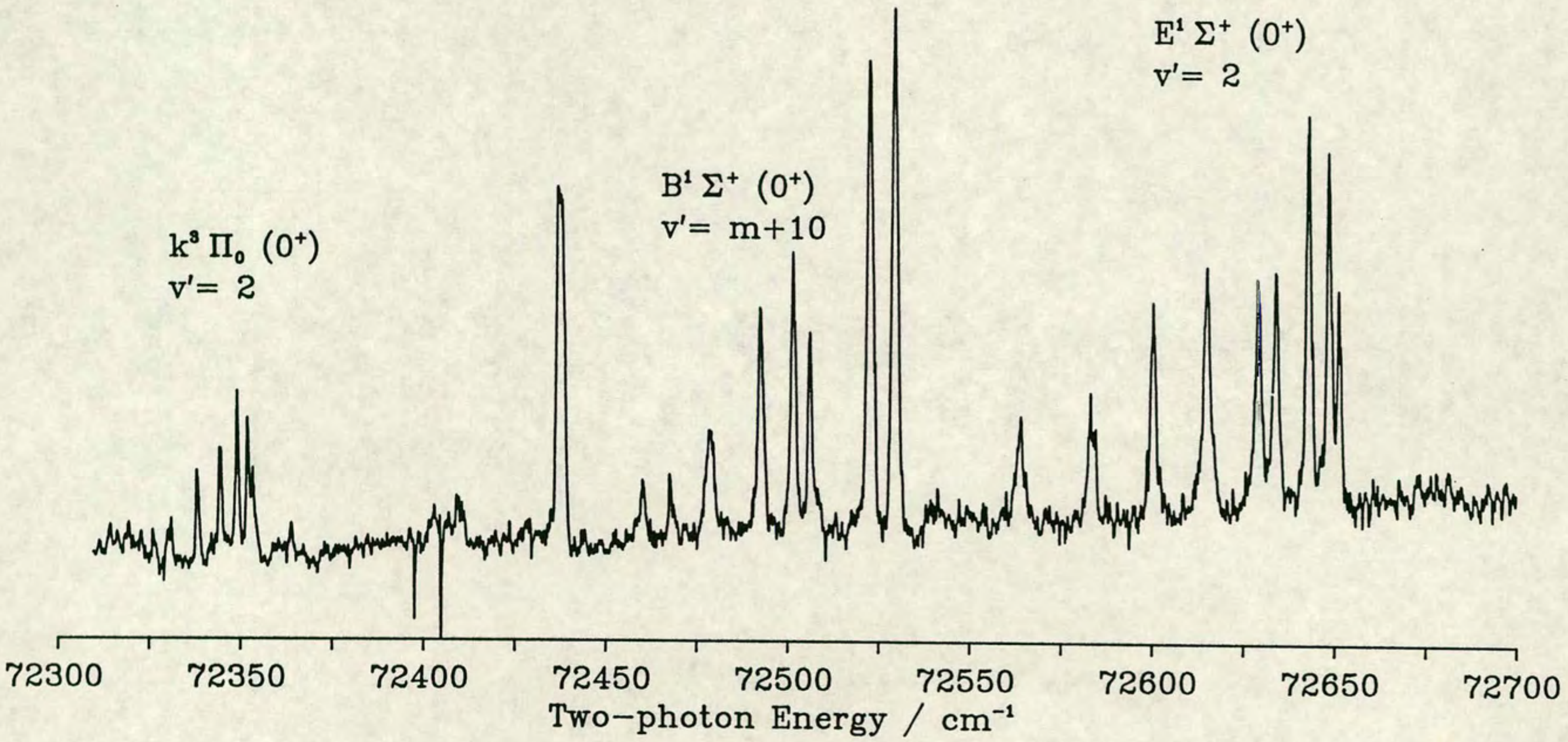

Figure 4.26 (2+1) REMPI Spectra of Rydberg States of HI

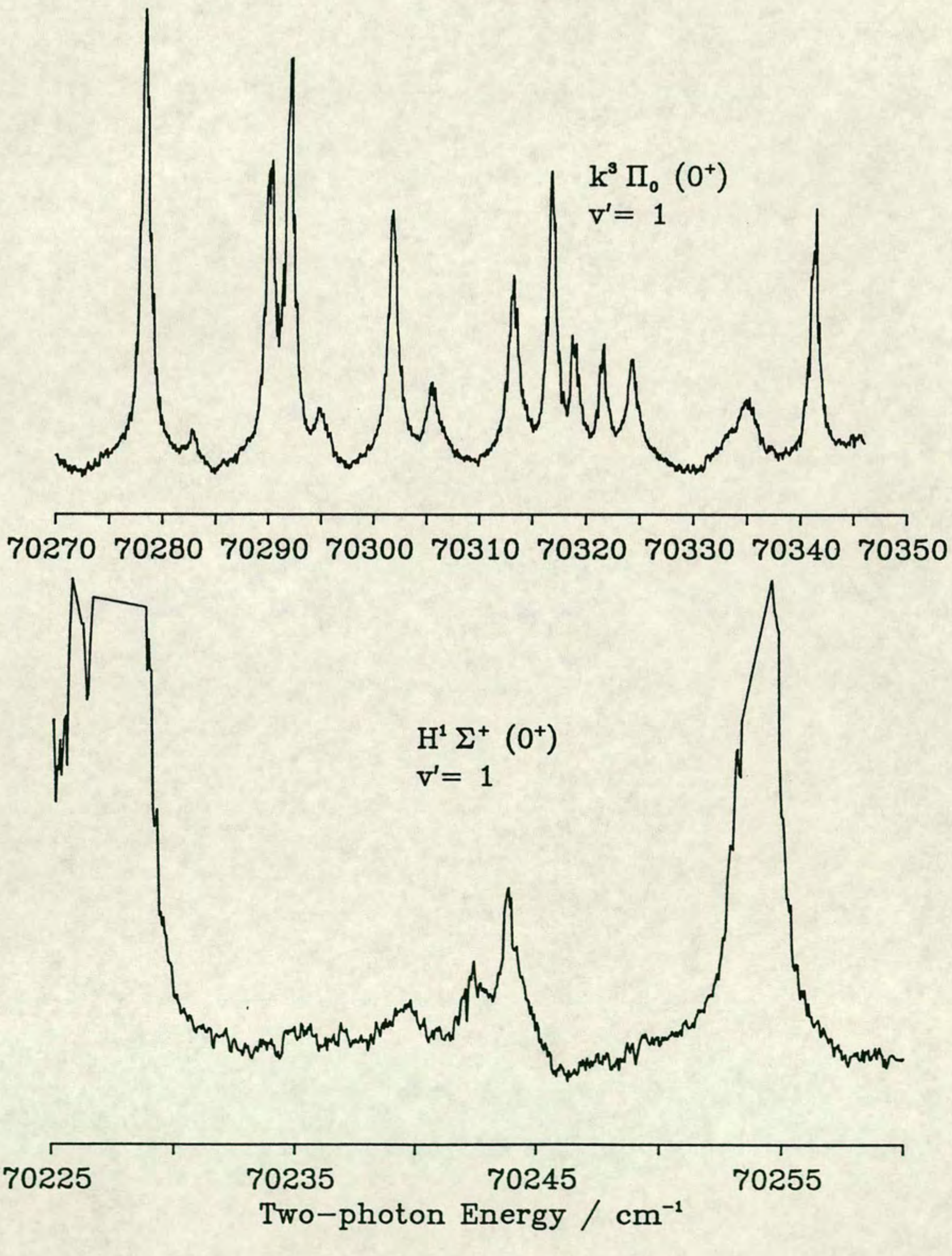

and Q(0-1, 3-5) for the $k^3\Pi_0\ (0^{\pm}) \leftarrow X^1\Sigma^+$ (0-0) transition. The Q(2) rotational line of the $k^3\Pi_0\ (0^{\pm}) \leftarrow X^1\Sigma^+$ transition was blended with the R(6) line of the $F^1\Delta_2\ (2) \leftarrow X^1\Sigma^+$ transition. Therefore only B_v was calculated from the (2+1)REMPI spectra. There were no atomic iodine two-photon absorption lines in this spectral region and so the wavelength correction for this spectrum was determined by comparison with the observed position of the R-branch lines of the $F^1\Delta_2\ (2) \leftarrow X^1\Sigma^+$ transition observed in single photon absorption [13].

The (2+1)REMPI spectrum of the Q-branch of the $k^3\Pi_0\ (0^{\pm}) \leftarrow X^1\Sigma^+$ (2-0) transition is show in figure 4.25. The intensity of the rotational lines falls of sharply with increasing J and only the first five lines of the Q-branch were observed. Because the rotational progression was so short only B_v was calculated for this state.

Unassigned 0^+ State

A previously unreported HI band, with three rotational branches (O, Q, and S), was observed in the (2+1)REMPI spectra. The origin of this band was at 71302.5 cm^{-1}. The (2+1)REMPI spectrum is presented in figure 4.27. The O-branch begins at O(2) (i.e. the lowest J' value is 0) indicating that the excited state is an $\Omega = 0$ state. The rotational constant determined from the observed line positions is consistent with a Rydberg state. Consequently this state has been assigned as an 0^+ Rydberg state. The rotational lines are all sharp and there is no evidence of a rotationally dependent predissociation. However, the higher J levels appear to be perturbed and, because of the congestion of the spectrum, could not be assigned for $J > 6$.

Figure 4.27 (2+1)REMPI Spectra of Previously Unreported 0^+ State in HI

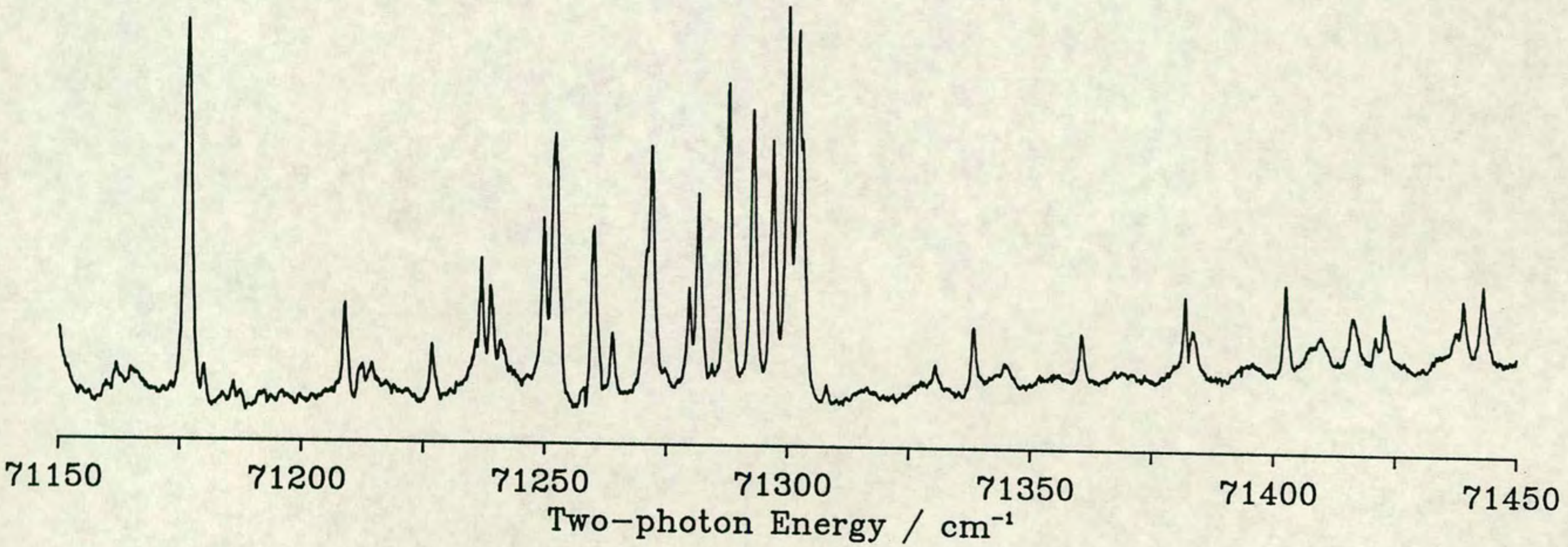

The $j^3\Sigma^-$ (0^+) and 0^+ Rydberg States

Figure 4.28 shows the (2+1)REMPI spectrum of the $j^3\Sigma^-$ (0^+) ← $X^1\Sigma^+$ (0-0) transition and also the (0-0) transition to a 0^+ Rydberg state derived from a higher lying electronic configuration 13. The $j^3\Sigma^-$ (0^+) v' =0 level can clearly be seen to suffer from rotational predissociation. Only the Q-branch of this transition was assigned from the (2+1)REMPI spectra, the O-branch could not be observed and, although a number of S-branch lines were observed, it was not possible to unambiguously identify the S-branch rotational lines. Only the Q-branch of the 0^+ state was observed in the (2+1)REMPI spectrum. A progression of sharp rotational lines was observed at higher energy but could not be assigned as a rotational branch of this state.

The $k^3\Pi_1$ (1) Rydberg State

Two $k^3\Pi_1$ (1) ← $X^1\Sigma^+$ transitions were observed in the (2+1)REMPI spectra of HI, namely the (1-0) and (2-0) bands, and the spectra of both transitions are presented in figure 4.29. For each vibrational level a short rotational progression was observed. The lowest resolved rotational line in each spectrum was the Q(3) and Q(4) line in the (1-0) and (2-0) bands, respectively. Both Q-branches were truncated at Q(7). The molecular constants determined from the observed rotational line positions contain a large degree of error because so few lines were observed but are in quite good agreement with the values derived from single photon absorption spectra.

Figure 4.28 (2+1)REMPI Spectrum of HI

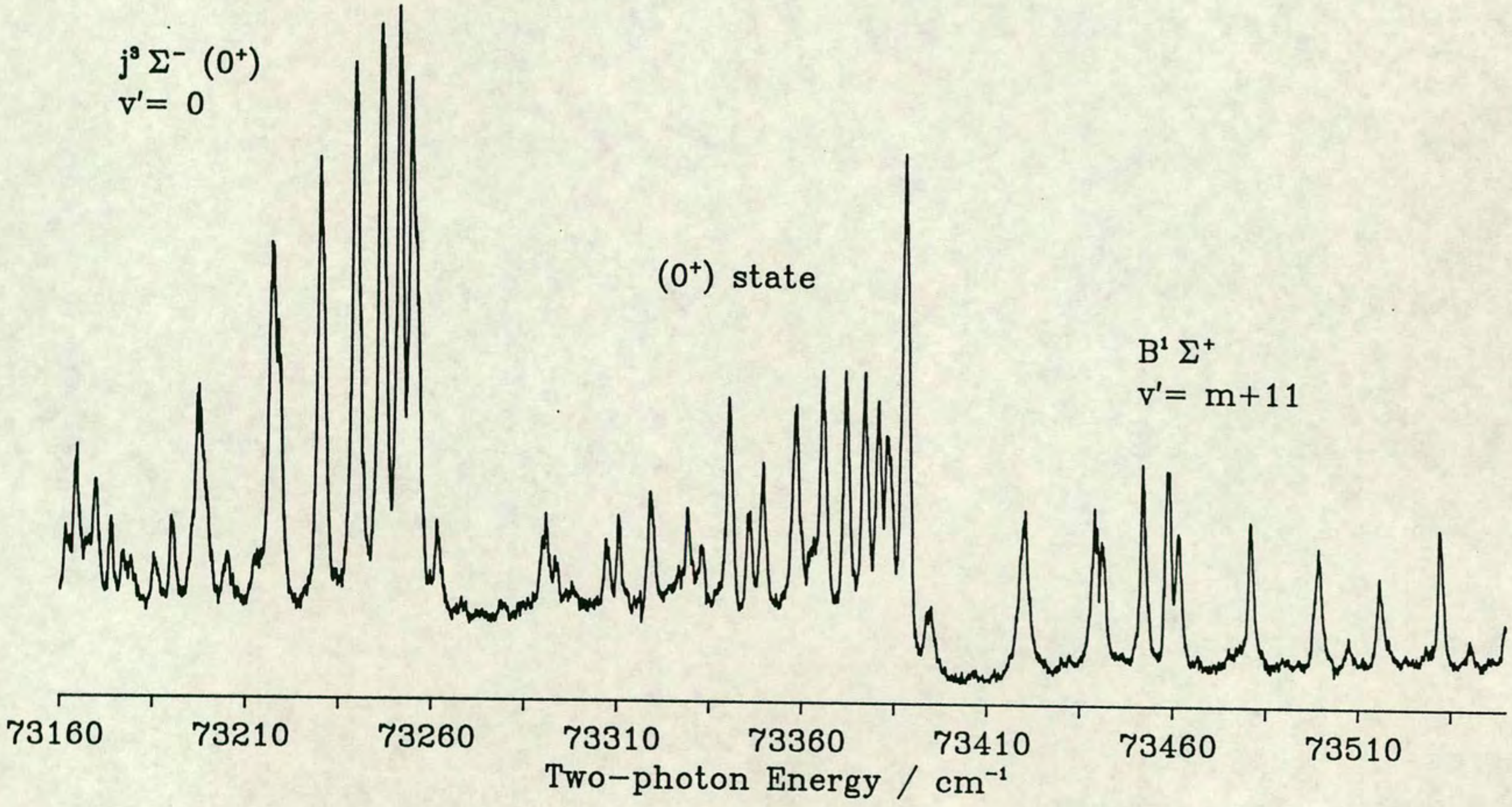

Figure 4.29 (2+1)REMPI Spectra of $k^3\Pi_1$ (1) Rydberg State in HI

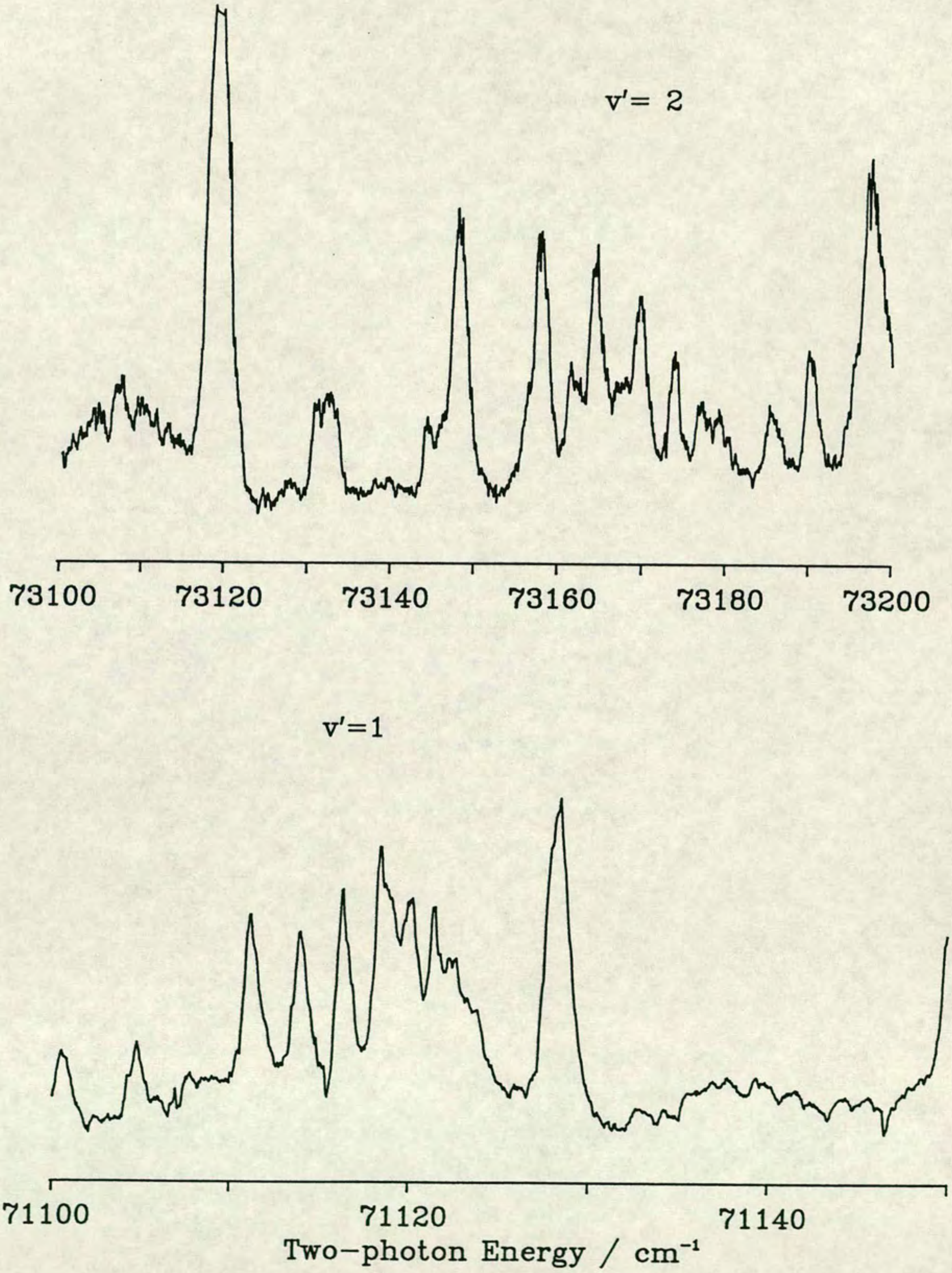

The $\Omega = 2$ Rydberg States

The $F^1\Delta_2$ (2) Rydberg State

The $F^1\Delta_2 (2) \leftarrow X^1\Sigma^+$ (0-0) transition was observed in (2+1)REMPI spectroscopy, see figure 4.30. Rotational constants for the $F^1\Delta_2$ (2) Rydberg state were determined using all of the observed line positions. All of the experimentally observed rotational linewidths were instrumentally limited but the intensity of the Q-branch drops off sharply with increasing J. Similar behaviour was noted for the $F^1\Delta_2$ Rydberg state of HCl which is subject to rotational predissociation [74] [77]. A number of weak but sharp lines were observed to the low energy side of the Q-branch of the transition which could not be assigned.

The $I^1\Delta_2$ (2) Rydberg State

One other $\Delta\Omega = 2$ transition was observed in the (2+1)REMPI spectra which is shown in figure 4.31. The term value of this transition, 71989 cm^{-1}, does not match any previously observed HI excited electronic state. A comparison of the observed term value with that for the $v' = 1$ vibrational level of the $F^1\Delta_2$ (2) state, calculated from the isotope shift observed for DI, gives a good match. However, an analysis of the hot band structure indicates that the observed $\Omega = 2$ state is at too low an energy [82] and accordingly this transition has been assigned as $I^1\Delta_2 (2) \leftarrow X^1\Sigma^+$ (0-0).

4.4.2 Fluorescence Excitation Spectroscopy of HI

The characteristic bound-free fluorescence from the ion-pair state of HI lies

Figure 4.30 (2+1)REMPI Spectrum of $F^1\Delta_2$ (2) State

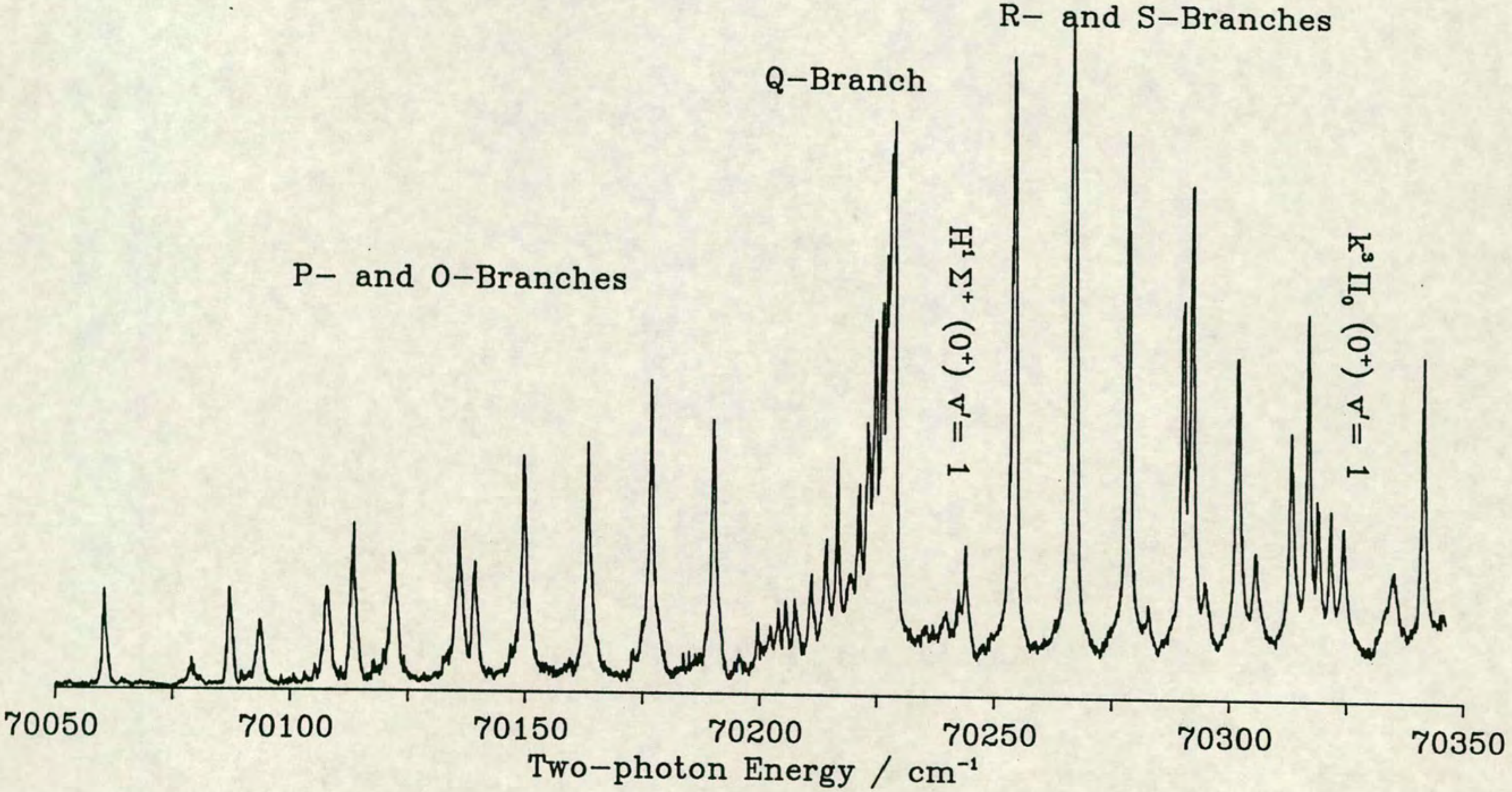

Figure 4.31 (2+1)REMPI Spectrum of the $I'\Delta_2$ (2) Rydberg State in HI

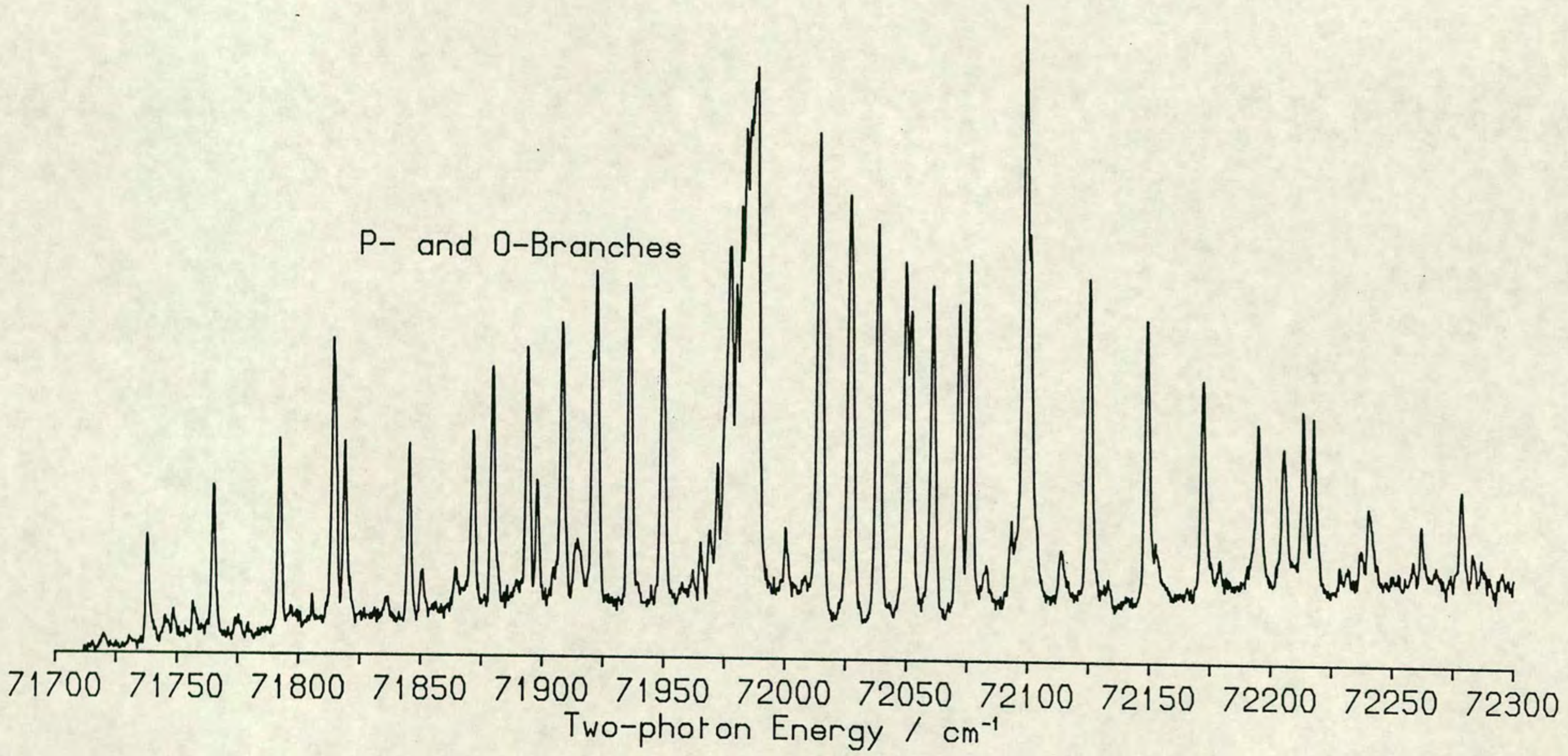

in the wavelength range 210-250 nm. For the $B^1\Sigma^+ (0^+) \rightarrow X^1\Sigma^+$ (m+6-0) transition there is a maximum in the high frequency modulation of the bound-free fluorescence spectrum at 220 nm. The upper trace in figure 4.32 shows a fluorescence excitation spectrum recorded for fluorescence emitted at this wavelength. The (2+1)REMPI spectrum recorded concurrently with the fluorescence excitation spectrum is shown in the lower trace of this figure.

Transitions to several vibronic states are evident in the (2+1)REMPI spectrum; $E^1\Sigma^+ (0^+)$ v' = 0, $B^1\Sigma^+ (0^+)$ v' = m+6, $k^3\Pi_1$ (1) v' = 1, and the 0^+ Rydberg state reported in the last section. In addition, there are numerous unassigned lines and atomic iodine transitions. All of the latter correspond to transitions from the spin-orbit excited state of the atom and are present, though with altered relative intensities, in the fluorescence excitation spectrum. However, the appearance of the HI molecular bands in the fluorescence excitation spectrum differs greatly from the (2+1)REMPI spectrum.

A strong fluorescence signal is observed for both the $E^1\Sigma^+ (0^+) \leftarrow X^1\Sigma^+$ and the $B^1\Sigma^+ (0^+) \leftarrow X^1\Sigma^+$ transitions. The $E^1\Sigma^+ (0^+)$ state is known to be vibronically couple to the ion-pair state and this level shows the characteristic ion-pair fluorescence emission. The O- and S- branches, which are observed in the (2+1)REMPI spectrum, are too weak to be observed in the fluorescence excitation spectrum. The unassigned 0^+ Rydberg state at 71302.5 cm^{-1} shows some very weak emission at 220 nm but no fluorescence is observed from the $k^3\Pi_1$ (1) v' = 1 state. Also, the weak unassigned progression of lines observed to higher energy than the iodine line at 78592.75 cm^{-1} is missing in the fluorescence excitation spectrum.

Figure 4.32 Fluorescence Excitation Spectrum of HI

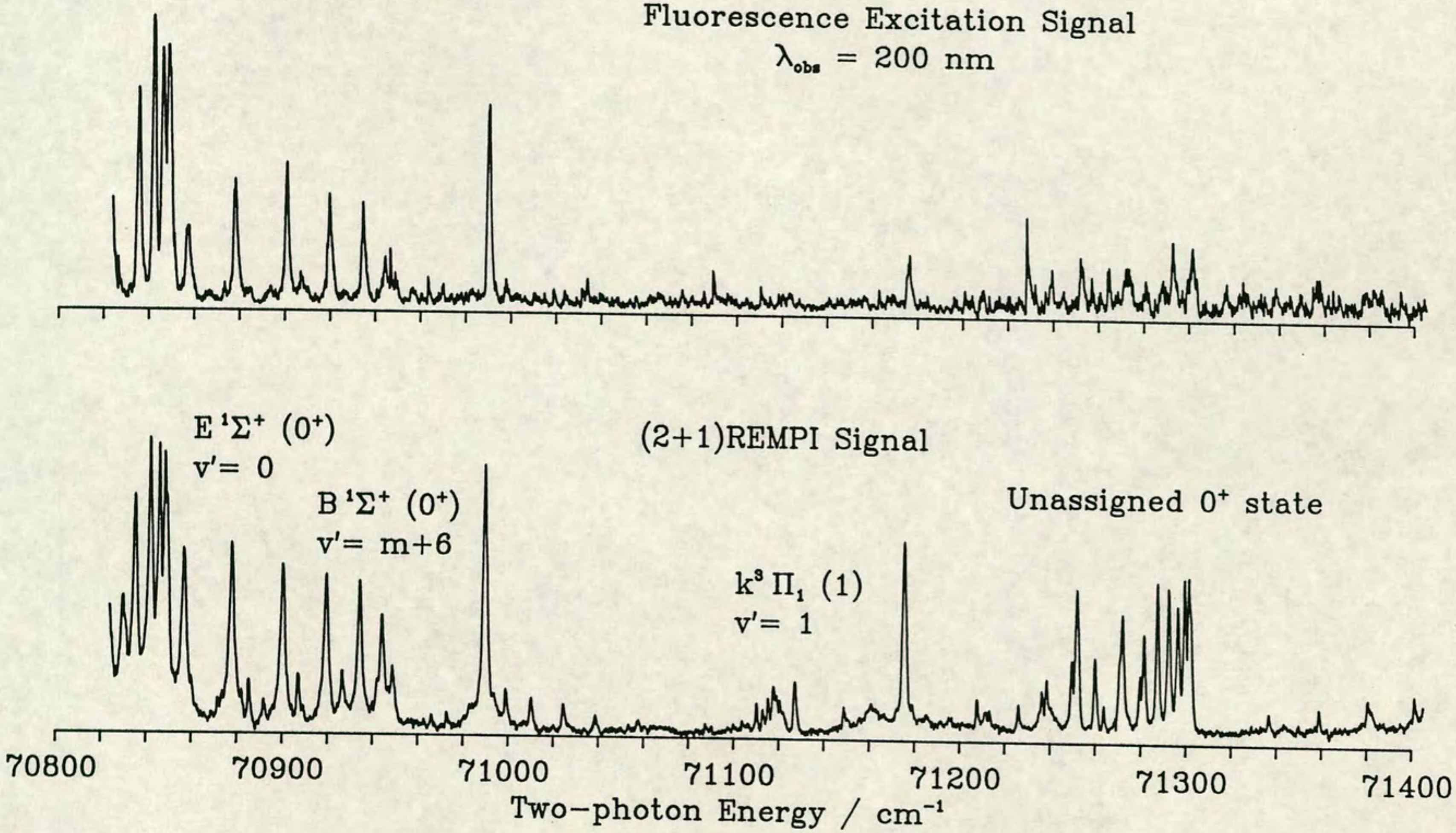

A slightly different picture is obtained if the detection wavelength is set to 227 nm. This is at a maximum in the $E^1\Sigma^+$ (0^+) state emission but a minimum in the $B^1\Sigma^+$ (0^+) state emission. The fluorescence excitation spectrum, at this detection wavelength, of the $E^1\Sigma^+ (0^+) \leftarrow X^1\Sigma^+$ (0-0) and $B^1\Sigma^+ (0^+) \leftarrow X^1\Sigma^+$ (m+6-0) transitions is shown in figure 4.33, along with the simultaneously recorded (2+1)REMPI spectrum. It can be seen that this detection method discriminates against the ion-pair state level. The Q(7) rotational line of the $B^1\Sigma^+ (0^+) \leftarrow X^1\Sigma^+$ transition is missing in the fluorescence spectrum and thus can be clearly identified in the (2+1)REMPI spectrum.

The third fluorescence excitation spectrum of HI which is reported here was recorded with a detection wavelength of 340 nm. This spectrum is presented in figure 4.34, along with the simultaneously recorded (2+1)REMPI spectrum. The detection wavelength corresponds to the $D' \rightarrow A'$ fluorescence band of molecular iodine, I_2. Fluorescence from I_2 at this wavelength, and from the $D \rightarrow X$ band at 320 nm, was observed in many of the dispersed fluorescence spectra of HI. The intensity of this I_2 fluorescence is much greater than that of HI and, in some cases, greatly exceeds the level of the scattered laser radiation.

Apart from a weak non-resonant background signal the fluorescence intensity shows a strong dependence on the resonant HI excited state. Excitation of the two 0^+ Rydberg states results in strong I_2 fluorescence while almost no fluorescence is observed for excitation of the $v' = m+11$ level of the ion-pair state. Also, excitation of the atomic iodine transition $6p^4D^o_{1/2} \leftarrow {}^2P^o_{3/2}$, at 73387.18 cm^{-1}, produces very strong I_2 fluorescence while the $9p^4D^o_{7/2} \leftarrow {}^2P^o_{1/2}$, at 73342.29 cm^{-1}, does not result in I_2 fluorescence at this wavelength.

Figure 4.33 Fluorescence Excitation Spectrum of HI

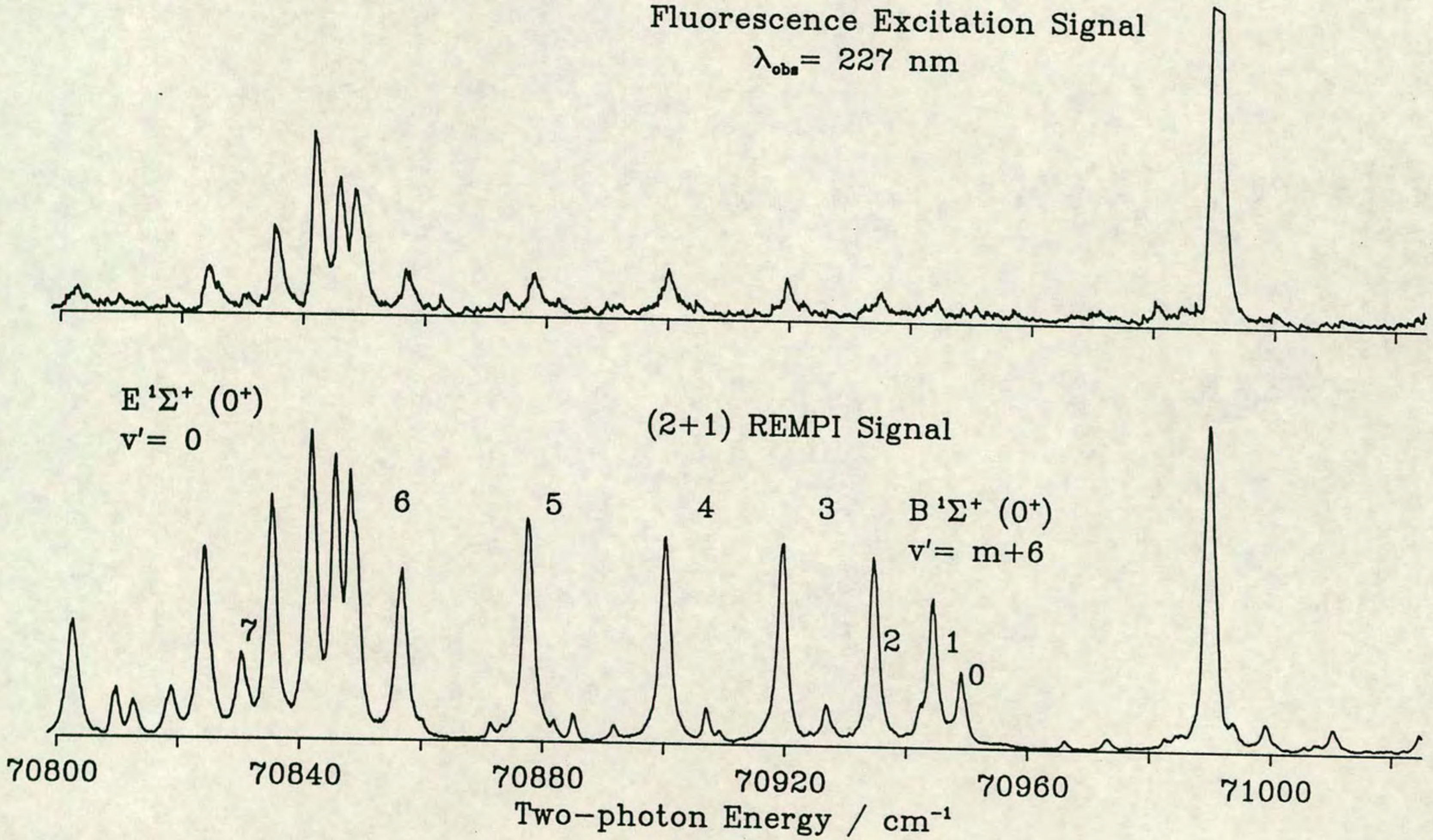

Figure 4.34 Fluorescence Excitation Spectrum of HI

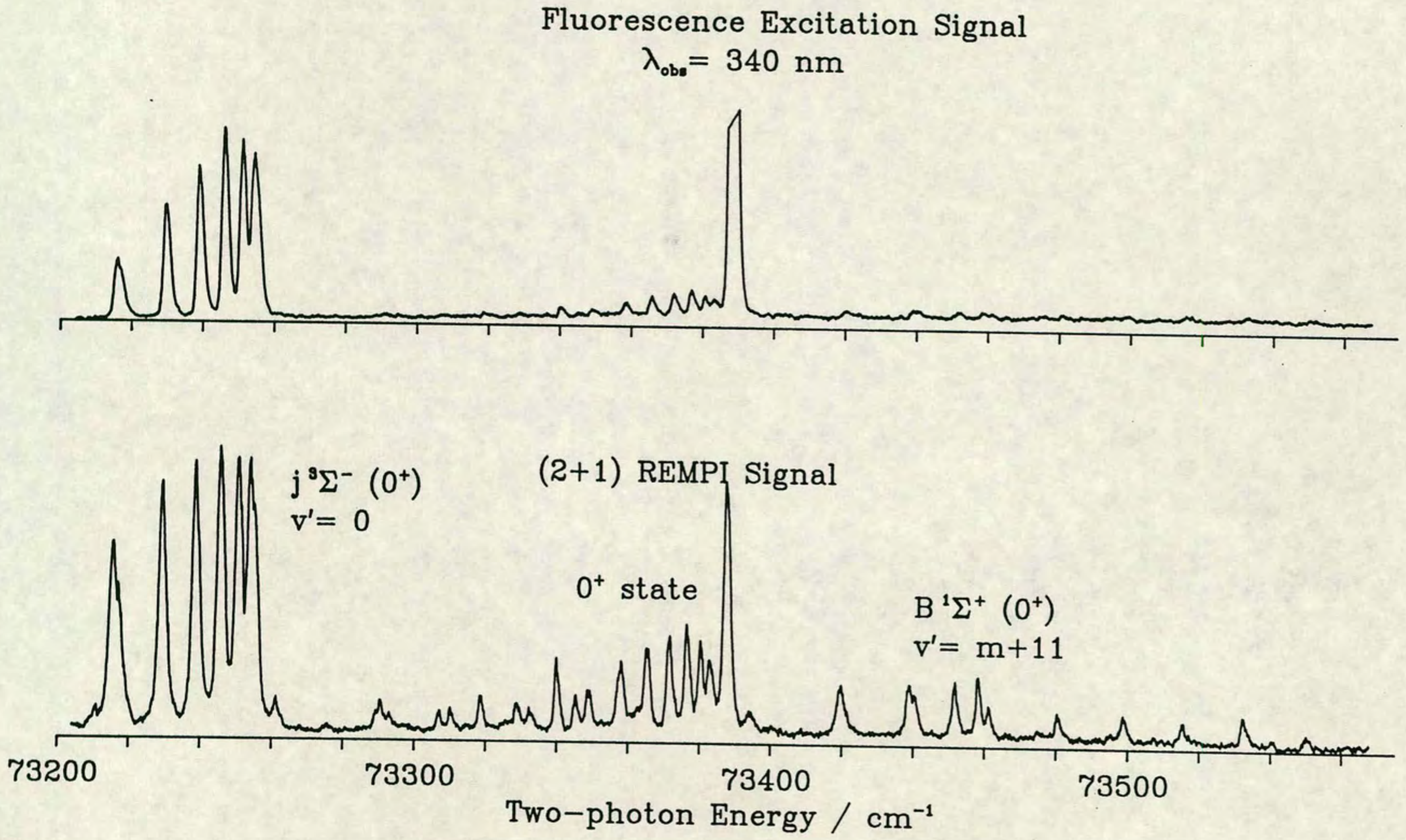

4.4.3 Dispersed Fluorescence Spectra of HI

Dispersed fluorescence spectra were recorded from three vibrational levels of the ion-pair state, from two vibrational levels of the $E^1\Sigma^+$ (0^+) Rydberg state, from v' = 0 of the $F^1\Delta_2$ (2) and $j^3\Sigma^-$ (0^+) Rydberg states, and from the previously unreported $\Omega = 2$ state. In general the level of HI fluorescence was very low and consequently many of the spectra have very poor signal to noise ratios. For the case of HI the characteristic ion-pair type fluorescence is observed at much shorter wavelength than the exciting laser wavelength, thus the difficulties encountered in HCl and DCl spectra due to the overlap of the exciting laser line with the fluorescence were avoided. However, the dispersed fluorescence spectra of HI were complicated by the presence of very strong atomic and molecular iodine fluorescence features.

Two I_2 fluorescence systems were identified, the D → X band at 320 nm and the D' → A' band at 342 nm. In addition to these bands, which are discussed in section 4.5, a number of other broadband features were observed in the fluorescence spectra. These features could not be assigned as either HI or I_2 fluorescence bands and it has not been possible to fully analyse them.

The $B^1\Sigma^+$ (0^+) Ion-pair State

Dispersed fluorescence spectra were recorded from three vibrational levels of the ion-pair state; v' = m+5, 6, and 10. Excitation of all of these levels gives rise to characteristic bound-free and bound-bound ion-pair fluorescence structure, similar to that observed for HCl and DCl. Representative dispersed fluorescence spectra from these vibrational levels are presented in figure 4.35. From the

Figure 4.35
Dispersed Fluorescence from the Ion-pair State in HI

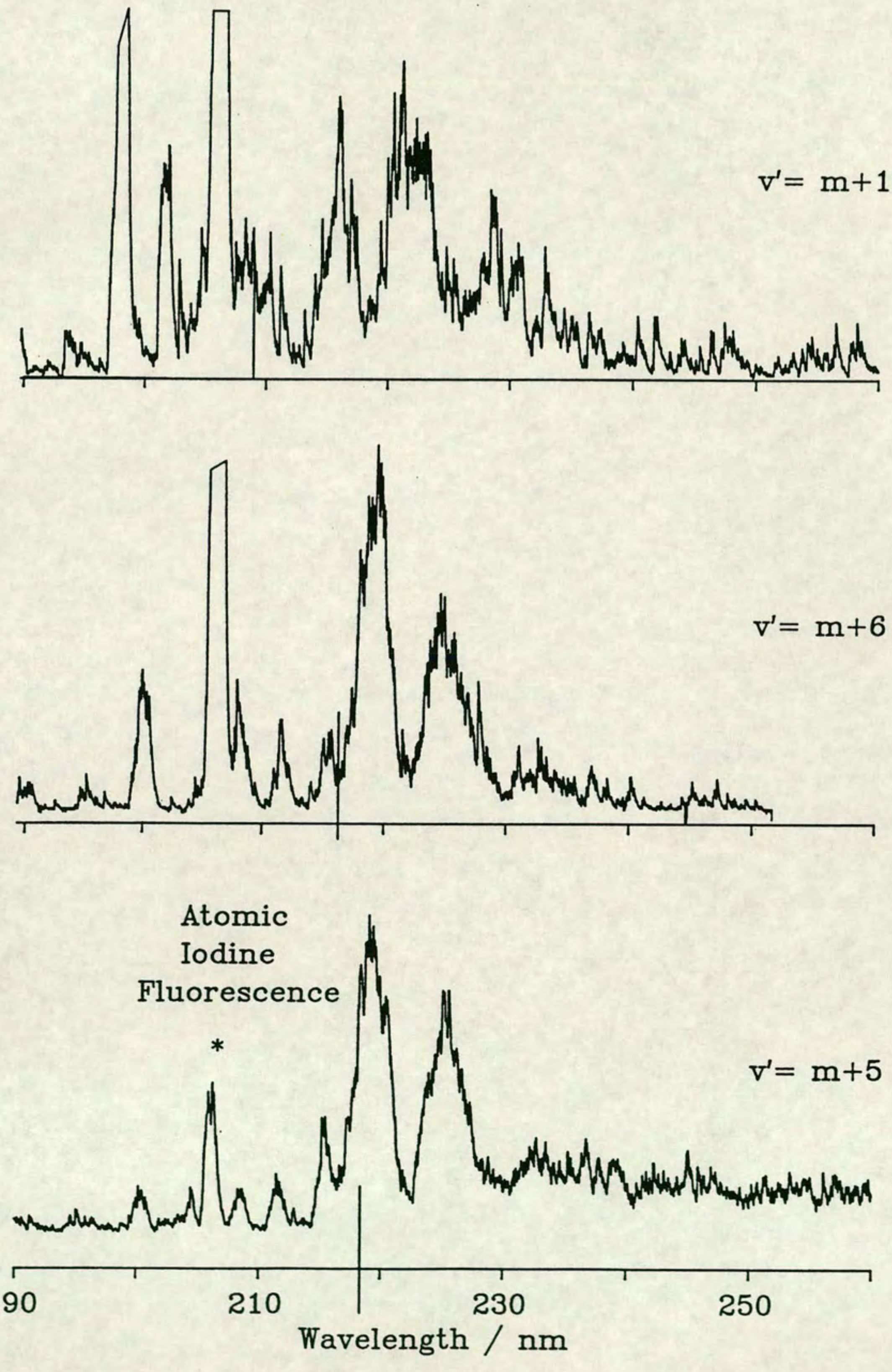

wavelength of the sharp bound-bound peaks and the known excitation wavelength, the energy of the ground state vibrational energy levels can be determined. This was done using the peak positions measured from the dispersed fluorescence from both ion-pair levels and the v' = 0 level of the $E^1\Sigma^+$ (0^+) Rydberg state. The calculated ground state energy levels are presented in table 4.3. Because of the low resolution of the detection system there is a large uncertainty in the position of the spectral peaks and hence in the energy levels calculated from the spectra.

The position of the bound-free to bound-bound fluorescence boundary is indicated for each of the spectra shown in figure 4.35. For the v' = m + 5 vibrational level there is a very intense fluorescence peak at the bound-free boundary and only two other maxima are observed in the bound-free fluorescence region of the spectrum. The very narrow width of the bound-free fluorescence band indicates that v' = m + 5 is a low vibrational level and hence that m is a small integer. The continuum structure of the emission from the v' = m + 6 level is very similar to that from the v' = m + 5 level but, because of the higher term value, extends further into the blue.

The dispersed fluorescence from the v' = m + 10 level of the ion-pair state was considerably weaker than that from the two lower levels. The characteristic ion-pair fluorescence structure can, however, be clearly seen despite the poor signal to noise ratio. As with the other spectra the atomic iodine peak at 206.229 nm is observed but there is also a further peak at 198.1 nm which could not be identified.

Table 4.3 Observed Vibrational Energy Levels of the Ground State of HI

$^{a}v'$	$^{b}G_v$ / cm^{-1}	^{c}Error / cm^{-1}	ΔG_v / cm^{-1}	^{d}No of points
10	19675.0	± 25		4
			1272.0	
11	20947.0	± 60		4
			1233.5	
12	22180.5	± 22		6
			1003.4	
13	23183.9	± 9		7
			851.4	
14	24035.3	± 26		7
			747.4	
15	24726.8	± 12		7
16	-	-		-
			893.6	
17	25620.4	± 37		2

Notes

a Estimated from extrapolation of ω_e and $\omega_e x_e$ and from number of vibrational levels of *ab initio* potential.

b Average of calculated vibrational energies with $J'' = 0$ relative to the minimum of the ground state. The rotational energy was estimated from the rotational constants calculated from tabulated potentials.

c Standard deviation of calculated vibrational energy.

d The number of observed peaks used to calculate each vibrational energy.

Apart from the $B^1\Sigma^+ (0^+) \rightarrow X^1\Sigma^+$ fluorescence no other HI fluorescence features were observed in emission from the ion-pair state of HI. Since the $B^1\Sigma^+ (0^+) \rightarrow A^1\Pi$ bound-free emission bands observed in HCl and DCl were noted to be considerably weaker than the $B^1\Sigma^+ (0^+) \rightarrow X^1\Sigma^+$ bands it is unlikely that they would be observed in HI which had a much lower fluorescence intensity. Although a number of broad emission features were observed to the red of the $B^1\Sigma^+ (0^+) \rightarrow X^1\Sigma^+$ fluorescence, these were not reproduceable and could not be assigned to HI fluorescence bands.

The $E^1\Sigma^+ (0^+)$ Rydberg State

For HI it was possible to record dispersed fluorescence spectra from both the $v'=0$ and $v'=1$ vibrational levels of the $E^1\Sigma^+ (0^+)$ state. The dispersed fluorescence spectrum from the $v'=0$ vibrational level of the $E^1\Sigma^+ (0^+)$ state is shown in figure 4.36 along with a comparable spectrum from the $v'=m+6$ level of the ion-pair state. Both show a very similar pattern of bound-free and bound-bound fluorescence features. The spectra have a relatively poor signal to noise ratio but it can be seen from figure 4.36 that there is a small red shift of some of the peaks in the fluorescence from the $E^1\Sigma^+ (0^+)$ state. The $E^1\Sigma^+ (0^+)$ state was excited on the Q(3) rotational line, which does not coincide with an ion-pair state rotational line. Collisional transfer of energy is not important in the hydrogen halides at the pressures used, see section 4.2.2. The differences in the fluorescence excitation spectra of the ion-pair state and Rydberg state levels indicate that there is a considerable difference between the emission of the two levels. Therefore the observed fluorescence from this $E^1\Sigma^+ (0^+)$ state level is a result of the vibronic coupling of the Rydberg state with the ion-pair state. In

Figure 4.36
Dispersed Fluorescence from E $^1\Sigma^+$ (0^+) Rydberg State in HI

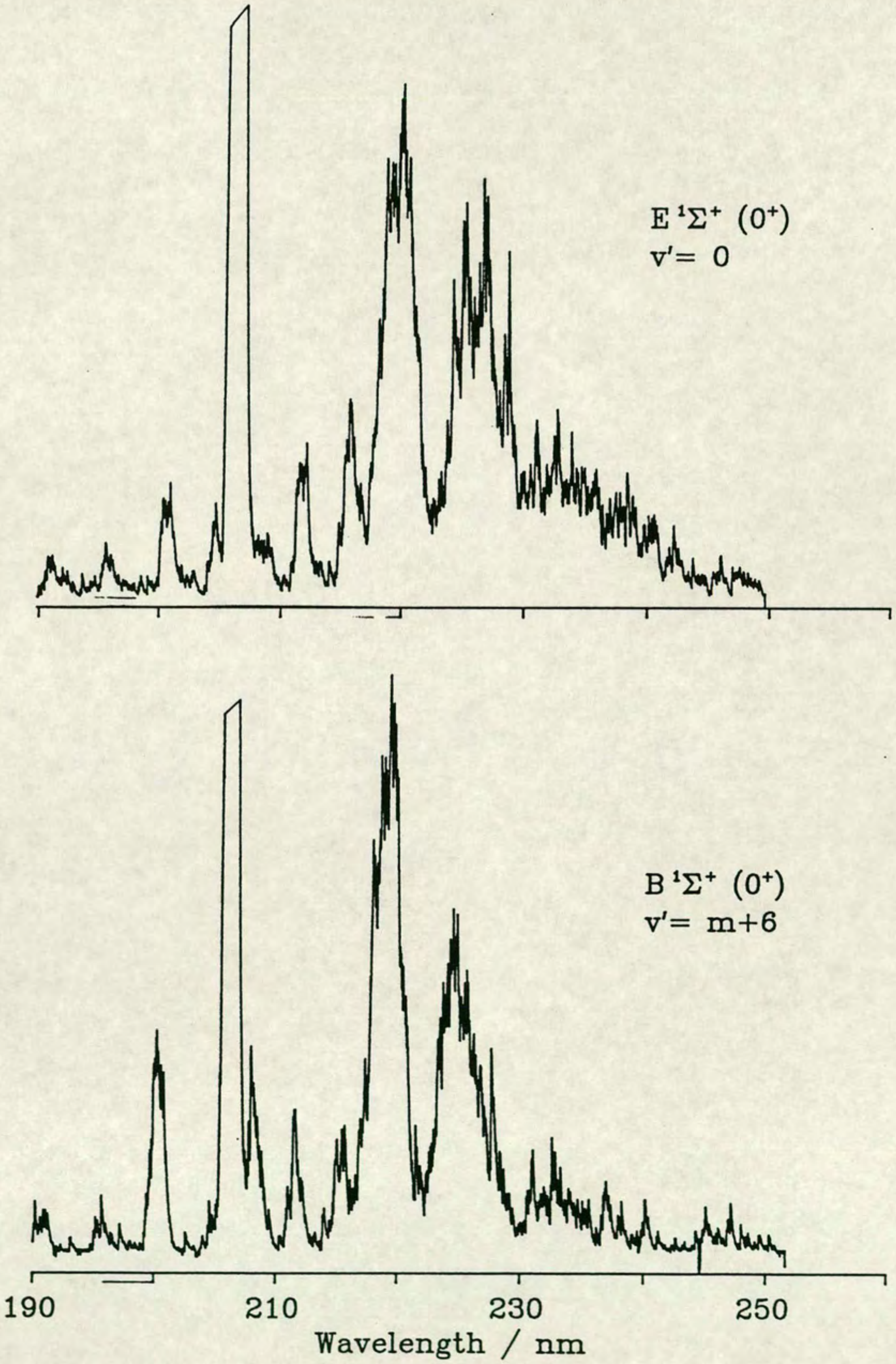

common with the ion-pair state levels, no other HI fluorescence emission bands were observed from the $E^1\Sigma^+$ (0^+) state $v'=0$ vibrational level.

The dispersed fluorescence spectrum from the $v'=1$ level of the E state exhibits very different structure to that observed from the $v'=0$ level and is shown in figure 4.37. There is no obvious sign of the ion-pair type fluorescence structure observed from $v'=0$ but at shorter wavelength than the atomic iodine peak are two peaks, similar to those observed for bound-bound transitions in the spectrum from the $v'=m+10$ level of the ion-pair state. The wavelengths of these peaks match the energy of the $v''=$ 13 and 14 vibrational levels of the ground state calculated from the dispersed fluorescence spectra from ion-pair state levels. They cannot be assigned to either atomic iodine or I_2 transitions. Although they appear in isolation of any other recognisable HI fluorescence features they have been assigned as HI fluorescence due to the coupling of the E state with the ion-pair state.

To longer wavelength there is a single broad maximum in the fluorescence spectrum which has been assigned as $E^1\Sigma^+$ $(0^+) \rightarrow A^1\Pi$ $(v'=1)$ bound-free fluorescence. Although a double peak is expected in the fluorescence from a $v'=1$ vibrational level to a repulsive state, the longer wavelength peak is obscured by overlap with another fluorescence system.

The most striking feature in the spectrum shown in figure 4.37 is a very strong progression of sharp peaks on top of a broad background to the red of the scattered laser light. Similar fluorescence spectra are observed if the excitation wavelength is not resonant with an HI energy level. The upper trace in

Figure 4.37 Dispersed Fluorescence from v'= 1 of $E\,^1\Sigma^+$ (0^+) Rydberg State in HI

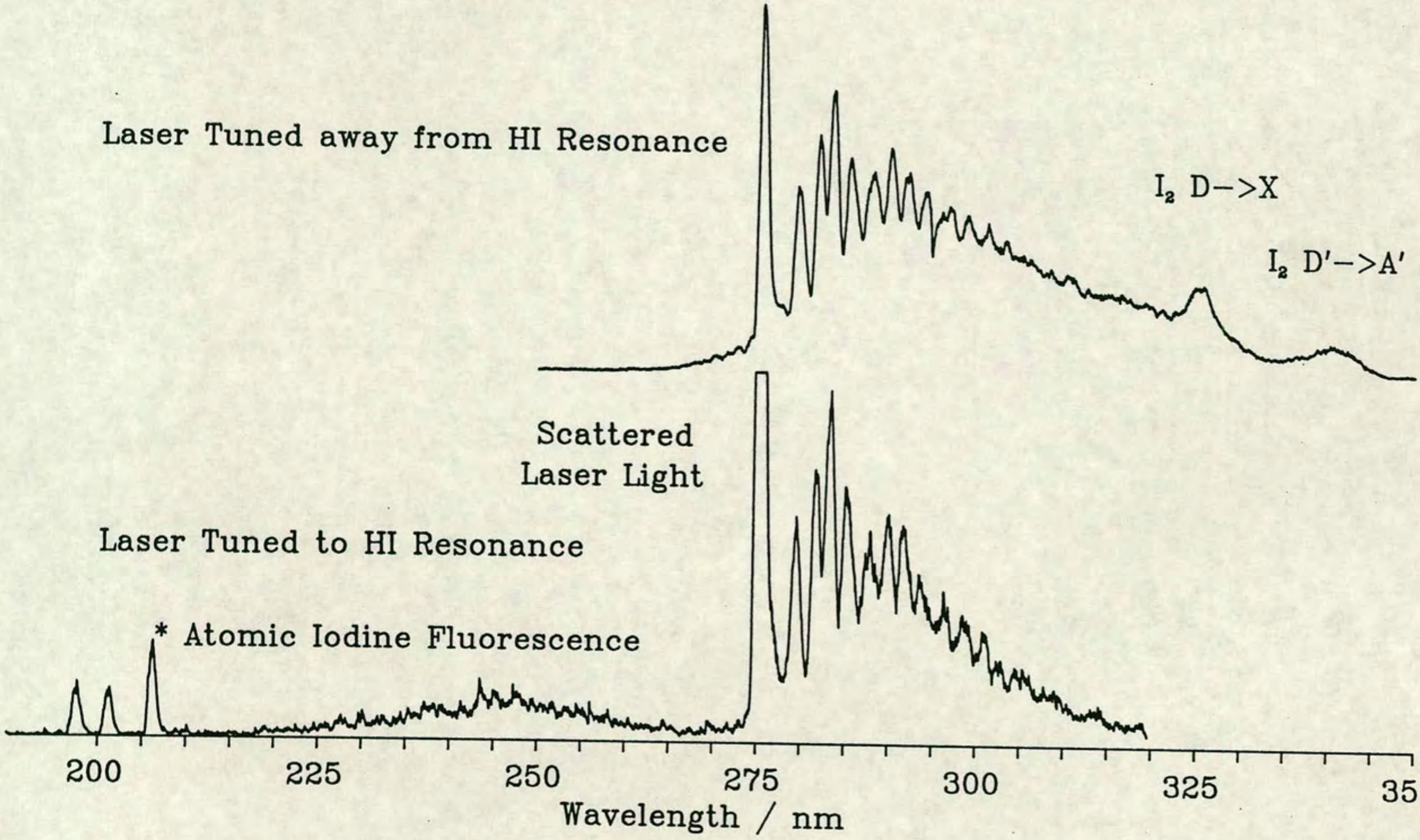

figure 4.37 was recorded with the laser tuned far from any HI two-photon resonance. The progression is irregular but has an average spacing of 250 cm^{-1}. Because of the wavelength at which the progression lies it cannot be assigned as an HI emission band. Also the peak spacing is too great for this to be a bound-bound transition of I_2. While its structure is reminiscent of a bound-free emission band, no similar feature has been observed in I_2 [83]. The structure of the band was not exactly reproduced in different spectra and so it may have been due to contamination of the HI sample. Unfortunately there was insufficient time to conduct a more thorough investigation of this fluorescence band.

The $j^3\Sigma^-$ (0^+) Rydberg State

Dispersed fluorescence spectra were recorded following excitation of $v'=0$ level of the $j^3\Sigma^-$ (0^+) Rydberg state. A dispersed fluorescence spectrum from this state is shown in figure 4.38. At short wavelength can be seen a relatively strong atomic iodine transition while at long wavelength quite weak molecular iodine fluorescence can be noted. However, it is also possible to identify two weak HI fluorescence bands.

There is a broad band feature, centred near 255 nm which can be assigned to $j^3\Sigma^-$ $(0^+) \rightarrow A^1\Pi$ bound-free fluorescence. As expected for a $v'=0$ level the band is very broad and appears to be symmetrical about the central wavelength. This bound-free band partially overlaps the red end of the much weaker ion-pair type fluorescence. Although the ion-pair fluorescence is very weak it is possible to identify a number of the high frequency maxima in the bound-free region of the spectrum in addition to three bound-bound transitions.

Figure 4.38 Dispersed Fluorescence from v′= 0 of j $^3\Sigma^-$ (0$^+$) Rydberg State in HI

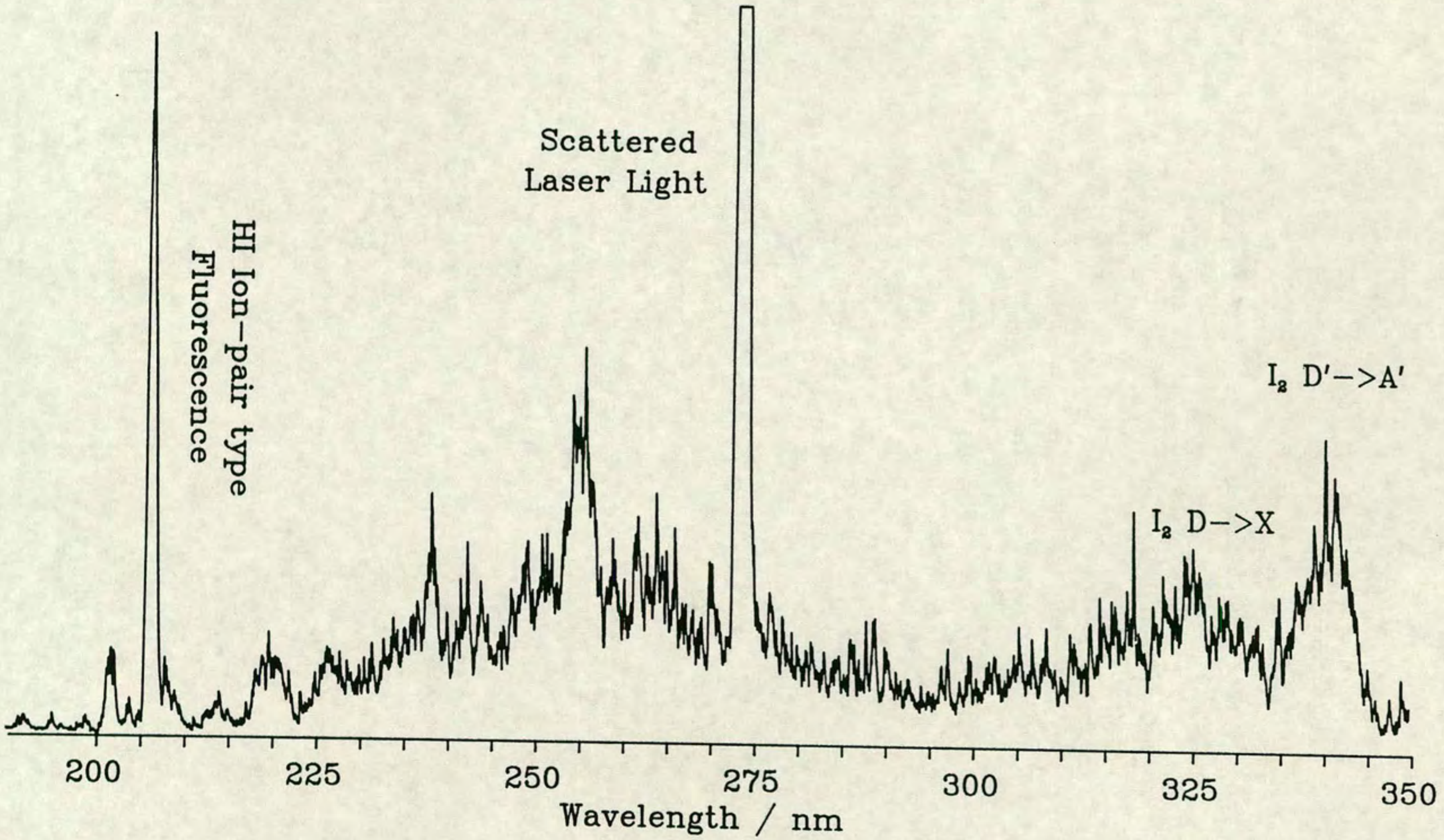

The $F^1\Delta_2$ (2) and $I^1\Delta_2$ (2) Rydberg States

Dispersed fluorescence spectra were recorded from the v' =0 level of the $F^1\Delta_2$ (2) Rydberg state and from the v' =0 level of $I^1\Delta_2$ (2) Rydberg state. The spectra both show the single maximum, continuum fluorescence band expected which peaks at 245 nm and 235 nm.

4.5 Atomic and Molecular Iodine Fluorescence

One [illegible] strong fluorescence line, $6s\,^2P_{3/2} \rightarrow {}^2P^o_{1/2}$, at 206.229 nm, was observed in all of the dispersed fluorescence spectra recorded. The energy of this atomic level with respect to the ground state is 56092.88 cm^{-1}. Since the dissociation energy of HI is $\simeq$ 24000 cm^{-1} this is at greater energy than all but the most energetic two-photon resonant states of HI studied in this work. HI molecules in the two-photon resonant excited states can be photodissociated by absorption of a third photon to a higher lying repulsive state. This has been observed for HCl [33] [65] and HBr [77] but only the ion-pair and the Rydberg states coupled to it were photodissociated. There are no repulsive states at the correct energy above the potential minima of the Rydberg states, although the ion-pair state potential extents to much greater internuclear separation and photodissociates at large R. However because the density of states in HI is much greater than that for HCl and HBr there may be a repulsive state at the appropriate energy for photodissociation of the pure Rydberg states in HI. The intensity of the 206.229 nm atomic iodine fluorescence line varies both with the HI state excited and between different spectra of the same ro-vibronic level. No correlation was determined between the observed fluorescence intensity and any of the experimentally adjustable parameters. A similar lack of reproducability was noted for the I_2 fluorescence bands which were observed.

The generation of excited states of I_2 by photoexcitation of iodine-containing molecules has been studied in some detail [84]. In particular the D and D' ion-pair states are of interest as the upper levels for excimer laser transitions [84] [85] [86] [87]. It has been shown that excited iodine atoms in the $6p(^4P)$ metastable states can be collisionally quenched by iodine containing molecules to produce I_2^* in the D and D' states. From the dispersed fluorescence spectra presented previously it is apparent that excited atomic iodine in n=6 states is produced when exciting both ion-pair and Rydberg states of HI. Therefore if the mechanism for the production of I_2 in the D and D' states is:

$$I^*(\text{metastable, } n=6) + HI \rightarrow H + I_2^* \tag{4.1}$$

then both the ion-pair and Rydberg states should be observed in the fluorescence excitation spectrum presented in figure 4.34. The photodissociation of the ion-pair state will occur at larger internuclear separation than for the Rydberg states and so will involve different repulsive states. If this produces $I^*(n=6)$ atoms with short fluorescence lifetimes or with different values of principal quantum number then it would explain why little or no fluorescence is observed at 340 nm when exciting the $v' = m+11$ level of the ion-pair state.

It is also possible to propose mechanisms involving charged species to explain the observation of $D' \rightarrow A'$ and $D \rightarrow X$ emission when exciting HI ion-pair and Rydberg states. The mechanism involving the atomic ion I^+ is:

$$I^+ + HI \rightarrow H^+ + I_2^* \qquad (4.2)$$

Although this mechanism would explain the non-resonant background fluorescence because of the direct three-photon ionisation of atomic iodine it cannot explain why no fluorescence is observed when exciting the ion-pair levels of HI or the $9p^4D^o_{7/2}$ state of atomic iodine. The other iodine containing ion which is present is the HI^+ molecular ion but it will also be produced by the excitation of both the ion-pair and Rydberg states of HI. Therefore only the neutral mechanism appears to be capable of explaining the origin of the $D' \rightarrow A'$ and $D \rightarrow X$ bands in the spectra.

Chapter 5
Simulation and Fitting Techniques

One of the central aspects of the work described in this thesis was the comparison of experimental observations with the predictions from theoretical models. The models were refined to improve the fit of simulated spectra and calculated energy levels and molecular constants. Of great importance in these calculations is the determination of accurate potential energy curves to describe the electronic states.

5.1 Potential Energy Curves

A number of numerical methods have been developed to determine potential energy curves with an analytic form from spectroscopic data. The Morse and Dunham potentials are two forms which have achieved wide acceptance [48] [88] [89] [90]. The coefficients of these curves are determined from the vibrational and rotational constants of the electronic state. The range of internuclear separations, R, over which such potentials are valid is limited to the region near the equilibrium separation, R_e. Ogilvie [59] has developed a variation of the Dunham potential which may be used over a much wider range of R. However, although analytical potential functions offer many advantages in terms of computational speed [91], their use in this thesis is limited to states in which only a few vibrational levels have been observed.

The first order semiclassical inversion technique of Rydberg Klein and Rees [90] [92] is a more widely applicable technique which does not assume a particular form for the potential energy curve. But, it is limited to unperturbed energy levels. In the RKR method the vibrational and rotational energy level spacing is used to determine the classical turning points of each energy level. The potential energy curves are constructed by interpolating between the RKR turning points. Because the RKR method is a semiclassical technique, the curves generated by it do not exactly reproduce the observed energy levels in quantum calculations. However, for states with long, regular vibrational and rotational progressions the agreement is often very good.

An improved fitting of observed levels can be produced by extending the RKR method to second order or by subjecting the RKR potential energy curve to an Inverse Perturbational Analysis (IPA) [93] [94]. This latter technique adjusts the potential with small perturbing functions. The coefficients of the perturbations are tuned in a least mean square manner to reduce the differences between observed and calculated energy levels.

In the case of the hydrogen halides the above techniques are of limited use. The gross perturbations present in the spectra of the ion-pair state and the Rydberg states to which it is coupled prevent the use of the RKR method for HBr and HI, although it can be used for the lowest vibrational levels in HCl [16] [40] [41] and HF [4] [21] which are unperturbed. Because of the short vibrational progressions observed in the unperturbed Rydberg states only a few RKR turning points can be determined and these cannot accurately reproduce the observed energy levels. Rather analytical potential energy curves must be used which are adequate for only the lowest vibrational levels. However, the ground state of HCl is well known and extensive vibrational and rotational progressions have been observed in the ground states of HBr [67] and HI [68] (see Table 2.1 in Chapter 2).

5.1.1 Ground Electronic State

Hydrogen Chloride

The ground state potential energy curve for the four isotopomers of HCl have been fully analysed by Coxon and co-workers [95] in a series of recent papers. The potential energy curves were determine by a second order RKR technique and refined by the IPA method. The curve defined in reference [40] has been used throughout this work, but extended to large R with a dispersion curve. At small R a Born repulsive term [96] [97] was used. This has the form:

$$V(R) = C + AR^{-n} \tag{5.1}$$

where $9 \leqq n \leqq 15$ and C and A are chosen to fit smoothly onto the known potential energy curve. The calculated energy levels near dissociation are fairly insensitive to the choice of n within this range. Also the wavefunctions of the continuum levels only undergo a small phase shift as n is varied. The greatest effect would be noticed for the highest energy levels which have the smallest wavelength and experience the greatest variation in the repulsive wall. In these calculations the highest energy level is at 15000 cm^{-1} above dissociation . At this energy the shift in the potential curve between $n=9$ and $n=15$ is 0.02 Å which is small compared to the asymptotic wavelength. A value of $n=13$ has been used.

The tabulated HCl ground state potential energy curve covers the range $0.7 \text{ Å} \leqq R \leqq 7.5 \text{ Å}$ which is sufficient for the accurate calculation of the bound and continuum wavefunctions in the energy range of interest. The calculated

Table 5.1a Observed and Calculated Energy Levels of the Ground State of HCl

v'	G_v / cm^{-1}		B_v / cm^{-1}	
	Calculated[1]	Literature[2]	Calculated[3]	Literature[1]
0	1483.29	1483.88	10.457	10.440
1	4369.61	4369.86	10.153	10.136
2	7151.50	7151.86	9.851	9.834
3	9829.67	9830.66	9.552	9.535
4	12404.93	12406.71	9.253	9.236
5	14878.24	14880.15	8.952	8.937
6	17249.18	17250.73	8.650	8.637
7	19517.09	19517.75	8.345	8.335
8	21680.63	21680.00	8.036	8.029
9	23737.39	23735.54	7.723	7.717
10	25684.55	25681.61	7.401	7.396
11	27518.46	27514.56	7.068	7.064
12	29234.26	29229.64	6.718	6.714
13	30825.50	30820.32	6.346	6.344
14	32283.78	32278.11	5.944	5.945
15	33598.22	33592.39	5.502	5.503
16	34753.71	34747.88	5.000	5.006
17	35730.46	35725.02	4.413	4.419

---

[1] Calculated to within 0.1 cm^{-1} by bisection as discussed in text

[2] References [40] and [41], uncertainty in G_v < 0.01 cm^{-1} and B_v < 0.001 cm^{-1}.

[3] Calculated from the difference in G_v values for J = 0 and J = 1

Table 5.1b Observed and Calculated Energy Levels of the Ground State of DCl

v'	G_V / cm^{-1}	B_V / cm^{-1}		
	Calculated	Literature[1]	Calculated	Literature[1]
0	1066.02	1066.60	5.381	5.392
1	3157.34	3157.66	5.288	5.280
2	5195.11	5193.03	5.177	5.168
3	7178.71	7179.05	5.066	5.057
4	9109.03	9109.99	4.956	4.946
5	10986.40	10988.03	4.846	4.836
6	12811.08	12813.25	4.735	4.726
7	14583.59	14585.68	4.624	4.616
8	16303.64	16305.20	4.512	4.506
9	17970.96	17971.62	4.400	4.395
10	19584.95	19584.59	4.288	4.284
11	21145.06	21143.62	4.175	4.169
12	22650.53	22648.05	4.060	4.055
13	24100.42	24097.07	3.944	3.939
14	25493.64	25489.41	3.825	3.821
15	26828.82	26823.89	3.704	3.699
16	28104.35	28098.70	3.578	3.574
17	29318.14	29311.77	3.448	3.445
18	30467.68	30460.84	3.312	3.309
19	31549.93	31542.57	3.169	3.165
20	32561.46	32553.63	3.017	3.015
21	33497.71	33489.22	2.852	2.850
22	34352.87	34344.20	2.673	2.672
23	35120.62	35111.95	2.475	2.470

See notes for Table 5.1a

[1] References [4] and [20]

energy levels and B_v values are compared with the experimentally determined values in table 5.1.

Hydrogen Bromide and Hydrogen Iodide

There is much less experimental information available for the ground states of these two molecules than for HCl. Primarily this is due to the lack of progress on the analysis of the discharge emission spectra of HBr and HI from which it is possible to determine the energy levels near dissociation. Therefore the potential energy curves can only be determined directly from experimental data over a short range of R near R_e.

However, all of the members of this isovalent series of molecules should have similar ground state potential energy curves. Approximate potential energy curves for HBr and HI can therefore be determined by scaling the well known HCl curve to fit the observed HBr and HI molecular constants [98] [99] [100]. To preserve the correct curvature near R_e a harmonic oscillator scaling function is used to reduce the HCl potential energy curve to a dimensionless form. The reduced variables V^* and ε are defined as:

$$V^* = \frac{V}{D_e} \qquad V^* = \frac{1}{2} x^2$$

$$\xi = \sqrt{\frac{D_e}{k}} \tag{5.2}$$

$$x = \left(\frac{r - r_e}{\xi}\right)$$

where k is the force constant of the harmonic oscillator with frequency ω_e. The dimensionless curve is re-scaled with the molecular constants of HBr and HI. A

Table 5.2 Observed and Calculated Energy Levels of the Ground State of HBr and HI

v'	G_v / cm^{-1}		B_v / cm^{-1}	
	Calculated	Literature	Calculated	Literature
HBr				
0	1313.37	1312.75[1]	8.348	8.348[1]
1	3872.66	3870.28	8.113	8.117
2	6341.60	6337.38	7.881	7.885
3	8721.69	8714.14	7.626	7.654
4	11013.64	11000.45	7.399	7.422
5	13220.08	13196.06	7.136	7.188
6	15341.11	15300.53	6.853	6.951
7	17375.67	17313.24	6.557	6.710
HI				
0	1144.32	1144.59[2]	6.434	6.426[2]
1	3374.52	3374.17	6.263	6.255
2	5524.95	5523.81	6.078	6.083
3	7595.93	7592.62	5.920	5.909
4	9587.73	9579.30	5.716	5.732
5	11501.15	11482.06	5.521	5.551
6	13334.94	13298.58	5.310	5.365
7	15086.27	15025.72	5.066	5.173
HI *ab initio* Potential[3]				
0	1143.37		6.447	
1	3367.81		6.270	
2	5509.37		6.095	
3	7567.26		5.917	
4	9538.39		5.736	
5	11422.47		5.552	
6	13217.46		5.361	
7	14921.24		5.165	
8	16530.32		4.960	
9	18040.87		4.746	
10	19447.62		4.516	
11	20744.39		4.271	
12	21924.30		4.003	
13	22976.83		3.703	
14	23889.45		3.364	
15	24648.41		2.970	

See notes to Table 5.1

[1] Reference [67]

[2] Reference [68]

[3] Potential energy curve from reference [47]

comparison of the energy levels calculated from the re-scaled curves with those of a curve produced by the RKR method and the observed levels is shown in table 5.2 [67] [68].

The RKR curves accurately reproduce the observed energy levels but cover only a small range of R. Therefore the re-scaled curves are joined smoothly onto the RKR curves to ensure that they have the correct behaviour over a sufficiently wide range of R.

5.1.2 Dissociative Valence States

Potential energy curves for the dissociative valence states of the hydrogen halides have been determined by both *ab initio* [42] [37] [66] [47] methods and from the analysis of experimental spectra [25] [64]. The molecules HCl and HI have received the greatest attention. The former because it is small enough for accurate *ab initio* calculations and the later because of its importance in the production of translationally hot atomic hydrogen. The study of the dissociative valence states of HBr has been limited to a brief analysis of the photoabsorption spectrum.

The potential energy curve of the $A^1\Pi$ state of HCl and the transition dipole moment functions, $\mu_{el}(R)$, for transitions between this and a number of other states have been calculated by Dalgarno et al [37]. The observed spectrum is well reproduced by these calculated curves. However, it is also possible to reproduce the absorption observed spectrum with the *ab initio* curve of Peyerimhoff using a constant value of $\mu_{el}(R)$. Simulated absorption spectra using both curves are presented in figure 5.1. There is too little information available in the continuum

Figure 5.1 Simulated Absorption Spectrum for HCl $A^1\Pi \leftarrow X^1\Sigma^+$

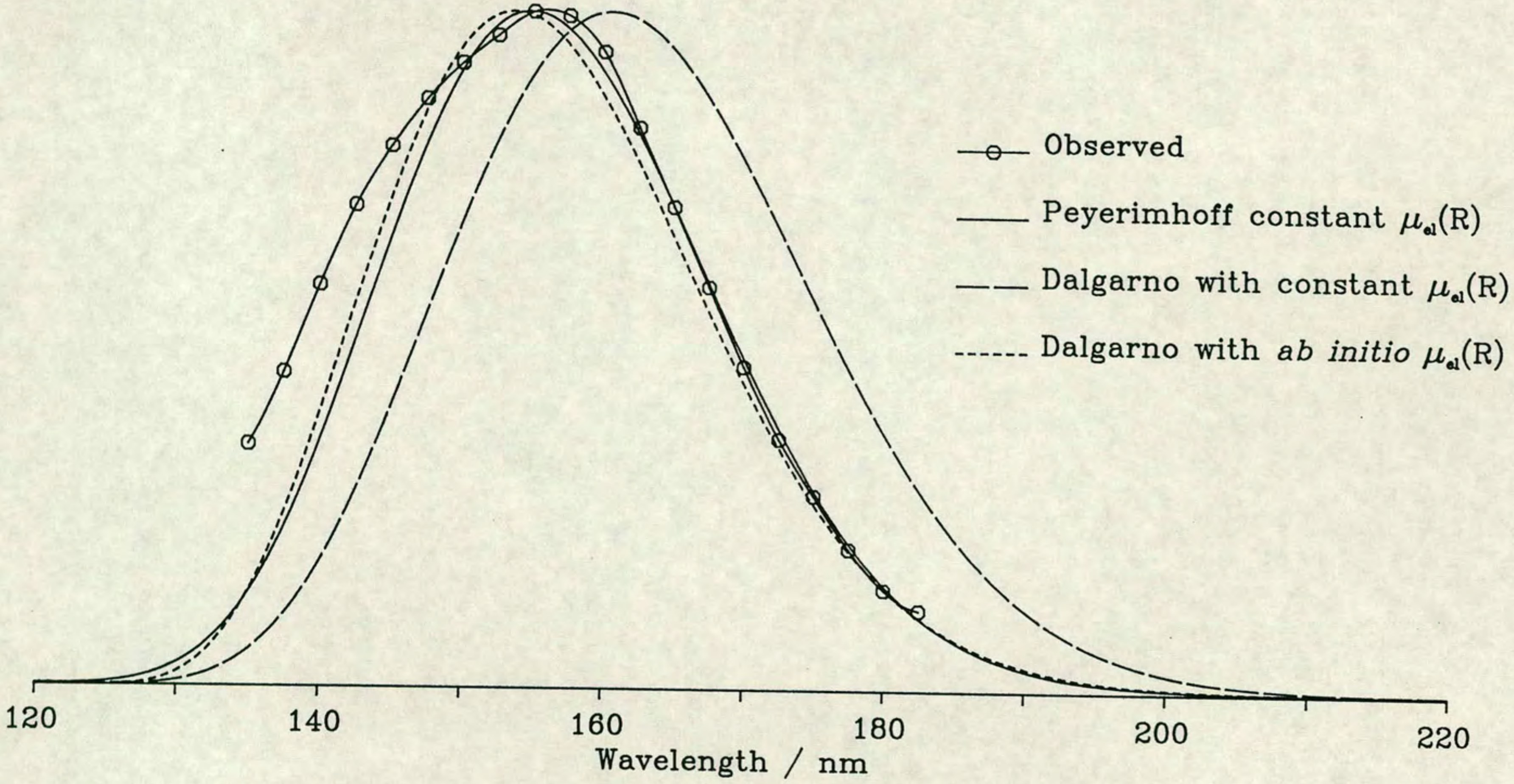

absorption spectrum to determine which curve is the most appropriate and both have been used in the simulation of dispersed fluorescence spectra.

Ab initio curves have also been determined for HI [47]. However, there have been no calculations of transition dipole moment functions for this molecule. The experimental analysis of the continuum spectrum of HI has used the δ-function method which compares the probability distribution in the ground state with the intensity of the absorption spectrum as a function of wavelength [64]. But, in HI the analysis is further complicated because there are three dissociative valence states which may contribute to photo-dissociation. The $A^1\Pi$, $a^3\Pi_1(1)$, and $a^3\Pi_0{}^+(0^+)$ states all have strongly allowed transitions from the ground electronic state [56] [57] [58]. Of these, however, only the $a^3\Pi_0{}^+(0^+)$ state dissociates to yield spin-orbit excited iodine (I^*). Clear et al [25] included the I^*/I ratio in a non-linear least squares fit to the observed photo-dissociation spectrum. From this additional information they were able to determine potentials for each of the repulsive states.

5.1.3 Rydberg States

Potential energy curves of the Rydberg states were required for the simulation of the observed fluorescence spectra of HCl, DCl and HI. They were also necessary for calculations of the vibronic coupling of the Rydberg states with the ion-pair state. Only short vibrational progressions of the Rydberg states of the hydrogen halides have been observed, generally only $v' = 0$ and 1 but higher levels have been seen for a few states. The longest vibrational progression was observed for the lowest lying Rydberg states, $b^3\Pi$ and $C^1\Pi$ (1). For the

Figure 5.2
Potential Energy Curves of The Rydberg States of HCl

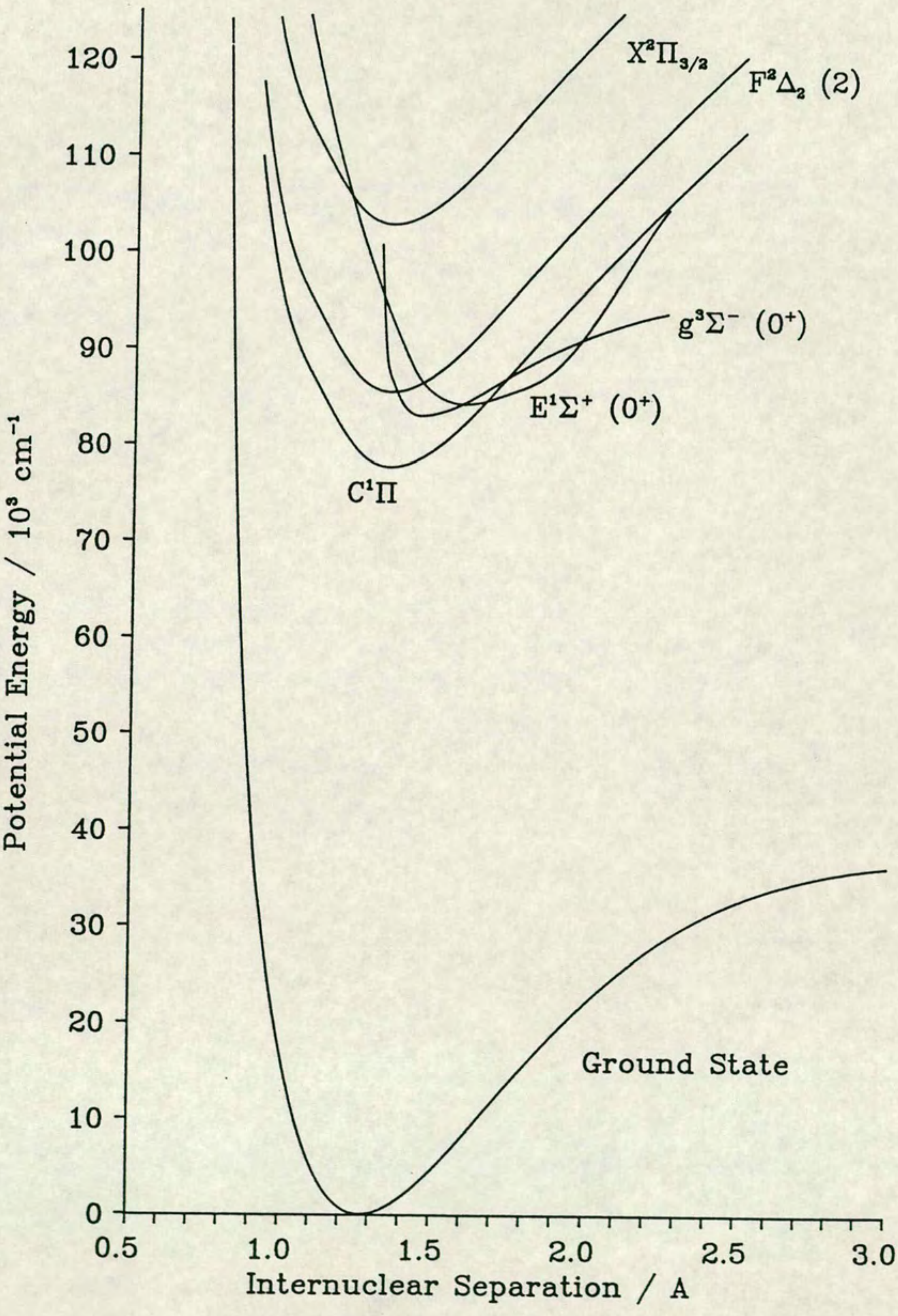

$C^1\Pi$ (1) state v' =0 to 4 have been observed in both HCl and DCl. Although the higher levels are weak and diffuse, the calculated molecular constants can be used to determine RKR turning points. A single RKR curve, derived from either the HCl or DCl data, provides a good fit to both HCl and DCl vibrational energy levels and B_v values. In the case of the $F^1\Delta_2$ (2) Rydberg state the three lowest vibrational levels were observed in DCl and a Morse oscillator curve was used rather than an RKR analysis. Both ω_e and $\omega_e x_e$ were calculated from the vibrational spacing measured in (2+1)REMPI spectra [24]. D_e is given by the formula:

$$D_e = \frac{\omega_e^2}{4\omega_e x_e} \tag{5.3}$$

and R_e was adjusted to give the correct value of B_v for the observed levels. The calculated and observed energy levels are presented in table 5.3.

No such simple procedure could be used for the $g^3\Sigma^-$ (0^+) and $E^1\Sigma^+$ (0^+) coupled Rydberg states. In HCl a single level has been assigned as v' =2 [12] [24] for both states because it was not possible to clearly identify to which vibrational progression it belonged. For DCl only v' =0 of the $g^3\Sigma^-$ (0^+) state has been observed but v' =0, 1 and 2 of the $E^1\Sigma^+$ (0^+) state are seen in (2+1)REMPI spectroscopy [24]. Although the states are perturbed by the ion-pair state interaction the RKR turning points were calculated for HCl. These were then altered to improve the fit to the observed levels. The curves which were developed in this manner are shown in figure 5.2. They show little resemblance to either the ground state of HCl or of HCl^+, the limit to which the Rydberg states converge. Although they achieve some success in fitting the

Table 5.3 Calculated Energy Levels of the Rydberg States of HCl

Vibrational Energy Levels / cm $^{-1}$

v'	$X^1\Sigma^+$	$C^1\Pi$ (1) Observed[1]	Calculated	$F^1\Delta_2$ (2)	$X^2\Pi_{3/2}$ [2]
0	1483.88	1395.8	1395.81	1301.22	1323.79
1	4369.86	4079.8	4096.29	3817.40	3892.40
2	7151.86	6635.0	6664.61	6218.58	6355.82
3	9830.66	9055.0	9098.72	8504.13	8714.06
4	12406.71	11390.5	11408.35	10675.13	10967.15

Rotational Constants / cm $^{-1}$

v'	$X^1\Sigma^+$	$C^1\Pi$ (1) Observed[1]	Calculated	$F^1\Delta_2$ (2)	$X^2\Pi_{3/2}$ [2]
0	10.440	9.333	9.373	10.035	9.823
1	10.136	9.296	9.183	9.705	9.528
2	9.834	9.0	9.097	9.372	9.234
3	9.535		9.083	9.034	8.936
4	9.236		9.059	8.691	8.633

Constants for HCl Morse Oscillator Potentials

	$X^1\Sigma^+$	$C^1\Pi$ (1) Observed[1]	Calculated	$F^1\Delta_2$ (2)	$X^2\Pi_{3/2}$ [2]
D_e	37243 [3]		30888	30095	39230.5
ω_e	2990.95		2812	2631	2673.7
$\omega_e x_e$	52.82		64	57.5	52.6
R_e	1.275		1.348	1.300	1.315

See notes on Table 5.1

[1] Reference [5]

[2] Reference [101]

[3] References [40] and [48]

observed data for the Rydberg states these curves can provide no further information on the vibronic coupling of the Rydberg and ion-pair states. The characteristic ion-pair type fluorescence which is observed from both these Rydberg states cannot be reproduced with these curves unless they are used in coupling calculation with the ion-pair state. However, they are not appropriate for coupling calculations in either the adiabatic or the diabatic representation. In the former the v' =0 level of the $E^1\Sigma^+$ (0^+) state is the first level of the inner minimum of the double minimum $B^1\Sigma^+$ (0^+) curve. For the diabatic case the Rydberg states should be free of any coupling. It is therefore more appropriate to use a curve such as that determined for the 'pure' Rydberg $F^1\Delta_2$ (2) state or the limiting molecular ion ground state curve.

All of the observed Rydberg states have a ($\sigma^2\pi^3$) ion core which is the configuration of the electronic ground state of the molecular ion, HX^+. An accurate Morse potential energy curve has been determined experimentally for the $X^2\Pi_{3/2}$ ground state of HCl^+ [101]. It is very similar to the RKR curve derived for the $C^1\Pi$ (1) and $F^1\Delta_2$ (2) Rydberg states with which it is compared in figure 5.2. The energy level spacings of the two curves are shown in table 5.4 for both HCl and DCl. The Morse oscillator curve for the ground state of the molecular ion has therefore been used to represent the Rydberg states of HCl and DCl if no more accurate representation was available.

5.1.4 Ion-pair States

A considerable degree of experimental information has been obtained for the ion-pair state in HCl and DCl [11-16]. For both of these molecules the lowest

Table 5.4 Vibrational Spacings and Rotational Constants of the Coupled Rydberg States of HCl and DCl

	$X^1\Sigma^+$	$E^1\Sigma^+$ (0^+)		$g^3\Sigma^-$ (0^+)		$X^2\Pi_{3/2}$
		Observed	Calc.	Observed	Calc.	
HCl						
ΔG_{2-1}	2885.98[1]	2138.5[2]	2140.4	2707.3[2]	2734.3	2568.5[3]
ΔG_{3-2}	2782.00	2226.3	2222.5	2352.0	2398.2	2463.3
B_0	10.440	6.642	6.629	7.633	7.635	9.823
B_1	10.136	6.331	6.330	8.12	6.919	9.528
B_2	9.834	6.3	6.275	6.3	6.250	9.234
DCl						
ΔG_{2-1}	2091.1[4]	1187.9[2]	1544.7	[2]	2011.1	1870.1[5]
ΔG_{3-2}	2035.4	1680.1	1522.4		1877.9	1823.9
B_0	5.392	3.296	3.432	4.4	3.971	5.093
B_1	5.280	3.855	3.292		3.748	4.986
B_2	5.168	3.7	3.247		3.521	4.891

---

[1] Reference [40]

[2] References [4], [12] and [19]

[3] Reference [101]

[4] Reference [20]

[5] Calculated From Morse Oscillator potential for HCl^+ [101]

energy vibrational levels have been observed in emission spectra. Classical turning points for the observed levels have been determined by the RKR method and T_e and R_e values determined. In contrast, very little is known about the ion-pair state in HBr and HI. Also there have been several detailed *ab initio* calculations of the electronic structure of the excited electronic states of HCl [42] [37] [66] [43] [44] [45] but none for either HBr or HI. Therefore, while the potential energy curves determined for HCl and DCl are based on a great deal of experimental evidence the curves for HBr and HI have few experimental or theoretical constraints, other than the coulombic attraction which should dominate at large R. Because of the dearth of information on HBr and HI the potential curves determined for the ion-pair state in these molecules are less reliable than for HCl and DCl.

A potential energy curve for the lowest 6 vibrational levels of HCl (8 for DCl) is generated by smoothly interpolating between the RKR turning points. A much wider curve, extending from the potential minimum to near the dissociation limit, is required for the calculations in this work. Also, the curve must conform to the appropriate representation for the coupling scheme which is to be used [54]. Thus a diabatic curve will have a single minimum while a curve in the adiabatic representation will have an additional, inner minimum because of the interaction with the $E^1\Sigma^+$ (0^+) Rydberg state. Potential energy curves were developed in both representations.

There are several methods which may be used to generate a potential curve for the ion-pair state based on the experimental and theoretical data: the *ab initio* potential curves can be adapted to fit the observed data, an analytical function

Table 5.5 Calculated Energy Levels and Rotational Constants from *ab initio* Potential in HCl

v'	G_v / cm $^{-1}$			B_v / cm^{-1}		
	Single Minimum	Double Minimum	Observed	Single Minimum	Double Minimum	Observed
0	407.81	407.81	431.1	2.802	2.800	2.740
1	1253.21	1253.23	1276.6	2.825	2.819	2.765
2	2097.33	2097.39	2091.0	2.801	2.791	2.792
3	2886.13	2886.50	2875.0	2.881	2.878	2.832
4	3630.26	3632.39	3631.0	2.949	2.937	2.874
5	4344.67	4352.55	4360.6	2.962	2.925	2.921
6	5051.56	5075.96	5065.0	3.050	2.936	2.968
7	5657.20	5804.66	5746.5	7.274	2.931	3.046
8	5787.21	6156.26	6402.6	3.844	9.905	3.156
9	7566.55	6526.56	7016.8	4.591	2.904	3.682
10	8057.56	7237.26	7610.8	4.743	2.876	4.808
11	8595.06	7933.81	7957.0	3.985	2.844	6.642
12	9190.64	8614.75	8384.4	3.550	2.810	4.301
13	9796.60	9127.11	8923.6	3.521	9.651	4.012
14	10379.43	9282.21	9454.3	3.757	2.777	4.270
15	10930.55	9936.41	9849.6	3.925	2.740	5.877
16	11475.96	10577.60	10095.5	3.695	2.704	6.331
17	12038.08	11205.99	10582.4	3.354	2.667	3.809
18	12609.16	11700.78	11108.6	3.164	9.280	3.756
19		11821.62	11641.2		2.630	3.591
20		12424.87	12144.3		2.592	4.335
21			12321.8			6.3

can be fit through the RKR points and the coulomb potential, or a purely empirical potential can be used. This latter form was found to be the most appropriate. *Ab initio* potential energy curves for HCl have not yet reached the level of accuracy at which they can be used. The calculated energy levels of an *ab initio* potential recently determined for the ion-pair state of HCl [37] [66] are shown in table 5.5 along with experimental values. There is some agreement with the experimental results but much closer agreement can be obtained by a small adjustment of the potential.

Analytical functions, as used for the Rydberg and repulsive valence states, can be used to generate ion-pair state curves in the diabatic representation. A Morse oscillator function provides a good fit to the lowest energy levels of the ion-pair state but the dissociation energy of this curve is one quarter of that observed experimentally. An alternative function is that proposed by Rittner which been used with good effect to represent the ion-pair states of the halogens and inter-halogens [102]. It has the form:

$$V(R) = A\exp(-R\beta) - \frac{e^2}{4\pi\varepsilon_0 R} - \frac{1}{2}\frac{\alpha_{Cl^-} \cdot e^2}{4\pi\varepsilon_0 R^4} \qquad (5.4)$$

where the final two terms describe the ionic attraction and the leading term is a repulsion term. Although this would appear to be an appropriate form for the potential energy curve of an ion-pair state it provides very poor results for the hydrogen halides. This is illustrated in figure 5.3 with a Rittner curve which is a good fit to the RKR points but which tends to negative infinity at small R. If the repulsive term is strengthened and the potential energy constrained to increase for all R less than R_e then the potential energy curve becomes much more

Figure 5.3
Rittner Function Potenials for the Ion–pair State of HCl

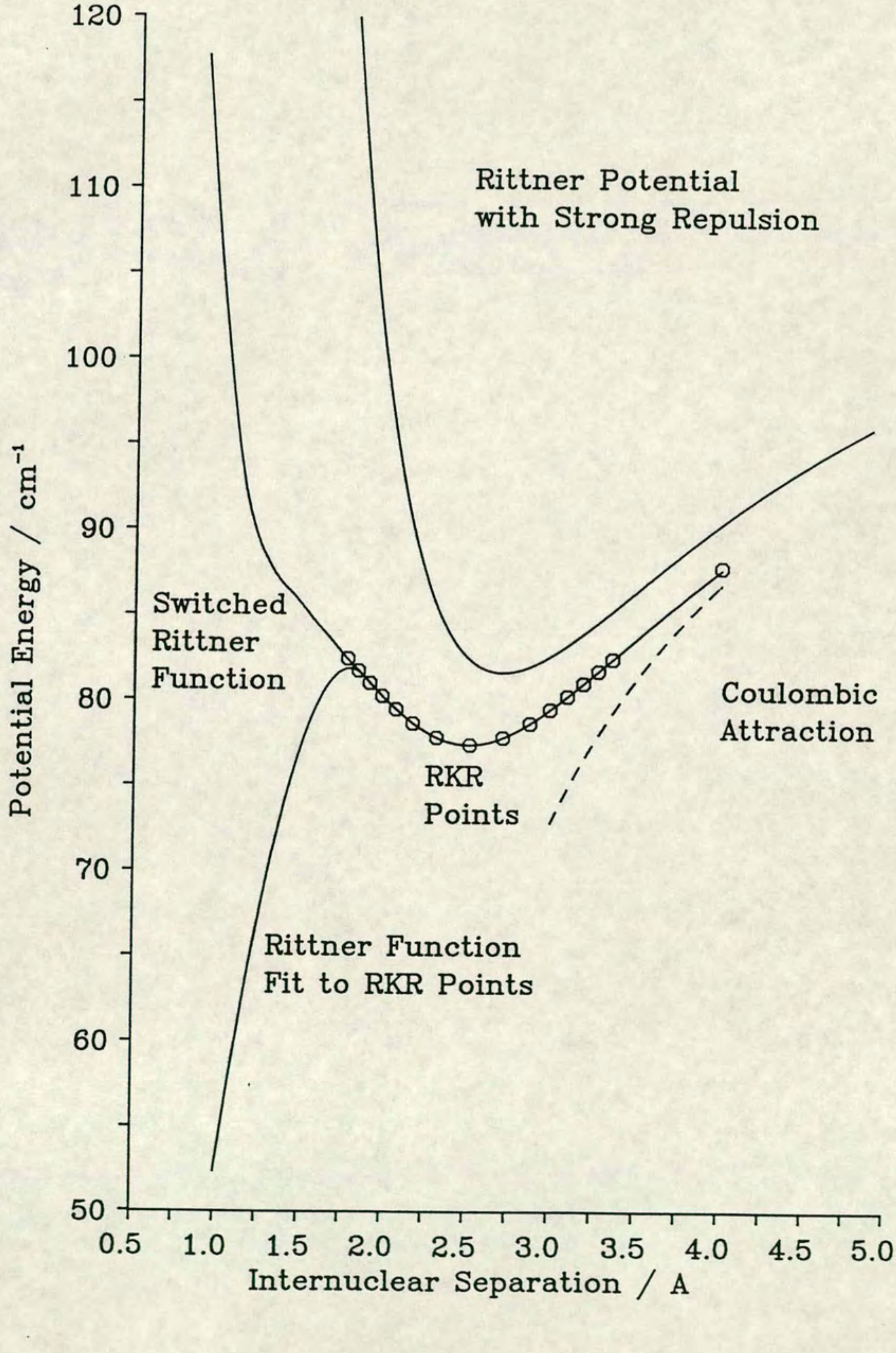

shallow and T_e is forced to higher energy. A much improved fit, over the whole range of R, is achieved if a switching term is included to reduce the effect of the coulombic term at small R. The modified Rittner function for the hydrogen halides has the form:

$$\begin{aligned} V(R) &= \frac{1}{2}\left(1+\tanh\left(\beta(R_c-R)\right)\right)\left(A\exp\left(-R\beta\right)\right) \\ &- \frac{1}{2}\left(1+\tanh\left(\beta(R-R_c)\right)\right)\left(\frac{e^2}{4\pi\varepsilon_0 R} - \frac{1}{2}\frac{\alpha_{Cl^-} e^2}{4\pi\varepsilon_0 R^4}\right) \end{aligned} \tag{5.5}$$

This curve fits the observed RKR points and the coulombic limb and also has the correct behaviour at short R to reproduce the average vibrational energy spacing in the ion-pair state. Although this analytical form gives a good approximation to the data it is rather inflexible. Similar results can be obtained with an empirical curve, defined by a set of knot points including the RKR points, a number of points on the coulombic limb and a few points to define the repulsive limb. The benefit of this curve over the modified Rittner function is that the repulsive limb can be varied independently of the other regions of the potential.

Several potential energy curves of this type were developed, in the diabatic representation, for both HCl and DCl and are shown in figure 5.4. Only the points on the repulsive limb were altered in the trial and error fitting of the calculated energy levels to the observed values. While it was possible to adjust the points on the attractive limb they were constrained by the coulombic term and so could not be varied much from their calculated positions. Also, moving these points by even quite significant amounts had little effect. The observed

Figure 5.4 Potential Energy Curves for the Ion-pair State of HCl

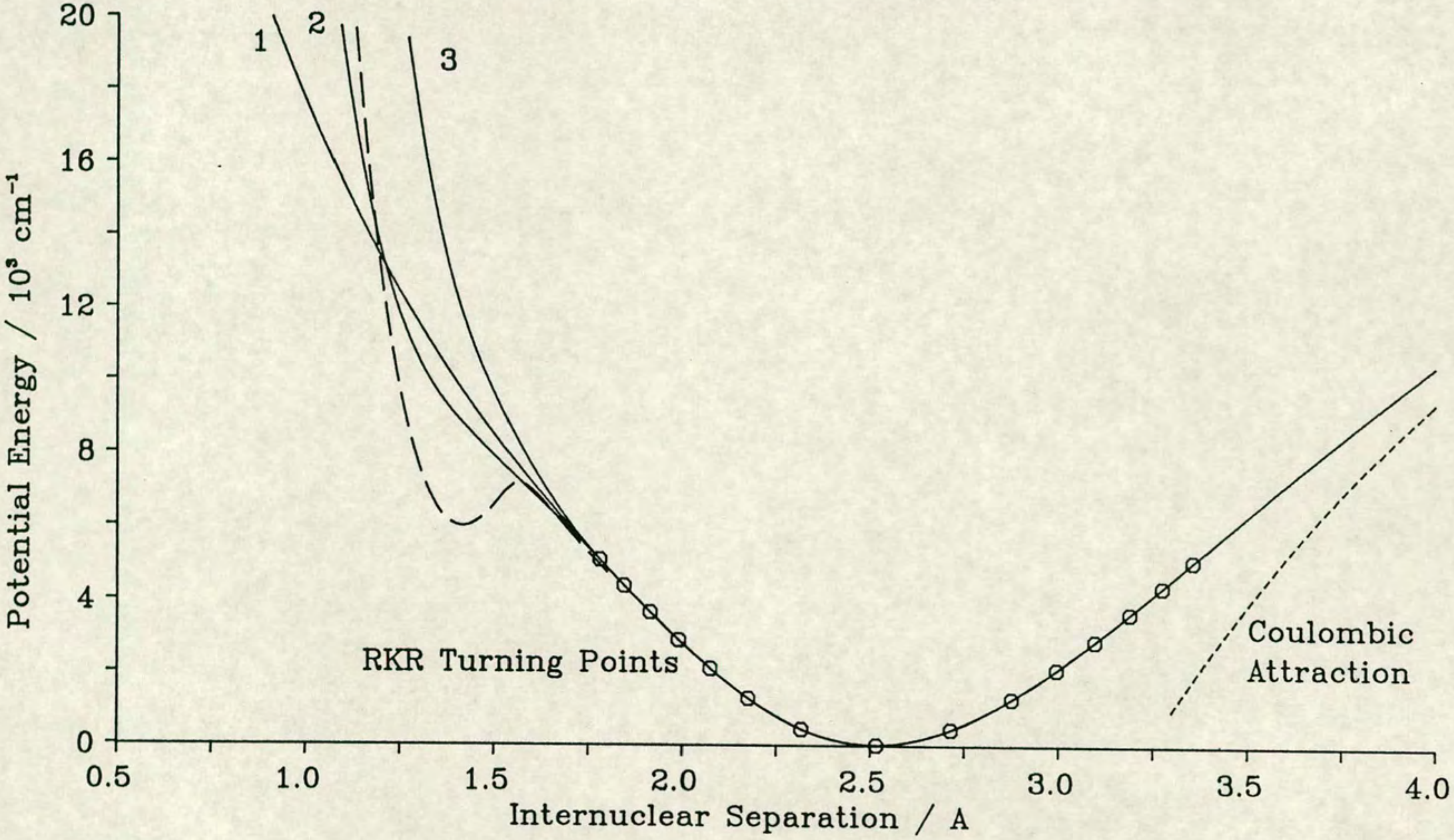

energy levels used for comparison were those associated predominantly with the outer, ion-pair, potential minimum. The observed average vibrational energy level spacing in both HCl and DCl could be approximately matched using a tabulated curve with only one point on the repulsive limb other than the RKR points (curve 1 of figure 5.4). The calculated vibrational energy levels and B_v values are shown in table 5.6. The agreement between calculated and observed data is obviously best for HCl. The largest deviations from the observed values occurs at the energies at which the $E^1\Sigma^+$ (0^+) state levels are observed. The expected effect of the interaction with the Rydberg state on the ion-pair state levels is to repel the vibrational energy levels away from the perturbing levels and increase the B_v values of the nearby ion-pair levels. Therefore the repulsive limb of this curve is probably still too weak. A steeper curve would give a poorer fit to the vibrational energy levels while improving the fit of the B_v values for HCl, though not for DCl. In DCl, because of its greater reduced mass, the perturbing levels are closer together and none of the vibrational levels above $v' = 10$ are free of a strong perturbation by the Rydberg state.

An improved fit to the observed data can be achieved if more points are used on the repulsive limb (see curve 2 of figure 5.4). Two additional knot points force this curve to dip below the other curve somewhat above the energy of the first level of the $E^1\Sigma^+$ (0^+) state. This decreases the vibrational energy level spacing and increases the B_v values of a few of the levels but decreases the B_v values of the highest levels in HCl. However, the fit to the DCl data is better for this curve, giving a better overall fit. The results for this curve are also presented in table 5.6.

Table 5.6 Calculated Energy Levels and Rotational Constants of the Ion-pair State of HCl and DCl

Vibrational Energy Levels of HCl

v'[1]	Observed	Curve 1	Curve 2	Curve 3	Adiabatic Curve
0	431.2	431.4	431.4	431.4	431.1
1	1276.6	1276.8	1276.8	1276.8	1276.5
2	2091.0	2091.0	2091.0	2091.0	2091.0
3	2875.0	2875.5	2875.5	2875.6	2875.0
4	3631.0	3631.6	3631.5	3631.7	3630.2
5	4360.6	4361.5	4361.0	4361.9	4359.6
6	5065.0	5066.8	5064.9	5068.3	5065.0
7	5746.5	5749.6	5743.7	5754.5	5747.0
8	6402.6	6412.3	6397.3	6424.7	6406.4
9	7016.5	7057.6	7026.7	7083.6	7043.2
10	7610.8	7688.0	7635.0	7734.5	7618.9
11	7957.0				7946.7[2]
12	8384.4	8304.7	8227.1	8378.3	8394.0
13	8923.6	8908.8	8807.4	9014.8	8966.9
14	9454.3	9501.1	9378.6	9643.4	9523.2
15	9849.6	10082.2	9943.1	10263.6	10048.3
16	10095.5				
17	10582.4	10652.2	10503.4	10874.7	10568.3
18	11108.6	11211.3	11060.4	11476.0	11103.2
19	11641.2	11759.7	11613.5	12067.2	11644.6
20	12144.3	12297.5	12161.9	12647.7	12180.6
21	12321.8				
22	12742.2	12824.9	12704.9	13217.4	12706.9
23	13263.6	13342.0	13241.4	13776.1	13225.1
24	13784.6	13849.1	13770.6		13737.7

See notes to Table 5.7

[1] Vibrational numbering scheme includes levels of the $E^1\Sigma^+(0^+)$ Rydberg state.

[2] One additional minimum in the potential energy curve which gives one additional vibrational level

Rotational Constants for HCl

v'	Observed	Curve 1	Curve 2	Curve 3	Adiabatic Curve
0	2.740	2.762	2.744	2.744	2.743
1	2.765	2.762	2.768	2.773	2.760
2	2.792	2.795	2.798	2.806	2.782
3	2.832	2.835	2.840	2.835	2.833
4	2.874	2.878	2.878	2.877	2.872
5	2.921	2.926	2.930	2.924	2.921
6	2.968	2.980	2.990	2.972	2.973
7	3.046	3.035	3.065	3.011	3.030
8	3.156	3.089	3.157	3.034	3.092
9	3.682	3.140	3.262	3.037	3.229
10	4.808	3.188	3.365	3.024	4.377
11	6.642				6.635
12	4.301	3.232	3.449	3.000	3.944
13	4.012	3.272	3.511	2.972	3.659
14	4.270	3.309	3.548	2.938	3.918
15	5.877	3.341	3.551	2.899	4.148
16	6.330				
17	3.809	3.369	3.519	2.855	4.003
18	3.756	3.392	3.464	2.807	3.744
19	3.591	3.411	3.399	2.757	3.609
20	4.335	3.427	3.327	2.704	3.572
21	6.3				
22	3.790	3.440	3.253	2.650	3.548
23	3.282	3.449	3.181	2.595	3.483
24	3.298	3.456	3.111		3.385

Vibrational Energy Levels of DCl

v'	Observed	Curve 1	Curve 2	Curve 3	Adiabatic Curve
0	310.6	311.1	311.1	311.1	310.8
1	923.2	923.9	923.9	923.9	923.4
2	1519.3	1520.1	1520.1	1520.1	1520.0
3	2099.3	2100.8	2100.8	2100.8	2100.8
4	2663.9	2665.9	2665.9	2665.6	2665.5
5	3213.8	3216.3	3216.3	3216.3	3215.1
6	3749.5	3752.6	3752.6	3752.6	3750.9
7	4272.1	4275.5	4275.3	4275.6	4273.9
8		4785.6	4785.0	4786.1	4784.4
9		5283.6	5281.8	5285.0	5281.9
10		5770.4	5765.4	5774.0	5766.9
11		6246.9	6235.7	6255.2	6241.8
12	6702.0	6714.4	6693.0	6730.6	6708.7
13	7149.2	7173.6	7138.3	7201.5	7165.3
14	7498.9	7625.3	7573.8	7668.4	7563.0
15	7704.7				7713.1
16	8058.0	8069.8	8001.1	8131.5	8090.9
17	8423.7	8507.7	8421.1	8590.9	8503.4
18	8712.1	8939.3	8835.0	9046.3	8877.7
19	8891.6				
20	9239.6	9364.9	9244.2	9497.7	9227.0
21	9602.6	9784.6	9650.2	9944.8	9598.6
22	9979.3	10198.6	10053.7	10387.4	9989.4
23	10347.0	10606.9	10455.4	10825.2	10380.1
24	10571.8			10855.7	10764.8

Rotational Constants for DCl

v'	Observed	Curve 1	Curve 2	Curve 3	Adiabatic Curve
0	1.408	1.410	1.416	1.410	1.410
1	1.417	1.418	1.418	1.418	1.417
2	1.426	1.416	1.428	1.416	1.427
3	1.438	1.439	1.447	1.439	1.429
4	1.452	1.453	1.459	1.453	1.451
5	1.467	1.467	1.467	1.467	1.467
6	1.484	1.484	1.484	1.484	1.482
7	1.501	1.502	1.503	1.502	1.499
8		1.522	1.524	1.520	1.519
9		1.542	1.548	1.538	1.541
10		1.563	1.577	1.552	1.560
11		1.582	1.612	1.560	1.575
12	1.82	1.602	1.652	1.563	1.592
13	2.20	1.620	1.691	1.561	1.648
14	2.86	1.637	1.726	1.556	2.861
15	3.296				3.257
16	2.17	1.654	1.760	1.548	1.832
17	2.41	1.670	1.791	1.539	1.950
18	3.25	1.685	1.815	1.528	2.266
19	3.855				
20	2.22	1.698	1.829	1.516	2.297
21	2.14	1.711	1.833	1.502	2.075
22	2.09	1.722	1.828	1.487	1.976
23	2.28	1.732	1.813	1.471	1.982
24	3.7		1.791		1.992

While both diabatic curves give an acceptable fit to the observed data neither is a good representation of an unperturbed ion-pair state. One effect of the interaction of the ion-pair state with the Rydberg states is the reduction of the average vibrational spacing in the ion-pair state. As a result of this the repulsive limb of both potential energy curves is too weak. This can be most clearly seen in the behaviour of B_v which constantly increases with increasing v. Although this may be valid for low v, at higher energy B_v must decrease with vibrational quantum number, v. The repulsive limb must be steeper than the very weak coulombic limb. This causes a decrease in $\langle \psi | R^{-2} | \psi \rangle$ and hence in B_v. Curve 2 in figure 5.4 does become steeper at small R but only with the introduction of a kink. An accurate, purely diabatic curve for the ion-pair state would have to be much steeper than either of the two curves above and hence would not be able to fit most of the available data for HCl and DCl. Such a curve is shown as curve 3 in figure 5.4.

An adiabatic, double minimum potential curve for the ion-pair state of HCl and DCl was produced in a similar manner but using the repulsive limb of Peyerimhoff's curve as a starting point. Trial and error fitting of the repulsive limb of the curve improved the fit to the observed data which also included energy levels from the $E^1\Sigma^+$ state. It was only possible to reproduce the lowest vibrational level of the coupled Rydberg state. An additional potential minimum is required in the ion-pair state to fit each additional level of the Rydberg state. But, it is possible to achieve a good fit to all of the ion-pair levels and $v' = 0$ of the $E^1\Sigma^+$ (0^+) state of both HCl and DCl with a single potential energy curve. The substitution of the DCl RKR points improves the fit for this molecule at lower energy levels without markedly altering the higher energy levels. The potential energy curve is shown in figure 5.4 and the calculated energy levels are compared with the observed values in table 5.6. For the perturbing level of the $E^1\Sigma^+$ (0^+) state the calculated G_v and B_v values are well represented by this double minimum curve. Close agreement is also achieved for the nearby ion-pair levels although there is still a significant error in B_V for those levels out of the range of the RKR analysis. As in the diabatic case the fit is better for HCl than for DCl. However, this curve is a good representation of the ion-pair state of HCl and DCl up to energies just above the first perturbation by the Rydberg state.

Potential energy curves for the ion-pair state in HBr and HI were produced by similar methods to those used for the diabatic curve of HCl. But, with less experimental data available the curves produced were less well constrained.

Close agreement between calculated and observed vibrational energy levels can be achieved for HBr with a double minimum empirical potential energy curve. It has a coulombic attractive limb which is smoothly joined onto a Morse potential minimum and the repulsive limb has been altered by trial and error to reproduce the observed vibrational spacing. However, there is very poor agreement with the reported B_v values, as indicated in table 5.7. Also absolute numbering of the ion-pair state vibrational progression determined from this curve is in poor agreement with observations for HF and HCl. Therefore, although it is possible to fit much of the available information the resulting curve is not an accurate representation of the ion-pair state.

Table 5.7 Energy Levels and Rotational Constants of the Ion-pair State of HBr

	G_V / cm $^{-1}$					B_V / cm $^{-1}$		
v'	Double Minimum	v'	Single Minimum	v'[2]	Observed[1]	Double Minimum	Single Minimum	Observed[1]
0	72327.6					2.56		
1	82969.5					2.58		
2	73589.3					2.55		
3	74190.8					2.57		
4	74779.1	0	74758.9			2.60	2.33	
5	75356.7	1	75325.8			2.63	2.33	
6	75924.9	2	75924.9	m	75923.0	2.68	2.37	3.4
7	76484.9	3	76537.7	m+1	76514.2	2.68	2.53	3.42
8	77037.3	4	76965.2	m+2	76962.0	2.72	3.75	4.46
9	77582.6	5	77322.6	m+3	77344.3	2.75	3.08	4.40
10	78121.2	6	77863.7	m+4	77832.0	2.79	2.97	3.9
11	78653.5	7	78382.5	m+5	78389.5	2.83	3.15	3.79
12	79179.7	8	78916.7	m+6	78941.2	2.87	3.09	3.63
13	79700.0	9	79476.8	m+7	79480.6	2.92	3.10	4.2
14	80214.5	10	80039.2	m+8	80027.0	2.96	3.15	4.86
15	80723.4	11	80605.4	m+9		3.01	3.18	
16	81226.7	12	81175.7	m+10	81197.2	3.06	3.21	3.36
17	81724.5	13	81745.9	m+11	81683.4	3.11	3.25	4.9
18	82216.8	14	82315.9	m+12	82418.0	3.17	3.26	4.0
19	82703.7	15	82885.5	m+13	82915.2	3.22	3.27	3.6

See notes to Table 5.1

[1] Reference [11]

[2] Only relative vibrational numbering known

A curve more consistent with the observations in HF and HCl and which fits the observed vibrational levels with some success is generated for HBr with a modified Morse oscillator function. However, the minimum of this curve is unconstrained by experimental data and so no unique solution could be found for the ion-pair state potential energy curve.

The degree of experimental information available for HI is similar to that for HBr but in this case it was also possible to observe dispersed fluorescence spectra from the ion-pair state. This additional information does constrain the minimum of the potential energy curve, but only within a large energy range so that once again no unique solution can be obtained. The calculated energy levels for the potential energy curve determined for the ion-pair state of HI are compared with the observed values in table 5.8. The potential used is also based on a modified Morse oscillator function with has been altered by trial and error to fit the observed energy levels and simulate the observed dispersed fluorescence spectra.

5.2 Simulation of Dispersed Fluorescence Spectra

The simulation of dispersed fluorescence spectra was an important technique in the determination of potential energy curves for the excited electronic states of the hydrogen halides. Central to this was the numerical solution of the radial Schroedinger wave equation. This topic has been discussed in detail by a number of authors [103] [104] [105] [106]. In the present case the matrix

Table 5.8 Vibrational Energy Levels and Rotational Constants for the Ion-pair State of HI

v'	G_v / cm^{-1}		B_v / cm^{-1}		v'[2]
	Calculated	Observed[1]	Calculated	Observed[1]	
0	66047.04		2.219		
1	66541.09		2.289		
2	67034.73		2.362		
3	67526.84		2.429		
4	68016.24	68004.4	2.506	2.84	m
5	68502.64	68489.4	2.567	3.3	m+1
6	68986.34	68927.3	2.643	3.19	m+2
7	69468.29	69418.5	2.701	3.20	m+3
8	69949.27	69909.9	2.751	3.273	m+4
9	70429.73	70512.1	2.794	3.80	m+5
10	70909.56	70948.6	2.832	4.095	m+6
11	71388.31	71481.8	2.865	3.26	m+7
12	71865.54	71920.3	2.894	3.972	m+8
13	72340.74	72022.4	2.918	2.792	m+9
14	72813.32	72506.0	2.938	4.106	m+10
15	73282.58	73457.8	2.953	3.177	m+11
16	73747.77	73589.5	2.964	2.294	m+12
17	74208.13	73822.7	2.969	3.769	m+13
18	74662.89	74090.0	2.969	3.724	m+14

See notes to Table 5.1

[1] Reference [13]

[2] Only relative vibrational numbering known

formulation of Lawley and Wheeler [106] was employed for calculation of both energy levels and vibrational wavefunctions.

In the continuous case the wave equation is:

$$(-\nabla^2 + V^*(r))\psi(r) = E^*\psi(r) \tag{5.6}$$

where all the parameters are expressed in reduced energy and distance units. For a discrete potential the second derivative is replaced by an expansion in central differences. Neglecting all except the leading term in this expansion and converting to a matrix form this becomes

$$^{(2)}\mathbf{H}\psi^{(2)} = [\varepsilon^{-2}\delta^{(2)} + \mathbf{V}^*]\psi^{(2)} = {}^{(2)}E^*\psi^{(2)} \tag{5.7}$$

where ε is the grid spacing, $\mathbf{V}$ is a diagonal matrix containing the tabulated potential, the superscript $^{(2)}$ refers to the approximation of using only the second central difference and δ is the finite difference matrix operator. This is a tridiagonal matrix with the diagonal elements all equal to 2 and the upper and lower diagonal elements all equal to -1. The eigenvalues of the tridiagonal matrix $\mathbf{H}^{(2)}$ can be found rapidly using bisection and the Sturm sequence technique [107]. The latter determines the number of eigenvalues below the current trial value of $E^{(2)}$ which is equivalent to finding the number of nodes in the wavevector $\psi^{(2)}$. The eigenvectors of the Hamiltonian are determined by back substitution into the matrix eigenvalue equation.

The accuracy with which the eigenvalues of the Hamiltonian can be determined is ultimately limited by the precision of the computer, [104] but such errors are not important in this work. More significant errors in the numerical solution of the wave equation arise from the truncation of the expansion of finite differences, the finite grid spacing and the truncation of the potential energy curve at some point, R_{max}. However, the accuracy of the calculation can be improved quite simply. If the wavevector $\psi^{(2)}$ is also calculated, a correction to the eigenvalue can be determined by first order perturbation theory [106]. Also, the error introduced by a finite grid spacing decreases quadratically with ε and so an appropriate choice of ε gives the required level of accuracy with the minimum of calculation. The truncation of the calculation at R_{max} imposes the condition that the eigenvector has decayed to zero. As the decay of the eigenvector is exponential for $E<V$ this condition is valid for sufficiently large R_{max}. For the calculations reported here the zeroth order second finite difference was found to be sufficiently accurate in all cases. Although the first order correction to the eigenvalue was used in the calculation of wavefunctions for simulated spectra essentially identical results were obtained without this term.

The simulation of dispersed fluorescence spectra was achieved by initially calculating the matrix elements for the transition from the excited rovibronic level to a range of bound and continuum levels in the lower state. This was most often the ground electronic state. It was assumed that the electronic and vibrational elements of the vibronic wavefunction could be separated and that the electronic overlap was a slowly varying function of R, $\mu_{el}(R)$. Therefore the line strength factor, S_{if}, is given by the square of the overlap integral:

$$S_{if} \propto | \langle \chi_f \mid \mu_{el}(R) \mid \chi_I \rangle |^2 \tag{5.8}$$

Numerically, this integration is performed using Simpson's rule over the limits of the upper state wavefunction (eigenvector). The calculated line strength factors are converted to relative intensities using the formula:

$$I(\nu) = S_{if}c\nu^5 \qquad (5.9)$$

where c is a constant and the factor ν^5 includes the frequency dependence of the Einstein A coefficient plus a factor of ν^2 for the response of the photomultiplier tube.

Unless $\mu_{el}(R)$ and the number of excited molecules are both known only relative intensities can be calculated. The line strength factors for all of the bound-bound and bound-free transitions in the required wavelength region are calculated and the resulting stick spectrum is finally convoluted by a response function for the monochromator used. If the wavelength dependence of the experimental detection system is known it may also be included in the simulated spectrum. Although each excited rovibronic level may give rise to more than one rotational branch this was ignored in the simulated spectra because it was below the resolution of the monochromator. A similar procedure to that outlined above was used to simulate the absorption spectra presented above.

It was possible to simulate all of the experimentally observed dispersed fluorescence spectra of the hydrogen halides reported in this thesis. In the following sections many of these spectra are presented and compared with the corresponding experimental spectra. Since the calculations do not exactly reproduce the observed energy levels a small wavelength dependent shift is introduced into the simulated spectra. For an error in the calculated energy level of +100 cm^{-1} the spectral shift varies from -0.4 nm at 200 nm, -0.627 nm at 250 nm, -1.6 nm at 400 nm, -2.5 nm at 500nm, to -4 nm at 600 nm, the longest wavelength at which fluorescence was observed. On the scale on which the simulations are shown this is either negligible or appears as a small overall shift of the spectrum.

The instrument response function for the monochromator used to record DCl fluorescence spectra was determined experimentally for $\lambda \geqq 200$ nm and a sixth order polynomial fit was made to the curve. This function was not valid for $\lambda < 200$ nm. Over the wavelength range $200 \text{ nm} < \lambda < 250 \text{ nm}$ the monochromator correction had little effect on the simulated spectra and so was not employed in the calculations of $B^1\Sigma^+ (0^+) \rightarrow X^1\Sigma^+$ fluorescence spectra. All other simulated spectra covered a much wider wavelength range and so the correction was included for these.

5.2.1 $B^1\Sigma^+ (0^+) \rightarrow X^1\Sigma^+$ Fluorescence Spectra of HCl and DCl

Simulated dispersed fluorescence spectra were calculated for the $B^1\Sigma^+ (0^+) \rightarrow X^1\Sigma^+$ transition from all observed upper state vibrational levels using each of the four curves discussed above to represent the ion-pair state. In each simulation the same ground state curve and transition dipole moment function were employed. The simulated spectra are presented in figures 5.5 to 5.16 along with the appropriate experimental spectra. The characteristic ion-pair state bound-free interference structure is seen in the simulated spectra. However, in general there was poor agreement between the observed and simulated spectra.

In all cases there is a good simulation for at least one excited state vibrational level. But, it is obvious that, despite the close fit to the observed vibrational

Figure 5.5
HCl Simulated Spectra using diabatic curve 1.

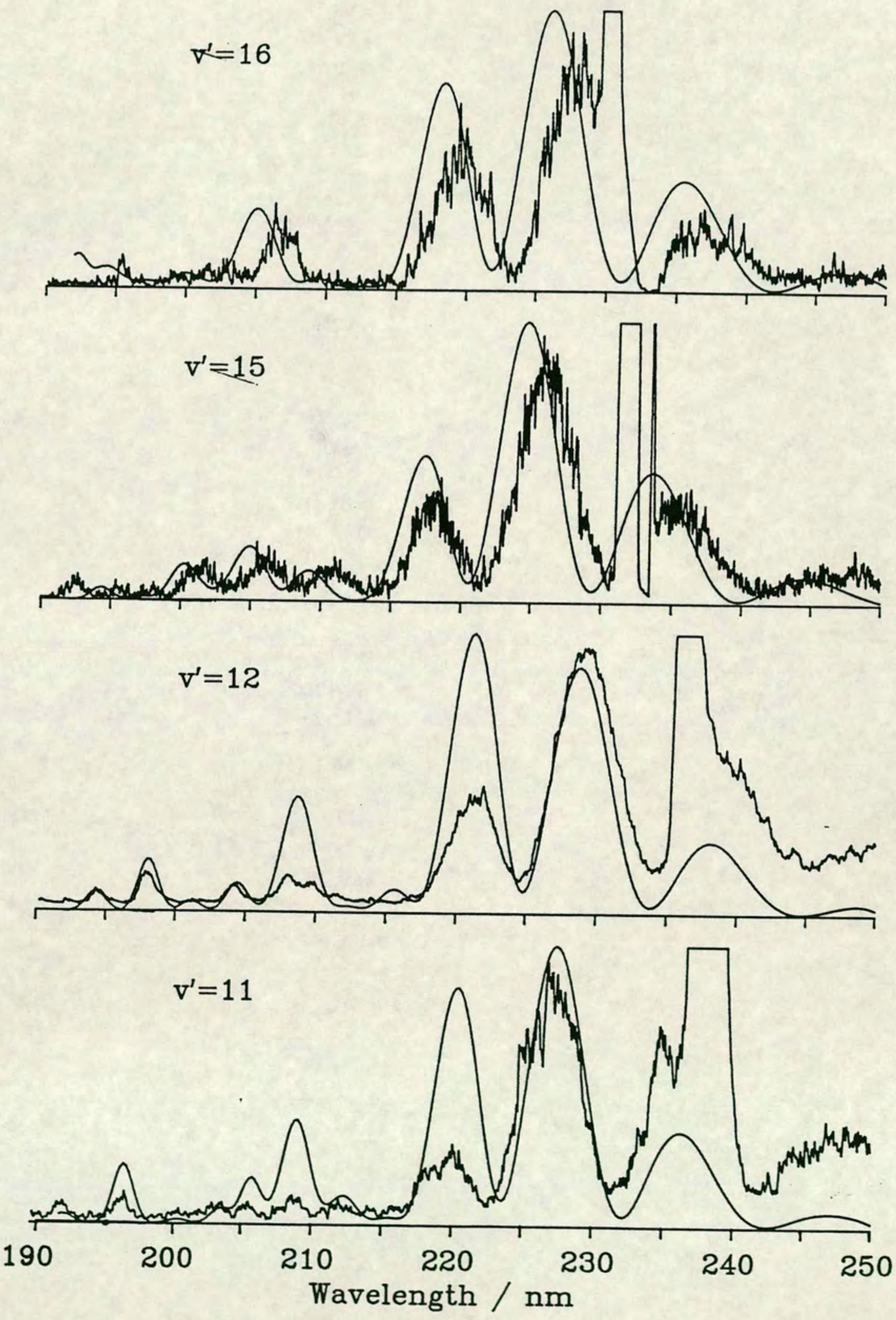

Figure 5.6
HCl Simulated Spectra using diabatic curve 2.

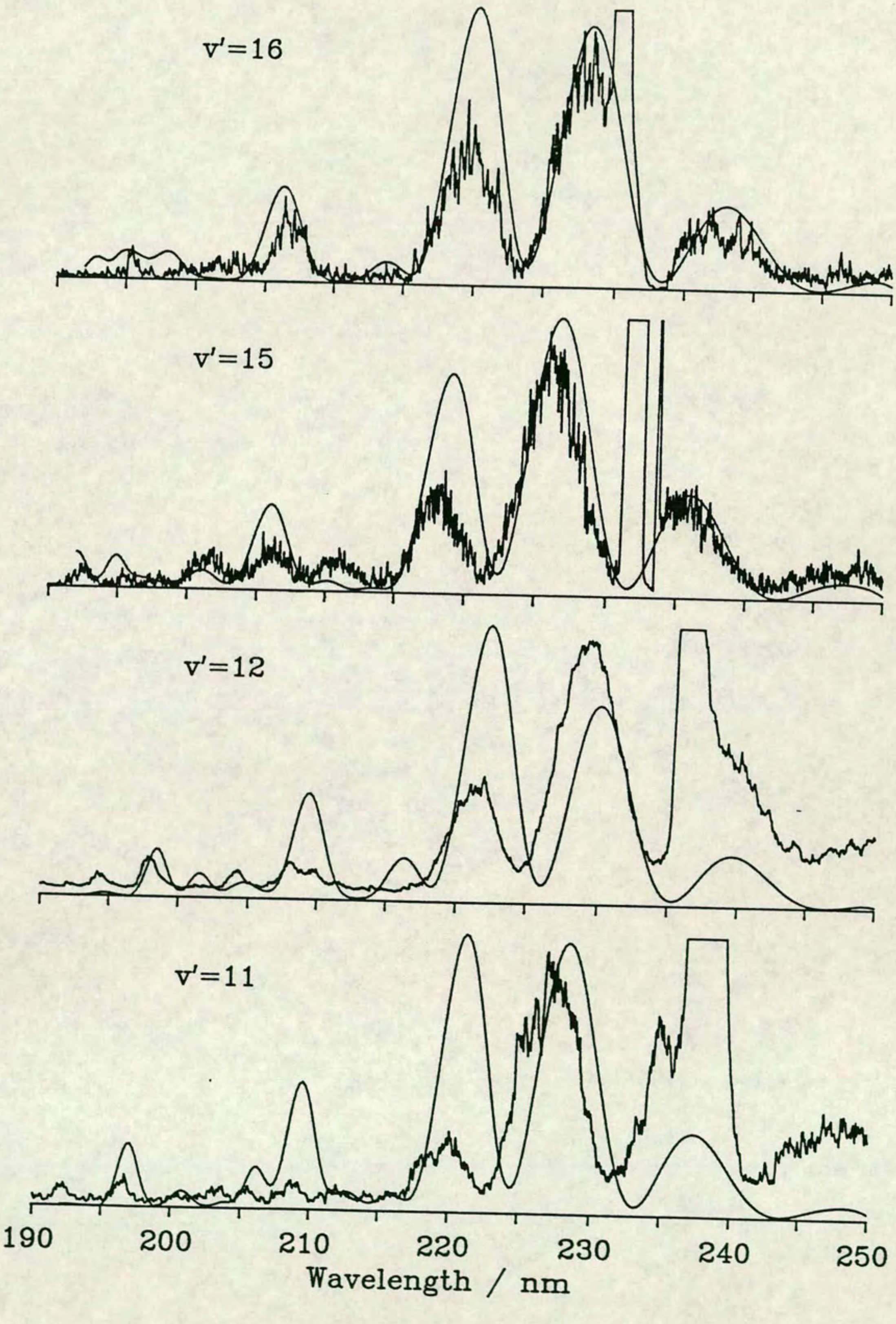

Figure 5.7
HCl Simulated Spectra using diabatic curve 3.

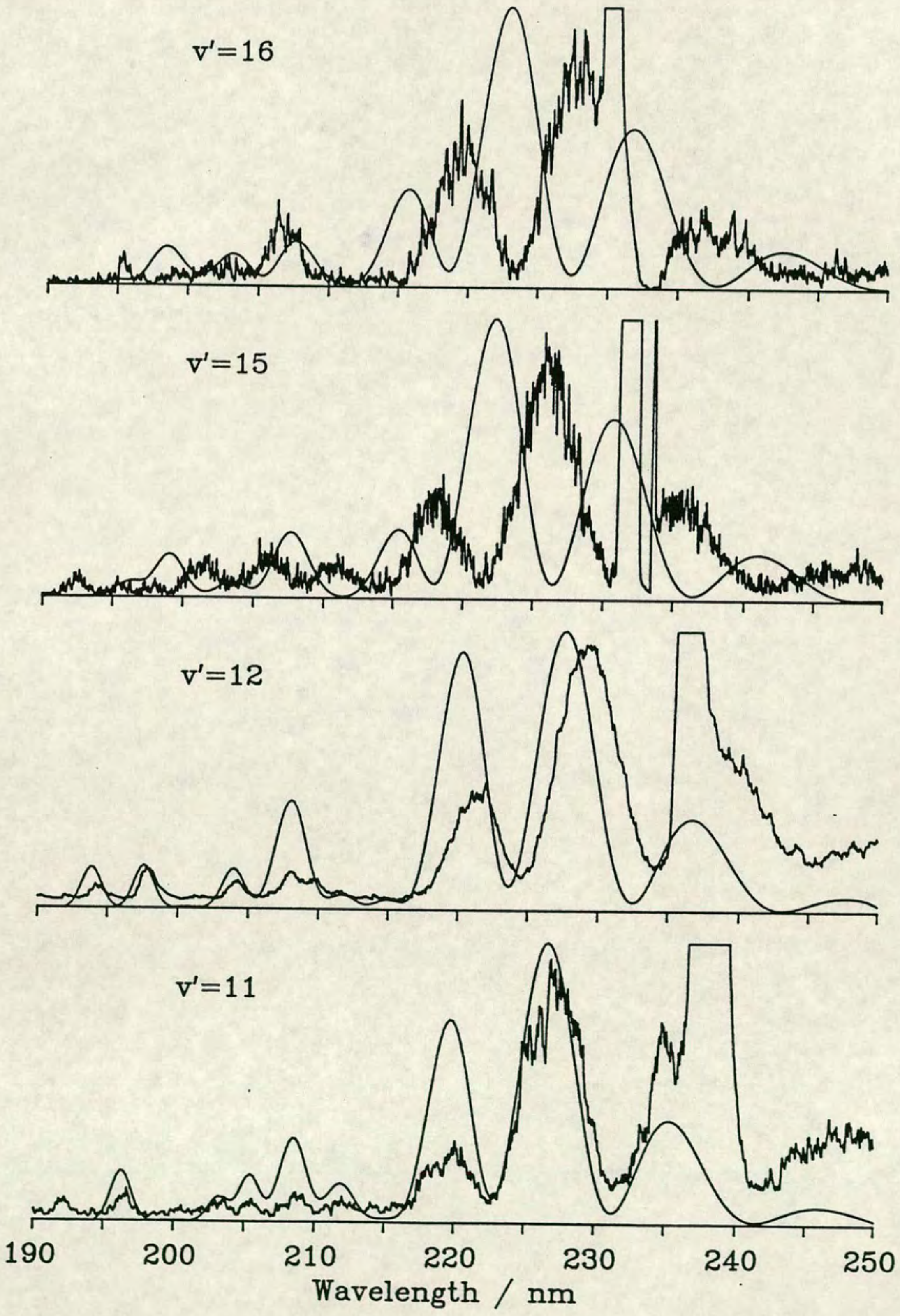

Figure 5.8
HCl Simulated Spectra using adiabatic curve.

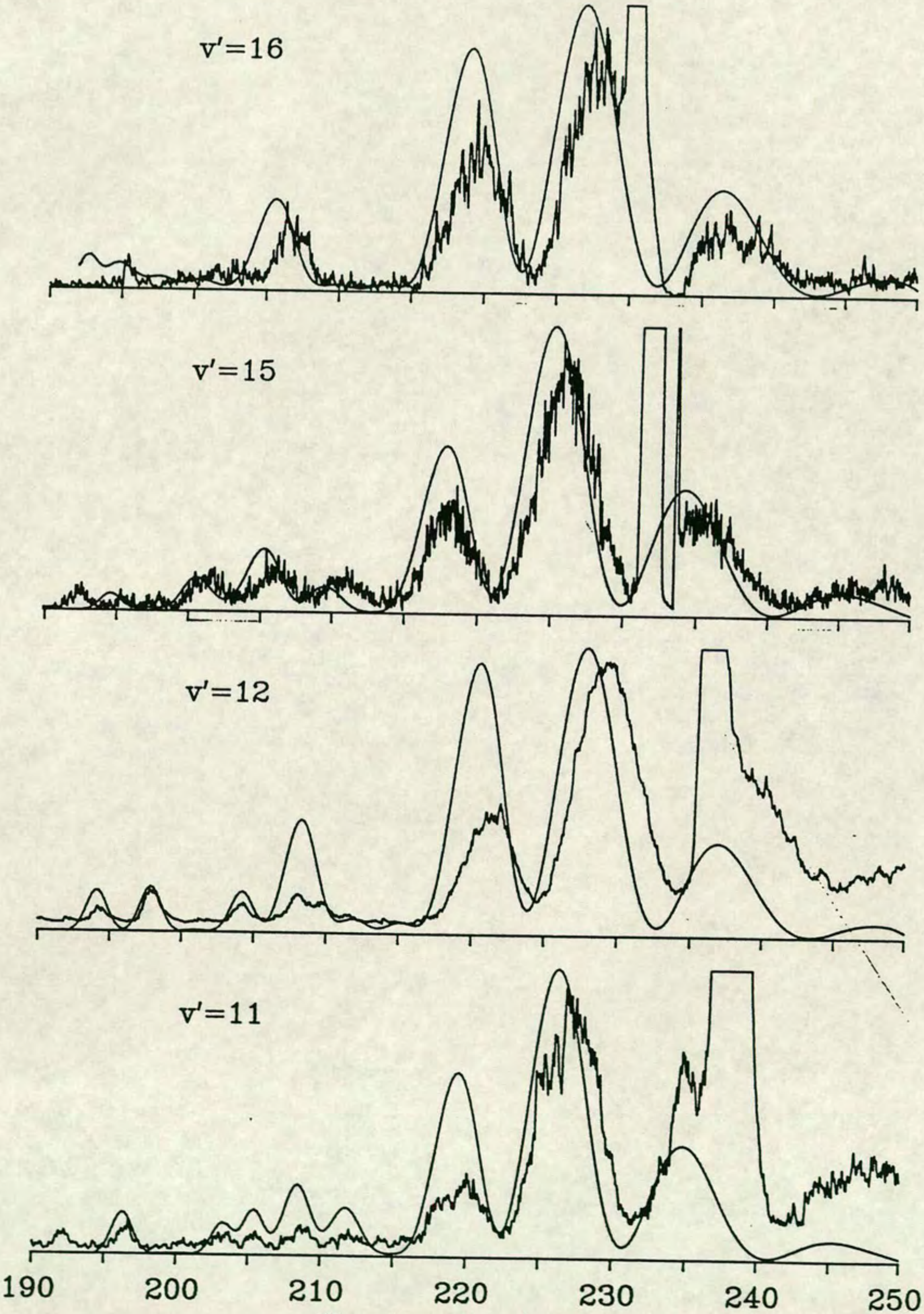

Figure 5.9
DCl Simulated Spectra using diabatic curve 1.

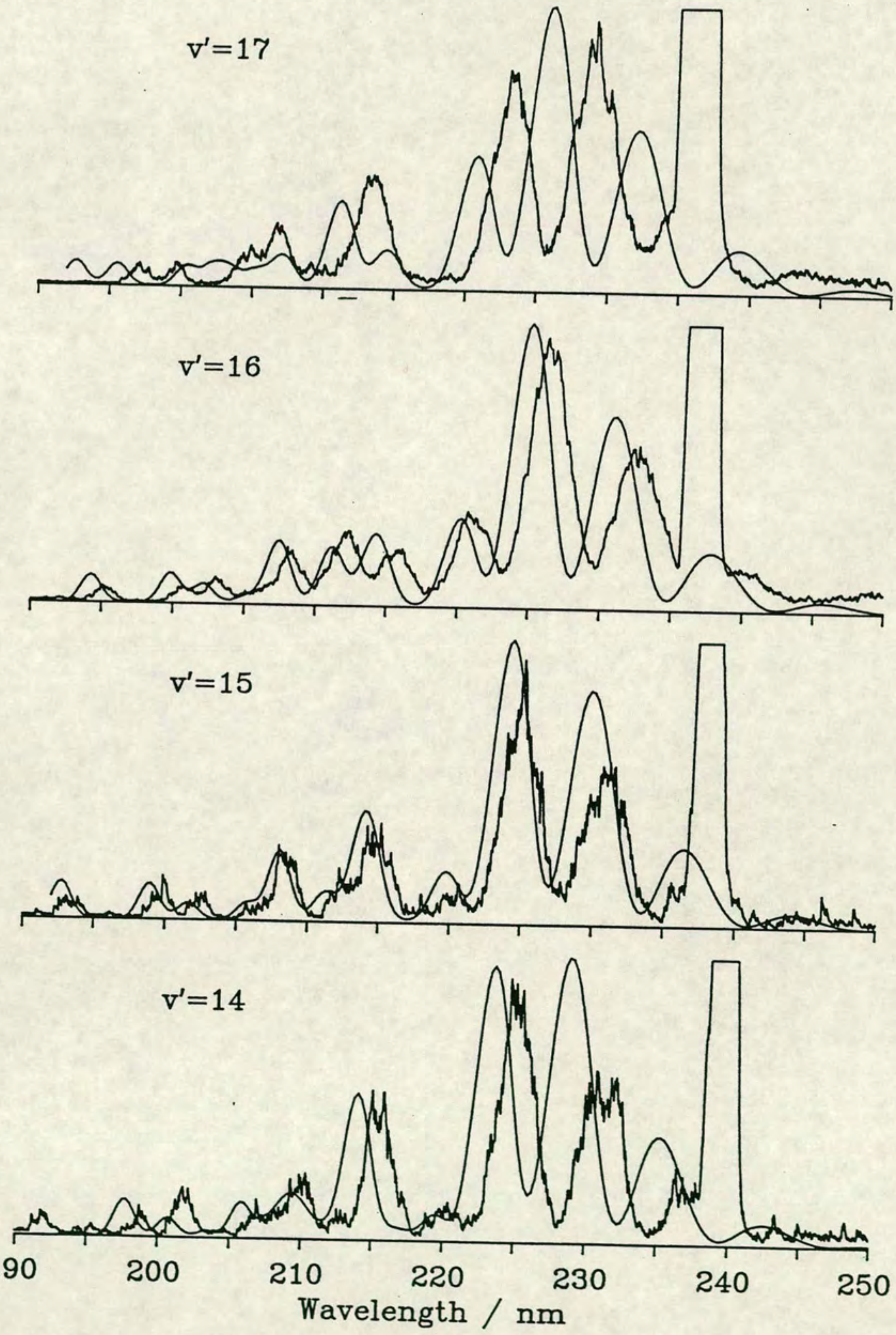

Figure 5.10
DCl Simulated Spectra using diabatic curve 1.

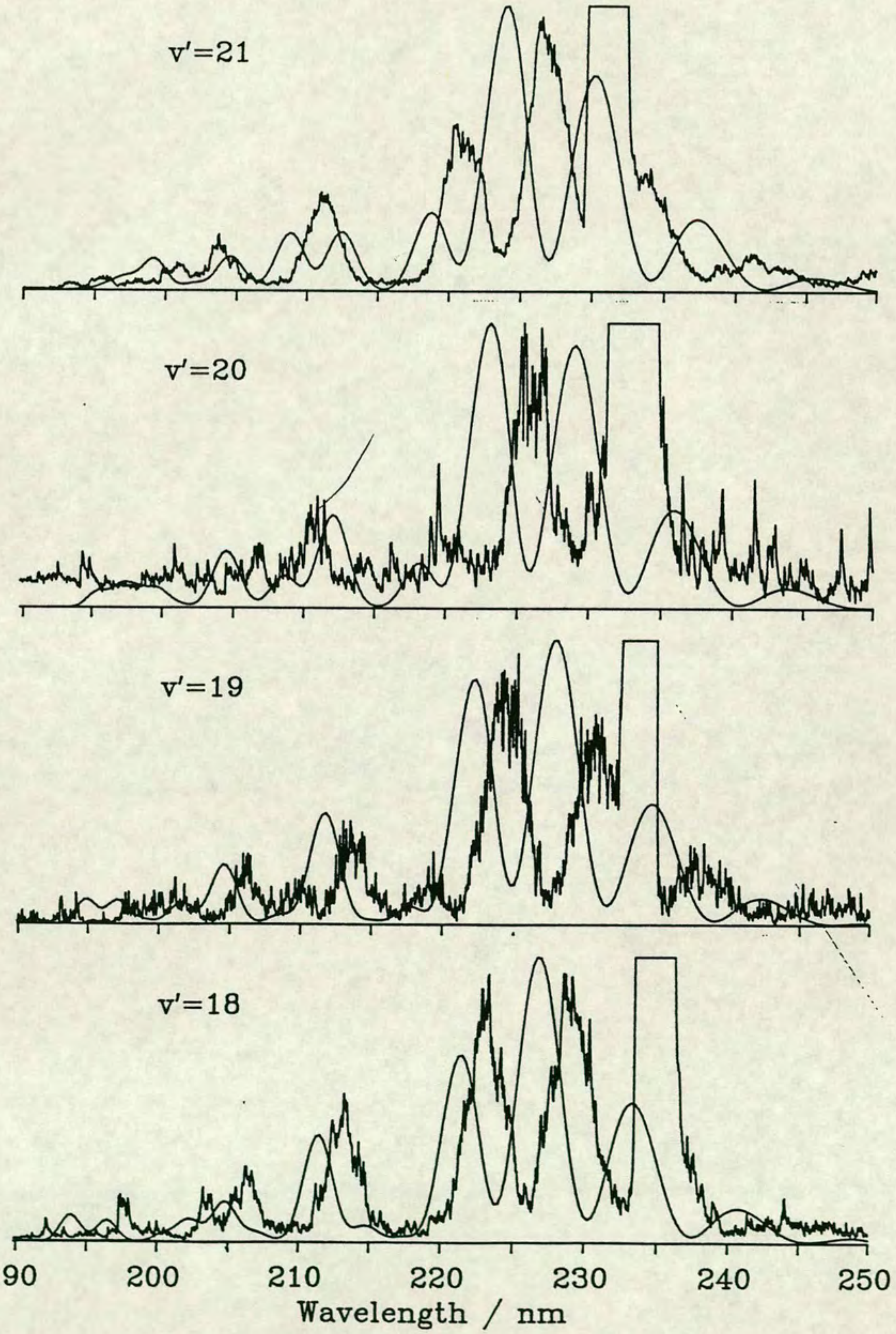

Figure 5.11
DCl Simulated Spectra using diabatic curve 2.

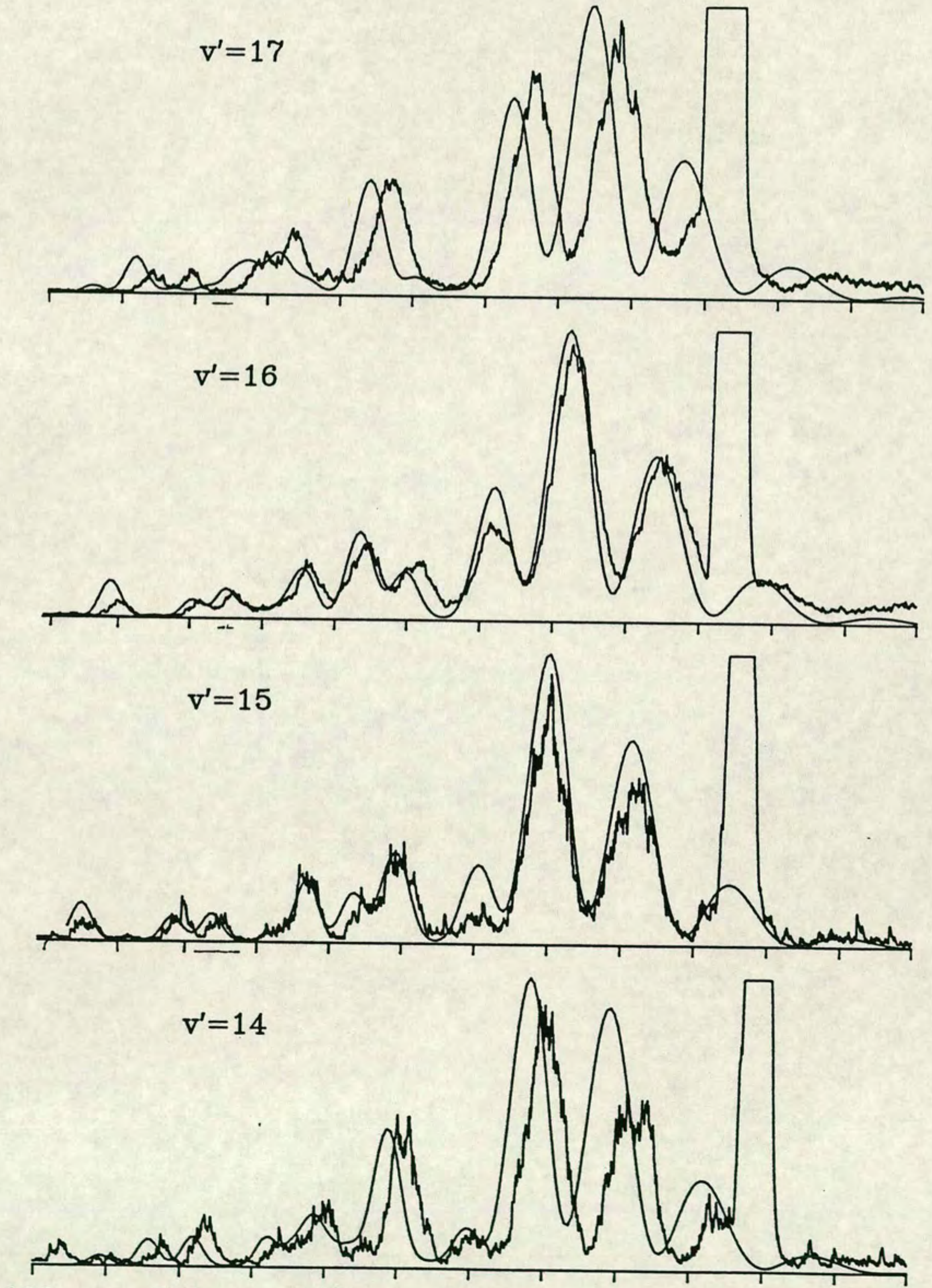

Figure 5.12
DCl Simulated Spectra using diabatic curve 2.

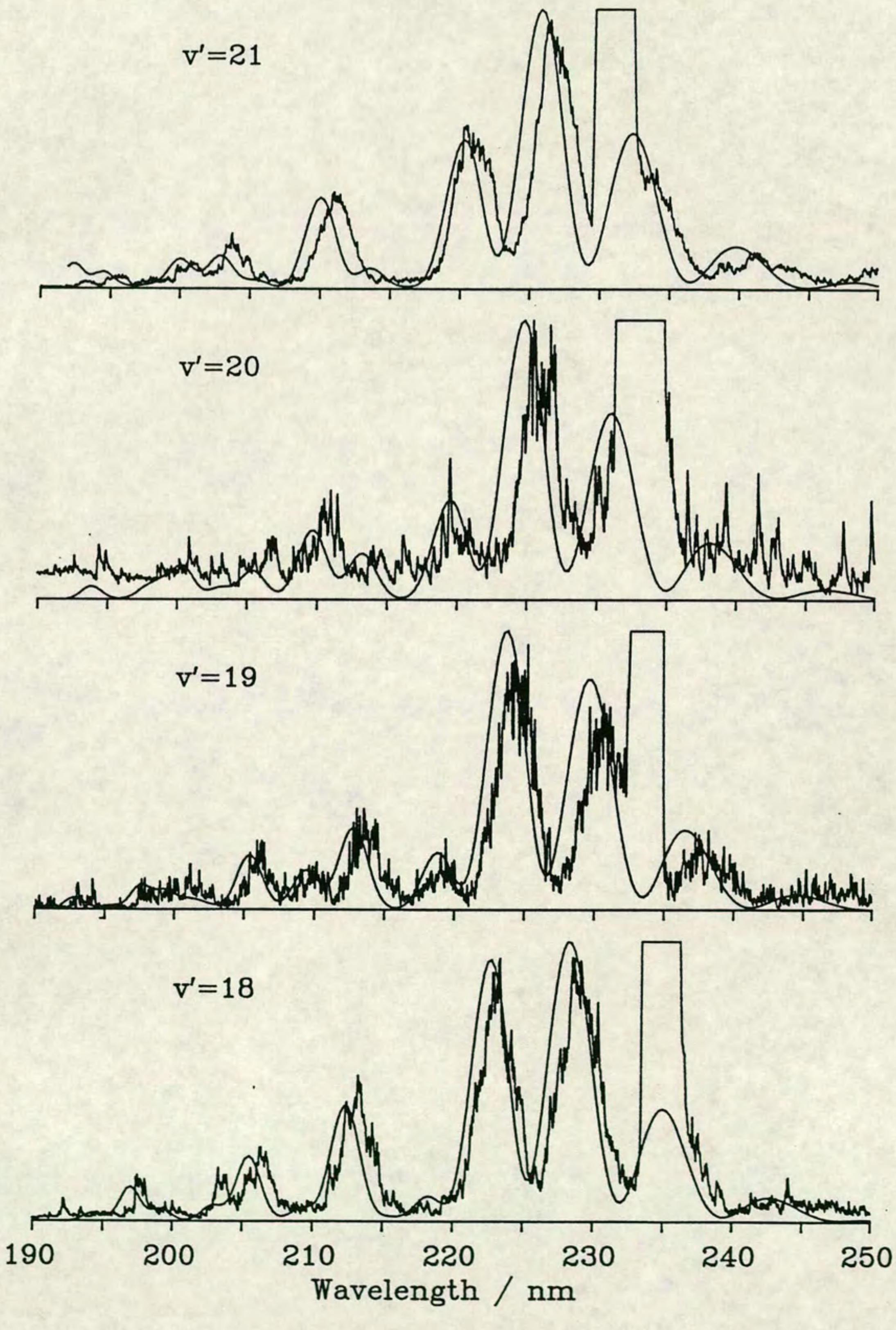

Figure 5.13
DCl Simulated Spectra using diabatic curve 3.

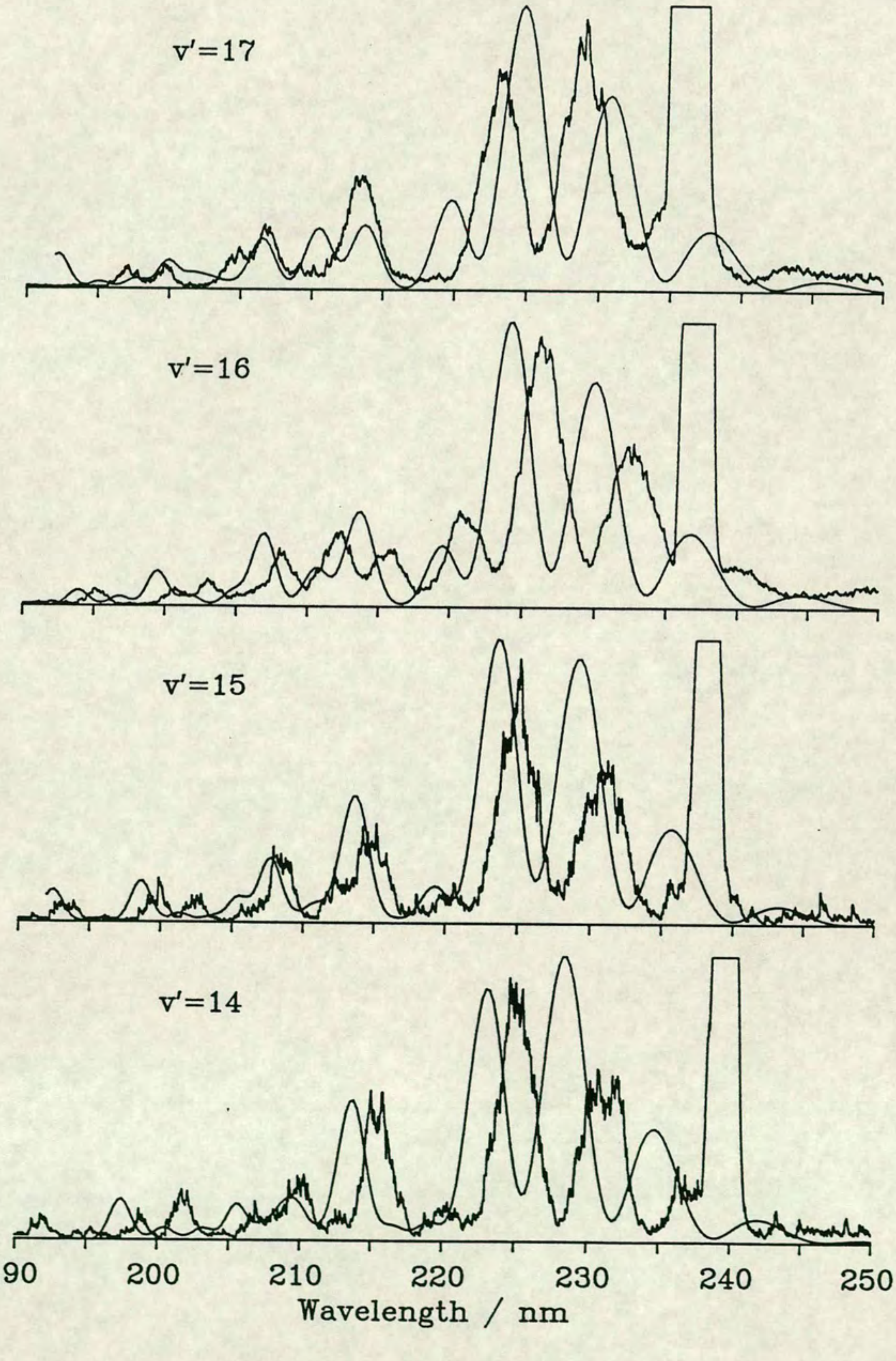

Figure 5.14
DCl Simulated Spectra using diabatic curve 3.

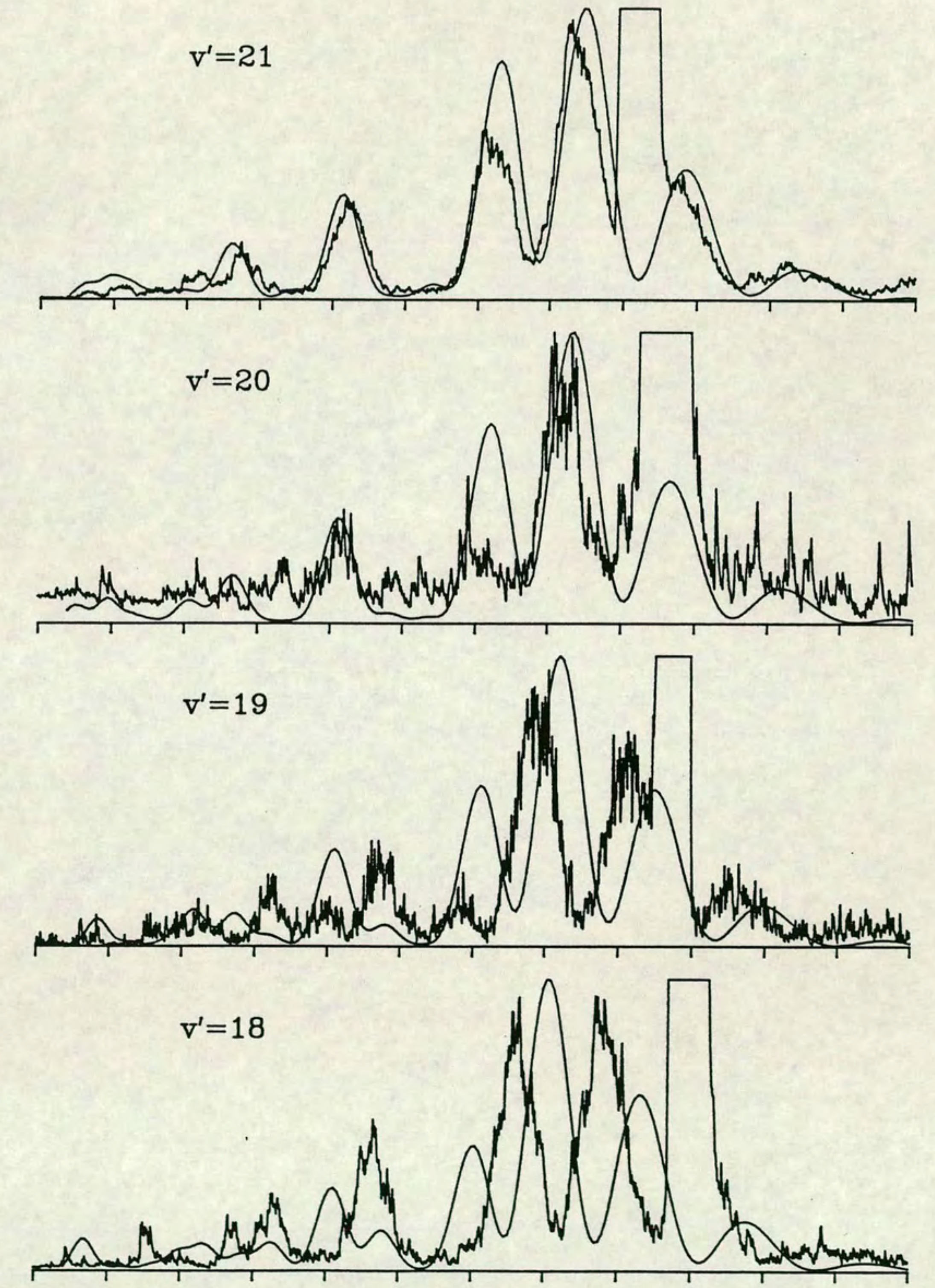

Figure 5.15
DCl Simulated Spectra using adiabatic curve.

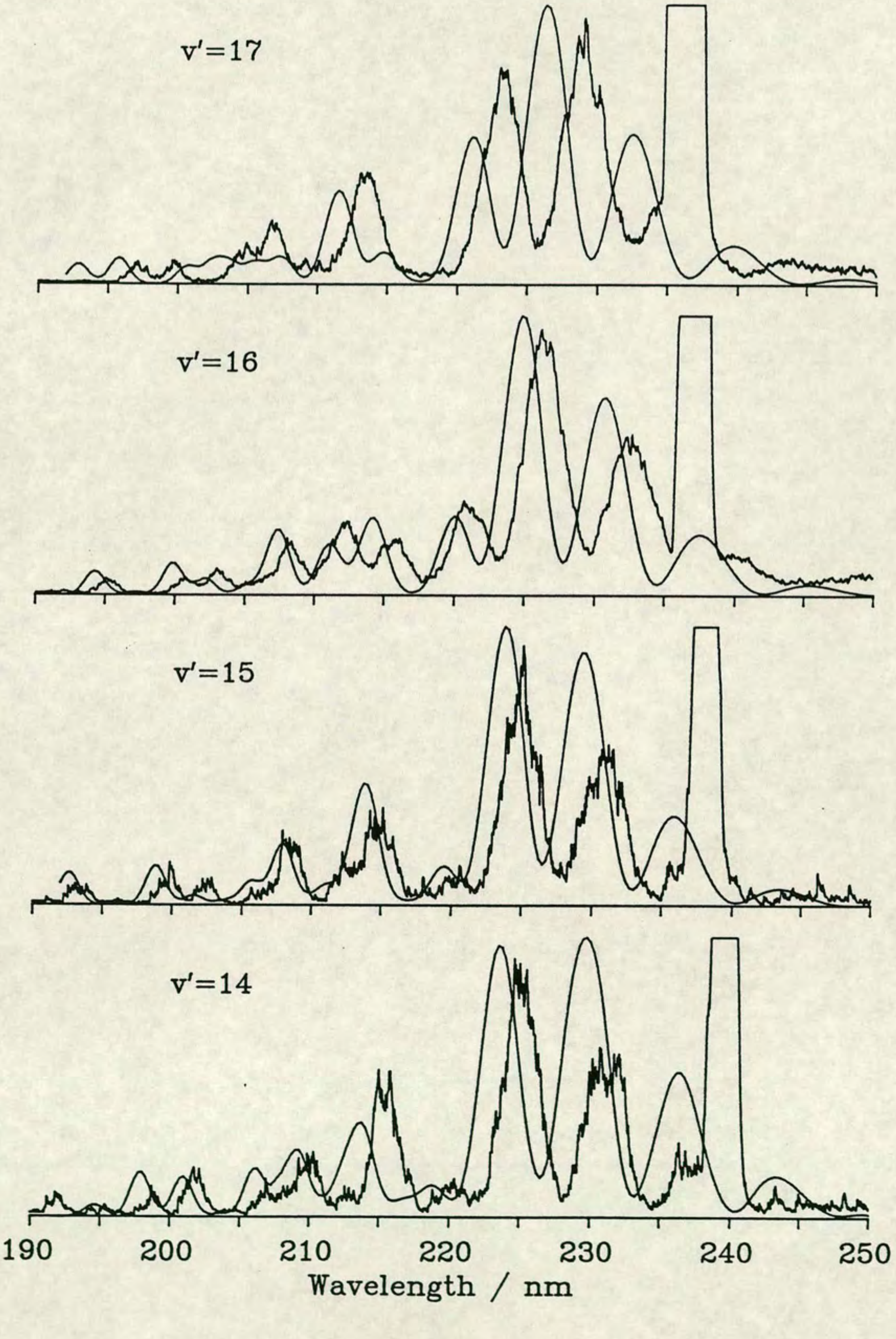

Figure 5.16
DCl Simulated Spectra using adiabatic curve.

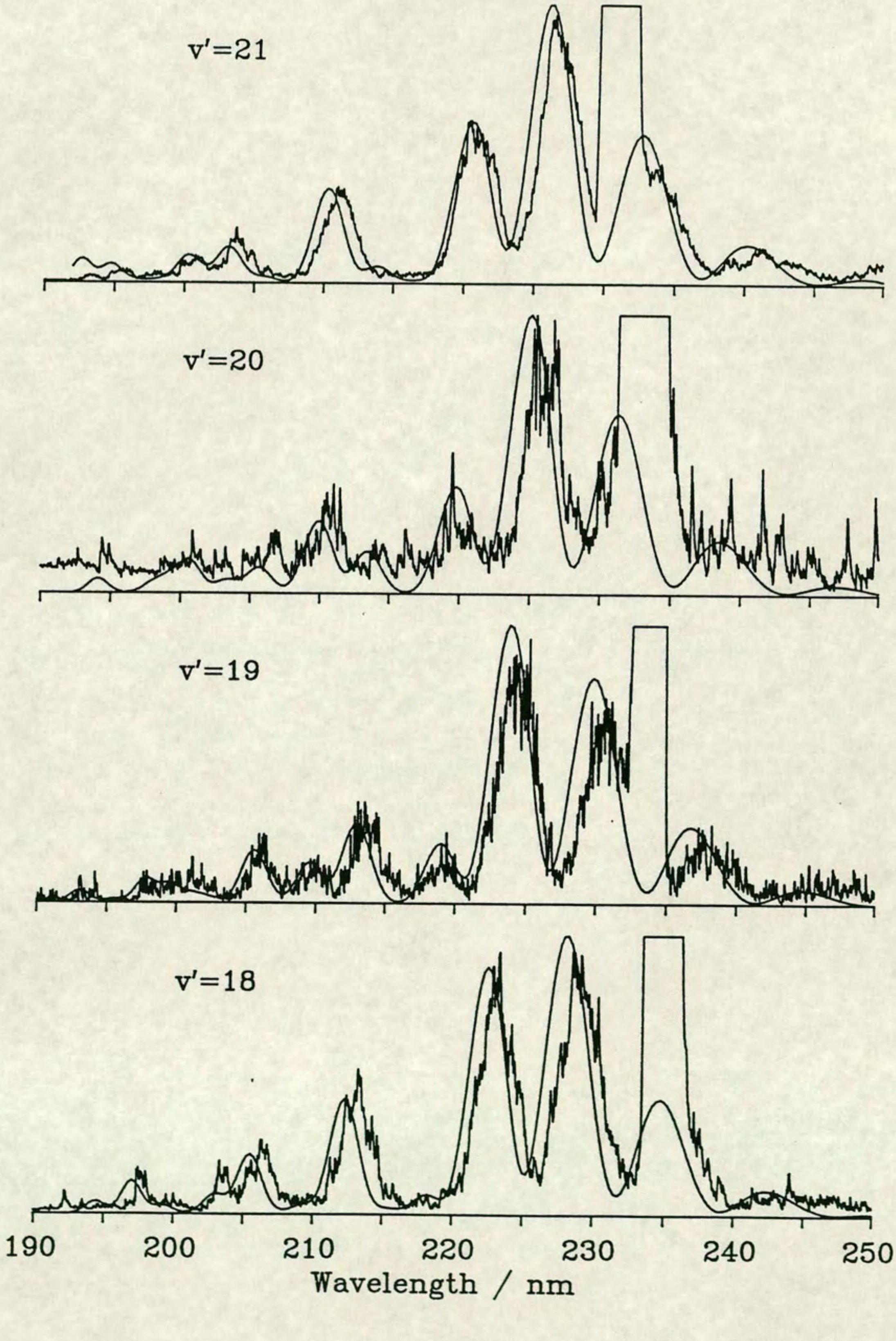

energy levels and B_v values achieved for each curve, none of these is capable of reproducing all of the observed spectra.

Also, there is poor agreement between the HCl and DCl simulations. If the simulations performed using diabatic curve 1 are considered then it can be seen that there is a quite good fit for v' =11 and 12 of HCl but that for the DCl vibrational levels at a similar energy, v' =15, 16, 17 and 18, the fit is comparatively poor. A similar lack of agreement between data for the different isotopomers is observed for the other ion-pair state potential energy curves. Although HCl and DCl differ only in mass it was not possible to fit both sets of experimental spectra with a single potential energy curve. The perturbations in the ion-pair state are obviously too great to allow this simple approach of using a single potential energy curve for both HCl and DCl. By using different curves for each molecule it may be possible to correctly simulate all of the observed fluorescence spectra. However, this approach does not directly address the central problem of the vibronic coupling of the excited states. The alternative is to explicitly consider this coupling and its effect on the vibrational energy levels, B_v values and fluorescence spectra of the ion-pair and Rydberg states. This is discussed in detail in section 5.3.

The transition dipole moment function, $\mu_{el}(R)$, used in the simulations presented above was a Gaussian function with the form:

$$\mu_{el}(R) = \exp(2(R-2.8)^2) \qquad (5.10)$$

This function was chosen to match the observed peak height as closely as possible. The effect on the simulated spectra of varying $\mu_{el}(R)$ is illustrated in figure 5.17 for the transition from the v' = 15 level of HCl using the adiabatic double minimum curve.

For a constant $\mu_{el}(R)$ the strongest peaks in the simulated spectrum occur near the transition from discrete to continuum emission. In the experimental spectrum these peaks are the weakest in the spectrum. The shorter wavelength peaks must therefore be attenuated with the $\mu_{el}(R)$ function. The greatest contribution to the overlap integrals for these transitions occurs at large R near the outer turning point of the vibrational motion in the upper state. $\mu_{el}(R)$ is expected to decrease with increasing R at large R [42] and so a tanh function of the form:

$$\mu_{el}(R) = \tfrac{1}{2}(1 + \tanh(2.5(3.3 - R))) \tag{5.11}$$

was used to model the large R behaviour. This suppresses the short wavelength peaks compared to the long wavelength peaks but not enough. Translation of the centre of the tanh function or variation of its width does not significantly improve the fit. There is also a contribution to the overlap integral at small R, corresponding to the inner limb of the difference potential. This can be reduced if the Gaussian $\mu_{el}(R)$ above is used. The centre of this function is near the maximum of the difference potential and so it selects the longest wavelength emission. This function was used in the simulation of all $B^1\Sigma^+ (0^+) \rightarrow X^1\Sigma^+$ spectra for HCl and DCl. For comparison a simulation using the *ab initio* transition dipole moment function of reference [42] is also shown. It is similar to the Gaussian used but is shifted to smaller R and so the shorter wavelength fluorescence is too strong.

Figure 5.17
HCl Simulated Spectra with various $\mu_{el}(R)$.

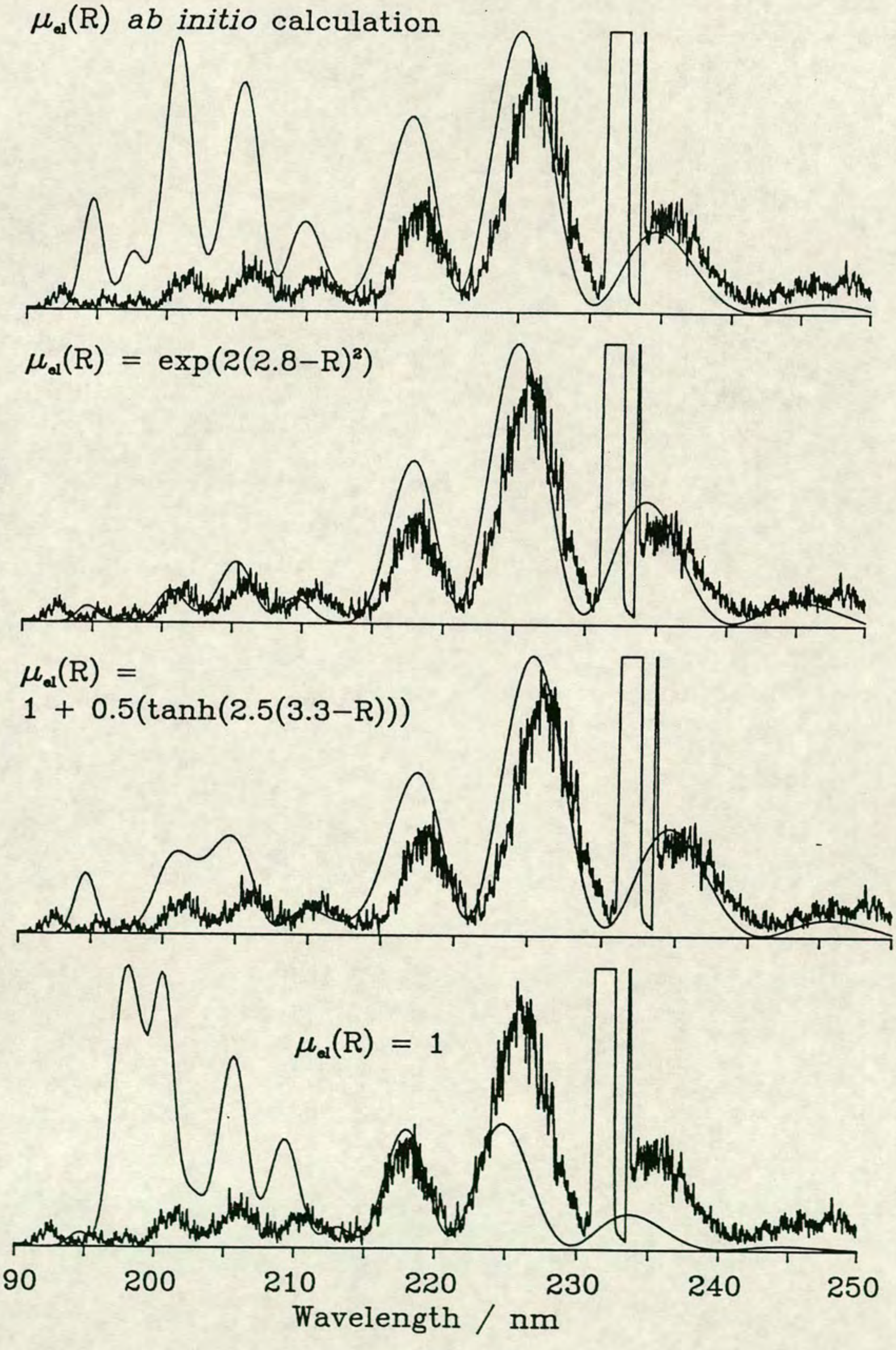

The chosen form of $\mu_{el}(R)$ gives a good match to the peak height ratios measured experimentally but, it decays to zero at small R and will therefore suppress bound-bound emission at short wavelength. In this work it was not possible to record vacuum ultraviolet fluorescence and so the major part of the bound-bound spectrum of the $B^1\Sigma^+ (0^+) \rightarrow X^1\Sigma^+$ emission could not be observed. However, the short wavelength emission spectrum has been recorded, at low resolution, for a number of vibrational levels in the ion-pair state [69]. The difference potential for the discrete spectrum is single valued and so the variation of $\mu_{el}(R)$ with R can be determined in this region by comparing the calculated and observed peak height ratios. Although it is not possible to accurately determine the form of $\mu_{el}(R)$ from the reported spectra, it can be clearly seen that the emission to low v" is of a similar order of magnitude to that seen for the bound-free fluorescence. A modified Gaussian function, which does not decay as rapidly with decreasing R as the pure Gaussian, gives the same behaviour for the bound-free emission without suppressing the discrete fluorescence.

5.2.2 $B^1\Sigma^+ (0^+) \rightarrow A^1\Pi$ Fluorescence Spectra of HCl and DCl

In the fluorescence spectra of many of the ion-pair state levels of HCl and DCl some weak continuum structure was noted to the red of the $B^1\Sigma^+ (0^+) \rightarrow X^1\Sigma^+$ emission. The appearance of this emission does not vary significantly between different ion-pair vibrational levels or between the spectra of HCl and DCl. Since it occurs to the red of the emission to the ground state it has been attributed to the transition $B^1\Sigma^+ (0^+) \rightarrow A^1\Pi$, which is a two electron transition and so is much weaker than the one electron $B^1\Sigma^+ (0^+) \rightarrow X^1\Sigma^+$ transition.

Figure 5.18
HCl $B^1\Sigma^+ <- A^1\Pi$ Simulated Fluorescence Spectra

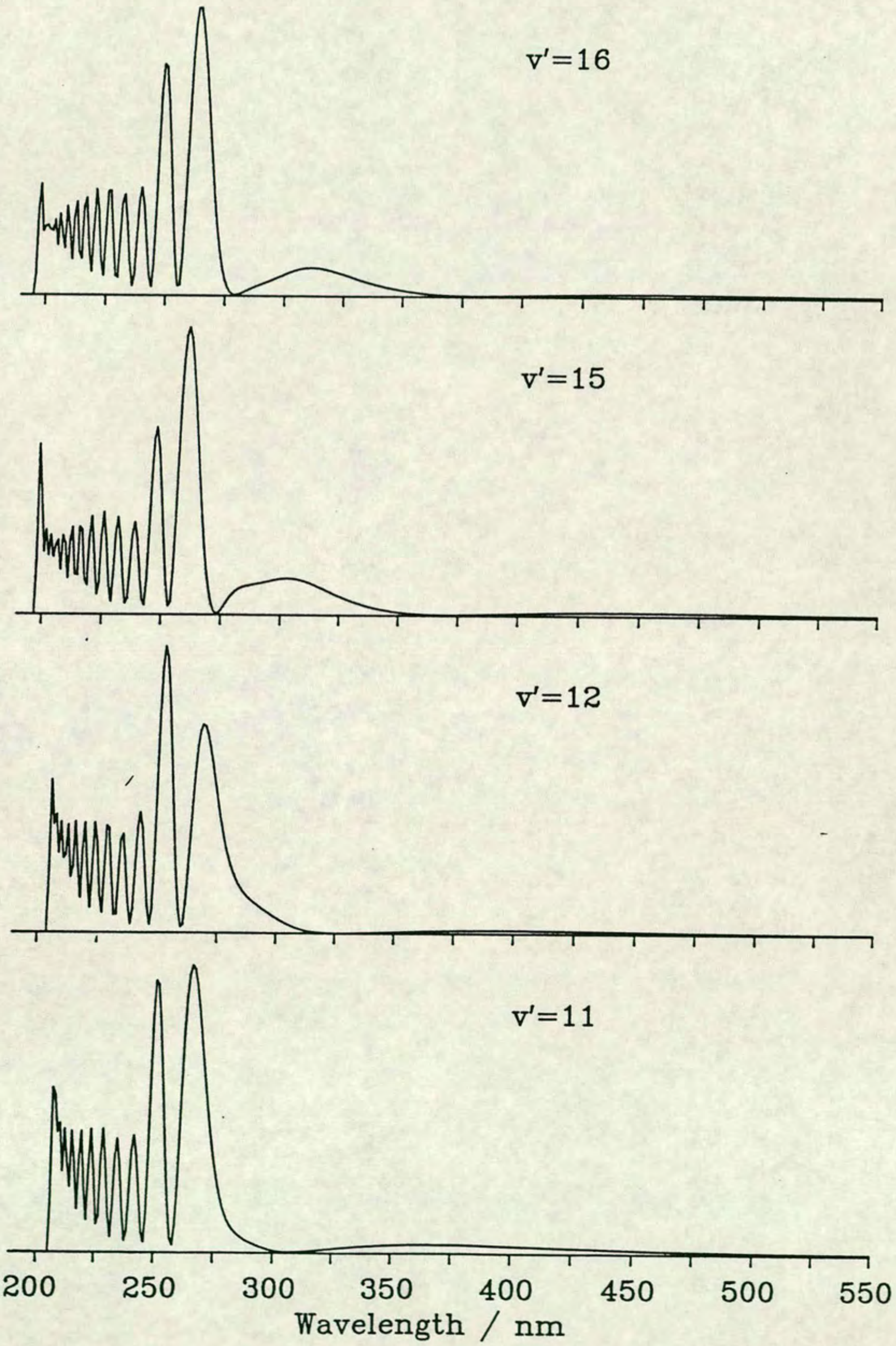

Figure 5.19 Simulated $B^+\Sigma^+$ -> $A^1\Pi$ Dispersed Fluorescence from DCl

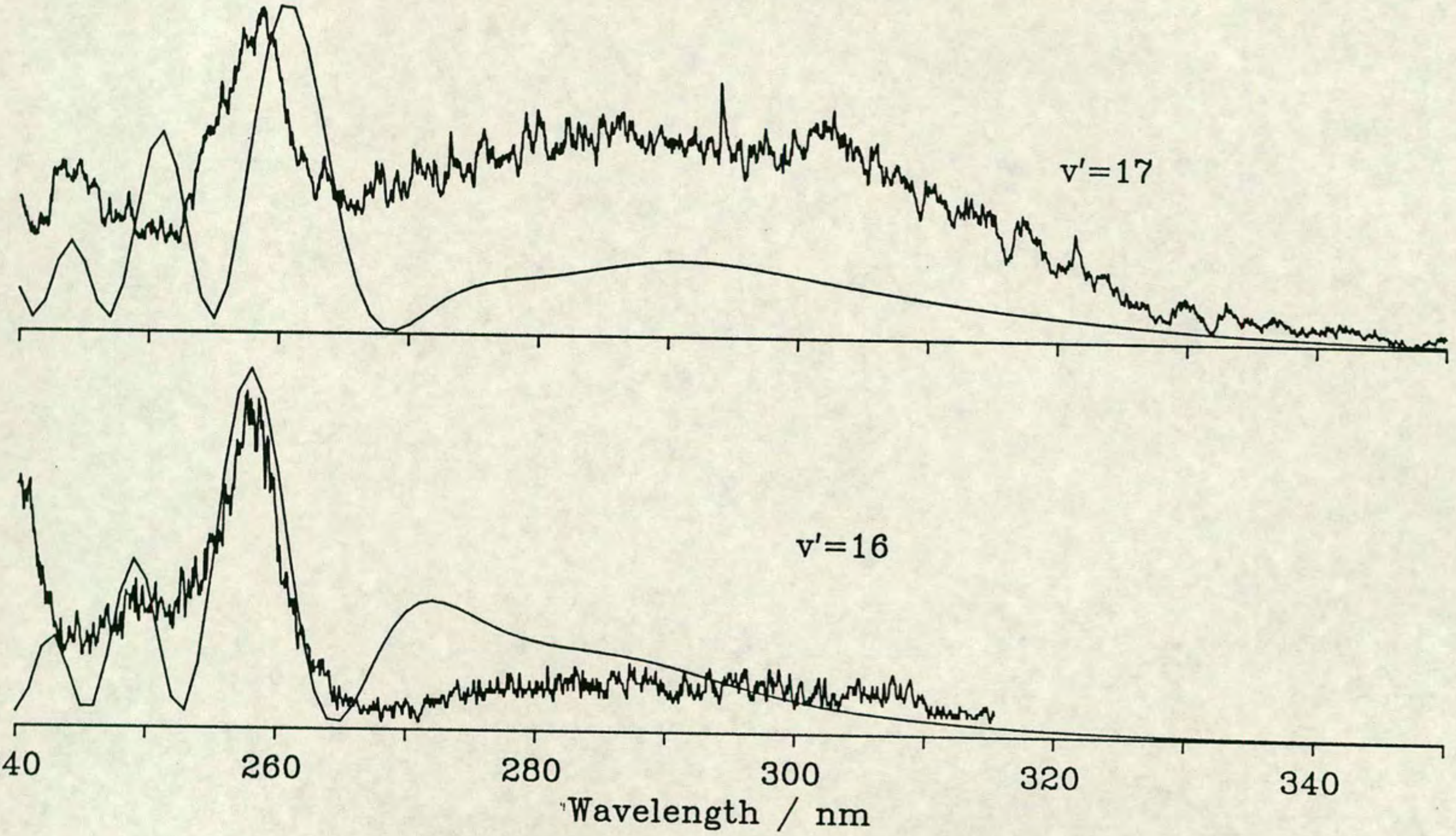

The simulated spectra of this transition show a number of closely spaced, narrow peaks for $\lambda < 250$ nm which become broader with increasing wavelength and are most intense between 250 and 275 nm. The spectra shown in figure 5.18 were calculated using the double minimum curve for the ion-pair state and Peyerimhoff's *ab initio* curve [66] for the repulsive valence state with a constant $\mu_{el}(R)$. The broad features of the spectra were found to be fairly independent of not only the ion-pair state vibrational level but also the choice of potential energy curve. If Dalgarno's *ab initio* [42] $A^1\Pi$ potential and $\mu_{el}(R)$ are used the longer wavelength peaks shift to the blue and the long wavelength fluorescence becomes more intense at the expense of the shorter wavelengths.

The finer structure present in the simulated spectra could not be observed experimentally because of the very low intensity of the observed fluorescence and the overlap of the two emission bands. However, the relatively strong peak observed near 260 nm is reproduced by the simulation as is the broader maximum at longer wavelength. This is illustrated in figure 5.19 for $v' = 16$ and $v' = 17$ in DCl. The close agreement between the simulated and observed spectra confirm the assignment of these bands to the $B^1\Sigma^+ (0^+) \rightarrow A^1\Pi$ transition.

5.2.3 Fluorescence Spectra of the Rydberg States of HCl and DCl

The $F^1\Delta_2$ (2) Rydberg State

The fluorescence observed from the $F^1\Delta_2$ (2) Rydberg state was typical of that expected for a Rydberg → dissociative state transition. It is broad, with no sharp features, and reflects the vibrational wavefunction of the upper state. Apart from $v' = 1$ in DCl the simulated spectra give a very good fit to the

Figure 5.20
Simulated $F^1\Delta_2 \rightarrow A^1\Pi$ Dispersed Fluorescence Spectra from HCl and DCl

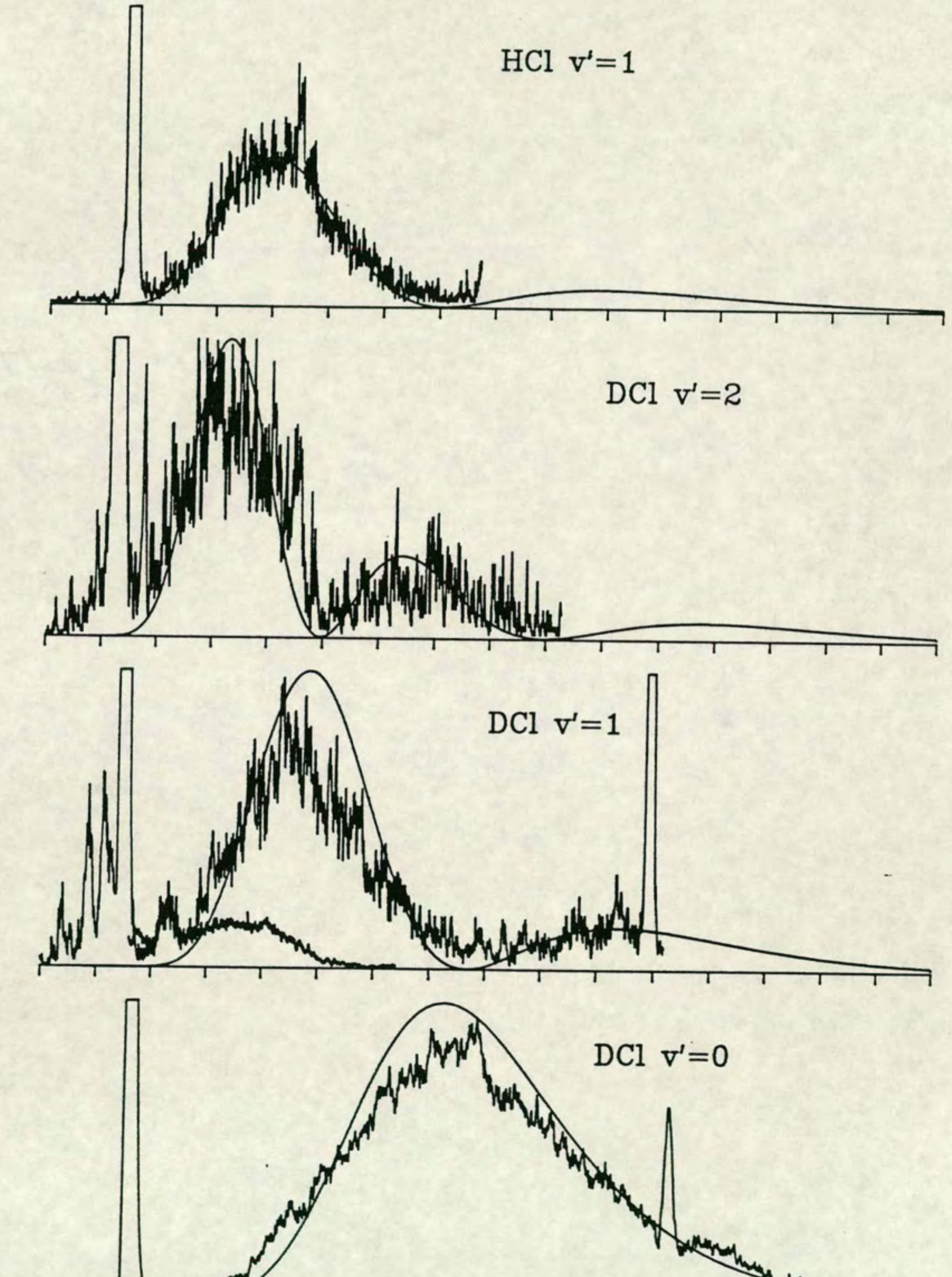

experimental spectra, as shown in figure 5.20. The calculations were performed with the Morse oscillator curve for the Rydberg state determined from the DCl (2+1)REMPI spectra [24], an *ab initio* $A^1\Pi$ repulsive curve [66] and a constant $\mu_{el}(R)$. It was necessary to shift the Morse potential by 0.025 Å to larger R in order to reproduce the positions of the maxima and minima of the fluorescence. This decreases the calculated B_v values below those reported from (2+1)REMPI spectra [24] which are, however, based on an incomplete rotational analysis. The form of $\mu_{el}(R)$ was not adjusted to improve the fit of the simulated spectra in this case.

The poor agreement observed for the $v'=1$ level of DCl results from the overlap of the Rydberg fluorescence by that from the $v'=17$ level of the ion-pair state. As discussed earlier, the Q(2) rotational line of the $F^1\Delta_2$ (2) ← $X^1\Sigma^+$ (1-0) transition, which was the transition excited when the fluorescence spectrum was recorded, lies at the same energy as the Q(9) rotational line of the $B^1\Sigma^+$ (0^+) ← $X^1\Sigma^+$ (17-0) transition. Exciting the molecule at this energy therefore gives rise to $B^1\Sigma^+$ (0^+) → $X^1\Sigma^+$, $B^1\Sigma^+$ (0^+) → $A^1\Pi$ and $F^1\Delta_2$ (2) → $A^1\Pi$ fluorescence. An appropriately scaled spectrum of the $B^1\Sigma^+$ (0^+) → $A^1\Pi$ fluorescence from $J'=3$ of the ion-pair level is also shown in figure 5.20. The overlap of this fluorescence band causes the apparent shift to shorter wavelength of the peak in the spectrum of the $F^1\Delta_2$ (2) → $A^1\Pi$ transition.

The $f^3\Delta_2$ (2) Rydberg State

A broad continuum fluorescence band was observed in emission from the $v'=0$ level of the $f^3\Delta_2$ (2) Rydberg state of DCl. Although this was similar to the emission spectrum of the v' =0 level of the $F^1\Delta_2$ (2) Rydberg state, simulated spectra, calculated using the same potential energy curves, did not give a good fit. There is a red shift of 60 nm between the observed and simulated spectra. Obviously this very large shift can not be corrected by translation of the upper curve by a small amount from R_e or by the substitution of a slightly different Rydberg state curve. Similarly the small effect which can be produced by altering $\mu_{el}(R)$ from the constant used is insufficient to shift the spectrum by such a large amount.

A good fit to the observed spectrum can be made if the T_e of the upper state is increased by the energy difference between the peak of the observed fluorescence and that of the simulated spectrum. This is a shift of 4200 cm^{-1} which compares well with the calculated energy difference between the $A^1\Pi$ and $a^3\Pi$ repulsive valence states near the R_e of the upper state, 3630 cm^{-1} [37]. An accurate potential energy curve was not available for the $a^3\Pi$ state but it appears to be nearly parallel to the $A^1\Pi$ state curve over the range of the vibrational motion in the v' =0 level of the $f^3\Delta_2$ (2) Rydberg state. Therefore the *ab initio* curve for the $A^1\Pi$ state was used. The calculated spectrum for the shifted $A^1\Pi$ state curve compares well with the observed spectrum, as shown in figure 5.21. Although there are three components to this repulsive state the splitting between them is expected to be small and any effects resulting from the spin-orbit multiplicity would not be apparent in the dispersed fluorescence spectrum. Therefore only a single curve, approximating the $a^3\Pi$ state was required in the simulated spectrum.

Figure 5.21 Simulated $f^3\Delta_2$ -> $a^3\Pi$ Dispersed Fluorescence Spectrum for DCl

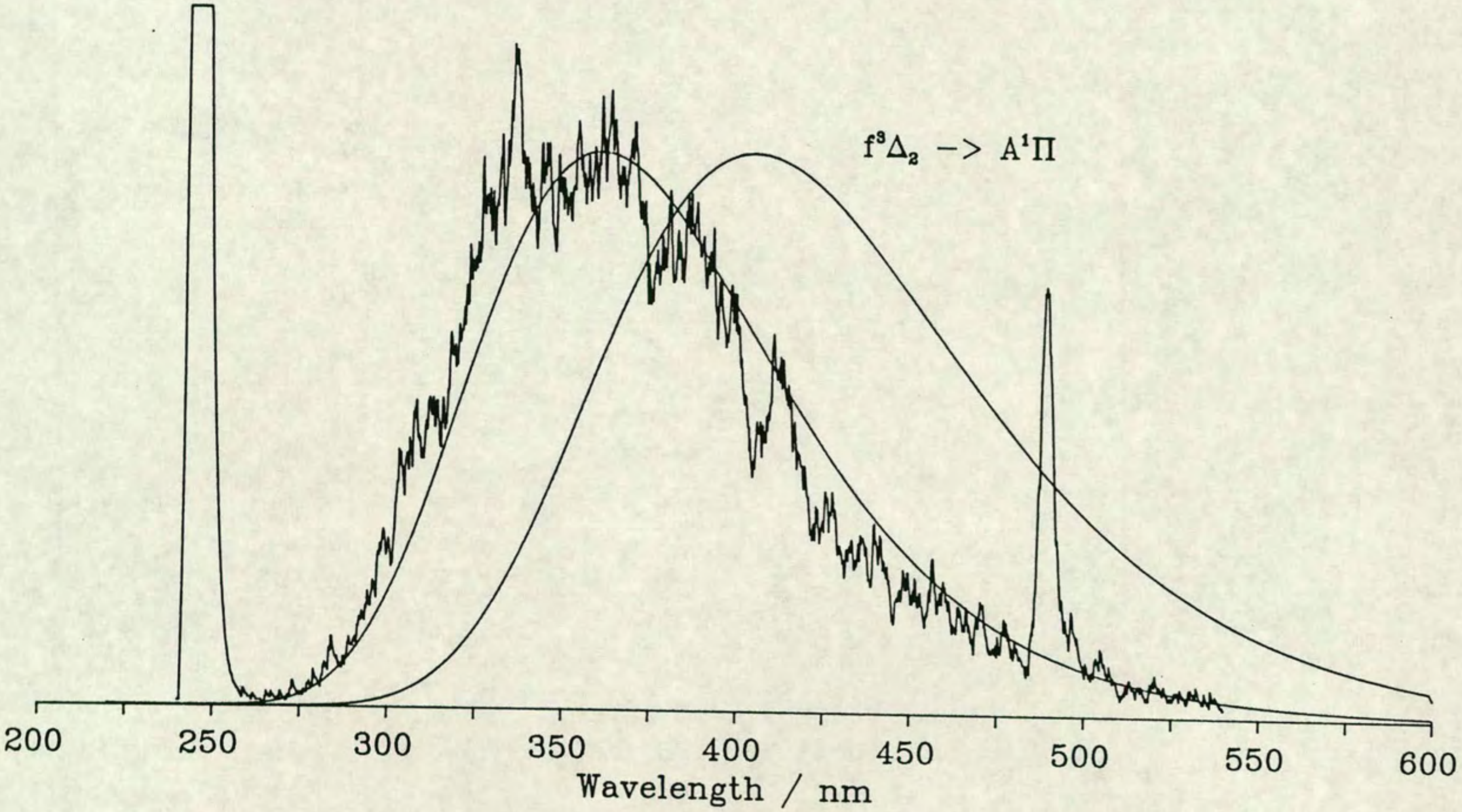

The $g^3\Sigma^-$ (0^+) Rydberg State

In the dispersed fluorescence spectrum of the v' =0 level of the $g^3\Sigma^-$ (0^+) Rydberg state of DCl, presented in figure 5.22, there are two distinct fluorescence bands. An unresolved ion-pair type band is observed to the blue of the laser line because of the coupling of this state with the ion-pair state. No attempt was made to simulated this band since the $g^3\Sigma^-$ (0^+) state coupling was not included in the adiabatic curve for the ion-pair state. The major feature of the spectrum is, however, a broad, asymmetric continuum band centred near 350 nm and slightly more than 100 nm wide. This was initially assumed to be due to the transition $g^3\Sigma^-$ (0^+) $\rightarrow$ $A^1\Pi$ and simulated spectra were calculated on this basis. These are shown in figure 5.22.

Using the HCl^+ Morse oscillator curve for the $g^3\Sigma^-$ (0^+) state gave a poor fit to the observed spectrum. The potential energy curve developed for the $g^3\Sigma^-$ (0^+) Rydberg state from an analysis of its vibrational energy levels may also be used as an upper state for the simulation of fluorescence. The $g^3\Sigma^-$ (0^+) $\rightarrow$ $A^1\Pi$ emission simulated with this curve is blue shifted relative to that seen with the ionic curve and gives a much closer match to both the blue edge and the peak position. It also has a narrower spectral width. This change in the behaviour of the fluorescence is principally a result of the larger R_e, 1.447 Å, of this curve which causes a lower, less steep section of the repulsive curve to be sampled. The relative intensity of the red tail of this band can be increased to improve the simulation using $\mu_{el}(R)$ but would have to vary very rapidly over a short range of R because of the narrow range of vibrational motion in the v' =0 level of the $g^3\Sigma^-$ (0^+) state. The required change in $\mu_{el}(R)$ is greater than two orders of

Figure 5.22 Simulated $g^3\Sigma^+ \rightarrow a^3\Pi$ Dispersed Fluorescence Spectra for DCl

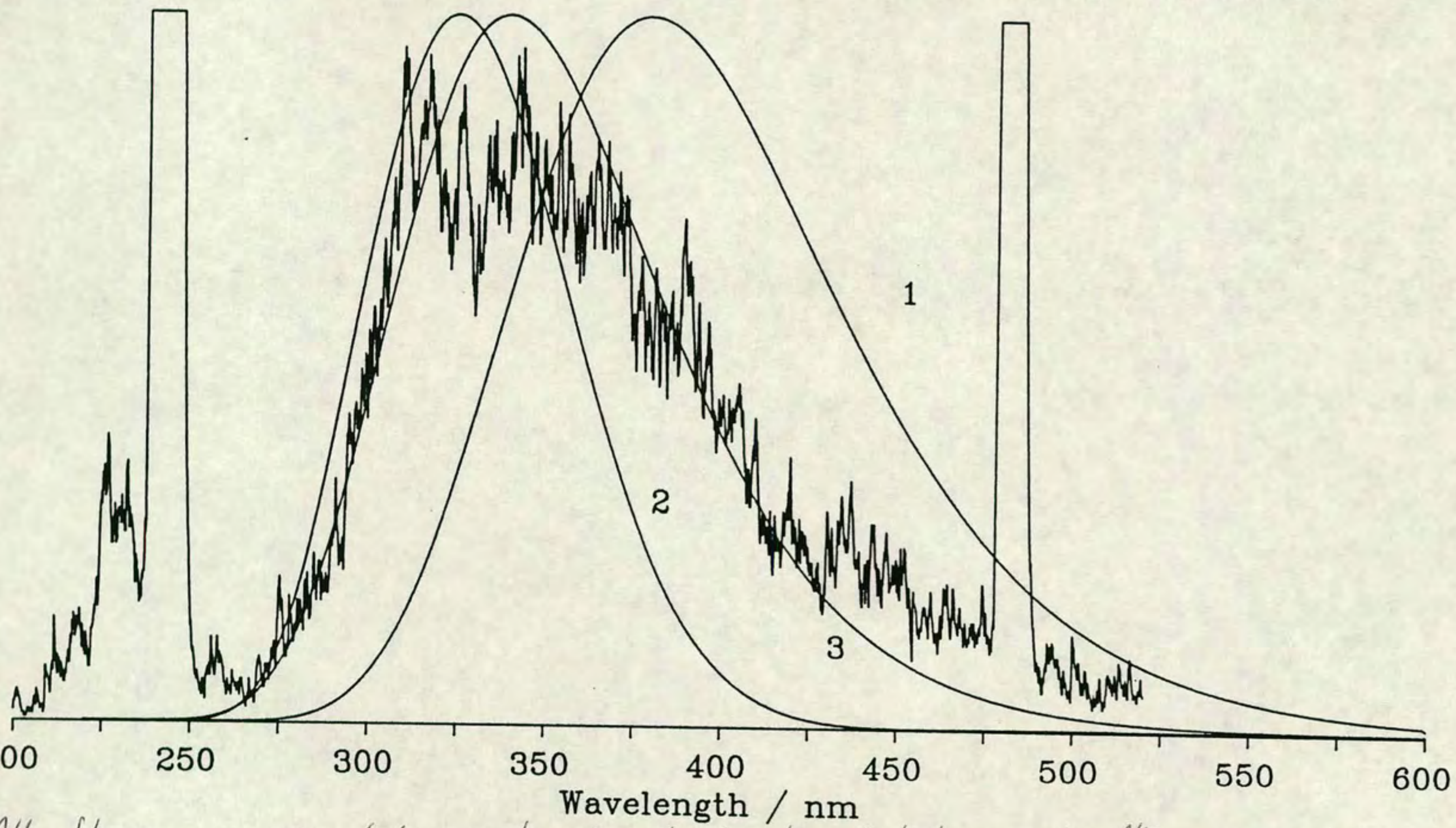

All fluorescence simulations performed with ab initio potential curve for $A^1\Pi$ repulsive valence state [38][66] while the upper state curve was modeled with: 1) HCl^+ Morse oscillator curve [101], 2) RKR curve determined from absorption spectra data [4] [24], or 3) HCl^+ Morse oscillator curve [101] shifted in energy by 4000 cm^{-1} as discussed in text.

magnitude over the range of R between the classical turning points for v' =0 of the upper state, 0.2 Å. Such a rapidly changing $\mu_{el}(R)$ would only occur for rapidly changing electronic configurations in one or both of the initial and final states. There is no evidence in the *ab initio* calculations to suggest that this occurs [37]. A simpler solution is suggested by the similarity of the dispersed fluorescence spectrum from the $g^3\Sigma^-$ (0^+) v' =0 level and that from the $f^3\Delta_2$ (2) state, inferring that this is a $g^3\Sigma^-$ $(0^+) \rightarrow a^3\Pi$ transition not a $g^3\Sigma^-$ $(0^+) \rightarrow A^1\Pi$ transition.

The third simulated spectrum shown in figure 5.22 was calculated with the HCl^+ Morse oscillator curve for the upper state, the *ab initio* $A^1\Pi$ state curve, a constant $\mu_{el}(R)$, and the T_e value adjusted for the calculated difference between the *ab initio* $A^1\Pi$ and $a^3\Pi$ curves. There is very good agreement between the simulated and observed spectra. The slightly longer red tail of this spectrum could be an indication that there is also some $g^3\Sigma^-$ $(0^+) \rightarrow A^1\Pi$ emission but could also be due to the variation of $\mu_{el}(R)$ for the $g^3\Sigma^-$ $(0^+) \rightarrow a^3\Pi$ transition.

The similarity between the emission from the $g^3\Sigma^-$ (0^+) and $f^3\Delta_2$ (2) states strongly supports the use of the HCl^+ Morse oscillator curve for the $g^3\Sigma^-$ (0^+) state. Consequently the observed fluorescence has been assigned as $g^3\Sigma^-$ $(0^+) \rightarrow a^3\Pi$ on the basis of these simulated spectra.

The $E^1\Sigma^+$ (0^+) Rydberg State

Three possible potential energy curves can be used for this state: the ionic curve, the RKR curve and, for v' =0 only, the double minimum adiabatic curve of the ion-pair state. For HCl two levels, v' =0 and 1, of this state have been

Figure 5.23 Simulated Dispersed Fluorescence from the Coupled Rydberg State

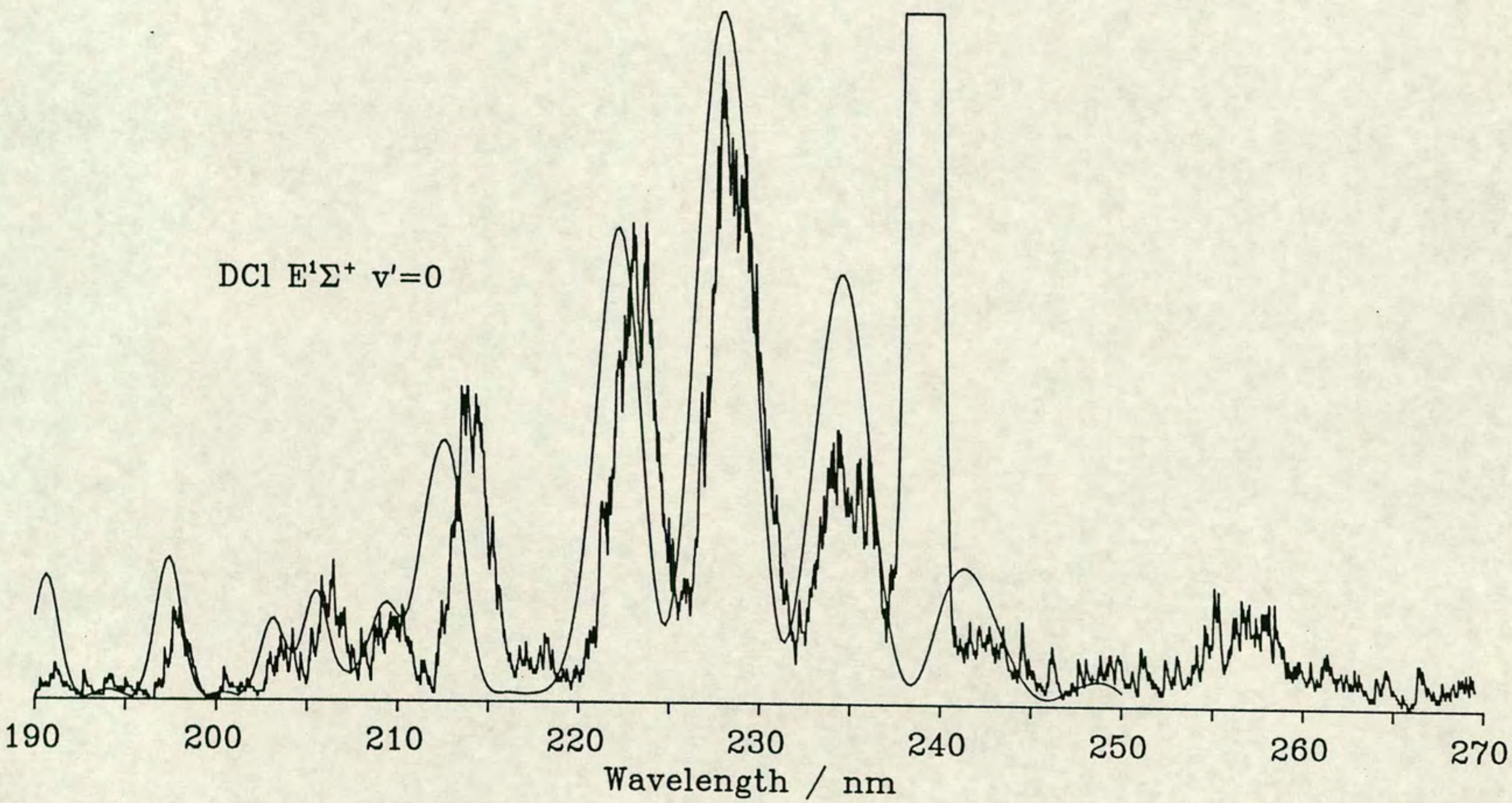

observed in emission while only the v' =0 level has been observed for DCl. Ion-pair type fluorescence is observed for all three levels but can only be simulated for v' =0 using the double minimum curve. A good fit is achieved for DCl with only a small phase shift at shorter wavelength. This spectrum is shown in figure 5.23.

Long wavelength fluorescence was also observed but bore little resemblance to the Rydberg → repulsive state fluorescence observed from other states and there was little success in fitting the observed spectra with Rydberg type simulated spectra. If the RKR curve is used the peak of the fluorescence for v' =0 occurs too far to the blue, 270 nm and the band is too narrow. Also, for v' =1 of HCl the typical bimodal structure seen in the simulation does not match the observed fluorescence. Very little improvement is found if the ionic curve is used. Although the simulated spectrum for the v' =0 level of HCl does fit the observed long wavelength band [74] it does not fit the band at shorter wavelength and there is no correlation between the observed and simulated spectra for DCl.

Fitting the spectra with ion-pair type fluorescence gives much better agreement as shown in figure 5.24. For HCl in particular there is an excellent match for the $B^1\Sigma^+$ $(0^+) \rightarrow A^1\Pi$ fluorescence at all wavelengths longer than the laser line. At shorter wavelengths the spectrum is dominated by the $B^1\Sigma^+$ $(0^+) \rightarrow X^1\Sigma^+$ emission. Although the result for DCl is not as good it is still quite clear that the observed fluorescence is due to a $B^1\Sigma^+$ $(0^+) \rightarrow A^1\Pi$ transition rather than a Rydberg → repulsive state transition.

Figure 5.24 Simulated $E^+\Sigma^+$ -> $A^1\Pi$ Dispersed Fluorescence from HCl and DCl

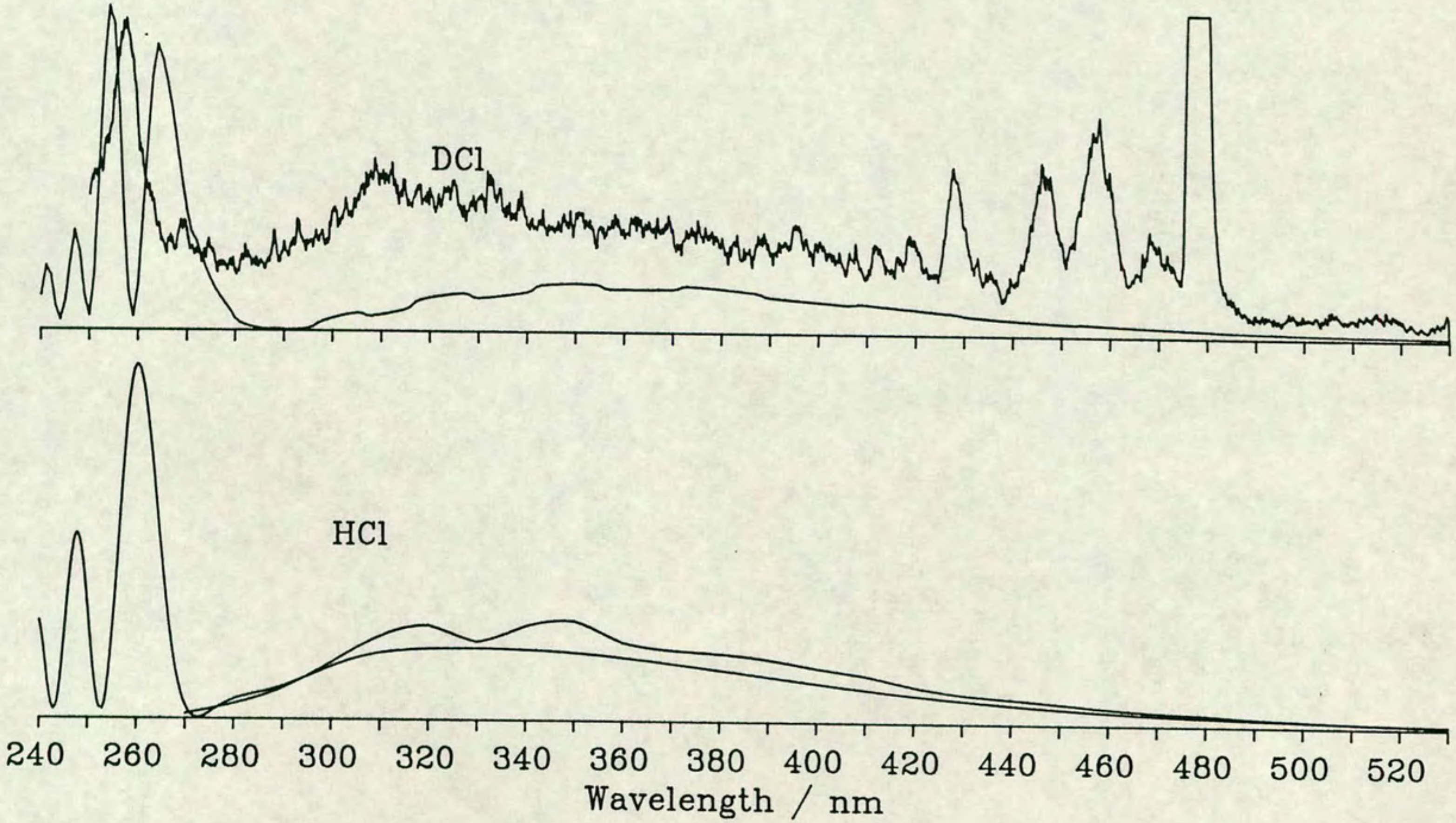

5.3 Coupling of Excited States

The earlier analysis of the potential energy curves of the ion-pair state of HCl and DCl and the simulation of fluorescence from this state have illustrated the strong coupling which exists between this state and a number of 0^+ Rydberg states. It is apparent that the approach used, treating each state individually and developing a potential for it, is unsuccessful. The electronic structure and spectra of the ion-pair state are dominated by its interaction with the 0^+ Rydberg states and therefore the coupling between the states must be explicitly included in any calculation of the molecular constants and simulated spectra.

The breakdown of the Born-Oppenheimer approximation and the homogeneous coupling of electronic states were considered in detail in Chapter 2 and the two limiting cases of diabatic and adiabatic coupling introduced. In this section the coupling of the ion-pair state and the Rydberg states of HCl is discussed and results of calculations on the coupled system are presented. The diabatic representation was used for all of the calculations. Although the adiabatic representation would appear to be more appropriate for the ion-pair state there were no sufficiently accurate adiabatic potential energy curves available. In the diabatic representation the Rydberg states can be represented by the potential determined experimentally for the ground state of the molecular ion or for the relatively unperturbed Rydberg states. Also, there is enough experimental data for the ion-pair state to construct an approximate diabatic potential for this state. Moreover, the diabatic coupling element can be taken as a constant while the adiabatic coupling element is a rapidly varying function of internuclear separation [54].

It is important to recognize that the diabatic (and the adiabatic) representation is, even at its best, an approximation to the true nature of the excited states. Further approximations are introduced in this case by restricting the number of states which can interact. The ion-pair state appears to interact to some extent with all of the 0^+ Rydberg states but the greatest effect is seen for the $E^1\Sigma^+$ (0^+) state and, to a lesser extent, the $g^3\Sigma^-$ (0^+) state, and only these will be considered in the coupling calculations. This restricts the range of the ion-pair state levels to those below 12000 cm^{-1}, corresponding to $v' = 19$ in HCl, above which interactions with other 0^+ Rydberg states, such as the $H^1\Sigma^+$ (0^+) state, become important. Two coupling schemes were considered: the ion-pair interacting with a single Rydberg state and with two Rydberg states simultaneously.

5.3.1 Two Coupled States

The numerical methods used to calculate the energy levels and wavefunctions of a system of two coupled states are very similar to those employed for the case of a single, uncoupled state. However, in this case there are two, coupled, Schroedinger wave equations which must be solved simultaneously. If the total vibronic wavefunction for the coupled system, ψ, is the sum of the Born-Oppenheimer product functions for the two diabatic states 1 and 2 then we have:

$$\psi = \phi_1\chi_1 + \phi_2\chi_2 \text{[1]} \tag{5.12}$$

Substituting this into the Schroedinger wave equation, multiplying by ϕ_1^*, and integrating over the electronic coordinate we get, after rearrangement:

$$-\nabla^2\chi_1 + V_1\chi_1 + H_{12}^{el}\chi_2 = E\chi_1 \tag{5.13}$$

Multiplying by ϕ_2^* instead we get the second coupled equation:

$$-\nabla^2\chi_2 + V_2\chi_2 + H_{12}^{el}\chi_1 = E\chi_2 \tag{5.14}$$

Employing the same approximations which were used for the case of an uncoupled electronic state we have the matrix equations:

$$\mathbf{H}\chi = E\chi \tag{5.15}$$

where **H** is a 2nx2n penta-diagonal matrix and χ is a vector of order 2n. Here n is the number of points in the range of the vibrational motion of the coupled system. The Hamiltonian matrix **H** is given by:

$$\mathbf{H} =$$

$$\begin{bmatrix}
E-V_1-2 & -H_{12}^{el} & 1 & & & & & \\
-H_{12}^{el} & E-V_2-2 & 0 & 1 & & & & \\
1 & 0 & E-V_1-2 & -H_{12}^{el} & 1 & & & \\
 & 1 & -H_{12}^{el} & E-V_2-2 & 0 & 1 & & \\
 & 1 & 0 & E-V_1-2 & -H_{12}^{el} & 1 & & \\
 & & 1 & -H_{12}^{el} & E-V_2-2 & & 0 & 1 \\
 & & & & & & & \\
 & & & & & & &
\end{bmatrix}$$

---

[1] ϕ_i and χ_i are the electronic and nuclear parts of the product function Ψ_i as defined in Chapter 2, page 29, equation (2.5).

and the eigenvector χ by:

$$\chi = \begin{bmatrix} {}^{1}\chi_1 \\ {}^{1}\chi_2 \\ {}^{2}\chi_1 \\ {}^{2}\chi_2 \\ \cdot \\ \cdot \\ \cdot \\ \cdot \\ {}^{i-1}\chi_1 \\ {}^{i-1}\chi_2 \\ {}^{i}\chi_1 \\ {}^{i}\chi_2 \\ {}^{i+1}\chi_1 \\ {}^{i+1}\chi_2 \\ \cdot \\ \cdot \\ \cdot \\ \cdot \\ {}^{n-1}\chi_1 \\ {}^{n-1}\chi_2 \\ {}^{n}\chi_1 \\ {}^{n}\chi_2 \end{bmatrix}$$

The solution of the eigenvalue value equation proceeds in almost the same manner as for the tri-diagonal matrix. However, it is not necessary to solve the penta-diagonal matrix for all n. The coupled wave equations differ from the single state equation only by the coupling term, $H^{el}_{12}\chi_i$ which tends to zero because of the exponential decay of χ_i in a classically forbidden region. Therefore, away from R_c, the single state equation can be used for each state. This is illustrated in figure 5.25 which shows the vibrational wavefunctions for the Rydberg and ion-pair states of a coupled system. Between points R_1 and R_2 the ion-pair wavefunction, χ_2, is zero and only the tri-diagonal form is required. From point R_2 out to R_3 the penta-diagonal form is used because χ_1 and χ_2 are non-zero. For all R greater than R_3 χ_1 has decayed to zero and therefore between this point and the outer turning point, R_4, the tri-diagonal form is used

Figure 5.25
Potential Curves and Wavefunctions of Coupled Ion−pair and Rydberg States

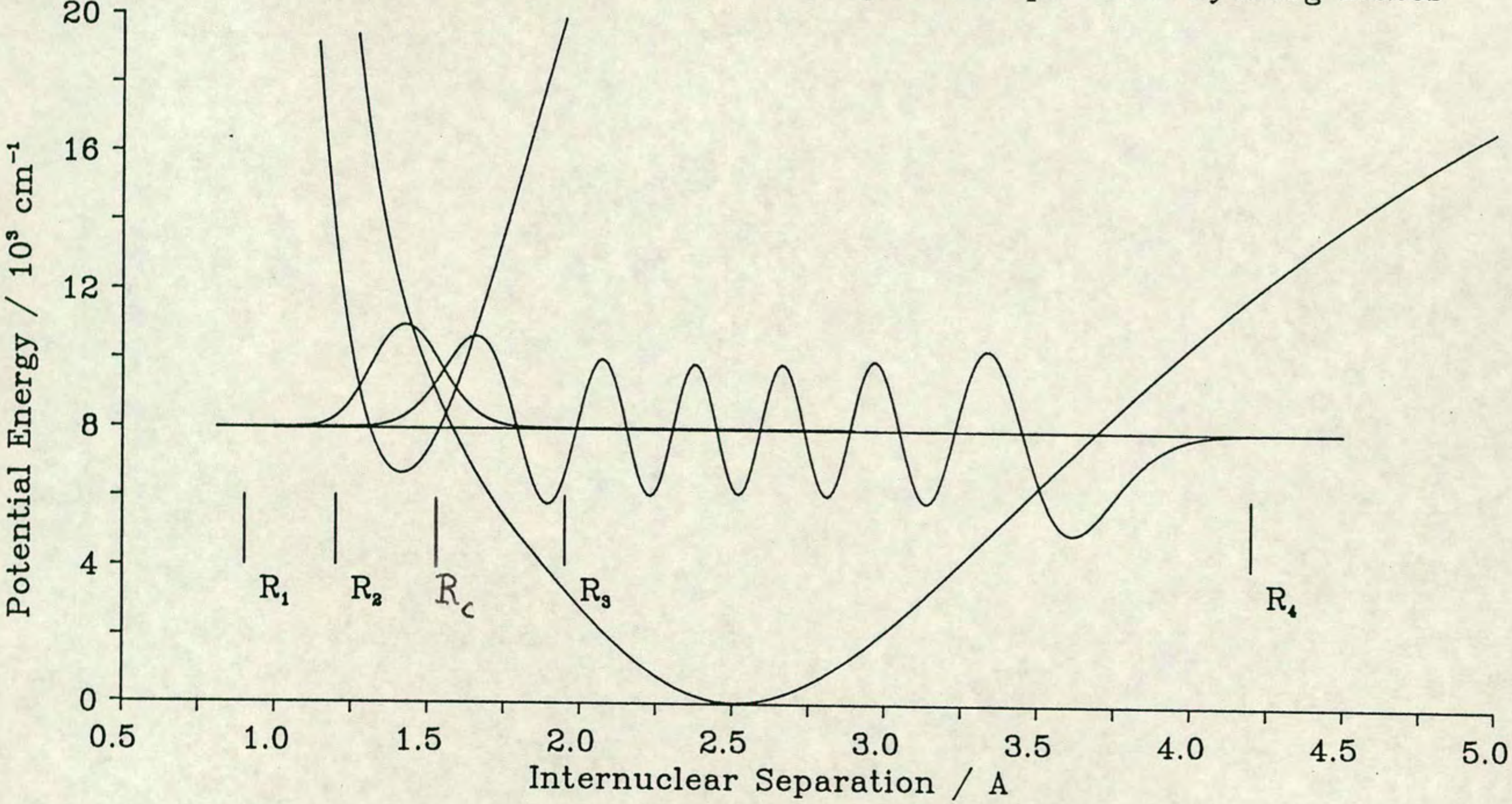

for state 2. The "switching off" of the coupling outside of the region near R_c also prevents any instability in the numerical solution which would result from the trial value of E being far from an eigenvalue of the system.

The two state diabatic coupling scheme was used to calculate the energy levels and B_v values for the coupled Rydberg - ion-pair system. The Rydberg potential, $V_1(R)$, was the Morse oscillator curve taken from the ground state of the molecular ion. The diabatic potential curve 3 of figure 5.4 was used for the ion-pair state. The relative term value of the Rydberg state was adjusted so that, at zero coupling, the v' =0 level was at the correct energy with respect to the potential minimum of the ion-pair state. A constant coupling factor, $H^e = H^{el}_{12}$, was used for all calculations. The value of H^e was varied from zero coupling, $H^e = 0\ cm^{-1}$, to strong coupling, $H^e = 1500\ cm^{-1}$, to investigate the effect of the coupling on the vibrational energy levels and rotational constants of the coupled system. Figures 5.26 shows the effect of increasing H^e on the vibronic energy levels of the coupled system closest to the two lowest levels of the Rydberg state.

The most obvious effect of the coupling between the states is the decrease in vibrational energy for all levels below v' =17. This level is pushed to higher energy. The lowering of all of the vibrational energy levels on the introduction of vibronic coupling was not expected but can be explain by considering the coupling as a perturbation of the ion-pair state by the Rydberg state. From second order perturbation theory it can be seen that interacting levels of different electronic states should repel each. The energy shift of an ion-pair level, i, perturbed by a series of Rydberg levels, k, is given by:

Figure 5.26
Variation of vibronic energy with coupling

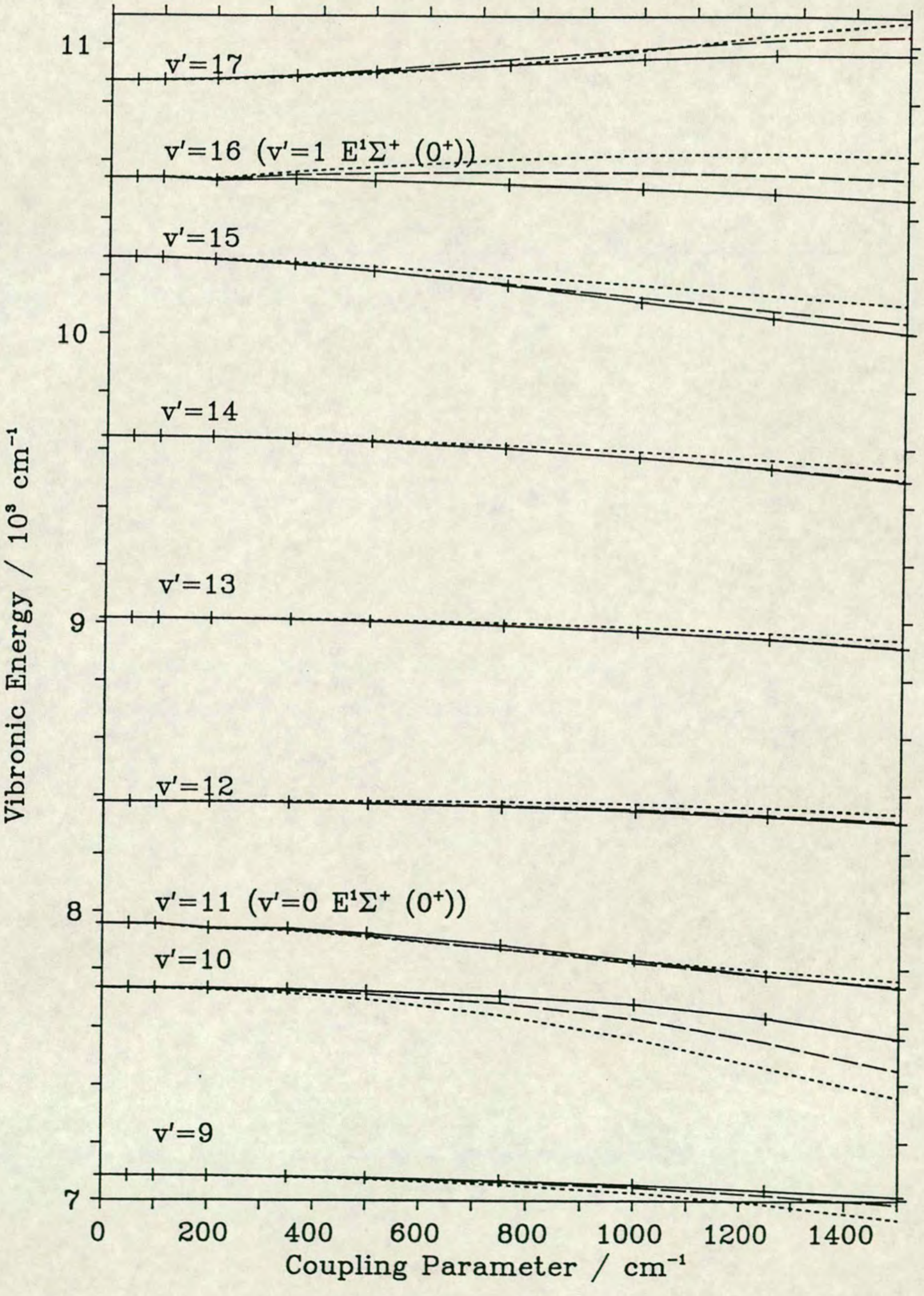

$$\Delta E_i = \sum_{k}^{\text{all}} |\langle \chi_k^o \mid H_{12}^{el} \mid \chi_i^{o} \rangle|^2 (E_i - E_k)^{-1} \qquad (5.16)$$

where the superscript ^{o} indicates that the wavefunctions are unperturbed by coupling between the states [108]. A similar expression gives the shift of each ion-pair level because of its interaction with each of the Rydberg levels. The energy level shifts were not calculated, but, relative values for the shift of the Rydberg levels due to each of the ion-pair levels are presented in table 5.9. The interaction of the v' =0 Rydberg level with the ion-pair state is almost an order of magnitude lower than that of the v' = 1 level. This is due to the poor overlap of the v' =0 wavefunction with the ion-pair wavefunctions. The ion-pair levels nearest to the v' =0 Rydberg level all have a negative shift because they have a much stronger interaction with the v' = 1 level than with the lower one.

The variation of the rotational constants of the coupled system with the coupling parameter, H^e, is shown in figure 5.27. At zero coupling the v' = 11 and v' = 16 levels are of purely Rydberg character and consequently have very high B_v values. As the coupling between the states is increased from zero there is a small increase in the rotational constants of these levels but they then decrease as the Rydberg levels become more strongly mixed with the ion-pair levels. For the strongest coupling used the rotational constants of the v' = 11 and v' = 16 levels have fallen below those of the next lowest levels which are, nominally, ion-pair levels. The v' = 16 level mixes more strongly than the v' = 11 level as shown by the more rapid decrease in rotational constant with increasing coupling of the states. The greatest change in rotational constant of the ion-pair levels is seen for the level immediately below the Rydberg level: for

$H^e = 1000\ \text{cm}^{-1}$, $\Delta B_{10} = 42\%$ but $\Delta B_{12} = 6\%$. The difference between the two levels below and above v' = 16 is less marked, 60% and 31% respectively, but shows the same behaviour. The change in the rotational constant of the coupled levels can not be explained from the simple perturbation theory approach outlined above.

These initial coupling calculations show that it is possible to approximately reproduce the correct rotational constants of the coupled system. However, it is apparent from these calculations that the v' = 1 Rydberg level can not be reproduced with any accuracy using the Morse oscillator curves which have previously been determined. The spacing between the two Rydberg levels with zero coupling puts the v' = 1 level 500 cm^{-1} above its observed position and the shift of the upper level resulting from the coupling with the ion-pair state is too little to correct for such a large shift. In addition at a coupling strength of 750 cm^{-1} the v' = 0 level has the correct rotational constant but is shifted down by the coupling. To compensate for this the relative term value of the Rydberg state must be increased by approximately 200 cm^{-1} which would increase the error in the v' = 1 level by a similar amount. Any increase in the relative term value of the Rydberg state was found to have almost no effect on the vibrational energy of the ion-pair levels of the coupled system. Increasing the Rydberg term value by 50 cm^{-1} produces an increase of approximately 50 cm^{-1} in the vibronic energy of each of the Rydberg levels but less than 3 cm^{-1} in the nearest ion-pair levels. But, this also has the effect of increasing the rotational constant of the Rydberg level and decreasing those of the ion-pair levels which must be compensated for by increasing the coupling between the states.

Table 5.9 Calculated Relative Energy Shifts of Ion-pair Energy Levels due to Interaction with Rydberg State Energy Levels

Ion-pair	Unshifted Rydberg Potential		Shifted Rydberg Potential	
v'	$v'_E = 0$	$v'_E = 1$	$v'_E = 0$	$v'_E = 1$
7	0.04	0.52	0.25	1.89
8	0.17	1.85	0.71	4.35
9	0.71	6.58	1.69	8.15
10	5.65	44.73	3.64	13.47
Rydberg $v'_E = 0$				
12	5.33	35.64	7.11	19.64
13	3.44	19.45	13.49	27.09
14	3.18	15.16	27.82	38.73
15	3.18	12.78	100.00	89.27
Rydberg $v'_E = 1$				
17	3.22	10.87	84.73	43.27
18	3.24	9.16	28.87	6.71
19	3.18	7.58	15.60	0.93

Figure 5.27
Variation of Rotational Constant with Coupling

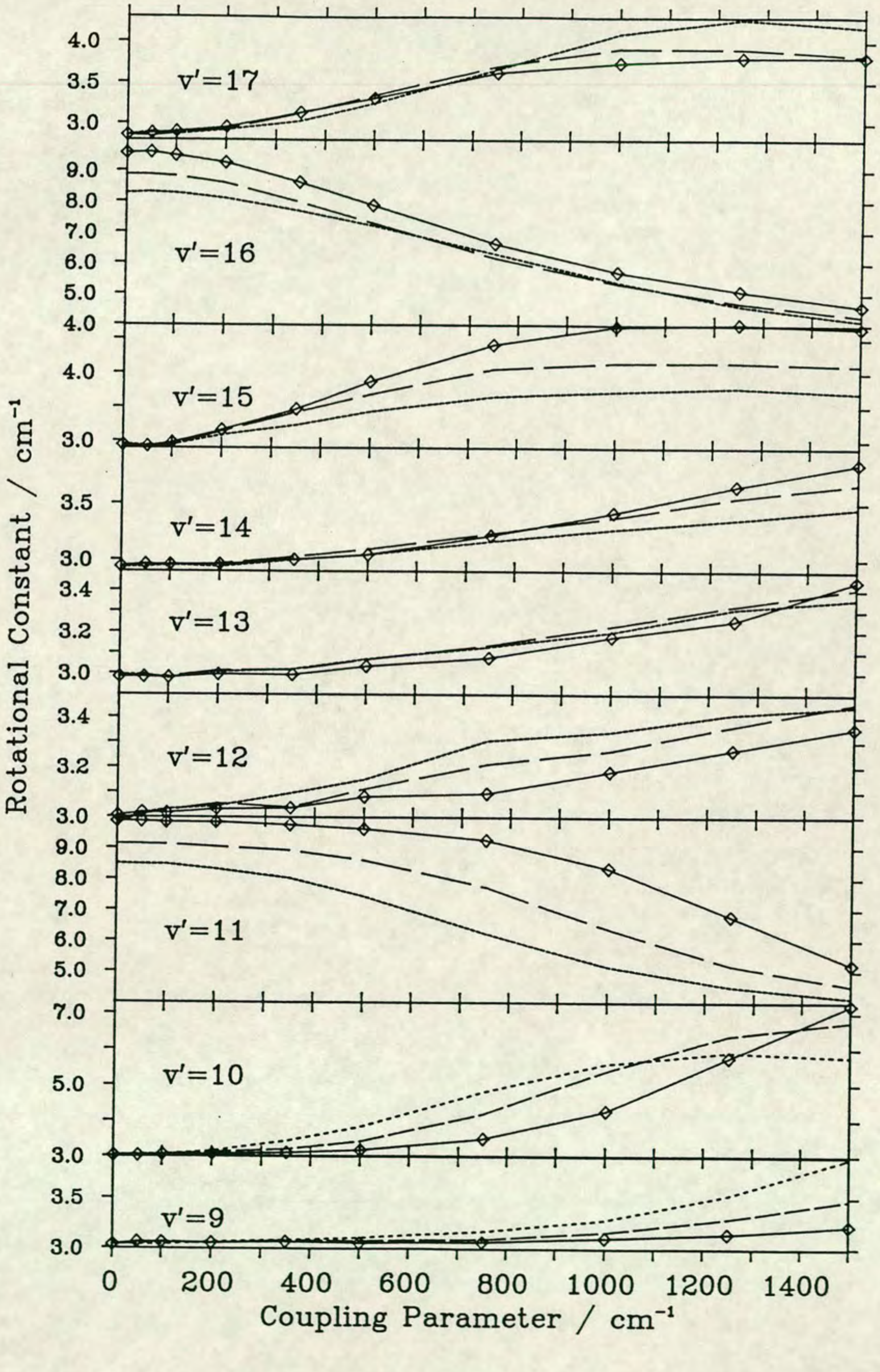

The term value of the Rydberg state and the coupling parameter were varied to try to match the observed vibronic energy and rotational constant of the $v' = 11$ level of the coupled system but it was not possible to fit both parameters simultaneously. This appears to result from the decrease in the interaction of the $v' = 11$ level with the $v' = 10$ level because of the increasing energy difference between the levels. This is only partially compensated for by the increase in the coupling parameter.

The overlap of the wavefunction of the $v' = 11$ level with the $v' \leqq 10$ levels of the ion-pair state, and hence the interaction between these levels, can be increased by translating the Rydberg potential to greater R. The relative values of the shift of ion-pair levels, induced by the coupling with the $v' = 0$ and $v' = 1$ energy levels of this Rydberg potential, are shown in table 5.9 for comparison with those for the original potential.

The translation of the Rydberg potential increases the overlap integral for the $v' = 0$ Rydberg level with all of the ion-pair levels in the energy band near both these two Rydberg levels. An increased overlap with the $v' = 1$ Rydberg level is also seen for most of the ion-pair levels. It is clear from table 5.9 that the shift of the Rydberg potential by 0.1 Å increases the interaction of the $v' = 0$ Rydberg level so that it is of a similar magnitude to that of the $v' = 1$ level. This is apparent in the behaviour of both the vibrational energy levels and the rotational constants with increasing coupling. The variation of the coupled vibrational energy levels with the coupling parameter, H^e, is shown in figure 5.26 where the dashed line is the data for the Rydberg potential translated by 0.05 Å, and the dotted line translated by 0.1 Å from its original position. Also the rotational

Table 5.10 Energy Levels of Two Coupled States for HCl

	G_v / cm^{-1}			B_v / cm^{-1}		
v'	Observed	Zero Coupling	Optimum Coupling	Observed	Zero Coupling	Optimum Coupling
0	431.2	431.4	431.4	2.740	2.744	2.713
1	1276.6	1276.8	1275.5	2.765	2.773	2.780
2	2091.0	2091.0	2086.2	2.792	2.806	2.823
3	2875.0	2875.6	2866.4	2.832	2.835	2.840
4	3631.0	3631.7	3620.1	2.874	2.877	2.870
5	4360.6	4361.5	4348.8	2.921	2.924	2.924
6	5065.0	5068.3	5051.8	2.968	2.972	2.990
7	5746.5	5754.5	5733.5	3.046	3.011	3.063
8	6402.6	6424.7	6398.4	3.156	3.034	3.089
9	7016.5	7083.6	7046.1	3.682	3.037	3.175
10	7610.8	7734.5	7650.0	4.808	3.024	4.078
11	7957.0	8174.5	7956.0	6.642	8.498	6.659
12	8384.4	8378.3	8392.5	4.301	3.000	3.448
13	8923.6	9014.8	9002.4	4.012	2.972	3.161
14	9454.3	9643.4	9615.7	4.270	2.938	3.124
15	9849.6	10263.6	10210.3	5.877	2.899	3.433
16	10095.5	10757.4	10701.4	6.330	8.268	5.448
17	10582.4	10874.7	10993.3	3.809	2.855	4.588
18	11108.6	11476.0	11492.7	3.756	2.807	3.067

See notes to Table 5.1

[1] Coupling strength, H^{e}, = 750 cm^{-1}

[2] Coupled levels with Rydberg state origin.

constants for the two Rydberg levels do not diverge with increasing H^e as observed for the original Rydberg potential.

Moreover, with the translated Rydberg potential, it is possible to simultaneously match the vibrational energy and rotational constant of the $v' = 0$ Rydberg level although the rotational constants of the $v' = 10$ and $v' = 12$ ion-pair level are too low by between 15 and 20%. The vibrational energy levels and rotational constants for coupled system are shown in table 5.10. A poor match is achieved for the $v' = 1$ Rydberg levels and the higher ion-pair levels. The initial large errors in the vibrational energy of these levels are increased by the coupling of the states which suggests that the potentials used are not suitable for the coupling calculations.

5.3.2 Three Coupled States

In the previous section the coupling of the ion-pair state with a single Rydberg state, the $E^1\Sigma^+$ (0^+) state, was discussed. A second Rydberg state, the $g^3\Sigma^-$ (0^+) state, also interacts strongly with the ion-pair state at a similar energy. The very low rotational constants observed for the $v' = 0$ levels of both Rydberg states suggest that the coupling strength for the interaction of the $g^3\Sigma^-$ (0^+) state with the ion-pair state is of a similar magnitude to that for the $E^1\Sigma^+$ (0^+) state. If the effect of the coupling was a local perturbation of the ion-pair state vibrational levels then the two interactions could be treated separately. However, it can be seen from the results of the two state coupling calculations that a single Rydberg vibrational level perturbs a wide range of ion-pair vibrational levels. Therefore the coupling of the ion-pair state with each of the two Rydberg states should be considered simultaneously.

The three state coupling scheme was developed in the same manner as the two state coupling scheme. The wavefunction for the coupled system, ψ, was a sum of three Born-Oppenheimer product functions:

$$\psi = \phi_1\chi_1 + \phi_2\chi_2 + \phi_3\chi_3 \tag{5.17}$$

where state 1 was the $E^1\Sigma^+$ (0^+) state, 2 was the $g^3\Sigma^-$ (0^+) state, and 3 the ion-pair state. The three coupled Schroedinger wave equations for this system are:

$$-\nabla^2\chi_1 + V_1\chi_1 + H^{el}_{13}\chi_3 = E\chi_1 \tag{5.18}$$

$$-\nabla^2\chi_2 + V_2\chi_2 + H^{el}_{23}\chi_3 = E\chi_2 \tag{5.19}$$

$$-\nabla^2\chi_3 + V_3\chi_3 + H^{el}_{13}\chi_1 + H^{el}_{23}\chi_2 = E\chi_3 \tag{5.20}$$

where the coupling between the two Rydberg states, H^{el}_{12}, was assumed to be zero. The eigen value problem was solved in a similar manner to that described earlier for the single state and for the two coupled state caculations. But in this case the node count was achieved by direct numerical quadrature rather than by the Sturm sequence technique. As in the two state coupling scheme the coupled equations were only used near the crossing of the potentials. The two Rydberg states were tabulated over the same range of R. In fact the Rydberg potentials were identical apart from their relative term values, and all three potentials had the same starting point. The three coupled equations were integrated outwards simultaneously from the common starting point to the point where both Rydberg wavefunctions had decayed effectively to zero. The wave equation for the ion-pair state was then integrated by itself. Wavefunctions for the coupled levels were generated by back substitution into the matrix form of the wave equation.

Effect on Energy Levels

The Rydberg state potential used for both the $g^3\Sigma^-$ (0^+) and $E^1\Sigma^+$ (0^+) Rydberg states was the same as that used for the $E^1\Sigma^+$ (0^+) state in the two coupled state calculations. The shift in the potential by 0.1 Å to larger R was also used. Only the band of energy levels near the two Rydberg v' =0 levels were considered in the coupling calculations for the reasons discussed earlier. The vibrational levels of the coupled system were v' =7 to v' =14 which correspond to v' =7, 8, and 9 of the ion-pair state, v' =0 of the $g^3\Sigma^-$ (0^+) state, v' = 10 of the ion-pair state, v' =0 of the $E^1\Sigma^+$ (0^+) state, and v' =11 and 12 of the ion-pair state, respectively. The relative term values of the Rydberg states were chosen so that the v' =0 levels had the correct vibrational energy at zero coupling of the states. These were T_e = 6633 cm^{-1} and T_e = 5940 cm^{-1} for the $E^1\Sigma^+$ (0^+) and $g^3\Sigma^-$ (0^+) states, respectively.

The coupling strength and term value of the $g^3\Sigma^-$ (0^+) state were adjusted to match the observed values of the vibrational energy and the rotational constant. A coupling strength of 640 cm^{-1} and an increase in the term value of 85 cm^{-1} were required to match the experimental data. All of the ion-pair state vibrational energy levels were shifted to lower energy by the coupling which improved the fit of most of these levels. The shift in the v' = 7 and 13 levels increases the error in the calculated energy of these levels. The calculated vibrational energy levels and rotational constants for the coupled system are shown in table 5.11 along with the observed data.

Table 5.11 Three State Coupling of the Ion-pair and Rydberg States of HCl

v'	Observed	Zero Coupling	Two States	Three States	DCl Parameters
Vibrational Energy Levels					
7	5746.5	5777.0	5743.2	5721.3	5734.8
8	6402.6	6425.0	6409.0	6381.1	6398.8
9	7016.5	7084.2	7044.2	7005.0	7035.0
10[1]	7264.4	7264.5	7264.8	7264.5	7270.0
11	7610.8	7735.1	7730.8	7646.8	7689.4
12[2]	7957.0	7957.5	7557.5	7957.4	8033.6
13	8384.4	8379.0	8363.2	8383.1	8387.2
14	8923.6	9015.5	8987.3	8980.6	8991.8
Rotational Constants					
7	3.046	3.012	3.029	3.058	3.039
8	3.156	3.034	3.079	3.132	3.093
9	3.682	3.037	3.636	3.653	3.495
10[1]	7.633	8.501	7.611	7.639	7.865
11	4.808	3.024	3.220	4.206	3.622
12[2]	6.642	8.501	8.501	6.643	7.315
13	4.301	3.001	3.106	3.649	3.600
14	4.012	2.972	3.153	3.315	3.213
Coupling Parameters					
T_e of State 1		6633	6633	6853	6845
T_e of State 2		5940	6025	6010	6000
H_{13}		0	0	1005	725
H_{23}		0	640	500	475

See notes to Table 5.1

[1] Coupled level originating from v'=0 level of $g^3\Sigma^-(0^+)$ Rydberg state

[2] Coupled level originating from v'=0 level of $E^1\Sigma^+(0^+)$ Rydberg state

The coupling between the $E^1\Sigma^+$ (0^+) state and the ion-pair state was increased from zero and the term value increased to compensate for the resulting shift of the Rydberg level to lower energy. The increased coupling of this state had the unexpected effect of increasing the apparent coupling of the $g^3\Sigma^-$ (0^+) state with the ion-pair state although the coupling element between the two Rydberg states was zero. The coupling between the $g^3\Sigma^-$ (0^+) state and the ion-pair state was reduced to maintain the correct value of the rotational constant of this level. An improvement was seen in the vibrational energy of the ion-pair levels because of the coupling of the $E^1\Sigma^+$ (0^+) state: the v' = 13 level was shifted to higher energy, closer to the observed energy of this level, and the v' = 11 level was shifted to lower energy. The lowest ion-pair vibrational levels also experience a downward energy shift and are pushed below their observed energy by a small amount. A good fit to the observed data was achieved with the coupling strengths and relative term values shown in column three of table 5.11, which were optimised for the Rydberg levels. The very large rotational constants observed experimentally for some of the ion-pair levels could not be reproduced without a much greater coupling which gave very poor results for the vibrational energy of all of the coupled levels and for the rotational constants of the Rydberg levels.

The three state coupling calculation was also applied to DCl using the same potentials as used for HCl. Very poor results were obtained using the coupling parameters which gave the best fit to the HCl data but they could be improved by reducing the strength of the coupling of the $E^1\Sigma^+$ (0^+) state with the ion-pair state. These parameters did not give a good fit if used for HCl. The calculated

[1] A 'good fit" is achieved if the calculated values are within 20 cm^{-1} (20%) of the observed values for G_v (B_v).

Table 5.12 Three State Coupling of the Ion-pair and Rydberg States of DCl

v'	Observed	Zero Coupling	Set One	Set Two	HCl Parameters
Vibrational Energy Levels					
12	6702.0	6731.1	6699.8	6692.1	6679.0
13	6895.9	6952.0	6893.0	6889.4	6885.4
14	7149.2	7202.0	7170.5	7161.1	7146.9
15	7498.9	7668.9	7581.4	7550.7	7500.6
16	7704.7	7805.0	7713.9	7700.7	7678.3
17	8058.0	8132.1	8096.7	8090.4	8077.4
18	8423.7	8591.4	8514.3	8505.4	8488.4
19	8712.1	8924.9	8791.4	8789.1	8788.8
Rotational Constants					
12	1.82	1.563	1.662	1.679	1.716
13	4.4	4.389	4.225	4.201	4.133
14	2.2	1.561	1.685	1.724	1.806
15	2.86	1.556	2.616	2.859	3.144
16	3.296	4.389	3.177	2.879	2.533
17	2.17	1.548	1.744	1.773	1.802
18	2.41	1.539	2.001	2.006	2.017
19	3.25	4.308	3.245	3.225	3.109
Coupling Parameters					
T_e of State 1		6845	6845	6855	6853
T_e of State 2		6000	6000	6000	6010
H_{13}		0	725	850	1005
H_{23}		0	475	475	500

See notes to Table 5.1

[1] Coupled levels originating from the $v'=0$ and 1 levels of the $g^3\Sigma^-(0^+)$ Rydberg state.

[2] Coupled level originating from the $v'=0$ level of the $E^1\Sigma^+(0^+)$ Rydberg state.

vibrational energy levels and rotational constants are shown in table 5.12 for the case of zero coupling, two sets of parameters which gave good fits for DCl, best fit coupling for HCl and the observed values. The observed rotational constant of the v' =0 level of the $g^3\Sigma^-$ (0^+) state, 4.4 cm^{-1}, is slightly greater than the calculated value for zero coupling of this state with the ion-pair state, which is the maximum value that the rotational constant can have. The calculated value can be increased by decreasing the shift which was applied to the Rydberg potentials to give a good fit to the HCl data. But, the coupling scheme is an approximation and was not expected to exactly reproduce the observed data and so the Rydberg potentials were left unaltered.

The vibrational levels at higher energy than those considered above were not well reproduced in the three state coupling scheme. The calculated vibrational energy level spacing for the Rydberg states is much greater than the observed spacing and the coupling with the ion-pair state does not shift the Rydberg levels far enough to lower energy. Moreover the vibrational levels of the uncoupled ion-pair state also have too great a vibrational spacing at higher energies although some of the lower levels, such as v' =5, 6, 7, and 8 are at too low an energy when the Rydberg state coupling is included. Apart from these problems, which stem from incorrect potentials for the ion-pair and Rydberg states, at higher energy there are other Rydberg states which can interact with the ion-pair state. Because of the strength of the interactions, all of the states which couple with the ion-pair state should be included in a multi-state coupling scheme but at the lower energies it is possible to use only the $g^3\Sigma^-$ (0^+) and $E^1\Sigma^+$ (0^+) Rydberg states.

Table 5.13 Energy Levels and Rotational Constants for Adiabatic Potentials Calculated from Diabatic Coupling Strengths in HCl

	G_V / cm^{-1}		B_V / cm^{-1}	
v'[1]	Calculated	Observed	Calculated	Observed
0	430.8	431.2	2.743	2.740
1	1274.9	1276.6	2.771	2.765
2	2087.3	2091.0	2.803	2.792
3	2869.8	2875.0	2.842	2.832
4	3623.1	3631.0	2.888	2.874
5	4349.4	4360.6	2.943	2.921
6	5049.9	5065.0	3.007	2.968
7	5725.3	5746.5	3.094	3.046
8	6368.4	6402.6	3.328	3.156
9	6912.2	7016.5	4.769	3.682
10	7268.6[2]	7264.4[5]	5.286[2]	7.633[5]
11	7785.6	7610.8[6]	3.689	4.808
12	7915.0[3]	7957.0	8.380[3]	6.642[6]
13	8386.4	8384.4	3.433	4.301
14	8985.6	8923.6	3.462	4.012
15	9569.1	9454.3	3.544	4.27
16	10139.7	9849.6	3.552	5.877
17	10346.3[3]	9969.7[5]	8.171[3]	8.12[5]
18	10707.6	10095.5[6]	3.444	6.330[6]
19	11153.6[4]	10582.4	7.156[4]	3.809
20	11278.5	11108.6	3.287	3.756
21	11850.5	11641.2	3.147	3.591
22	12419.1	12144.3	3.042	4.335
23	12792.7[3]	12321.7[5,6]	8.007[3]	6.3[5,6]
24	12980.3	12742.2	2.967	3.79
25	13531.9	13263.6	2.907	3.282

See notes to Table 5.1

[1] Vibrational numbering includes all levels of the three state coupled system

[2] Level localised in inner minimum of double minimum adiabatic potential.

[3] v'=0,1 and 2 of the second adiabatic potential, see figure 5.28

[4] v'=0 of the third adiabatic potential, see figure 5.28

[5] Coupled levels derived from the $g^3\Sigma^-(0^+)$ Rydberg state

[6] Coupled levels derived from the $E^1\Sigma^+(0^+)$ Rydberg state.

All of the coupling calculations were conducted in the diabatic representation which may not be the most appropriate starting representation for the interaction of the Rydberg and ion-pair states of HCl. There is, however, a direct connection between the potential energy curves of states which are coupled in the diabatic and in the adiabatic representations. This was discussed in chapter 2 for the case of two coupled states and can be extended to the case of three coupled states so that adiabatic potentials can be constructed for the three states from the diabatic potentials and coupling factors. The calculated vibrational energy levels and rotational constants for the adiabatic potentials are shown in table 5.13 for comparison with the observed data and the diabatic and adiabatic potentials are shown in figure 5.28. For the lowest levels, $v' < 16$, there is quite good agreement for the vibrational energy level but a poor match for the rotational constants. At higher energies the calculated vibrational energies are too high and force the Rydberg and ion-pair levels out of step with each other. The energy levels were calculated with no coupling between the states because the matrix elements were not known. Both potentials and coupling matrix elements can be calculated by *ab initio* methods in the adiabatic representation. These would have been of great assistance in this project but were not available.

Effect on Dispersed Fluorescence Spectra

Simulated dispersed fluorescence spectra for the coupled Rydberg - ion-pair → ground state transitions were calculated using vibrational wavefunctions for the emitting level generated by the three state diabatic coupling program. Essentially the same simulation program was used to calculate these spectra as was used for the simulation of all other fluorescence

Figure 5.28
Potential Curves of Coupled States in the Diabatic and Adiabatic Repesentations

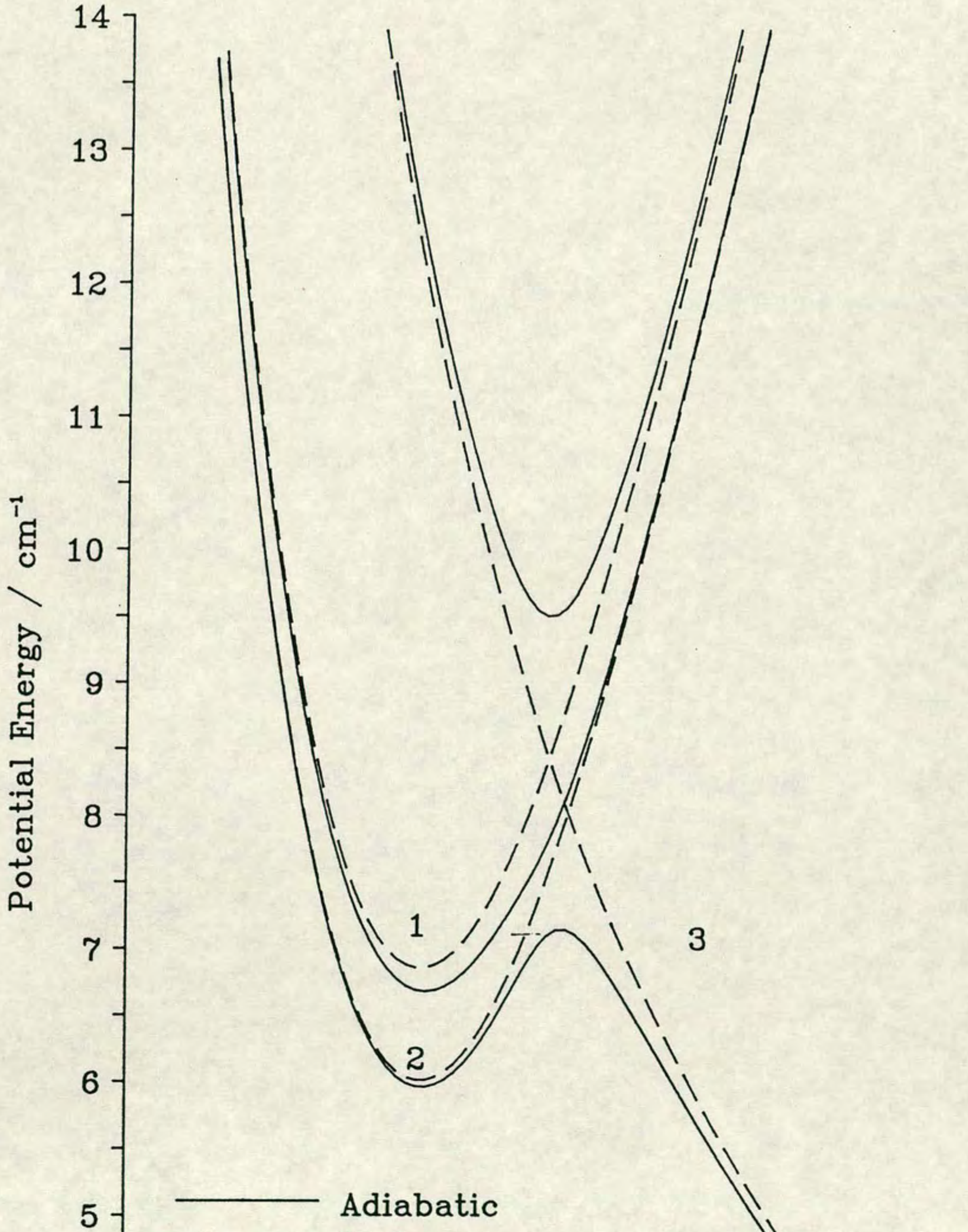

spectra. The program was altered to accept the vibrational energy, the inner and outer turning points and the tabulated wavefunction of the initial state of the transition rather than determining these internally from a tabulated potential. A check was made to ensure that the two methods of calculating fluorescence spectra gave compatible results. For a number of vibrational levels of the ion-pair state of HCl and DCl simulated dispersed fluorescence spectra of the $B^1\Sigma^+ (0^+) \rightarrow X^1\Sigma^+$ transition were calculated using *a)* just the simulation program and *b)* the combination of the coupling program to generate a wavefunction and the simulation of the spectrum using this wavefunction. The same ion-pair state potential was used in both cases with zero coupling strength between the ion-pair state and the Rydberg states. A comparison of the two wavefunctions generated by the two programs revealed only slight differences between them, which were due to the differences in the accuracy with which the energy levels of the potential were determined and the different techniques used to determine the wavefunctions. The resulting differences in the simulated spectra were of a negligible size.

The wavefunction of a vibrational energy level of the coupled Rydberg ion-pair system is a linear combination of the vibrational wavefunctions of the individual states. Because the Rydberg states have a very much smaller range of vibrational motion than the ion-pair state the coupled wavefunction in the outer well will remain the same as the uncoupled one, apart from a change of phase. This can be seen if we consider the WKB approximation to the wavefunction:

$$\chi_v(R) = (k_v)^{-\frac{1}{2}} \sin\left(\int_{R''}^{R} k_v dR + \delta \right) \tag{5.21}$$

where k_v is the local wavenumber

$$k_v = \hbar(2\mu(E - V_v))^{\frac{1}{2}} \tag{5.22}$$

R" is the inner classical turning point and δ is a phase shift. For the primitive WKB wavefunction of an uncoupled potential δ is taken as $\pi/4$ and compensates for motion in the classically forbidden region. It has a term dependent on the momentum at the current internuclear separation and a phase term which depends on the behaviour on the potential at shorter R. The phase shift of the coupled wavefunction relative to the uncoupled one will depend on the strength of the coupling and on the phase and local wavelength of the Rydberg state wavefunction at the energy of the coupled level. For a vibrational level which at zero coupling was a pure Rydberg level the wavefunction in the outer well has the form of the nearest pure ion-pair vibrational level. Generally the amplitude of the wavefunction in the outer well will be considerably smaller than that in the inner well.

The calculated vibrational wavefunction for the v' = 13 and v' = 15 coupled Rydberg - ion-pair levels of HCl and DCl are show in figure 5.29 with the wavefunction of the corresponding pure ion-pair levels. The coupling parameters were: T_e of state 1 = 6853 (6845) cm^{-1}, T_e of state 2 = 6010 (6000) cm^{-1}, H_{13} = 1005 (725) cm^{-1}, and H_{23} = 500 (475) cm^{-1} for HCl (DCl). At large R, in the outer well of the coupled state, there is, as expected, a great similarity between the coupled and uncoupled wavefunctions. The phase shift between the two wavefunctions for the HCl level is effectively zero. A larger, but still quite

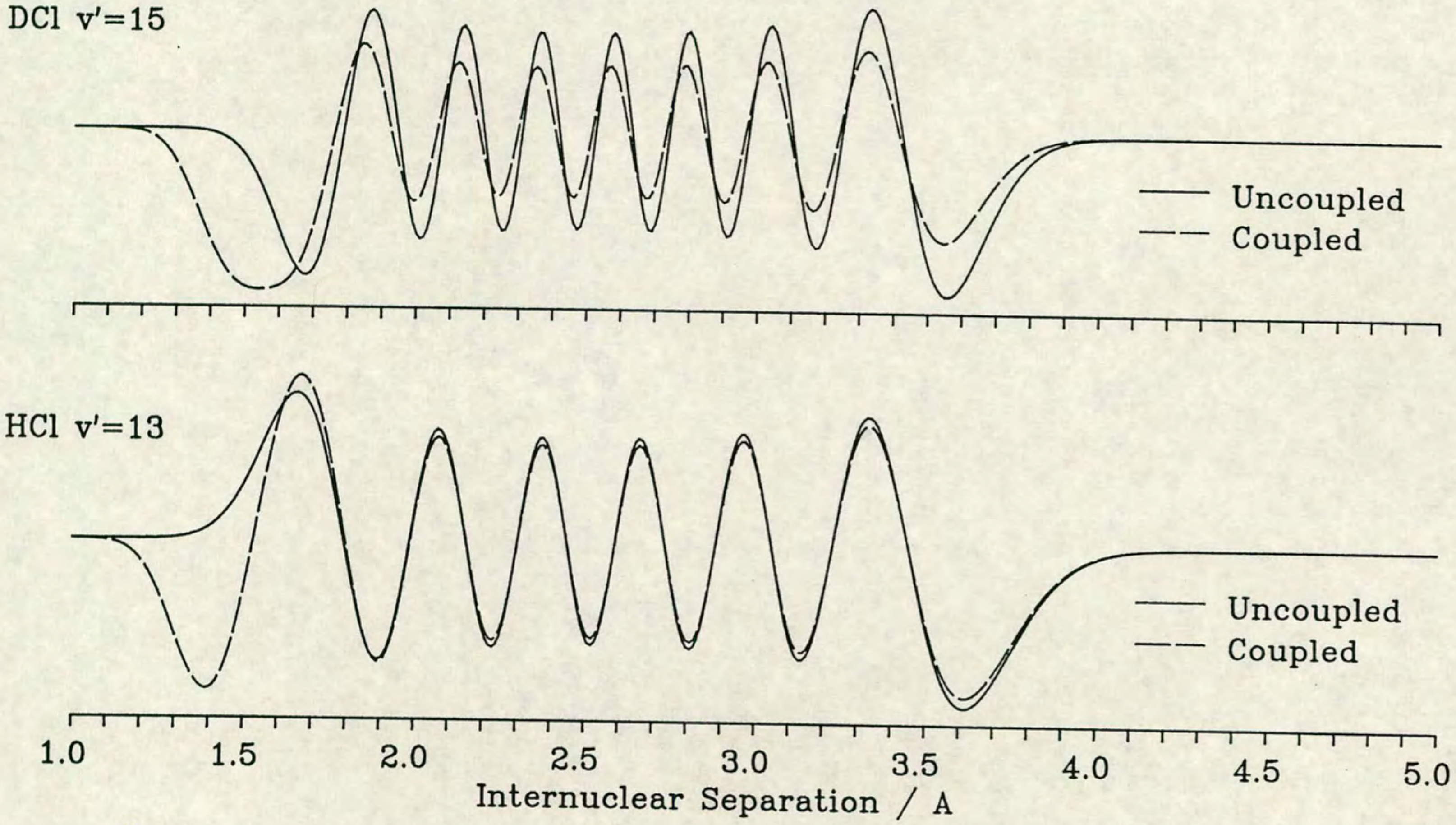

Figure 5.29 Wavefunctions of Coupled Vibronic Levels

small, shift is seen for DCl. The change in the wavefunction because of the coupling will be reflected in the fine structure of the bound-free fluorescence spectrum of the $B^1\Sigma^+$ $(0^+) \rightarrow X^1\Sigma^+$ transition.

Near R_e the wavefunctions undergo a much greater perturbation when the coupling is introduced. In both the HCl and DCl levels the ion-pair state interacts most strongly with the $E^1\Sigma^+$ (0^+) Rydberg state. The contribution of the $g^3\Sigma^-$ (0^+) state to the coupled wavefunction is an order of magnitude less than that of either the $E^1\Sigma^+$ (0^+) state or the ion-pair state. For DCl, the $v'=15$ coupled level is at lower energy than $v'=0$ of the uncoupled Rydberg state. Therefore, there is no additional node introduced into the coupled wavefunction by the coupling. For HCl, the coupled level, $v'=13$, lies at higher energy than $v'=0$ of the Rydberg state and this forces an extra node into the wavefunction. By chance, the phase shift of the wavefunction at large R is zero.

Bound-free $B^1\Sigma^+$ $(0^+) \rightarrow X^1\Sigma^+$ fluorescence spectra from three vibrational levels of DCl, namely $v'=15$, 17 and 18 (or $v'=14$, 15 and 16 as assigned in reference [20]), and two levels of HCl, namely $v'=13$ and 14 (or $v'=11$ and 12), in the energy range considered in the three state diabatic coupling calculations were observed experimentally. They are compared with the spectra simulated for these transitions using wavefunctions calculated by the coupling program in figure 5.30 for HCl and figure 5.31 for DCl. For HCl the $v'=13$ level there is little change in the simulated spectrum from this level on the introduction of Rydberg state coupling which is consistent with the small or zero change observed in the vibrational wavefunction.

Figure 5.30
Simulated Fluorescence from the Ion-pair State of HCl using Coupled Wavefunctions

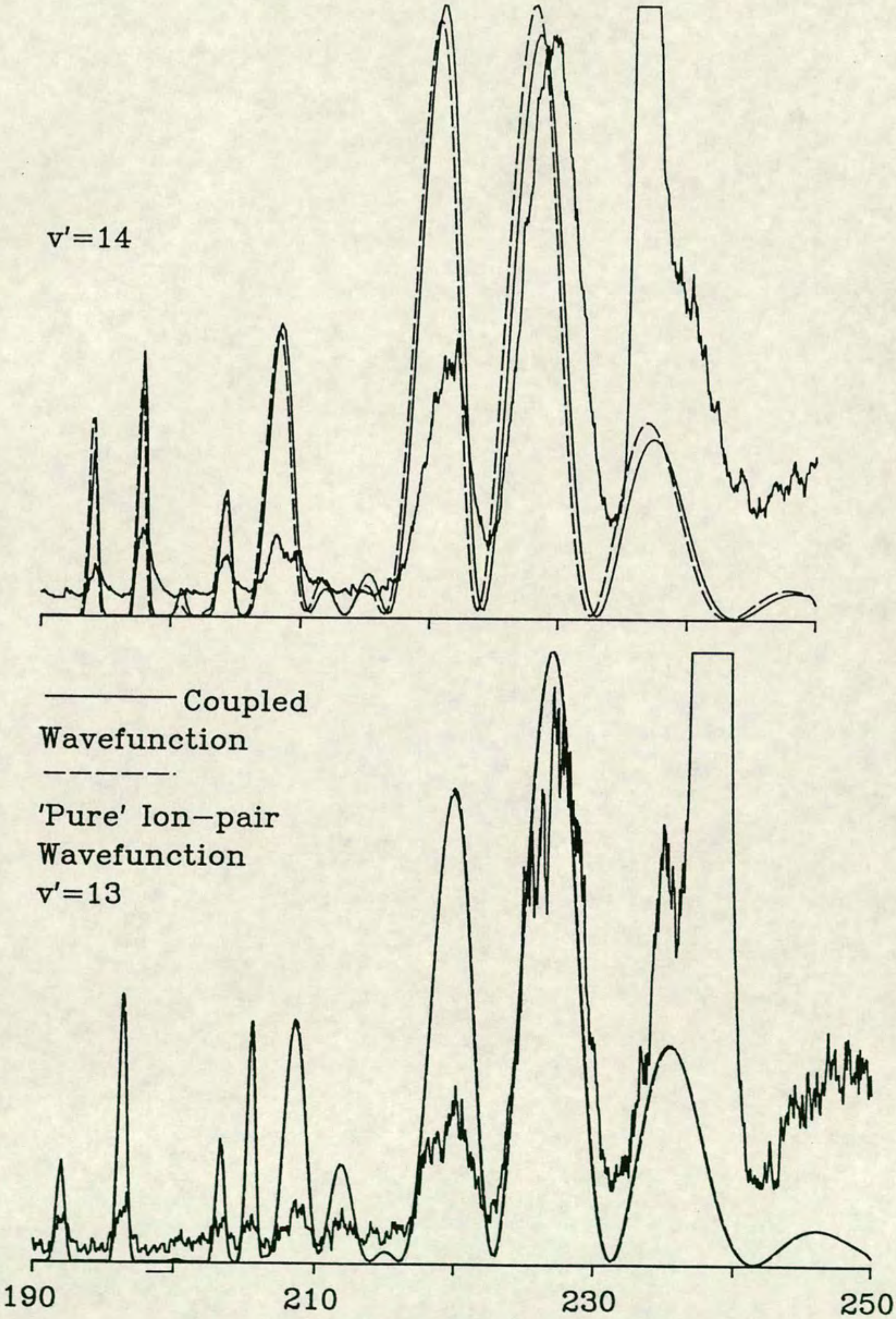

Figure 5.31
Simulated Fluorescence from the Ion–pair State of DCl using Coupled Wavefunctions

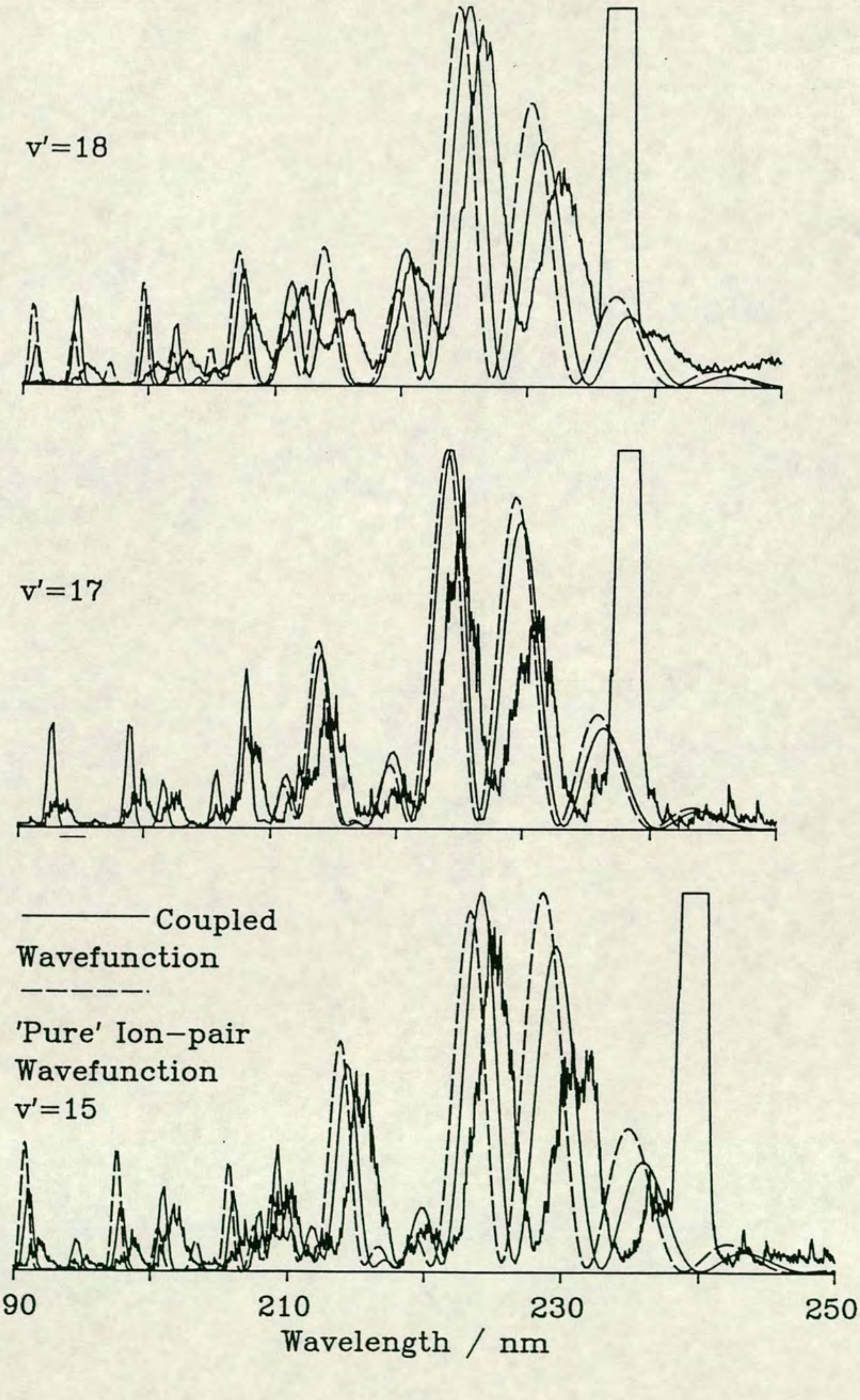

As for the $v' = 14$ level of HCl, all of the DCl levels experience a decrease in their vibrational energy which results in a small blue shift due to the lowering of the excitation energy of the excited state. However, this effect is less than that due to the phase shift of the wavefunction. Moreover, a change in the excitation energy merely shifts the spectrum to either longer or shorter wavelength but cannot explain the change in relative peak heights observed for the simulated spectra calculated with the coupled wavefunctions. Both effects of the coupling, the spectral shift and the peak height change, appear to improve the fit of the simulated spectra. Increased coupling of between the ion-pair state and the $E^1\Sigma^+$ (0^+) Rydberg state would further improve the agreement between the observed and simulated spectra but would adversely affect the calculated energy levels of the lower ion-pair state levels.

The coupling between the $E^1\Sigma^+$ (0^+) Rydberg state and the ion-pair state also allows the simulation of the ion-pair type fluorescence observed experimentally from the $v' = 0$ level of this state. The simulated and observed spectra are compared in figure 5.32. There is very good agreement between the two spectra.

---

[1] $v' = 0$ of the $E^1\Sigma^+$ (0^+) Rydberg state is $v' = 16$ of the coupled system.

Figure 5.32 Simulated Fluorescence from DCl Coupled Ion-pair Level v'=16

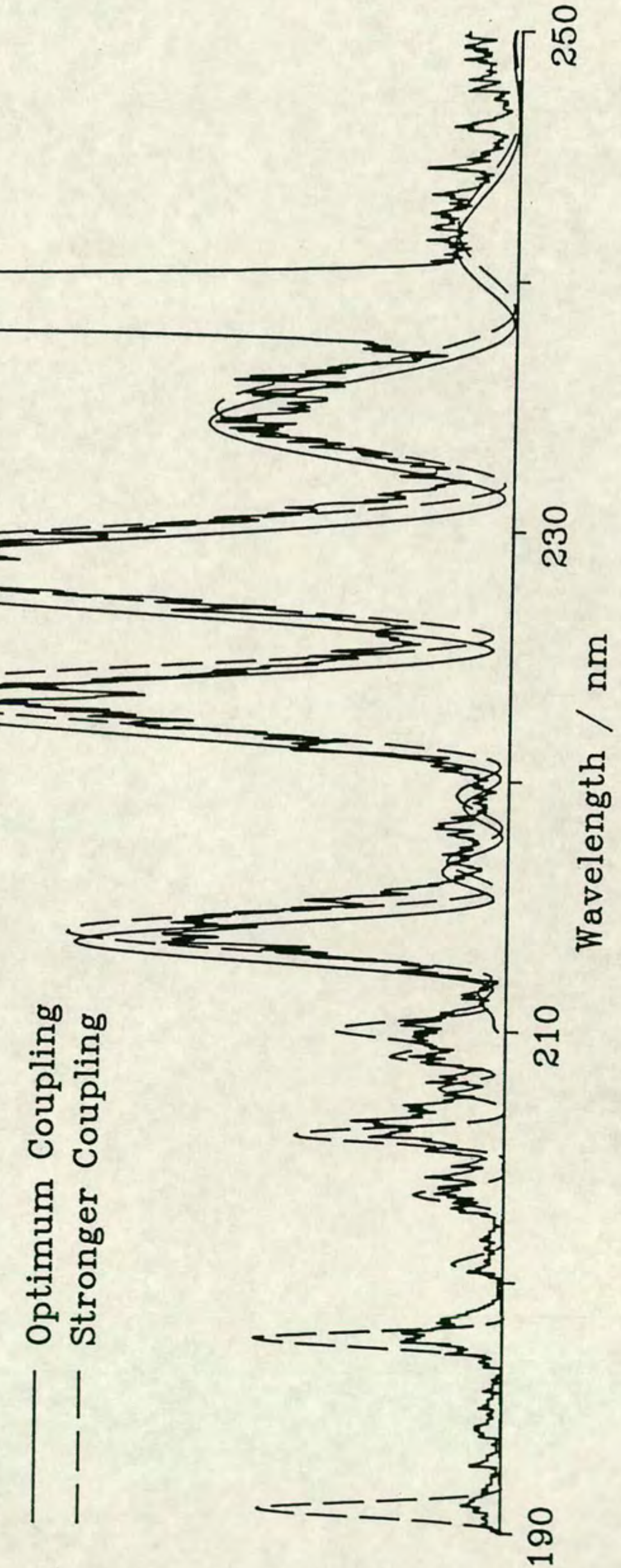

"Optimum Coupling" refers to the coupling parameters: set one on page 233, which give the best fit to the observed G_v and B_v values

With "Stronger Coupling" a poorer fit is achieved for G_v and B_v values but there is an improved fit to the fluorescence spectrum.

Chapter 6
Conclusion

A considerable body of experimental data was recorded for this work. The vibronic term values and rotational constants determined from the (2+1)REMPI spectra are in good agreement with the values reported in the literature [11] [13] [24] [77]. In practice two-photon absorption discriminated against the very strong $^1\Pi$ absorption bands which dominate the single photon absorption spectra of the hydrogen halides [24] and it was therefore possible to observed new states in HBr, DBr and HI. The (2+1)REMPI spectra of HBr also led to the reassignment of one of the states observed in single photon absorption and this too was in agreement with the literature [77]. Most of the experimental spectra recorded were fluorescence spectra which gave information on the interaction of the excited states of the hydrogen halides.

It has previously been shown that the ion-pair state in HCl [33] [65], DCl and HBr [77] is strongly homogeneously coupled to the 0^+ Rydberg states while there is no strong interaction between the ion-pair state and other Rydberg states. The dispersed fluorescence spectra recorded in this work support this analysis and indicate that this is also true for HI. These Rydberg states which are not homogeneously coupled to the ion-pair state exhibit only Rydberg type fluorescence which, in the case of DCl, can be analysed from simulation of the dispersed fluorescence spectra. The coupled Rydberg states exhibit characteristic ion-pair type fluorescence spectra. For DCl it was noted that there was ion-pair type fluorescence from the $E^1\Sigma^+$ (0^+) and $g^3\Sigma^-$ (0^+) Rydberg states, although that from the $g^3\Sigma^-(0^+)$ Rydberg state was much weaker than that from the $E^1\Sigma^+$ (0^+) state and was in addition to a very strong Rydberg type fluorescence band. However, it has been suggested in recent work on HCl using REMPI-TOFMS spectroscopy [33] that the $g^3\Sigma^-$ (0^+) state is not coupled to the ion-pair state because ionisation of HCl via this intermediate state gives only the molecular ion HCl^+. This was felt to be a diagnostic feature of the pure Rydberg states. This apparent contradiction arises because the coupling of the $g^3\Sigma^-$ (0^+) state to the ion-pair state is quite weak. In this case fluorescence spectroscopy is a more sensitive test of the coupling between the states than REMPI-TOFMS spectroscopy.

For HBr and DBr it was not possible to observed fluorescence from the excited states examined although the experimental setup used for DBr was identical to that used for DCl. Only very weak Br_2 fluorescence, analogous to that observed from HI, could be observed from DBr. This is indicative of a very short excited state lifetime in HBr and DBr because of rapid predissociation.

The dispersed fluorescence spectra recorded for HI confirm that this molecule is subject to the same homogeneous perturbation which is present in the lighter homologues, HCl and HBr. Dispersed fluorescence spectra were recorded from two 0^+ Rydberg states, the $E^1\Sigma^+$ (0^+) and $j^3\Sigma^-$ (0^+) states. Both exhibit characteristic ion-pair type fluorescence in addition to Rydberg fluorescence bands. The coupling of the $j^3\Sigma^-$ (0^+) state with the ion-pair state appears to be weaker that that for the $E^1\Sigma^+$ (0^+). As stated earlier it was also found that the $g^3\Sigma^-$ (0^+) state of DCl is less strongly coupled to the ion-pair state than the $E^1\Sigma^+$ (0^+) state. The reasons for this behaviour are discussed below.

The numerical simulations of fluorescence spectra were of considerable assistance in assigning the experimental spectra and analysing the coupling between the electronic states. In general it was possible to simulate the fluorescence observed from the uncoupled Rydberg states quite well. These spectra were not complicated by interaction with the ion-pair state and followed the expected behaviour for such transitions. For ion-pair type fluorescence, however, it was quite apparent that the potential energy curves for the ion-pair state were inadequate. A simple model in which only a single upper state potential was used could not adequately reproduce the experimental spectra. Therefore, in the simulation of fluorescence from HCl and DCl this approach was abandoned in favour of one which explicitly included the coupling of the ion-pair state and the 0^+ Rydberg states.

The calculation of energy levels and rotational constants of this coupled ion-pair - Rydberg system in the diabatic representation were quite successful in reproducing the observed data for HCl and DCl. The simpler of the two cases investigated, namely two state coupling, demonstrated that it was possible to reproduce the perturbations in the ion-pair state vibrational spacings and rotational constants due to the $E^1\Sigma^+$ (0^+) Rydberg state. Although the two state coupling model was rather limited it was of great use because the effect of the coupling between both states could be understood in terms of second order perturbation theory. The coupling strength used was of a similar order of magnitude to the vibrational spacing of the ion-pair levels and so it was necessary to consider several Rydberg vibrational levels rather than just the one nearest a given ion-pair level. It was found that a single Rydberg state could not account for the behaviour of the ion-pair state levels and an additional coupled Rydberg state, namely the $g^3\Sigma^-$ (0^+) state, had to be added.

The three state coupling scheme showed a marked improvement over the two state coupling scheme. It more closely matched the observed interactions in HCl and DCl where the two lowest 0^+ Rydberg states were strongly coupled to the ion-pair state. It was fortunate that in HCl and DCl there was an energy range in the ion-pair state over which only two strongly perturbing states were important. This was not the case in the heavier hydrogen halides. The coupling parameters determined for HCl and DCl were consistent with each other and in both cases it was found that the coupling of the $g^3\Sigma^-$ (0^+) state with the ion-pair state was approximately half of that for the $E^1\Sigma^+$ (0^+) state.

In the limit of Ω,ω angular momentum coupling, the $E^1\Sigma^+$ (0^+) and $g^3\Sigma^-$ (0^+) Rydberg states have pure doublet cores, $^2\Pi_{1/2}$ and $^2\Pi_{3/2}$, and will interact equally with the ion-pair state. As the coupling deviates from this limit the singlet character of the $E^1\Sigma^+$ (0^+) state will increase while the triplet character of the $g^3\Sigma^-$ (0^+) increases. Consequently the interaction between the $E^1\Sigma^+$ (0^+) state and the ion-pair state will increase while that between the $g^3\Sigma^-$ (0^+) state and the ion-pair state decreases. The angular momentum coupling in the Rydberg states in HCl and DCl is intermediate between Ω,ω and Λ,S coupling as described in Chapter 2. Therefore, the coupling element between the $E^1\Sigma^+$ (0^+) state and ion-pair state is greater than that between the $g^3\Sigma^-$ (0^+) state and the ion-pair state. The same behaviour would be expected for the $E^1\Sigma^+$ (0^+) and $j^3\Sigma^-$ (0^+) states in HI but in that case the difference between the coupling of the two states should be greater because the $j^3\Sigma^-$ (0^+) state is derived from a higher configuration and so would be expected to have a smaller interaction with the ion-pair state.

Fluorescence spectra simulated with the coupled wavefunctions also provided an improved fit to the observed dispersed fluorescence spectra of DCl and HCl over those obtained with a single uncoupled upper state potential. The phase shift induced in the ion-pair wavefunctions by coupling with the Rydberg states shifted the high frequency structure of the fluorescence without appearing to effect the low frequency Airy function envelope. The latter depends on the Mulliken difference potential which is not altered by the coupling, apart from a small shift in the vibrational energy of the upper state. The change in the fluorescence spectra was much greater than could be accounted for by this energy change.

While improvements have been made in the numerical modelling of the vibronic coupling between the ion-pair state and 0^+ Rydberg states of HCl and DCl there are still two limitations which must be overcome before this procedure can be extended in HCl, or applied to HBr and HI. The first is that many more states must be included in the coupling. In HCl and DCl the $H^1\Sigma^+$ (0^+) and $j^3\Sigma^-$ (0^+) states are the next highest set of Rydberg states above the $E^1\Sigma^+$ (0^+) and $g^3\Sigma^-$ (0^+) states. The $H^1\Sigma^+$ (0^+) state interacts with the ion-pair state and is at a low enough energy to affect the ion-pair vibrational levels near the $v' = 1$ level of the $E^1\Sigma^+$ (0^+) Rydberg state. The density of excited states is greater in HBr and HI so that all of the 0^+ Rydberg states are closer together and it is not possible to isolate one region of the ion-pair vibrational progression in which only two Rydberg states are important.

The second limitation is the lack of accurate *ab initio* or experimental potentials for the hydrogen halides. The *ab initio* potentials which have been reported in the literature for HCl do not give a good match to the observed data and could not be used in the coupling calculations. Also the experimentally determined Rydberg potentials used in this work are inadequate. This is partly due to the arbitrary choice of the inner limb of the ion-pair state potential. However, it is obvious that the vibrational spacing of the $E^1\Sigma^+$ (0^+) Rydberg state calculated for the coupled system is much greater than is observed experimentally.

In conclusion some progress has been made in understanding the vibronic coupling between the ion-pair state and the 0^+ Rydberg states of HCl and DCl. Before this can be extended further in HCl or to the other hydrogen halides it will be necessary to improve our knowledge of the electronic spectroscopy of the ion-pair state of HBr and HI to identify the minimum of this state. In addition detailed *ab initio* calculations of the electronic structure of the excited states of the hydrogen halides will be required. With the current advances in computational chemistry it is to be expected that such calculations will become available in the near future.

[1] J. Romand, Annales de Physique, 12^{e} serie, **4**, p 527, (1949)

[2] A.E. Douglas and F.R. Greening, Can. J. Phys., **57**, p 1650, (1979)

[3] F.R. Greening, Chem. Phys. Letts., **34**, p 581, (1975)

[4] G. Di Lonardo and A.E. Douglas, Can. J. Phys., **51**, p 434, (1973)

[5] S.G. Tilford, M.L. Ginter, and J.T. Vanderslice, J. Mol. Spec., **33**, p 505, (1970)

[6] M.L. Ginter and S.G. Tilford, J. Mol. Spec., **34**, p 206, (1970)

[7] S.G. Tilford, M.L. Ginter, and A.M. Bass, J. Mol. Spec, **34**, p 327, (1970)

[8] M.L. Ginter and S.G. Tilford, J. mol. Spec., **37**, p 159, (1971)

[9] S.G. Tilford and M.L. Ginter, J. Mol. Spec., **40**, p 568, (1971)

[10] M.L. Ginter, S.G. Tilford, and A.M. Bass, J. Mol. Spec., **57**, p 271, (1975)

[11] D.S. Ginter and M.L. Ginter, J. Mol. Spec., **90**, p 152, (1981)

[12] D.S. Ginter and M.L. Ginter, J. Mol. Spec., **90**, p 177, (1981)

[13] D.S. Ginter, M.L. Ginter, and S.G. Tilford, J. Mol. Spec., **92**, p 40, (1982)

[14] D.S. Ginter, M.L. Ginter, and S.G. Tilford, J. Mol. Spec., **92**, p 55, (1982)

[15] J.B. Nee, M. Suto, and L.C. Lee, J. Phys B, **18**, p L293, (1985)

[16] J.B. Nee, M. Suto, and L.C. Lee, J. Chem. Phys., **83**, p 2001, (1985)

[17] J.B. Nee, M. Suto, and L.C. Lee, J. Chem. Phys., **85**, p 719, (1986)

[18] J.B. Nee, M. Suto, and L.C. Lee, J. Chem. Phys., **85**, p 4919, (1986)

[19] J.A. Coxon and U.K. Roychowdhury, Can. J. Phys., **63**, p 1485, (1985)

[20] J.A. Coxon, P.G. Hajigeorgiou, and K.P. Huber, J. Mol. Spec., **131**, p 288, (1988)

[21] J.A. Coxon and P.G. Hajigeorgiou, J. Mol. Spec., **133**, p 45, (1989)

[22] S. Arepalli, N. Presser, D. Robie, and R.J. Gordon, Chem. Phys. Letts., **117**, p 64, (1985)

[23] S. Arepalli, N. Presser, D. Robie, and R.J. Gordon, Chem. Phys. Letts., **118**, p 88, (1985)

[24] S. Arepalli, N. Presser, D. Robie, and R.J. Gordon, J. Chem. Phys., **86**, p 5273, (1987)

[25] R.D. Clear, S.J. Riley, and K.R. Wilson, J. Chem. Phys., **63**, p 1340, (1975)

[26] B.J. Huebert and R.M. Martin, J. Phys. Chem., **72**, p 3046, (1968)

[27] J.G. Stamper and R.F. Barrow, J. Phys. Chem, **65**, p 250, (1961)

[28] R.F. Barrow and J.G. Stamper, Proc. Roy. Soc. A, **263**, p 259, (1961)

[29] R.F. Barrow and J.G. Stamper, Proc. Roy. Soc. A, **263**, p 277, (1961)

[30] R.F. Barrow and J.G. Stamper, Can. J. Phys., **40**, p 1279, (1962)

[31] L.M. Tashio, W. Ubachs, and R.N. Zare, J. Mol. Spec., **138**, p 89, (1989)

[32] G. Zimmerer, *Kinetics of Excited States Produced by Synchrotron Radiation*, In: Stud. Phys. Theor. Chem., 35(Photophysics and Photochemistry above 6eV), Edited by: F. Lahmani Elsevier, 1985

[33] T.A. Spiglanin, D.W. Chandler, and D.H. Parker, Chem. Phys. Letts., **137**, p 414, (1987)

[34] P. Brewer, P. Das, G. Ondey, and R. Bersohn, J. Chem. Phys., **79**, p 720, (1983)

[35] R. Callaghan, Y.L. Huang, S. Arepalli, and R.J. Gordon, Chem. Phys. Letts, **158**, p 531, (1989)

[36] T. Munakata, T. Midzukuki, A. Misu, M. Tsukakoshi, and T. Kasuya, Laser Chemistry, 7, (1985)

[37] M. Bettendorf, S.D. Peyerimhoff, and R.J. Buenker, Chem. Phys., **66**, p 261, (1982)

[38] M. Bettendorf, R.J. Buenker, S.D. Peyerimhoff, and J. Romelt, Z. fur Phys. A, **304**, p 124, (1982)

[39] J.A. Coxon and J.F. Ogilvie, J. Chem. Soc., Faraday Trans. 2, **78**, p 1345, (1982)

[40] J.A. Coxon, J. Mol. Spec., **117**, p 361, (1986)

[41] J.A. Coxon, J. Mol. Spec., **133**, p 96, (1989)

[42] E.F. van Dishoeck, M.C. van Hemert, and A. Dalgarno, J. Chem. Phys., **77**, p 3693, (1982)

[43] W.J. Stevens and M. Krauss, J. Chem. Phys., **77**, p 1368, (1982)

[44] D.M. Hirst and M.F. Guest, Molecular Physics, **41**, p 1483, (1980)

[45] H. Cribb, Chem. Phys., **88**, p 47, (1984)

[46] G.A. Segal and K. Wolf, Chem. Phys., **56**, p 321, (1981)

[47] D.A. Chapman, K. Balasubramanian, and S.H. Lin, Chem. Phys. Letts., **118**, p 192, (1985)

[48] G. Herzberg, *Molecular Spectra and Molecular Structure I. Spectra of Diatomic Molecules*, Van Nostrand, 1950.

[49] K.P. Huber and G. Herzberg, *Molecular Spectra and Molecular Structure IV. Constants of Diatomic Molecules*, Van Nostrand, 1976.

[50] P.R. Bunker, J. Mol. Spec., **28**, p 422, (1968)

[51] P.R. Bunker, J. Mol. Spec., **35**, p 306, (1970)

[52] P.R. Bunker, J. Mol. Spec., **37**, p 197, (1971)

[53] P.R. Bunker, J. Mol. Spec., **42**, p 478, (1972)

[54] H. Lefebvre-Brion and R.W. Field, *Perturbations in the Spectra of Diatomic Molecules*, Academic Press, Inc, 1986.

[55] C.E. Moore, *Atomic Energy Levels. Vols I-III*, U.S. department of Commerce National Bureau of Standards, Washington, 1952.

[56] R.S. Mulliken, Phys. Rev., **51**, p 310, (1937)

[57] R.S. Mulliken, J. Chem. Phys., **8**, p 382, (1940)

[58] R.S. Mulliken, Phys. Rev., **61**, p 277, (1942)

[59] J.F. Ogilvie, Chem. Phys. Letts., **140**, p 506, (1987)

[60] M.A. Brown, *Ph.D. Thesis*, University of Edinburgh, 1987.

[61] K.F. Purcell and J.C. Kotz, *Inorganic Chemistry*, Holt Saunders, 1977.

[62] J. Goodisman, J. Chem. Phys., **38**, p 2597, (1963)

[63] J.F. Ogilvie, W.R. Rodwell, and R.H. Tipping, J. Chem. Phys., **73**, p 5221, (1980)

[64] J.F. Ogilvie, J. Chem. Soc., Faraday Trans., **2205**, p 67, (1971)

[65] E. de Beer, B.G. Koenders, M.P. Koopmans, and C.A. de Lange, J. Chem. Soc. Faraday Trans. 2, **86**, p 2035, (1990)

[66] P.J. Bruna and S.D. Peyerimhoff, *Excited-State Potentials*, In: Adv. Chem. Phys 67(Ab Initio Methods in Quantum Chemistry - Part 1), Edited by: K.P. Lawley John Wiley and Sons, 1987

[67] P. Bernage and P.Niay, Can. J. Phys., **55**, p 1016, (1977)

[68] G. Guelachvili, P. Niay, and P. Bernage, J. Mol. Spec., **85**, p 253, (1981)

[69] M. Beland, *Internal Report to the Physics Faculty*, University of Hamburg, 1987.

[70] W. Demtröder, *Laser Spectroscopy*, Springer-Verlag, 1981.

[71] P.M. Johnson and C.E. Otis, *Molecular Multiphoton Spectroscopy with Ionization Detection*, Ann. Rev. Phys. Chem., **32**, pp 139-157, 1981

[72] D.H. Parker, *Laser Ionization Spectroscopy and Mass Spectrometry*, In: Ultrasensitive Laser Spectroscopy, Academic Press, Inc., pp 233-309, 1983

[73] J.B. Halpern, H. Zacharias and R. Wallenstein, J. Mol. Spec., **79**, p 1, (1980)

[74] M.A. Brown, *Ph.D. Thesis*, Edinburgh University, 1987

[75] T.E. Adams, R.S. Morrison, and E.R. Grant, Rev. Sci. Instrum., **51(1)**, p 141-2, (1980)

[76] R. Callaghan and R.J. Gordon, J. Chem. Phys., **93**, p 4624, (1990)

[77] Y. Xie, P.T.A. Reilly, S. Chilukuri, and R.J. Gordon, J. Chem. Phys., **95**, p 584, (1991)

[78] J. Tellinghuisen, *The Franck-Condon Principle in Bound-Free Transitions*, In: Adv. Chem. Phys 60(Photodissociation and Photoionzsation), Edited by: K.P. Lawley John Wiley and Sons, 1985

[79] R.S. Mulliken, J. Chem. Phys., **55**, p 309, (1971)

[80] K.M. Sandos and J.C. Wormhoudt, Phys. Rev., **A7**, p 1889, (1973)

[81] R. Schmiedl, H. Dugan, W. Meier, and K. Welge, Z. Phys. A, **304**, p 137, (1982)

[82] S. Singleton, *Ph.D. Thesis*, University of Edinburgh, 1990.

[83] T. Ridley *Private Communication*

[84] L.D. Mikheev, A.P. Shirokikh, A.V. Startsev, and V.S. Zuev, Opt. Comm., **26**, p 237, (1978)

[85] M. Martin, C. Fotakis, R.J. Donovan, and M.J. Shaw, Il Nuovo Cimento, **63B, N.1**, p 300, (1981)

[86] K.P. Killeen and J.G. Eden, Appl. Phys. Lett., **43**, p 539, (1983)

[87] K.P. Killeen and J.G. Eden, J. Opt. Soc. Am., **B2**, p 430, (1985)

[88] P.M. Morse, Phys. Rev., **34**, p 57, (1929)

[89] D. ter Harr, Phys. Rev., **70**, p 222, (1946)

[90] A.S. Coolidge, H.M. James, and E.L. Vernon, Phys. Rev., **54**, p 57, (1938)

[91] J.S. Wright, J. Chem. Soc., Faraday Trans. 2, **84(3)**, p 219-226, (1988)

[92] A.L.G. Rees, Proc. Phys. Soc. London, **59**, p 998, (1947)

[93] W.M. Kosman and J.Hinze, J. Mol. Spec., **56**, p 93, (1975)

[94] C.R. Vidal and H. Scheingraber, J. Mol. Spec., **65**, p 46, (1977)

[95] J.A. Coxon and P.G. Hajigeorgiou, J. Mol. Spec., **139**, p 84, (1990)

[96] I.M. Torrens, *Interatomic Potentials*, Academic Press, 1972.

[97] P.M. Johnson, *Introduction to Atomic and Molecular Collisions*, Plenum Press, 1982.

[98] F. Jenc, Adv. At. Mol. Phys., **19**, p 265, (1983)

[99] J.L. Graves and R.G. Parr, Phys. Rev., **A31**, p 1, (1985)

[100] J. Tellinghuisen, S.D. Henderson, D. Austin, K.P. Lawley, and R.J. Donovan, Phys. Rev. A, **39**, p 39, (1989)

[101] W.D. Sheasley and C.W. Matthews, J. Mol. Spec., **47**, p 420, (1973)

[102] Y.P. Varshni and R.C. Shukla, J. Mol. Spec., **16**, p 63, (1965)

[103] J.W. Cooley, Math. Comp., **15**, p 363, (1961)

[104] J.K. Cashion, J. Chem. Phys., **39**, p 1872, (1963)

[105] R.N. Zare, J. Chem. Phys., **40**, p 1934, (1964)

[106] K.P. Lawley and R. Wheeler, J. Chem. Soc., Faraday Trans. 2, **77**, p 1133,

(1981)
[107] J.H. Wilkinson, *The Algebraic Eigenvalue Problem*, Oxford University Press, 1965.
[108] A.S. Davydov, *Quantum Mechanics*, Pergamon Press, 1965.

Appendix A
A Brief Note on Spin-Orbit Coupling

A number of the Rydberg states in the hydrogen halides exhibit rotationally dependent predissociation. Therefore, in addition to the electrostatic coupling, there must be a spin or rotation coupling mixing the Rydberg states with the repulsive states. The spin-orbit operator has been suggested as being responsible for this interaction. It has the form:

$$\mathbf{H}^{SO} = L_z \cdot S_z + \tfrac{1}{2}(L_+ \cdot S_- + L_- \cdot S_+) \qquad (6.1)$$

where L_z and S_z are the projections of the orbital and spin angular momentum on the z-axis and L_+, L_-, S_+ and S_- are raising and lowering operators [54]. $\mathbf{H}^{SO}$ has the general selection rule; $\Delta\Omega = 0$. The first term, $L_z \cdot S_z$, has the selection rules; $\Delta\Lambda = \Delta\Sigma = 0$ and $\Delta S = 0, \pm 1$. For diagonal matrix elements of this term $\Delta S = 0$. This is the term which splits spin-orbit components in multiplets [54]. Off-diagonal matrix elements have the selection rule; $\Delta S = \pm 1$. They are non-zero for $\Omega = 1(\Lambda = 1,\ \Sigma = 0)$ states and give rise to mixing of singlet and triplet states from the same configuration (isoconfigurational mixing) [51].

The second term is an off-diagonal term which mixes states from different configurations [54]. The selection rules are; $\Delta\Omega = 0$, $\Delta\Lambda = -\Delta S = \pm 1$. A $^1\Pi$ state can therefore only mix with a $^3\Sigma$ state while a $^3\Pi$ state can mix with either a $^1\Delta$ or a $^5\Sigma$ state.

The $L_z \cdot S_z$ operator will not lead directly to predissociation because it only couples states arising from the same configuration. However, it mixes $^3\Pi$ and $^1\Pi$

states and this may have a small, indirect effect on predissociation. The raising and lowering operator will lead directly to predissociation but spin-orbit predissociation does not appear to be as important as electronic predissociation for states which possess the same symmetry as the repulsive states. For other Rydberg states, such as the $^1\Delta_2$, spin orbit effects will be dominant .

Appendix B
Semiclassical Derivation of Wavelength Dependence of Bound-Free Fluorescence Intensity in Ion-pair → Ground State Transitions

The results of the semiclassical analysis of fluorescence spectra have been briefly discussed in Chapter 4. This method provides a good qualitative description of the features observed in the fluorescence spectra of the hydrogen halides. However, more quantitative information may also be extracted from the observed spectra using these semiclassical methods.The intensity of the fluorescence emitted in a transition from an excited vibronic level to a lower level is dependent on the overlap integral of the wavefunctions of the two levels. Figure 4.2 illustrates the case where an excited vibronic level of the ion-pair state decays radiatively to the ground state. The vibrational and electronic parts of the wave function can be separated and the electronic overlap treated as a slowly varying function of R: the electronic transition dipole moment function $\mu_{el}(R)$. The overlap integral for the transition i→f is therefore given by

$$M_{if} = \langle \chi_f | \mu_{el}(R) | \chi_i \rangle \qquad 1$$

where χ_x is the primitive semiclassical wavefunction of the level x.The wavefunction is of the form

$$\chi_x = \left(\sqrt{k_x} \right)^{-1} \sin \varphi_x \qquad 2$$

here k_x is the local wavenumber

$$k_x = \hbar^{-1} \sqrt{2\mu \left(E - V_x(R) \right)}$$

φ_x is given by

$$\varphi_x = \int_{R''}^{R} k_x \, dR + \delta_x$$

R" is the inner classical turning point and δ_x is a phase shift. The phase shift for the primitive WKB wavefunction is $\frac{\pi}{4}$ if φ_x is defined relative to the inner classical turning point of the vibration. Substitution of the wavefunction (2) into the overlap integral (1) gives

$$M_{if} = \int_{-\infty}^{\infty} \left(\sqrt{k_i k_f}\right)^{-1} \mu_{el}(\,R\,) \sin \varphi_i \sin \varphi_f \, dR \qquad 3$$

This can be rearranged to

$$M_{if} = \int_{-\infty}^{\infty} \left(\sqrt{k_i k_f}\right)^{-1} \mu_{el}(\,R\,) (\cos \varphi_+ + \cos \varphi_-) \, dR \qquad 4$$

The φ_+ term is rapidly varying and has a mean of zero. Therefore it does not contribute significantly to the overlap integral. By the stationary phase the remaining cosine term will only contribute to the integral if the phase φ_- is slowly varying with R. The connection between this condition and the Franck-Condon principle and the Mulliken difference potential becomes apparent if a point of stationary phase is considered. At such a point

$$\frac{\partial \varphi_-}{\partial R} [\, = k_i - k_f \,] = 0 \quad .$$

This is equivalent to the Franck-Condon principle and it is evident that the points of stationary phase define the Mulliken difference potential.

The solution of equation (4) for a single valued difference potential is a sinusoidal variation in the fluorescence intensity which reflects the structure of the vibrational wavefunction of the emitting level. If the lower level is bound then the reflection structure will act as an envelope for the discrete vibronic transitions.

For a double valued difference potential then there will be a contribution to the overlap integral (4) from each stationary point corresponding to a particular wavelength, ω. Because the overlap integral must be squared to determine the fluorescence intensity the two terms will interfere. In this case for a bound-free transition the fluorescence spectrum has the form of a slowly varying sinusoidal function modulated by a higher frequency term. The low frequency envelope of the spectrum can be determined by assuming a parabolic form for the difference potential and considering emission to the maximum of the difference potential where the two interfering limbs coalesce.

The wavefunctions (2) are taken relative to the maximum of the difference potential, R_m. The overlap integral (4) thus becomes

$$M_{if} = \int_{-\infty}^{\infty} \left(\sqrt{k_i k_f}\right)^{-1} \mu_{el}(R) \cos \varphi_- \, dR \qquad 5$$

where

$$\varphi_- = \int_{R_m}^{R} k_i - k_f \, dR + \Delta\delta_{if} \quad .$$

The term $\Delta\delta_{if}$ is the difference in phase between the two wavefunctions at the point $R = R_m$. The integral (5) can be rearranged to

$$M_{if} = \int_{-\infty}^{\infty} \left(\left(\sqrt{k_i k_f}\right)^{-1} \mu_{el}(R) \left(\begin{array}{c} \cos \int_{R_m}^{R} k_i - k_f \, dR \cos \Delta\delta_{if} \\ - \\ \sin \int_{R_m}^{R} k_i - k_f \, dR \sin \Delta\delta_{if} \end{array} \right) \right) dR \qquad 6$$

The sine term is an odd function and, as the integration is over a small range of R near zero, integrates to zero. The $\cos\Delta\delta_{if}$ and the leading terms in the outer bracket are either constants or vary slowly with R near Rm. They can therefore be taken out of the integration to leave

$$M_{if} = \cos \Delta\delta_{if} \left(\sqrt{k_i k_f}\right)^{-1} \mu_{el}(R_m) \int_{-\infty}^{\infty} \left(\cos \int_{R_m}^{R} k_i - k_f \, dR \right) dR \quad . \qquad 7$$

The difference $(k_i - k_f)$ can reformulated in terms of experimental observables and parameters of the difference potential using the following relations

$$V_{if}(R) = V(R_m) + \frac{K}{2}(R - R_m)^2$$

$$V_{if}(R) = V_f(R) - E_i - V_i(R)$$

$$V(R_m) = E_i - h\nu_m$$

$$E_i - E_f = h\nu$$

and

$$V_x = E_x - \frac{h^2 k_x^2}{8\pi^2 \mu}$$

to give

$$k_i - k_f = \frac{8\pi^2 \mu}{h^2(k_i + k_f)}\left(h(\nu - \nu_m) + \frac{K}{2}(R - R_m)^2 \right).$$

8

Substituting (8) into (7) and integrating the integral (6) becomes

$$\int_0^\infty \cos\left(\frac{8\pi^2 \mu}{h^2(k_i + k_f)}\left(h(\nu - \nu_m)(R - R_m) + \frac{K}{2}(R - R_m)^3\right)\right) dR .$$

9

This is the integral form of the Airy function, a standard mathematical function. The variation in fluorescence intensity with wavelength, $I(\lambda)$, is thus given by

$$I(\lambda) = C(\lambda)\left(Ai\left(\left(\frac{K\overline{v}^2}{8\pi^2 h}\right)^{\frac{-1}{3}}(\nu - \nu_m)\right)\right)^2$$

10

where $\overline{v}^2$ is a mean velocity and the factor $C(\lambda)$ includes the instrument response function, the ν^3 dependency of the Einstein coefficient and the other factors indicated above. The electronic transition dipole moment function which is presumed to be constant in (7) above may vary with R. Assuming a linearly varying electronic transition dipole moment function $\mu_{el}(R)$,

$$\mu_{el}(R) = \mu_{el}(R_m) + \mu'_{el}(R - R_m)$$

11

is used then an additional term in R is introduced into the integral (6). Because the second term is odd the sine terms in (6) must be retained and we have an additional integral term

$$\int_0^\infty \mu'_{el}(R - R_m)\sin\left(\frac{8\pi^2 \mu}{h^2(k_i + k_f)}\left(h(\nu - \nu_m)(R - R_m) + \frac{K}{2}(R - R_m)^3\right)\right) dR$$

12

This is the integral from of the derivative of the Airy function with respect to ν. $I(\lambda)$ is therefore given by

$$I(\lambda) = C(\lambda)\left(\begin{array}{c} \cos \Delta\delta_{if} \mathrm{Ai}\left(\left(\frac{K\bar{v}^2}{8\pi^2 h}\right)^{\frac{-1}{3}}(\nu - \nu_m)\right) \\ + \\ \mu_{rel} \quad \sin \Delta\delta_{if}\left(\mathrm{Ai}'\left(\left(\frac{K\bar{v}^2}{8\pi^2 h}\right)^{\frac{-1}{3}}(\nu - \nu_m)\right)\right) \end{array}\right)^2 \qquad 13.$$

where μ_{rel} is the ratio of the slope of $\mu_{el}(R)$ to $\mu_{el}(R)$ at R_m. A scaling term $C(\lambda)$ is used to account for the arbitary units of the experimental spectrum and to adjust for the ν^3 factor in the Einstien coefficient for spontaneous emission. The angle $\Delta\delta_{if}$ is the phase difference at R_m between the upper state wavefunction and the lower state wavefunction. It is therefore a function of the emission wavelength and results in the high frequency structure observed in the emission spectra.

Appendix C
Observed Rotational Line Positions in (2+1)REMPI Spectra

Observed Rotational Lines in (2+1)REMPI Spectra of HBr

$B^1\Sigma^+ (0^+) \leftarrow X^1\Sigma^+$

J	(m+8-0) Q(J)	(m+10-0) $H^{79}Br$ Q(J)	(m+10-0) $H^{81}Br$ Q(J)	(m+11-0) Q(J)
0	80029.70	81198.04	81196.59	81685.87
1	80022.50	81188.45	81187.37	81678.46
2	80007.49	81170.89	81169.64	81664.87
3	79982.87	81138.88	81137.98	81643.87
4	79947.49	81102.75	81101.31	
5	79906.13			

$E^1\Sigma^+ (0^+) \leftarrow X^1\Sigma^+$

J	(0-0) Q(J)	(1-0) Q(J)
0	80168.80	82275.71
1	80164.05	82272.83
2	80156.34	82266.47
3	80145.08	
4	80130.84	82424.60
5	80116.02	82224.46
6	80098.84	82204.12

$H^1\Sigma^+ (0^+) \leftarrow X^1\Sigma^+$

J	(0-0) Q(J)	(1-0) $H^{79}Br$ Q(J)	(1-0) $H^{81}Br$ Q(J)
0	79647.72	81899.20	81898.25
1	79645.32	81893.24	81892.61
2	79640.22	81882.90	81882.27
3	79633.02	81867.55	81866.92
4	79623.71		
5	79612.61		
6	79599.72		
7	79584.14		
8	79565.26		

J	$j^3\Sigma^-$ (0^+) (0–0) Q(J)	$k^3\Pi_1$ (1) (0–0) Q(J)	$n^3\Pi_1$ (1) (2–0) Q(J)
0	82184.63		
1	82182.08	80392.17	82031.80
2	82176.38	80390.99	82029.83
3	82167.48	80389.79	82027.25
4	82154.45	80387.11	82024.33
5	82133.84	80384.12	82021.50
6	82103.05		82019.16

$f^3\Delta_1$ (1) ← $X^1\Sigma^+$ (0-0)

J	S(J)	R(J)	Q(J)
0	76703.76		
1		76687.60	
2		76701.06	76652.92
3		76713.85	76649.73
4		76726.01	76645.58
5			76640.77
6			76635.18
7			76628.47
8			76616.51

$F^1\Delta_2$ (2) ← $X^1\Sigma^+$ (0-0)

J	S(J)	R(J)	Q(J)	P(J)
0	77059.34			
1	77091.74	77042.89		
2	77124.46	77058.54	77010.51	
3	77157.04	77074.19	77009.68	76960.77
4	77188.35	77089.32	77008.62	76942.71
5	77218.44	77103.92	77007.28	76924.05
6	77247.98	77119.05	77005.53	76904.95
7				76886.67

$I^1\Delta_2$ (2) ← $X^1\Sigma^+$ (0-0)

J	S(J)	R(J)	Q(J)	P(J)
0	81362.98			
1	81392.88	81346.79		
2	81422.80	81360.49	81314.46	
3	81452.73	81372.94	81311.97	81264.11
4	81478.96	81384.78	81308.55	81244.26
5		81395.99	81304.37	81223.16
6		81406.58	81298.90	81202.07
7		81415.62	81292.68	
8			81285.55	
9			81276.53	

Observed Rotational Lines in DBr (2+1)REMPI Spectra of DBr

$B^1\Sigma^+ (0^+) \leftarrow X^1\Sigma^+$

	(m+8-0)	(m+8-0)	(m+10-0)	(m+11-0)
$D^{79}Br$		$D^{81}Br$	$D^{79}Br$	$D^{81}Br$
J	Q(J)	Q(J)	Q(J)	Q(J)
0	79666.14	79664.59	80905.90	80902.86
1	79661.61	79660.28	80899.58	80897.32
2	79653.93	79652.52	80890.14	80888.07
3	79641.81	79640.56	80875.46	80873.56
4	79625.70	79624.78	80856.98	80854.94
5	79600.91	79599.74	80833.86	80831.76
6	79574.73	79573.48	80807.62	80805.99
7	79542.88	79541.47	80779.11	80777.47

$E^1\Sigma^+ (0^+) \leftarrow X^1\Sigma^+$ (2-0)

$D^{79}Br$		$D^{81}Br$	$D^{79}Br$	$D^{81}Br$
J	Q(J)	S(J)	Q(J)	S(J)
0	80756.07	80791.18	80755.01	80790.12
1	80755.01	80803.16	80753.96	80802.10
2	80752.62	80813.01	80751.55	80811.95
3	80748.90	80820.74	80747.84	80819.41
4	80743.84		80742.78	
5	80737.21		80736.13	
6	80728.17		80727.10	
7	80714.89		80713.82	

$E^1\Sigma^+ (0^+) \leftarrow X^1\Sigma^+$ and $H^1\Sigma^+ (0^+) \leftarrow X^1\Sigma^+$

	(3-0)	(3-0)	$H^1\Sigma^+ (0^+)$
$D^{79}Br$		$D^{81}Br$	(0-0)
J	Q(J)	Q(J)	Q(J)
0	82204.70	82203.74	79716.98
1		82202.07	79715.12
2	82201.46	82200.49	79711.93
3	82198.64	82197.67	79707.67
4	82195.39	82193.99	79702.89
5	82190.64	82189.16	79698.11
6		82183.45	79692.53
7			79686.43
8			79680.32
9			79673.41

Unassigned State, v' > 0, and $m^3\Pi_1$ (1) $\leftarrow$ $X^1\Sigma^+$ (1-0)

		$m^3\Pi_1$ (1) (1-0)	
		D^{81}Br	D^{79}Br
J	Q(J)	Q(J)	Q(J)
0	79519.90		
1	79518.89		
2	79517.15	82871.11	82870.82
3	79514.48	82869.69	82869.24
4	79511.06	82867.35	82866.99
5	79506.49	82864.57	82864.12
6	79501.18	82861.39	82860.88
7	79494.67		
8	79486.69		

Unassigned $\Omega = 2$ State

J	S(J)	R(J)	Q(J)	P(J)
0	82777.55			
1	82797.33	82766.99		
2	82817.22	82776.12	82745.61	
3	82836.66	82784.98	82744.36	82713.26
4	82855.30	82793.39	82742.49	82701.02
5	82873.33	82801.36	82740.25	82688.51
6	82890.74	82808.71	82737.57	82675.57
7		82815.87	82734.26	82662.36
8		82822.59	82730.50	82648.53
9		82828.68	82726.57	
10		82833.88	82722.01	

Observed Rotational Lines in (2+1)REMPI Spectra of HI

$B^1\Sigma^+ (0^+) \leftarrow X^1\Sigma^+$

J	(m+5-0) Q(J)	(m+6-0) Q(J)	(m+7-0) Q(J)	(m+10-0) Q(J)	(m+11-0) Q(J)
0	70512.11	70948.29	71481.9	72506.03	73458.21
1	70506.73	70943.69	71475.4	72501.32	73451.54
2	70496.00	70934.31	71462.6	72492.21	73438.64
3	70480.78	70920.05	71443.0	72478.48	73419.56
4	70462.29	70900.79	71416.1	72459.88	73394.08
5	70439.05	70878.55	71383.7		
6	70414.04	70858.05	71338.2		
7					
8	70359.31				

J	$H^1\Sigma^+$ (0^+) (1-0) Q(J)	$k^3\Pi_0$ $(0^\pm)$ (1-0) Q(J)	$k^3\Pi_0$ $(0^\pm)$ (1-0) Q(J)	$E^1\Sigma^+$ (0^+) (0-0) Q(J)	$E^1\Sigma^+$ (0^+) (1-0) Q(J)
0	70243.83	70321.23	72352.51	70850.64	72651.80
1	70242.41	70318.62	72350.97	70849.61	72648.95
2	70240.99		72348.14	70847.09	72643.56
3		70305.49	72343.60	70843.24	72634.34
4		70296.45	72337.21	70836.99	72629.36
5		70282.71		70826.20	72615.49
6				70812.15	72600.65
7					72583.45
8					72564.22

J	$k^3\Pi_1$ (1) (1-0) Q(J)	$k^3\Pi_1$ (1) (2-0) Q(J)	$j^3\Sigma^-$ (0^+) (0-0) Q(J)	0^+ Q(J)
0				
1			73253.21	73382.51
2		73177.72	73249.86	73380.17
3	71122.0	73175.81	73245.02	73376.51
4	71120.7	73168.06	73238.09	73371.17
5	71116.8	73163.05	73228.71	73365.12
6	71114.4	73156.37	73215.69	73357.80
7	71111.6	73146.35	73195.51	73348.93
8				73339.52

Unassigned $\Omega = 0^+$ State

J	S(J)	Q(J)	O(J)
0	71338.2		
1	71360.4	71301.9	
2	71381.7	71299.8	71263.8
3	71402.4	71296.7	71236.8
4	71422.6	71292.6	71208.8
5		71287.6	
6		71281.5	

$F^1\Delta_2$ (2) ← $X^1\Sigma^+$ (0-0)

J	S(J)	R(J)	Q(J)	P(J)	O(J)
0	70266.75				
1	70292.02	70253.81			
2	70316.63	70266.19	70228.35		
3	70341.31	70278.17	70228.18	70189.92	
4	70363.47	70290.20	70227.67	70176.67	70139.32
5	70387.26	70301.68	70226.81	70163.26	70113.37
6	70411.06	70313.10	70226.02	70149.62	70086.99
7	70434.29	70324.30	70224.55	70135.82	70060.46
8		70335.16	70222.85	70121.74	
9			70221.26	70107.83	
10			70219.39	70093.54	
11			70216.55	70078.97	
12			70214.29		

$I^1\Delta_2$ (2) ← $X^1\Sigma^+$ (0-0)

J	S(J)	R(J)	Q(J)	P(J)	O(J)
0	72026.3				
1	72051.7	72013.3			
2	72076.0	72026.3			
3		72037.7		71949.0	
4	72125.0	72049.4		71935.7	71897.7
5	72148.6	72060.6		71921.9	71871.4
6	72171.5	72071.2	71983.2	71908.1	71844.9
7	72194.4	72082.9	71981.5	71893.8	71818.7
8			71979.5	71879.4	71792.0
9					71765.0
10			71972.1		71737.9
11			71965.0		
12			71962.0		

Appendix D
Courses and Conferences Attended

In accordance with the regulations of the Department of Chemistry, University of Edinburgh I have attended the following courses during my period of study:

1. Organic Photochemistry
2. Quantum Physics 2
3. Theoretical Chemistry
4. Laser Physics 2
5. The Gaseous Enviroment
6. Signal Processing
7. Technical German
8. Mass Spectroscopy
9. Reaction Dynamics
10. Introduction to EUCS
11. FORTRAN 77 Programming
12. Recent Advances in Physical Chemistry 1988
13. Recent Advances in Physical Chemistry 1989

In addition I have attended all Laser Chemistry research group meetings, deparmental seminars, joint Edinburgh - Heriot-Watt laser chemistry group meetings, and the following conferences:

1. XIth. International Symposium on Molecular Beam , Edinburgh, July 1987
2. Royal Society of Chemistry, Faraday Division, High Resolution Spectroscopy Group meeting, Birmingham, December 1988